THE UNIVERSITY OF QUEENSLAND

SCHOOL OF CIVIL ENGINEERING

REPORT CH111/18

NUMERICAL INVESTIGATIONS OF BOX CULVERT HYDRODYNAMICS WITH SMOOTH, UNEQUALLY ROUGHENED AND BAFFLED BARRELS TO ENHANCE UPSTREAM FISH PASSAGE

AUTHORS: Gangfu ZHANG and Hubert CHANSON

HYDRAULIC MODEL REPORTS

This report is published by the School of Civil Engineering at the University of Queensland. Lists of recently-published titles of this series and of other publications are provided at the end of this report. Requests for copies of any of these documents should be addressed to the Civil Engineering Secretary.

School of Civil Engineering
The University of Queensland
Brisbane QLD 4072
AUSTRALIA

Telephone: (61 7) 3365 4163
Fax: (61 7) 3365 4599

URL: http://www.civil.uq.edu.au/

ISBN No. 978-1-74272-197-2
First published in 2018 by
School of Civil Engineering
The University of Queensland, Brisbane QLD 4072, Australia

The University of Queensland, St Lucia QLD, Australia

Numerical Investigations of Box Culvert Hydrodynamics with Smooth, Unequally Roughened and Baffled Barrels to Enhance Upstream Fish Passage

by

Gangfu ZHANG
Postdoctoral Research Fellow, The University of Queensland, School of Civil Engineering,
Brisbane QLD 4072, Email: g.zhang3@uq.edu.au

and

Hubert CHANSON
Professor, The University of Queensland, School of Civil Engineering, Brisbane QLD 4072,
Australia, Email: h.chanson@uq.edu.au

HYDRAULIC MODEL REPORT No. CH111/18
ISBN 978-1-74272-197-2
The University of Queensland, School of Civil Engineering,
January 2018

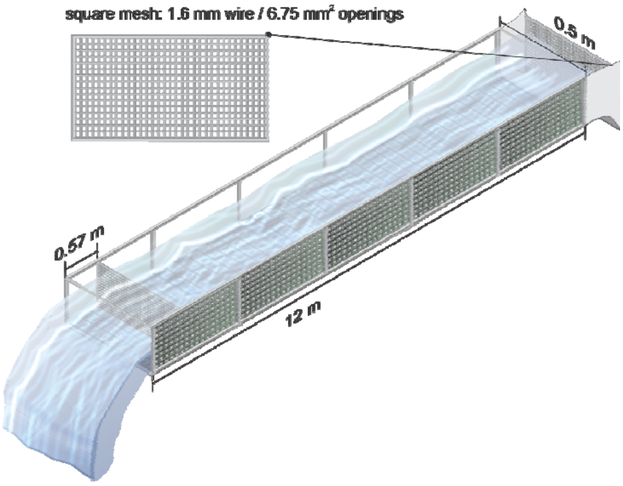

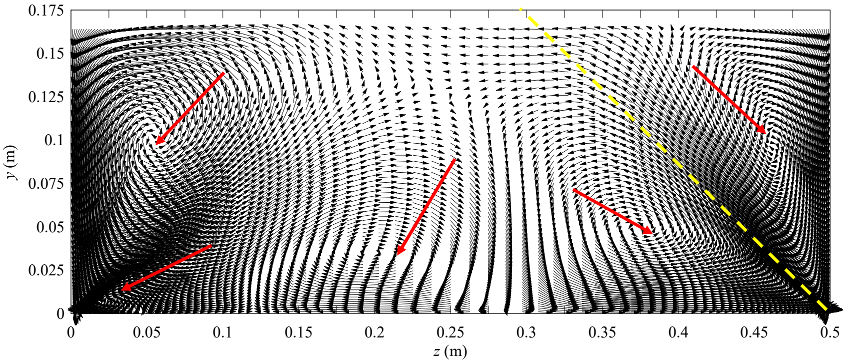

Top Left: Culvert outlet in operation beneath Canungra-Tamborine Road on 31 March 2017
Top Right: Sketch of experimental channel with rough bed and rough left sidewall
Bottom: Secondary flow patterns in a culvert barrel with rough bed and rough left sidewall

ABSTRACT

The hydrodynamics of box culverts configured with smooth, unequal and singular roughness were investigated numerically with three-dimensional (3D) computational fluid dynamics (CFD) modelling. Validation tests were conducted systematically against detailed physical data sets, for flow conditions corresponding to less-than-design flows. Results showed that free surface profiles were reasonably replicated with little mesh-dependence. The models were more successful at reproducing the most important flow features than to yield quantitative matches to the experimentally obtained velocity profiles, because of inaccuracies in grid settings and wall modelling. Nonetheless, the models were most informative to assess distinctive roughness behaviours responsible for the generation of low velocity zones (LVZs) for fish passage. These included corners, confluence between secondary flow cells and wakes behind singular obstacles. A visual assessment of low velocity regions for each culvert barrel boundary configuration underscored size and contiguity as the most desirable traits for upstream fish passage, particularly for weak swimmers. Overall, the present experience suggests a hybrid approach combining both numerical and experimental methods for future optimisations of culvert design for fish navigability. A comprehensive verification and validation of the CFD modelling model is most critical, requiring a detailed physical data set to compare systematically physical and numerical quantities of interest.

Keywords: Computational fluid dynamics CFD, Cavity ventilation, Fish passage, Large eddy simulation LES, Numerical modelling, Open channel flow, RANS, Roughness, Standard box culvert, Triangular baffle, Validation, Low velocity zones (LVZs).

TABLE OF CONTENTS

Page

Abstract ii
Keywords ii
Table of contents iii
List of symbols iv

1. Introduction 1

2. Numerical modelling 4

3. Box culvert with smooth bed and sidewalls 14

4. Box culvert with rough bed and left sidewall 20

5. Box culvert with small triangular baffles 34

6. Discussion 57

7. Conclusion 62

8. Acknowledgements 64

APPENDICES

Appendix A. Preliminary investigations 65

Appendix B. Box culvert with small triangular baffles: numerical results 75

Appendix C. On low velocity zones produced by different culvert configuration systems 95

REFERENCES R-1

Bibliography
Internet bibliography
Open Access Repositories
Bibliographic reference of the Report CH111/18

LIST OF SYMBOLS

The following symbols are used in this report:

C_{ij}	convection tensor (m^2/s^3);
C_{Smag}	Smagorinsky constant (=0.2);
C_u	a constant (= 0.09);
C_w	a constant (= 0.15);
$C_{\varepsilon 1}$	a constant (= 1.44);
$C_{\varepsilon 2}$	a constant (= 1.92);
C_1'	a constant (= 0.5);
C_2'	a constant (= 0.39);
$D_{L,ij}$	laminar diffusion contribution to T_{kij} (m^2/s^3);
$D_{T,ij}$	turbulent diffusion contribution to T_{kij} (m^2/s^3);
d	water depth (m);
E	a constant (= 9.793);
f	dimensionless boundary shear stress, expressed in the form of Darcy-Weisbach friction factor;
$G(\boldsymbol{r}, \boldsymbol{x})$	filter function used in large eddy simulation;
g	gravitational acceleration (m/s^2);
h_b	baffle height (m);
h_{max}	maximum cell edge length (m);
h_{wn}	wall-normal grid spacing (m);
k	turbulent kinetic energy (m^2/s^2);
k_p	turbulent kinetic energy at a near-wall point P (m^2/s^2);
k_s	equivalent sand roughness (m);
k_s^*	dimensionless roughness;
L	length (m);
L_b	baffle spacing (m);
N_z	number of cells in the z-direction;
n_k	the x_k component of the unit normal to the wall;
P	time-averaged static pressure (Pa); turbulent production (m^2/s^3);
P_{ij}	production tensor (m^2/s^3);
p	instantaneous pressure (Pa);
Q	discharge (m^3/s);
$\boldsymbol{Q}$	an arbitrary field quantity defined as a function of space and time;
$\bar{\boldsymbol{Q}}(\boldsymbol{x}, t)$	an arbitrary field quantity defined as a function of space and time, filtered with G;
q	unit discharge (m^2/s)
R_{ij}	pressure-rate-of-strain tensor
S	rate-of-strain tensor (1/s);
S_q	source term for phase q ($kg/m^3/s$);

$\overline{S}_{ij}$	filtered rate-of-strain tensor (1/s);
T_{kij}	Reynolds stress flux ($\mathrm{m}^2/\mathrm{s}^3$);
Tu	turbulence intensity;
$\vec{T}'$	turbulent energy flux ($\mathrm{m}^2/\mathrm{s}^3$);
t	time (s); tangential coordinate (m);
U	x component of time averaged velocity (m/s);
U_{max}	maximum time-averaged streamwise velocity in a vertical profile (m/s);
U_{mean}	bulk velocity (m/s);
U_p	time-averaged velocity at a near-wall point P (m/s);
U^*	dimensionless velocity (section 2.2.1);
u'	fluctuating streamwise velocity (m/s);
u_{rms}	root-mean-square of streamwise velocity fluctuations (m/s);
u_i	i^{th} component of instantaneous velocity (m/s);
$\overline{u}$	i^{th} component of instantaneous velocity (m/s), filtered with G;
$\vec{u}$	instantaneous mixture velocity (m/s);
V	time-averaged spanwise velocity (m/s);
v'	fluctuating spanwise velocity (m/s);
v_{rms}	root-mean-square of spanwise velocity fluctuations (m/s);
W	1- time-averaged bed-normal velocity (m/s); 2- channel width (m);
w'	fluctuating bed-normal velocity (m/s);
w_{rms}	root-mean-square of bed-normal velocity fluctuations (m/s)
x	streamwise coordinate (m);
x_b	streamwise coordinate of baffle (m);
$\boldsymbol{x}$	position (m);
y	spanwise coordinate (m);
y^+	distance from the wall normalised by the viscous length scale;
y^*	dimensionless distance from wall ;
z	bed-normal coordinate (m);
z_{Umax}	location of maximum streamwise velocity in a vertical profile (m);
$z_{urms,max}$	location of maximum streamwise velocity fluctuations in a vertical profile (m);

α_q	volume fraction of phase q;
Δ	characteristic length that accounts for grid anisotropies in LES model (m);
ΔB	wall roughness function;
Δ_x	grid spacing in x-direction (m);
Δ_y	grid spacing in y-direction (m);
Δ_x	grid spacing in z-direction (m);

δ_{ij}	Kronecker delta;
E	turbulent dissipation (m^2/s^3);
κ	von Kármán constant;
v	kinematic viscosity (m^2/s);
ν_T	eddy viscosity dependent on k and ε (m^2/s)
ν_t	subgrid-scale turbulent viscosity (m^2/s);
ρ_w	water density (kg/m^3);
σ_k	turbulent Prandtl number for kinetic energy (= 1.0);
σ_ε	turbulent Prandtl number for dissipation (= 1.3);
τ_{ij}^R	subgrid-scale stress tensor (Pa);
τ_0	wall shear stress (Pa);
Ω	vorticity (1/s);
$\varnothing$	diameter (m);

Subscripts

a	air;
in	inlet;
rms	root mean square;
w	water;

Abbreviations

DNS	direct numerical simulation;
LES	large eddy simulation;
LVZ	low-velocity zone;
NVD	normalised variable diagram;
RANS	Reynolds-averaged Navier-Stokes;
rms	root-mean-square;
RSM	Reynolds stress model;
SGS	sub-grid scale;
VOF	volume of Fluid;
WMLES	wall-modelled LES;
2D	two-dimensional;
3D	three-dimensional.

1. INTRODUCTION

A culvert is a relatively short hydraulic conduit designed to pass floodwater through an embankment (Fig. 1.1). Culvert designs require considerations of potential hydraulic, structural, geotechnical engineering implications onto the surrounding environment and eco-systems. Efficient culvert designs based on economical and hydraulic engineering considerations yield the smallest barrel size while achieving inlet control operation (Chanson, 2000, 2004). This often leads to excessive barrel velocities, which may hamper the upstream passage of targeted fish species during rainfall and runoff events. For example, the characteristic endurance speed of small-bodied Australian native fish species is typically less than 0.6 m/s (Hurst et al., 2007; Rodgers et al., 2014). The recent recognition of the ecological impacts of culverts on fish passage led to reconsiderations of culvert design guidelines (Behlke et al., 1991). In particular, roughness-induced effects on fish swimming performance have been investigated by a number of recent studies (Lacey and Rennie, 2012; Baki et al., 2014; Cassan et al., 2014). These flow features are often trackable and taken advantage of by the fish (David et al., 2012; Johnson and Rice, 2014). New evidences on the role which roughness plays are often conflicting. While several studies have associated upstream navigability in certain fish species with an increase in roughness (e.g. Heaslip, 2015), others reported minimum benefit to fish swimming performance (e.g. Nikora et al., 2013). Despite these inconsistencies, the common view remains that low velocity zones are favoured swimming zones by fish (Lupandin, 2005; Cotel, 2006), which often swim next to the sidewall and in the corners (Wang et al., 2016b; Cabonce et al., 2017; Wang and Chanson, 2017).

A number of culvert design options were developed to provide low velocity zones, to improve fish passage. Of particular interest, an asymmetrically roughened barrel was investigated by Wang et al. (2016a,b), and a simple small corner baffle system was tested by Cabonce et al. (2017). The first configuration involved the effects of both bed and sidewall roughness, and the interactions between multiple roughened sections. Such a design favours fish passage along the roughened side of the channel, in lieu of equal provisions on both sides in a smooth barrel. The installation of baffles, on the other hand, has been reviewed extensively as an alternative to reduce excessive barrel velocities to improve fish passage (Larinier, 2002; Olsen and Tullis, 2013; Duguay and Lacey, 2014; Chanson and Uys, 2016; Cabonce et al., 2017). The baffles generate recirculation zones in their rears, thus reducing the required effort to negotiate the obstacles. Baffles might drastically decrease the hydraulic capacity of culverts at certain range of discharges (Larinier, 2002; Olsen and Tullis, 2013). Yet a recent study (Chanson and Uys, 2016) has reported little hydraulic impact by a small triangular corner baffle system, implemented in a flat barrel. To date, the reconciliation between the economic and ecological aspects of culvert design remains a most significant challenge for the development of national guidelines (Fairfull and Witheridge, 2003; Hunt et al., 2012).

(a) Culvert outlet beneath Canungra-Tamborine Road QLD (Australia) on 31 March 2017

(b) Culvert system as part of an irrigation and flood control system on Tungkang River (Taiwan) on 27 December 2015

(c) Culvert inlet in operation on Norman Creek, Brisbane (Australia) on 25 February 2018 for a relatively small discharge

Figure 1.1 – Standard box culverts with multicell arrangement.

The combination of geometric and roughness factors in the barrel governs the hydrodynamic behaviours of a culvert system. A detailed characterisation of the hydrodynamics thereof is of paramount importance to any study, as significant deviations in behavioural responses may be induced to some fish (Papanicolaou and Talebbeydokhti, 2002). This calls for the ability to measure and quantify the three-dimensional flow features in a culvert barrel, which extends beyond a typical characterisation of velocity fields towards an inclusion of both turbulence quantities and secondary flow patterns. Properly validated Computational Fluid Dynamics (CFD) models provide a means for understanding the fundamental processes driving the hydrodynamic responses of each barrel configuration, which might dictate fish behaviours in turn. The numerical approach provides increased data fidelity and level of description in terms of flow parameters of key importance to the migrating fish, while keeping the study cost moderate (Pavlov et al., 2000; Hotchkiss, 2002; Nikora et al., 2003). For example, Feurich et al. (2012) used CFD models to check the effectiveness of spoiler baffle configurations on improving the upstream passage of small fish species, as well as their associated adverse impact on culvert conveyance, thus allowing informed design decisions to be made. In addition, filtered models (e.g. Large Eddy Simulation (LES)) provide further advantage by simulating the flow unsteadiness, which may be exploited by some fish species to allow an easier passage (Wang et al., 2010; Tarrade et al., 2011).

The present work extends the works of Wang et al. (2016a) and Cabonce et al. (2017) to investigate different roughness effects in a straight culvert barrel, using a numerical approach based upon three-dimensional (3D) computational fluid dynamics (CFD). Hydrodynamic characteristics were assessed for three boundary configuration scenarios, including: (1) a smooth barrel; (2) a barrel with roughened bed and left sidewall; (3) barrels with corner baffles at different combinations of baffle sizes and spacings; (4) a ventilated baffle with a circular opening through its centroid. The numerical results provide a comprehensive database for understanding the mechanisms associated with a strong compatibility with upstream fish passage, for flow conditions corresponding to less-than-design flows, and a reference to guide future optimisations of culvert design. Based the results, recommendations on the CFD modelling methods are provided in the conclusion.

2. NUMERICAL MODELLING

2.1 OVERVIEW

The hydrodynamics in box culverts are affected by a broad spectrum of turbulent motions with characteristic sizes ranging from the barrel cell's internal width down to the Kolmogorov scale. The interactions between these turbulent features and the main flow produce characteristic flow patterns which are unique to each boundary configuration and discharge. The objective herein is to reproduce reliably the velocity field, deemed as the most important quantity for fish passage, induced by each boundary configuration. Different methods may be warranted, with increasing computation times ([1]), since the nature of velocity field is influenced by additional complexities such as roughness asymmetry and transitory behaviours.

Considering the simplest case of a smooth barrel ([2]), it may be sufficient to solve the governing equations for a few mean quantities since the flow is statistically stationary. The flow is governed by the boundary layer originating from the bottom invert provided that the channel is sufficiently wide. Secondary circulations should have minor effects, and the results are expected to be comparable to a simplified 2D (x-z plane) model ([3]). Therefore, it is the case herein that the simplest turbulence model (i.e. standard k-ε model) is deemed sufficient for the purpose of the present investigation (Launder and Spalding, 1972). In narrow smooth culvert channels, sidewall effects become increasingly important, as the channel width reduces and 3D modelling must be conducted. The relative increase in sidewall to bed flow wetted perimeters alters the secondary currents in an open channel cross-section, which would result in more pronounced 'dips' in velocity contours and cause a downshift in the location where the maximum velocity occurs (Schlichting; 1979; Nezu and Rodi, 1986; Apelt and Xie, 2011). Further, the change may cause a breakdown in the standard wall model as the bed-normal velocity component increases in effect. It would be expected that the standard k-ε model decreases gradually in effectiveness, as the channel width reduces.

For the second, slightly more complicated case involving a rough bottom and a rough left side wall, the standard k-ε model is unlikely to yield satisfactory results because of its simplistic assumptions. Whilst stationarity is still assumed, the roughness asymmetry results in some turbulence anisotropy and strong secondary flow patterns which may have a substantial impact on the main flow.

---

[1] Computations were conducted on a Dell^{TM} Precision T5810 workstation with Xeon® Processor E5-2620 v4 (8C, 2.1GHz, 3.0GHz Turbo, 2133MHz, 20MB, 85W) and 128 GB RAM.

[2] Considering a multi-cell box culvert (Fig. 1.1), this study focuses on a single cell as a basic element.

[3] Also called 2DV model.

Consequently, the present study adopts the Reynolds stress model (RSM) to address the principal limitation of the standard k-ε model, namely an isotropic turbulent diffusivity, by solving six additional transport equations for each of the Reynolds stresses, in addition to an equation for the dissipation rate ε. The RSM has greater potential to accurately predict more complex flow types, including those involving turbulence anisotropy, streamline curvature, swirl, rotation, and rapid changes in strain rate, than standard one- or two-equation turbulence models (Pope, 2000).

For the last configuration which incorporates small triangular corner baffles, a traditional Reynolds-averaged Navier-Stokes (RANS) equations-based approach is unlikely to be sufficient as the flow becomes dominated by the separation zone behind each baffle which exhibits transitory behaviours. As such, the velocity field becomes time-dependent which stipulates the simulations be performed in a correspondent manner. A large eddy simulation (LES) becomes more suitable in this case as the largest eddies, being most important for momentum transport, are directly resolved, and it captures the full transient behaviours, without being nearly as taxing as a direct numerical simulation (DNS) (Rodi et al., 2013).

The abovementioned approaches are either turbulence model-based (i.e. k-ε and RSM) or simulation-based (LES). The turbulence model-based approaches involve solving the RANS equations to obtain mean quantities of interest (i.e. velocity) by either hypothesising a turbulent viscosity (k-ε) or solving modelled transport equations for the Reynolds stresses directly (RSM). The large eddy simulation directly recovers the time-dependent behaviours of the large scale motions whilst approximating the small scale motions by suitable models. The following subsections detail the basic equations and assumptions employed by each approach adopted in the present study ([4]).

2.2 RANS MODELS

2.2.1 Standard k-ε model

For the simplest smooth barrel configuration, a RANS-based approach is required in view of the required level of description, computational complexity, and computational resources. However, the RANS method gives rise to additional stress terms arising from a fluctuating velocity field, which leads to a closure problem (Chanson, 2009,2014).

The unknowns in the RANS equations (i.e. Reynolds stresses) may be determined either via the turbulent viscosity hypothesis or from modelled transport equations (Pope, 2000). The present study

---

[4] Herein the software ANSYS$^{\text{TM}}$ FLUENT version 18.0 was used and references to the turbulence modelling implementation in the software are included.

represents a case of simple turbulent shear flow, in which the mean velocity gradients and turbulence characteristics change relatively slowly following the mean flow. Thus the Reynolds stress balance is governed by local mean velocity gradients and the simple turbulent viscosity hypothesis may become reasonable. The standard *k*-*ε* model (Launder and Spalding, 1972) is the simplest and most widely incorporated complete turbulence model (i.e. flow dependent specification not required). It is adopted herein for benchmark purposes.

The selection of geometries and turbulence models for the preliminary simulations represents a compromise between the level of description and computational efficiency. A combination of 2D and 3D simulations using the standard *k*-*ε* model provided the simplicity required to examine ANSYS$^{\mathrm{TM}}$ FLUENT's capabilities within a reasonable amount of time. The chosen approach also provides length and time scale information to be used as a basis for future investigations. These models are widely accepted and incorporated into most CFD codes (Pope, 2000), and are well validated for 2D thin shear flows with small pressure gradient.

The standard *k*-*ε* model belongs to a family of two-equation models, in which the model transport equations for the turbulent kinetic energy *k* and dissipation *ε* are solved respectively. The exact transport equation for *k* is (Pope, 2000):

$$\frac{\partial k}{\partial t} + <\vec{u}> \cdot \nabla k = -\nabla \cdot \vec{T}^{'} + P - \varepsilon$$

where *P* is the production, *ε* is the dissipation, and $\vec{T}^{'}$ is the energy flux modelled with a gradient diffusion hypothesis:

$$\vec{T}^{'} = -\frac{\nu_T}{\sigma_k} \nabla k$$

where σ_k is the turbulent Prandtl number for kinetic energy, and ν_T is the eddy viscosity supposed to depend only on *k* and *ε*:

$$\nu_T = C_\mu \frac{k^2}{\varepsilon}$$

where C_μ = 0.09 is a model constant. Since the exact equation of *ε* pertains to the smallest scale motions in the dissipation range, an empirical treatment is adopted for its model equation (Pope, 2000):

$$\frac{\partial \varepsilon}{\partial t} + <\vec{u}> \cdot \nabla \varepsilon = \nabla \cdot \left(\frac{\nu_T}{\sigma_\varepsilon} \nabla \varepsilon \right) + C_{\varepsilon 1} \frac{P\varepsilon}{k} - C_{\varepsilon 2} \frac{\varepsilon^2}{k}$$

where the standard model constants are $C_{\varepsilon 1}$ = 1.44, $C_{\varepsilon 2}$ = 1.92, σ_k = 1.0, and σ_ε = 1.3 (Launder and Spalding, 1972).

Wall treatment

A challenge in CFD is the numerical treatment of the near wall sublayer, where viscous effects are important and large gradients are present. As the adoption of a fine grid can be very expensive, most industrial models have incorporated wall functions as an immediate solution. The present study adopts the standard wall functions implemented in the software ANSYS^{TM} FLUENT based upon the work of Launder and Spalding (1974). For pipes and channels, experiments indicate the existence of a semi-logarithmic near wall layer of the form:

$$\frac{U_p U^*}{\tau_0 / \rho} = \frac{1}{\kappa} ln(E \frac{\rho U^* y_p}{\mu}) - \Delta B$$

where U_p is the time-averaged velocity at a near-wall point P, τ_0 is the wall shear stress, $E = 9.793$ is an empirical constant, ΔB is a function of the form and size of the roughness, and U^* is a dimensionless velocity defined as:

$$U^* = C_\mu^{1/4} k_p^{1/2}$$

where $C_\mu = 0.09$ and k_p is the turbulent kinetic energy at the point P. The logarithmic law was valid for $30 < y^* < 300$, where:

$$y^* = \frac{\rho U^* y_p}{\mu}$$

For $y^* < 11.225$, FLUENT applies the laminar stress-strain relationship such that:

$$\frac{U_p U^*}{\tau_0 / \rho} = y^*$$

When $y^* > 11.225$, the log-law is employed (ANSYS).

FLUENT models the wall roughness effects (i.e. ΔB) in three distinct regimes, depending on the dimensionless roughness height:

$$k_s^* = \frac{\rho k_s U^*}{\mu}$$

$$k_s^* \leq 2.25 \text{ (hydrodynamically smooth)}$$

$$2.25 < k_s^* \leq 90 \text{ (transitional)}$$

$$k_s^* > 90 \text{ (rough)}$$

where k_s is the equivalent sand roughness height.

2.2.2 Reynolds stress model

The Reynolds stress model (RSM) is the most elaborate RANS-type turbulence model available in ANSYS. The RSM addresses the greatest limitation of the standard *k-ε* model, by solving six additional transport equations for each of the Reynolds stress components, in addition to an equation for the dissipation rate ε. Thus, the RSM has greater potential to accurately predict more complex flow types, including those involving turbulence anisotropy, streamline curvature, swirl, rotation, and rapid changes in strain rate, than standard one- or two-equation turbulence models (ANSYS).

The exact transport equations for the Reynolds stresses may be deduced from the Navier-Stokes equations as follows (Pope, 2000):

$$\frac{\partial}{\partial t}\left\langle u_i^{'}u_j^{'}\right\rangle + C_{ij} + \frac{\partial}{\partial x_k}T_{kij} = P_{ij} + R_{ij} - \varepsilon_{ij}$$

where C_{ij} is the convection tensor:

$$C_{ij} = U_k \frac{\partial\left\langle u_i^{'}u_j^{'}\right\rangle}{\partial x_k}$$

where T_{kji} is the Reynolds stress flux:

$$\frac{\partial}{\partial x_k}T_{kij} = -\left(D_{T,ij} + D_{L,ij}\right)$$

where $D_{T,ij}$ and $D_{L,ij}$ are the components of T_{kij} respectively attributed to turbulent and molecular diffusion:

$$D_{T,ij} = -\frac{\partial}{\partial x_k}\left(\left\langle u_i^{'}u_j^{'}u_k^{'}\right\rangle + \frac{1}{\rho}\left\langle u_i^{'}p^{'}\right\rangle\delta_{jk} + \frac{1}{\rho}\left\langle u_j^{'}p^{'}\right\rangle\delta_{ik}\right)$$

$$D_{L,ij} = \frac{\partial}{\partial x_k}\left(\nu\frac{\partial\left\langle u_i^{'}u_j^{'}\right\rangle}{\partial x_k}\right)$$

P_{ij} is the production tensor:

$$P_{ij} = -\left\langle u_i^{'}u_k^{'}\right\rangle\frac{\partial U_j}{\partial x_k} - \left\langle u_j^{'}u_k^{'}\right\rangle\frac{\partial U_i}{\partial x_k}$$

R_{ij} is the pressure-rate-of-strain tensor:

$$R_{ij} = \frac{1}{\rho}\left\langle p^{'}\left(\frac{\partial u_i^{'}}{\partial x_j} + \frac{\partial u_j^{'}}{\partial x_i}\right)\right\rangle$$

and ε_{ij} is the dissipation tensor:

$$\varepsilon_{ij} = 2\nu\left\langle\frac{\partial u_i^{'}}{\partial x_k}\frac{\partial u_j^{'}}{\partial x_k}\right\rangle$$

where the instantaneous velocity is decomposed into its mean and fluctuating components i.e. $u_i = U_i + u_i^{'}$, $p^{'}$ is the fluctuating pressure, δ_{ij} is the Kronecker delta, ρ is the density and ν is the kinematic viscosity.

In FLUENT, the turbulent diffusion tensor $D_{T,ij}$ is modelled based on a simplification (Lien and Leschziner, 1994) of the generalised gradient-diffusion model due to Daly and Harlow (1970):

$$D_{T,ij} = \frac{\partial}{\partial x_k}\left(\frac{\nu_T}{\sigma_k}\frac{\partial\left\langle u_i' u_j'\right\rangle}{\partial x_k}\right)$$

where $\sigma_k = 0.82$ and ν_T is computed similarly to the standard k-ε model:

$$\nu_T = C_\mu \frac{k^2}{\varepsilon}$$

where $C_\mu = 0.09$.

The pressure-rate-of-strain term R_{ij} is modelled with an ε-based linear approach due to Gibson and Launder (1978), Fu et al. (1987), and Launder (1989). The classical approach decomposes R_{ij} into a fast, a slow, and a harmonic component:

$$R_{ij} = R_{ij}^{(r)} + R_{ij}^{(s)} + R_{ij}^{(h)}$$

The rapid term $R_{ij}^{(r)}$ responds immediately to a change in the mean velocity gradients and is modelled as:

$$R_{ij}^{(r)} = -C_2\left[\left(P_{ij} - C_{ij}\right) - \frac{1}{3}\delta_{ij}\left(P_{kk} - C_{kk}\right)\right]$$

where $C_2 = 0.60$.

The slow term $R_{ij}^{(s)}$ is modelled as:

$$R_{ij}^{(s)} = -C_1\frac{\varepsilon}{k}\left(\left\langle u_i' u_j'\right\rangle - \frac{2}{3}\delta_{ij}k\right)$$

where $C_1 = 1.8$.

The harmonic term $R_{ij}^{(h)}$ is responsible for redistribution of stresses from the normal to the tangential direction next to the wall, which is modelled as:

$$\begin{aligned}R_{ij}^{(h)} = {} & C_1'\frac{\varepsilon}{k}\left(\left\langle u_k' u_m'\right\rangle n_k n_m \delta_{ij} - \frac{3}{2}\left\langle u_i' u_k'\right\rangle n_j n_k - \frac{3}{2}\left\langle u_j' u_k'\right\rangle n_i n_k\right)\frac{C_l k^{3/2}}{\varepsilon y_n} \\ & + C_2'\left(R_{km}^{(r)} n_k n_m \delta_{ij} - \frac{3}{2}R_{ik}^{(r)} n_j n_k - \frac{3}{2}R_{jk}^{(r)} n_i n_k\right)\frac{C_l k^{3/2}}{\varepsilon y_n}\end{aligned}$$

where $C_1' = 0.5$, $C_2' = 0.3$, n_k is the x_k component of the unit normal to the wall, y_n is the normal distance to the wall, and $C_l = C_\mu^{3/4} / \kappa$ with $\kappa = 0.4187$ (ANSYS).

The dissipation tensor ε_{ij} is modelled as:

$$\varepsilon_{ij} = \frac{2}{3}\delta_{ij}\varepsilon$$

where the scalar dissipation rate ε is computed similarly to the standard k-ε model.

The boundary conditions required for the individual Reynolds stresses $\langle u_i^{'} u_j^{'} \rangle$ and dissipation rate ε are obtained from the turbulence intensity and characteristic length. Using a local coordinate system, the Reynolds stresses at the wall-adjacent cells may be computed from the standard wall functions:

$$\frac{\langle u_t^{'2} \rangle}{k} = 1.098, \frac{\langle u_n^{'2} \rangle}{k} = 0.247, \frac{\langle u_\lambda^{'2} \rangle}{k} = 0.655, -\frac{\langle u_t^{'} u_n^{'} \rangle}{k} = 0.255$$

where t is the tangential coordinate, n is the normal coordinate, λ is the binormal coordinate, and k is obtained from solving its transport equation globally.

2.3 LARGE EDDY SIMULATION

The large-eddy simulation (LES) method conceptually involves applying a low-pass filter function to the governing conservation equations so that only the most energetic motions are directly resolved. The general filtering operation is defined as (Leonard, 1974; Pope, 2000):

$$\overline{\boldsymbol{Q}}(\boldsymbol{x},t) = \int G(\boldsymbol{r},\boldsymbol{x}) \boldsymbol{Q}(\boldsymbol{x}-\boldsymbol{r},t) d\boldsymbol{r}$$

where the integral is performed over the entire flow domain, and the filter function G satisfies the normalisation condition:

$$\int G(\boldsymbol{r},\boldsymbol{x}) d\boldsymbol{r} = 1$$

In FLUENT, the finite-volume discretisation implies an implicit filtering operation:

$$G(\boldsymbol{r},\boldsymbol{x}) = \begin{cases} 1/V, & \boldsymbol{r} \in V \\ 0, & \text{otherwise} \end{cases}$$

where V is the volume of a computational cell.

For an incompressible flow, the filtered continuity equation and equations of motion and Navier-Stokes equations can be written as (Pope, 2000):

$$\frac{\partial \overline{u}_i}{\partial x_i} = 0$$

$$\frac{\partial \overline{u}_i}{\partial x_i} + \frac{\partial}{\partial x_j}\left(\overline{u}_i \overline{u}_j\right) = -\frac{1}{\rho}\frac{\partial \overline{p}}{\partial x_i} + 2\nu \frac{\partial}{\partial x_j}\overline{S}_{ij} - \frac{\partial \tau_{ij}^R}{\partial x_j}$$

where $\overline{S}_{ij}$ is the filtered rate-of-strain tensor:

$$\overline{S}_{ij} = \frac{1}{2}\left(\frac{\partial \overline{u}_i}{\partial x_j} + \frac{\partial \overline{u}_j}{\partial x_i}\right)$$

and τ_{ij}^R is the subgrid-scale stress tensor:

$$\tau_{ij}^R = \overline{u_i u_j} - \overline{u_i u_j}$$

Closure of the filtered equations for u_i may be achieved by representing the residual stress tensor τ_{ij}^{R} .with appropriate choices of subgrid-scale (SGS) models.

Subgrid-scale (SGS) models

Turbulent flows are characterised by eddies encompassing a wide range of length and time scales (Hinze, 1959). Large eddies are crucial in terms of the transport of momentum and energy, and are typically problem specific. Small eddies tend to be more isotropic and are increasingly likely to satisfy a universal model. In LES, large and small eddies are respectively resolved and modelled. Thus, the approach falls in between DNS and RANS in terms of computational complexity and resolution of flow features. Since the large eddies reduce significantly in size in the near-wall region, the LES solution becomes Reynolds number dependent and its computational cost increases drastically to properly resolve wall-bounded flows. FLUENT adopts subgrid-scale (SGS) models based upon the Boussinesq hypothesis, such that:

$$\tau_{ij}^{R} - \frac{1}{3}\tau_{kk}^{R}\delta_{ij} = -2\nu_t \overline{S}_{ij}$$

where ν_t is the SGS turbulent viscosity, and τ_{kk} is the isotropic part of SGS stresses absorbed in the filtered pressure term in the governing LES equations.

A typical SGS model does not resolve the Reynolds number dependency of LES and hence requires an unrealistically fine mesh near wall. To overcome this limitation, the present study adopts the Algebraic Wall-Modelled LES Model (WMLES) (Shur et al., 2008), which activates a RANS portion in the inner part of the logarithmic layer, near the wall. In conjunction, the model provides a modified LES formulation for the outer part of the boundary layer. The original Algebraic WMLES computes the eddy viscosity using a hybrid length scale:

$$\nu_t = \min\left[\left(\kappa d_w\right)^2, \left(C_{Smag}\Delta\right)^2\right]\left\{1 - \exp\left[-\left(y^+ / 25\right)^3\right]\right\} S$$

where d_w is the wall distance, S is the strain rate, $\kappa = 0.41$, $C_{Smag} = 0.2$, and y^+ is the normal to the wall scaled by inner variables, and Δ accounts for the grid anisotropies in the LES model:

$$\Delta = \min\left[\max\left(C_w d, C_w h_{\max}, h_{wn}\right), h_{\max}\right]$$

where h_{max} is representative of the maximum cell edge length, h_{wn} is the wall-normal grid spacing, and $C_w = 0.15$ is a constant. This model vastly improves the Reynolds number scalability, with the following resolution requirement (ANSYS) for a typical boundary layer volume (δ^3):

$$\Delta_x = \frac{\delta}{10}, \quad \Delta_y = \frac{\delta}{20}, \quad N_z = 30 - 40$$

where x, y and z align with the streamwise, spanwise and normal directions respectively. The formulation allows for substantial reductions of several orders of magnitude in the number of required cells as well as the associated computational cost. One deficiency of the original WMLES formulation is that the model could overestimate eddy-viscosities in separating shear layers (e.g. behind baffles). ANSYS provides an enhancement of the original formulation by computing the LES portion of the model using the difference $|S-\Omega|$ instead of *S*, where Ω is the vorticity magnitude. This enhancement was adopted by the present work.

2.4 FREE SURFACE MODEL

When the culvert barrel is not flowing full, a free surface flow problem occurs, which consists of a flowing secondary phase (i.e. water) with a primary phase (i.e. air) above it. The two fluids are immiscible, and the interfacial length is significantly greater than the computational grid size. Hirt and Nichols (1981) proposed a Volume of Fluid (VOF) method that is advantageous under these conditions.

The VOF model adopted herein solves the governing continuity and momentum equations for the mixture, which results in a velocity field shared by both phases. The mixture density, viscosity, and velocity are calculated as sums of the component phases weighted by their respective volume fractions (α_q), the local values of which are also used to assign the appropriate fluid properties to each control volume in the domain. An interface exists for $0 < \alpha_q < 1$, which is tracked by solving the volume fraction equation corresponding to one or more secondary phases:

$$\frac{\partial\left(\alpha_q \rho_q\right)}{\partial t}+\nabla\cdot\left(\alpha_q \rho_q \vec{u}\right)=S_q+\sum_{p=1}^{n}\dot{m}_{pq}$$

where ρ_q is the density of phase q, $\vec{u}$ is the mixture velocity, S_q is a source term, and $\dot{m}_{pq}$ is the mass flux from phase p to q. The interface shape is assumed to be piecewise linear and can be modelled by computing a set of surface normals $\vec{n}_i = \nabla\alpha_{pi}$ such that the volume fraction of phase *q* in each cell *i* bounded by the interface is α_{qi}.

The VOF simulations have been performed in a time-accurate (i.e. transient) manner, where velocity and pressure were specified at the inlet and outlet respectively. Stability issues were observed frequently for steady-state simulations likely due to numerical diffusion of the free surface.

2.5 CONVERGENCE CRITERIA

The numerical package adopted herein solves all governing equations using a finite-volume approach. The associated discretisation and solution processes inevitably produce numerical imbalances throughout the computational domain. In FLUENT, the residual R^{ϕ} for a general conserved variable ϕ is computed as the sum of the imbalances in all cells P through the domain:

$$R^{\phi} = \sum_{P} \left| \sum_{nb} a_{nb}\phi_{nb} + b - a_P \phi_P \right|$$

where the absolute-value-signed term is the imbalance in cell P. To facilitate a better comparison, FLUENT scales the residual by a factor representative of the flow rate of ϕ through the domain:

$$R_S^{\phi} = \frac{R^{\phi}}{\sum_{P} \left| a_P \phi_P \right|}$$

where α_P is the centre coefficient, and ϕ_P is the value of the variable ϕ at cell P.

For the RANS simulations (i.e. smooth barrel & rough bed and left sidewall), the solution residuals (e.g. continuity, U_i, k, ε, α_2, $\left\langle u_i^{'} u_j^{'} \right\rangle$) were monitored constantly through iterations until the scaled residuals for all variables decreased by three orders of magnitude (i.e. 10^{-3}). Upon achieving this condition, the mass flux report was examined to ensure that the overall mass imbalance remained below 0.2%. All results presented in the following subsections conform to the abovementioned convergence criteria.

For the LES simulation (i.e. smooth barrel with baffles), the number of inner iterations for each initial timestep was adjust so that the scaled residuals for continuity and momentum equations decreased by three orders of magnitude (i.e. 10^{-3}). Each subsequent time step was iterated for up to 20 times terminating upon the scaled residuals reaching 10^{-3}. No mass imbalance was present as the mass flow rate was enforced as a boundary condition.

3. BOX CULVERT WITH SMOOTH BED AND SIDEWALLS

3.1 PRESENTATION

Numerical simulation was performed for a domain measuring 9.35 m × 0.5 m × 0.3 m (length × width × height), as a 1:1 model of the physical set up of Wang et al. (2016a) detailed in Figure 3.1. Figure 3.1 shows two upstream and downstream screens, used to prevent fish injuries. The channel dimensions would correspond to a single cell box culvert beneath a small countryside road or a single cell of a multi-cell culvert structure seen in Figure 1.1a. The streamwise extent of the domain was constrained by the locations of measurements available from Wang et al. (2016a), for flow conditions corresponding to less-than-design flows. In addition, a 2DV comparison case was constructed for the 3D effects in the base case to be reviewed, referred to as 2D model thereafter.

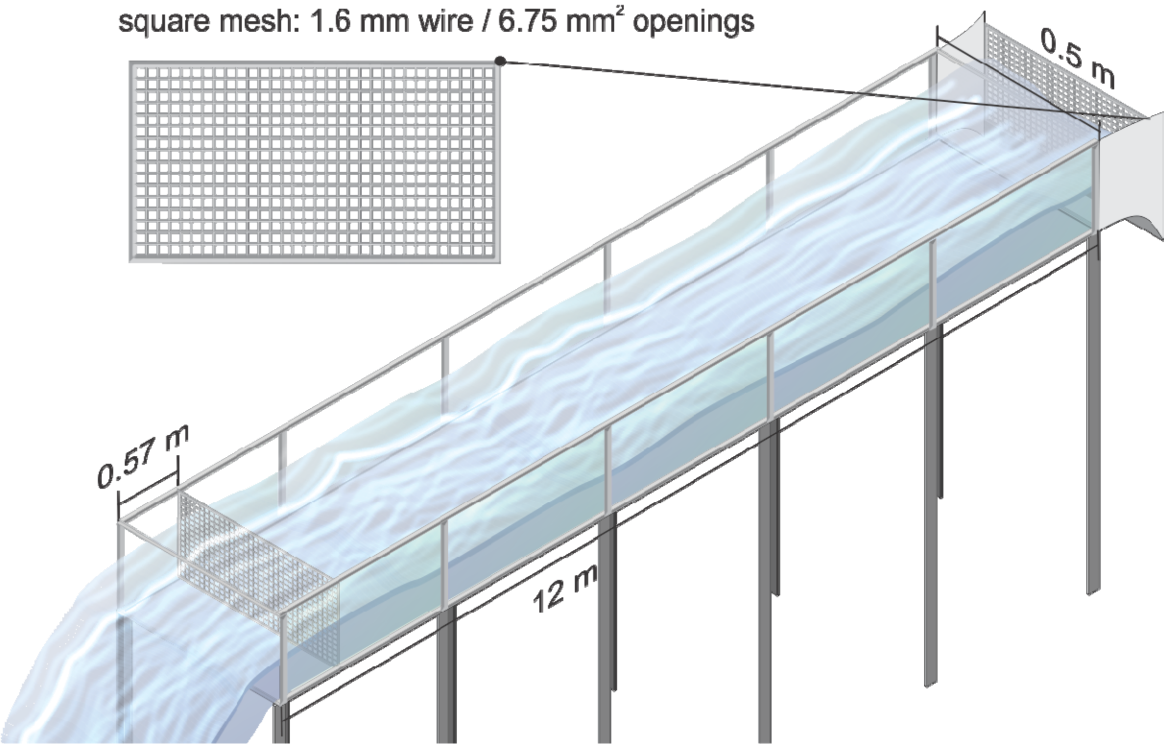

Figure 3.1 – Definition sketch of smooth channel used by Wang et al. (2016a).

The cuboid domain of the 3D base case is sketched in Figure 3.2. Note that the inlet and outlet faces were each divided into two smaller quadrilaterals – done to enforce the desired mass flow for the air and water phases respectively. The experimental data of Wang et al. (2016a) were used to size the water inlet i.e. the inlet is of the same height as the upstream physical measurement, which was mirrored by the outlet configuration due to meshing requirements. The same setup was preserved in the 2D comparison case after a domain reduction in the spanwise direction. As for all configurations, the mesh validation is herein undertaken mainly by experimental comparison.

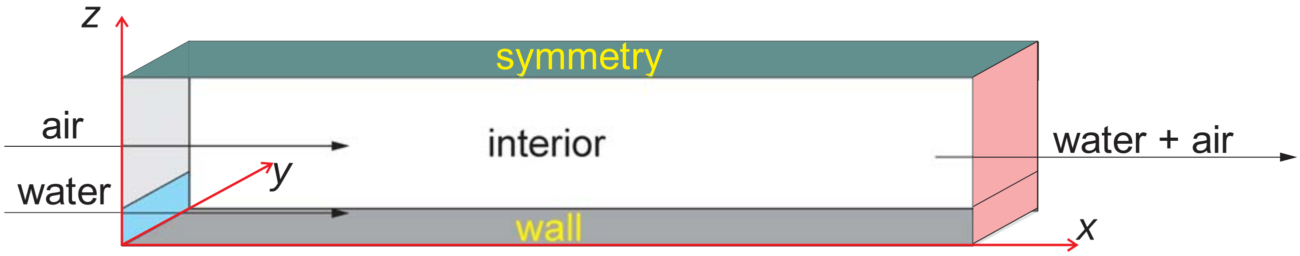

Figure 3.2 – Numerical domain for smooth channel - Flow direction from left to right.

The simplicity of the domain geometry allowed a mapping with structured hexahedral cells. The streamwise (x) and spanwise (y) directions were uniformly partitioned into 500 and 25 segments, respectively. On the inlet side, the bottom and top quadrilaterals (i.e. water and air inlets) were both divided into 50 partitions. This resulted in a much finer mesh resolution at the water inlet face, which was of primary interest. A growth factor of 1.2 was applied to ensure a smooth transition of vertical mesh sizes between the two regions. The resultant mesh was projected onto the outlet faces. The final mesh comprised 1,287,500 hexahedral cells.

The 2D domain of the comparison case was similarly mapped with structured quadrilateral cells. The mesh resolution was increased, to compensate for the substantial reduction in domain size. The streamwise and cross-stream resolutions of the air inlet were doubled, i.e. 1,000 and 100 divisions respectively, compared to the 3D case. The water inlet edge was divided into 1 mm segments, corresponding to an approximately four-time increase in resolution. The transition between the air and water inlet edges was adapted with a growth factor of 1.2. The procedure produced a final cell count of 303,000.

The boundaries of the respective numerical domain pertaining to the 3D and 2D models were classified into inlet, outlet, wall and far-field zones, as shown in Figure 3.2. The inlet velocity conditions were imposed on both the air and water inlet faces, the transition between which denoted the free-surface elevation. A pressure boundary condition was specified on the outlet faces (edges) to represent the experimentally-observed free surface level. The side and bottom boundaries were modelled as fixed solid walls, with an equivalent sand roughness of $k_s = 1.5 \times 10^{-6}$ m, corresponding physically to a smooth turbulent flow condition. The far-field was treated as a symmetrical boundary. The model configurations and flow conditions are summarised in Tables 3.1 and 3.2.

Table 3.1 – Summary of configurations for smooth channel (3D)

Class	Item	Configuration	Notes
Geometry	Model type	3D	-
	Length (x)	9.35 m	-
	Height (z)	1.0 m	-
	Width (y)	0.5 m	-
Mesh	Number of divisions (x)	500	hard^{*1}
	Number of divisions: air inlet (z)	50	soft^{*1}; primary phase inlet; growth factor = 1.2
	Number of divisions: water inlet (z)	50	hard; secondary phase inlet
	Number of divisions (y)	25	hard
	Smallest cell size	18.7 x 3.94 × 20 mm	$Q_w = 0.0556$ m^{3}s^{-1}
	Total cell count	1,287,500	hexahedral
Model	Turbulence model	Standard k-ε	Launder and Spalding (1972)
	Free surface model	One fluid VOF	Hirt and Nichols (1981)
Boundary condition	Top	Symmetry	far-field; no-flux
	Bottom	Wall	$k_s = 1.5 \times 10^{-6}$ m
	Sidewalls	Wall	$k_s = 1.5 \times 10^{-6}$ m
	Inlet (air)	Velocity	$U_{a,in} = 0$ m/s
	inlet(water)	Velocity	$U_{w,in} = 0.5645$ ms^{-1},
Solution	Type	Transient	-
	Scheme	Coupled	-
	Momentum	2nd order upwind	-
	Turbulent kinetic energy	2nd order upwind	-

Notes: *1 – In ANSYS, a hard constraint forbids the mesher from changing the mesh if it concludes a higher quality mesh could be produced; a soft constraint permits such adjustments;

*2 – In a two-component VOF, the primary phase is the phase with the lighter density

Table 3.2 – Summary of configurations for smooth channel (2D comparison scenario)

Class	Item	Configuration	Notes
Geometry	Model type	2D	-
	Length (x)	9.35 m	-
	Height (y)	1.0 m	-
Mesh	Number of divisions (x)	1,000	hard
	Number of divisions: air inlet (z)	100	soft; primary phase inlet; growth factor = 1.2
	Element size: water inlet (z)	1 mm	hard; secondary phase inlet;
	Smallest element size	9.35 × 1 mm	
	Total cell count	303,000	quadrilateral
Model	Turbulence model	Standard k-ε	Launder and Spalding (1972)
	Free-surface model	One fluid VOF	Hirt and Nichols (1981)
Boundary condition	Top	Symmetry	far-field; no-flux
	Bottom	Wall	$k_s = 1.5 \times 10^{-6}$ m
	Inlet (air)	Velocity	$U_{a,in} = 0$ m/s
	inlet(water)	Velocity	$U_{w,in} = 0.5645$ m/s, $q_w = 0.1112$ m^2/s
Solution	Type	Transient	-
	Scheme	Coupled	-
	Momentum	2nd order upwind	-
	Turbulent kinetic energy	2nd order upwind	-

3.2 VALIDATION AND RESULTS

The numerical results were validated against the experimental data of Wang et al. (2016a). Figure 3.3 shows the experimental and simulated free-surface profiles along the channel centreline, where L is the channel length (L = 12 m herein). All approaches predict a subcritical flow (i.e. $d/d_c > 1$) over the full length of the channel. The flow is thus controlled from the downstream boundary conditions, producing an H2 backwater profile for the horizontal bed slope (Bresse, 1860; Chow, 1959; Chanson, 2004). All results indicate a small decrease in free-surface elevation over the channel length, reflecting a small amount of energy loss caused by the smooth boundaries' friction. Both numerical models (2D and 3D) overpredict the water level by up to 7%, in comparison to the physical measurements in laboratory. Such a level of agreement is deemed reasonable, as the laboratory data could be affected by operator/instrumentation errors and free-surface perturbations. A comparison between the 2D and 3D cases indicates a slight increase in the free-surface levels, induced by the presence of the sidewalls.

Figure 3.4 presents a comparison between modelled and experimental centreline mean x-velocity profiles for both the developing (x = 2.15 m) and fully developed (x = 7.35 m) flow regions. In Figure 3.4, both the Pitot tube and ADV data recorded by Wang et al. (2016a) are reported. In the developing flow region (Fig. 3.4a), all data highlight a developing boundary layer characterised by steep velocity gradients, above which an approximately constant velocity profile is identified. A closer inspection reveals steeper near-wall velocity gradients in the experimental data than the simulated values. This discrepancy may be caused by multiple sources, including: (a) the uniform velocity profile specified at the upstream boundary; (b) the near wall treatment sensitive to the mesh resolution next to the wall; (c) instrument blockage next to the bottom boundary. In comparison to the 2D case, the 3D case data exhibit slightly larger velocities overall and observable effects due to interactions with the air phase, i.e. smaller velocities near the free-surface. Such larger centreline velocities correspond to a reduction in streamwise velocities next to the sidewalls, while the reason for the latter observation requires further investigation. In the fully developed region (Fig. 3.2b), a closer agreement between all data is observed. The 3D model results show an excellent agreement with the Pitot tube data, notably in the lower flow column. A slight overshoot in the 3D velocity profile is identified near z = 0.10 m, which is a consequence of the symmetry condition (top boundary). The 2D simulation reasonably reproduces the steep velocity gradients up to $z \approx 0.06$ m, and interactions with the upper air layer are barely noticeable.

Figure 3.5 presents the computed wall shear stresses τ_o along the channel centreline. The numerical data display a qualitative agreement with the physical data of Wang et al. (2016a), based upon the momentum integral method (Schlichting, 1979; Chanson, 2009). The largest discrepancies occur near the upstream boundary where the largest streamwise gradients are present, with the data agreement improving towards the fully developed flow region. At the downstream end, the experimental result reveals a slight increase that may be attributed to the presence of the downstream grid mesh (Fig. 3.1). A comparison indicates that the 2D model slightly underestimates the wall stresses because the sidewall effects were not modelled. All data are close in magnitude to the analytical solution for a zero-pressure-gradient turbulent boundary layer above a smooth plate (green line), with differences reflecting the variations in free-surface elevation as well as the presence of the meshes and sidewalls.

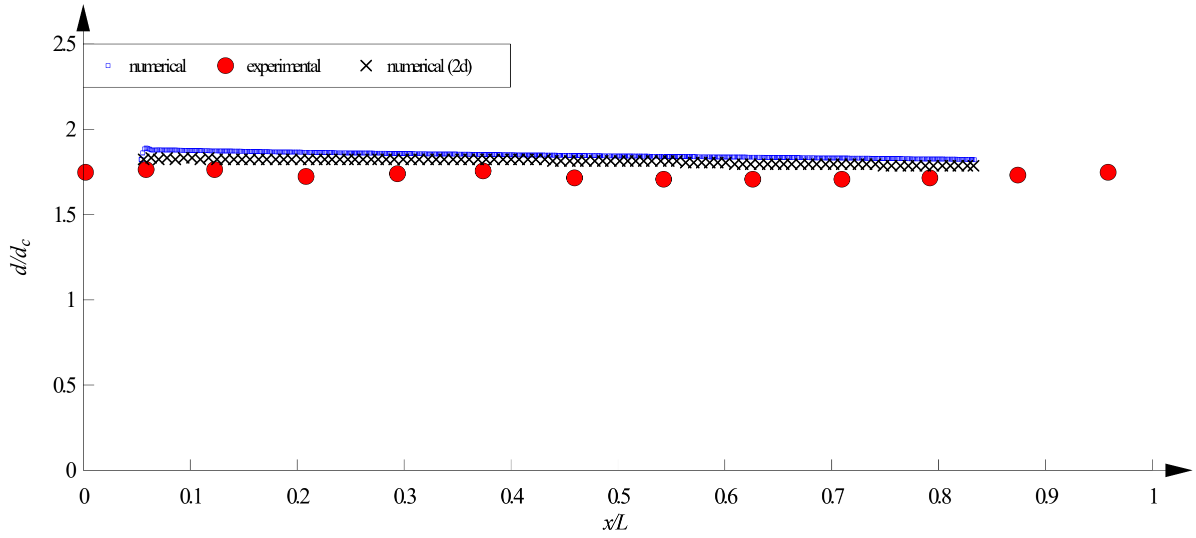

Figure 3.3 – Comparison between experimental and simulated free-surface profiles.

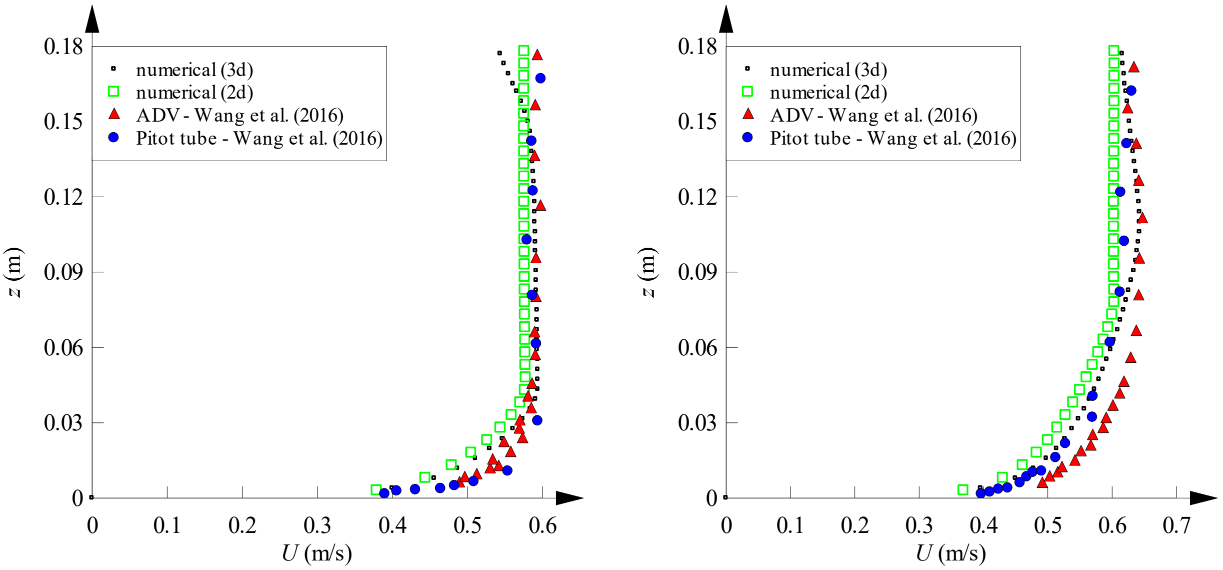

(a) $x = 2.15$ m (b) $x = 7.35$ m

Figure 3.4 – Comparison between experimental and CFD numerically calculated velocity profiles in the developing ($x = 2.15$ m) and fully developed ($x = 7.35$ m) flow regions on the channel centreline.

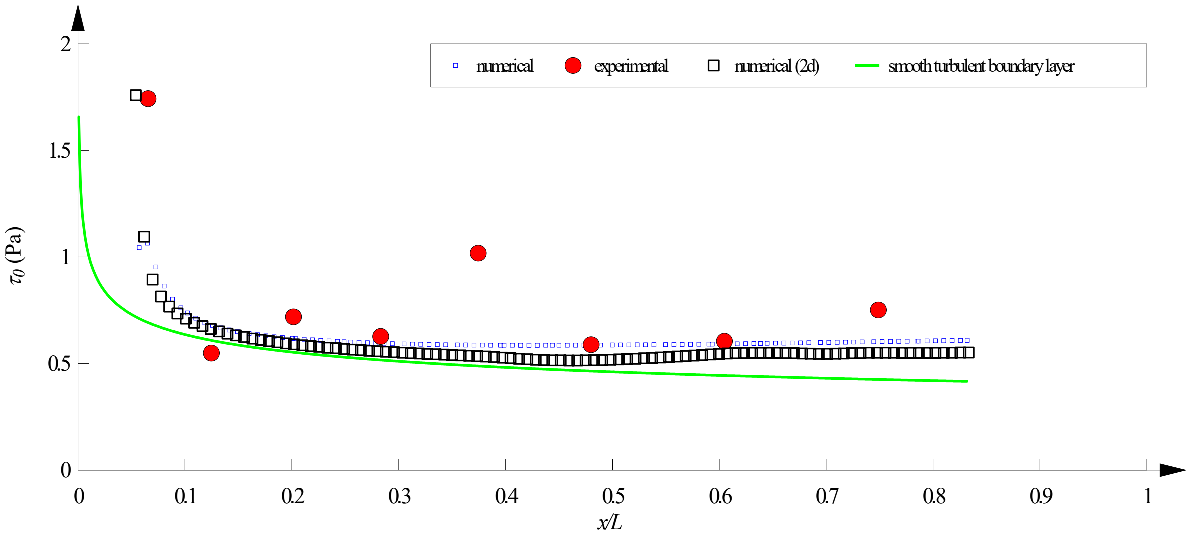

Figure 3.5 – Comparison between experimental and CFD numerically calculated bed shear stress profiles flow regions on the channel centreline.

3.3 SUMMARY

The flow patterns in a smooth barrel were examined in both 3D and 2D numerical configurations. The standard *k-ε* model and the one-fluid VOF model were adopted for turbulence modelling and free-surface tracking. A comparison with detailed physical data (Wang et al., 2016a) showed that the free-surface profile was reproduced reliably, with all data remaining within 7%. The experimental and computed centreline velocity profiles displayed an excellent agreement in the fully developed flow region, while some small difference was observed in the developing flow, likely caused by differences in inflow conditions. The numerical and experimental bed shear stress data also compared well in general, except at the downstream end of the channel, because of the presence of the downstream mesh in the physical channel.

The systematic comparison between 3D and 2D results showed that the 3D configuration yielded superior results, by accounting for the sidewall roughness, despite a reduction in the near wall mesh resolution. The standard *k-ε* model yielded acceptable predictions on the channel centreline, though more sophisticated models might be warranted if subtle features such as secondary flow cells are of importance.

Overall, the present experience suggests that a simple 3D RANS model may be sufficient for characterising the centreline properties in a smooth rectangular channel. In addition, a 2D model may yield a good approximation of the centreline free surface profile, when small sidewall effects are expected. Importantly, the case study highlights the importance of high-quality experimental data for calibration and validation of the numerical model.

4. BOX CULVERT WITH ROUGH BED AND LEFT SIDEWALL

4.1 PROBLEM SETUP

Some three-dimensional (3D) numerical simulation was performed for a domain measuring 12 m × 0.5 m × 0.5 m (length × width × height), with a very-rough invert, very rough left sidewall and smooth right sidewall, as sketched in Figure 4.1. The physical setup was studied by Wang et al. (2016a), testing boundary roughness as a remedial measure to assist upstream fish passage for less-than-design flows.

The domain length was twice the extent of data available (i.e. x = 2 m and x = 8 m at the upstream and downstream boundaries respectively), so that a buffer zone could be provided and uncertainties induced by the boundary conditions may be resolved outside the test section of interest. A velocity inlet was specified for the upstream boundary and a pressure outlet (i.e. water level) was defined for the downstream boundary in accordance with the data by Wang et al. (2016a). Detailed geometry and mesh statistics are summarised in Table 4.1. The bed and sidewall roughness (k_s = 0.020 m) corresponded to experimentally observed roughness height.

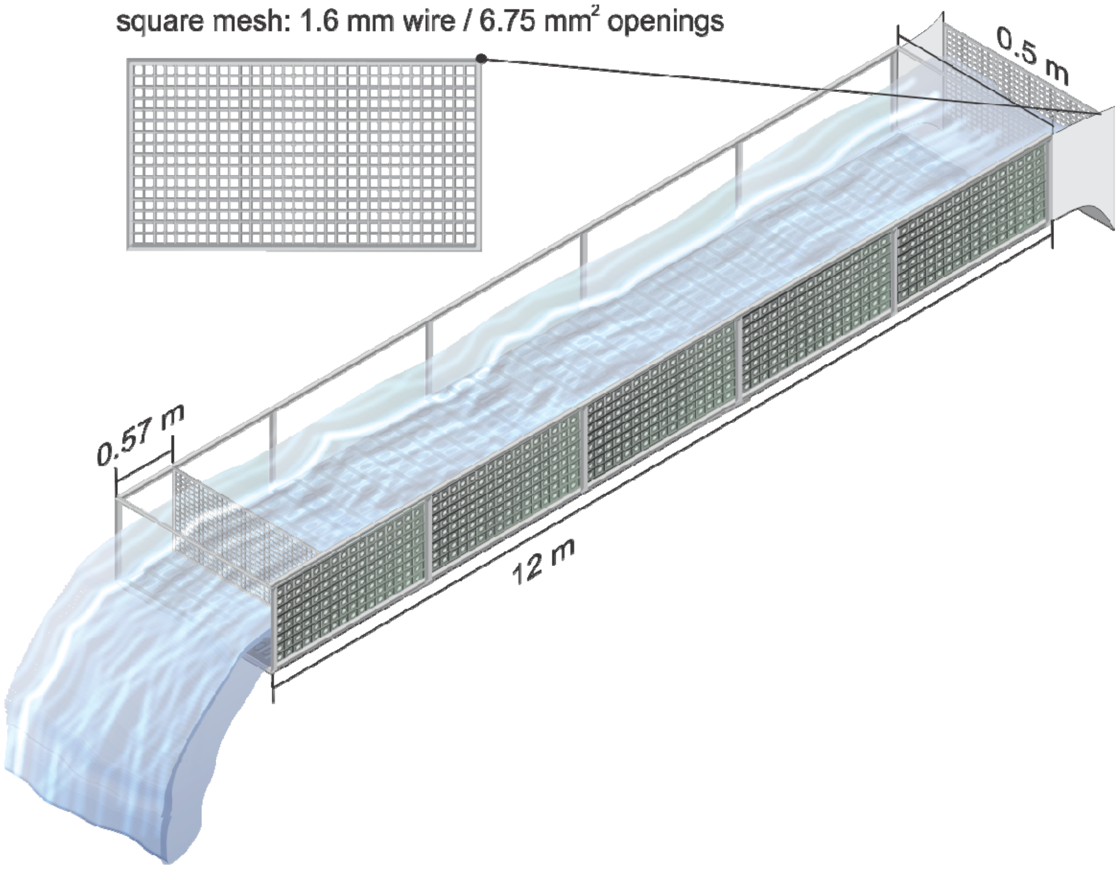

Figure 4.1 – Definition sketch of experimental channel with rough bed and rough left sidewall used by Wang et al. (2016a).

Table 4.1 – Summary of configurations for channel with rough bed and rough left sidewall

Class	Item	Configuration	Notes
Geometry	Model type	3D	-
	Length (*x*)	12.0 m	-
	Height (*z*)	0.5 m	-
	Width (*y*)	0.5 m	-
Mesh	Number of divisions (*x*)	300 – 500	Table 4.2.
	Number of divisions (*z*)	50 – 200	Table 4.2.
	Number of divisions (*y*)	25 – 100	Table 4.2.
	Total cell count	375,000 – 5,000,000	hexahedral
Model	Turbulence model	7-equation Reynolds stress model	Chou (1945), Rotta (1951)
	Free-surface model	one fluid VOF	Hirt and Nichols (1981)
Boundary condition	Top	symmetry	far-field; no-flux
	Bottom & Wall (left)	wall	$k_s = 2.0 \times 10^{-2}$ m
	Sidewall (right)	wall	$k_s = 2.0 \times 10^{-4}$ m
	Inlet	velocity	velocity and volume fraction data from Wang et al. (2016a)
	Outlet	pressure	water level data from Wang et al. (2016a)
Solution	Type	Transient	-
	Scheme	SIMPLE	-
	Momentum	2nd order upwind	-
	Turbulent kinetic energy	2nd order upwind	-

Table 4.2 – Summary of meshes used for the sensitivity tests

ID	Cells (x): bias*1	Cells (y): bias	Cells (z): bias	Total
1	300: 0	50: 12.38	25: 10	375,000
2	500: 0	100: 12.38	25: 10	1,250,000
3	500: 0	200: 12.38	25: 10	2,500,000
4	500: 0	50: 12.38	50: 10	1,250,000
5	500: 0	100: 12.38	100: 10	5,000,000

Note: *1 – ratio of largest to smallest cell sizes

4.2 VERIFICATION AND VALIDATION

As a direct consequence of the discretisation process, the numerical solution accuracy is heavily dependent upon the quality of the numerical domain mesh. Thus, solutions were computed for several meshes to verify the grid size effects on the primary numerical quantities. A summary of the grids is provided in Table 4.2. Herein the mesh validation is done mainly by experimental comparison. Typical results are presented in Figure 4.2.

Figure 4.2a compares the computed free-surface profiles at the channel centreline ($z = 0.25$ m) with the data of Wang et al. (2016a) for the five different meshes, specified in Table 4.1. All data show a very good agreement overall, and an H2 backwater profile is seen. The experimental data display small streamwise undulations, likely a result from the roughness-induced surface waves as well as the wake of the upstream screen in the physical channel. The results suggest that the free surface profiles exhibit a mesh-independent solution, within the investigated conditions (Tables 4.1 and 4.2).

Figure 4.2b illustrates the computed centreline longitudinal velocity profiles at the downstream end of the test section ($x = 8$ m), for five different meshes. The physical ADV velocity data on the channel centreline and at two adjacent transverse locations are shown for reference. The results indicate a difference of 5% to 10% between the simulated velocity profiles, as a result of both mesh count and aspect ratio. The latter appears to be of particular importance since the roughness configuration is asymmetrical. In absence of a mesh independent solution, mesh #5 ([1]) is adopted herein as a reference, since it features the largest cell count and smallest aspect ratio in the cross-sectional plane. A comparison between the numerical and experimental datasets highlights substantial underestimations of the channel velocities in the numerical models. It remains unclear whether the inability to completely resolve the roughness surface geometry could have been a cause. Careful continuity checks confirmed that both the numerical and experimental results satisfy mass conservation.

Figures 4.2c to 4.2e show the computed distributions of dimensionless boundary shear stress along the bed and sidewalls. Herein the dimensionless boundary shear stress was expressed in the form of Darcy-Weisbach friction factors ([2]). Low boundary shear stresses are observed in the bottom corners due to formations of small eddies. The boundary shear stress distribution is approximately uniform across the rough bed, with localised peaks at $y/W = 0.2 - 0.3$ and $0.8 - 0.9$, and a dip at $y/W \approx 0.6$, both of which arise from secondary flow motions, in response to the boundary roughness

---

[1] with 5,000,000 cells.

[2] The relationship between boundary shear stress τ_o and Darcy-Weisbach friction factor f is: $f = 8\,\tau_o/(\rho U_{mean}^2)$, where U_{mean} is the cross-sectional averaged velocity (Chanson, 2004).

configuration. Further the boundary shear stresses vary along the sidewalls, with lower values next to the free-surface and bottom corner, compared to the mid-flow region. Lower boundary shear stresses are observed along the right smooth sidewall, as expected. The results are moderately sensitive to the transverse mesh resolution which could affect the ability to resolve secondary motions adjacent to the sidewall. A further inspection shows that best mesh configurations (#4 and #5) agree within 5% - 10% of one another, despite a lack of evidence for mesh independence. Herein mesh #5 is adopted as the reference case whilst its limitations are acknowledged.

Lastly, it is worth nothing that Wang et al. (2016a) estimated the cross-sectional averaged Darcy frictions factor, based on the centreline free-surface profiles. Their analysis yielded dimensionless boundary shear stress f between 0.07 and 0.08 ([3]). However, the standard wall function produced notably smaller values using the experimentally determined k_s. This could be a result from the wall-normal flow motions breaking down the logarithmic layer near wall. A further examination shows that the first layer of boundary cells lie close to the upper bound of the applicable range of the log-law (i.e. $y^+ \approx 300$), where the wake component becomes increasing important. These discrepancies highlight the importance of the selection of an appropriate wall function and having a properly resolved mesh in the near-wall region.

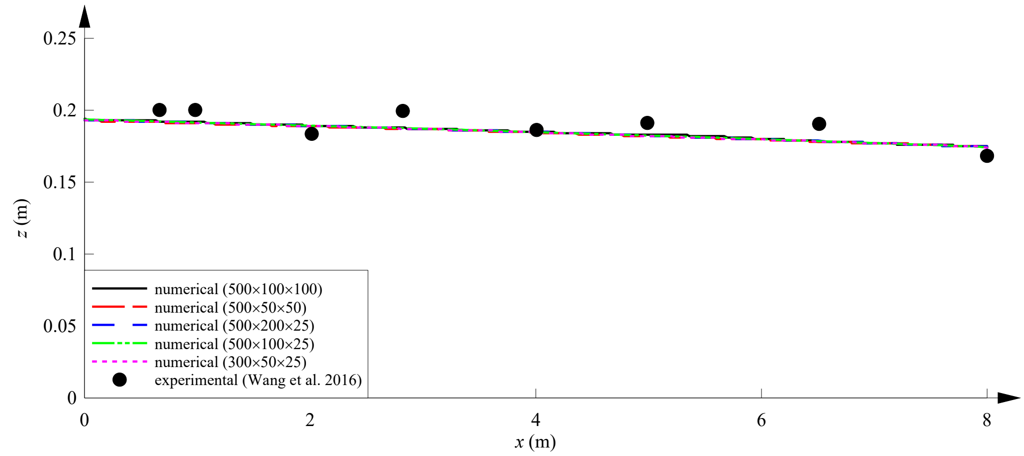

(a) Free-surface profiles at channel centreline (z = 0.25 m)

---

[3] corresponding to k_s = 20 – 25 mm (Wang et al., 2016a).

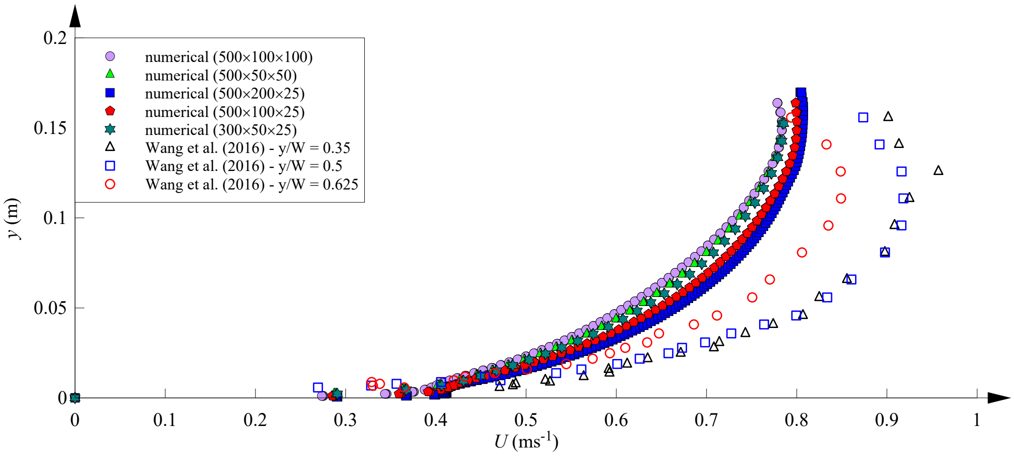

(b) Centreline longitudinal velocity profiles at outlet (x = 8 m)

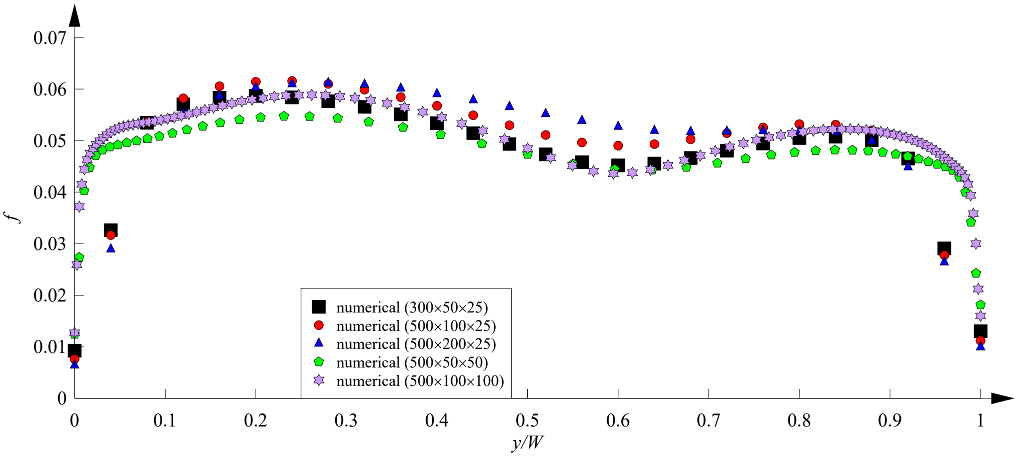

(c) Lateral distributions of bed friction factor at outlet (x = 8 m)

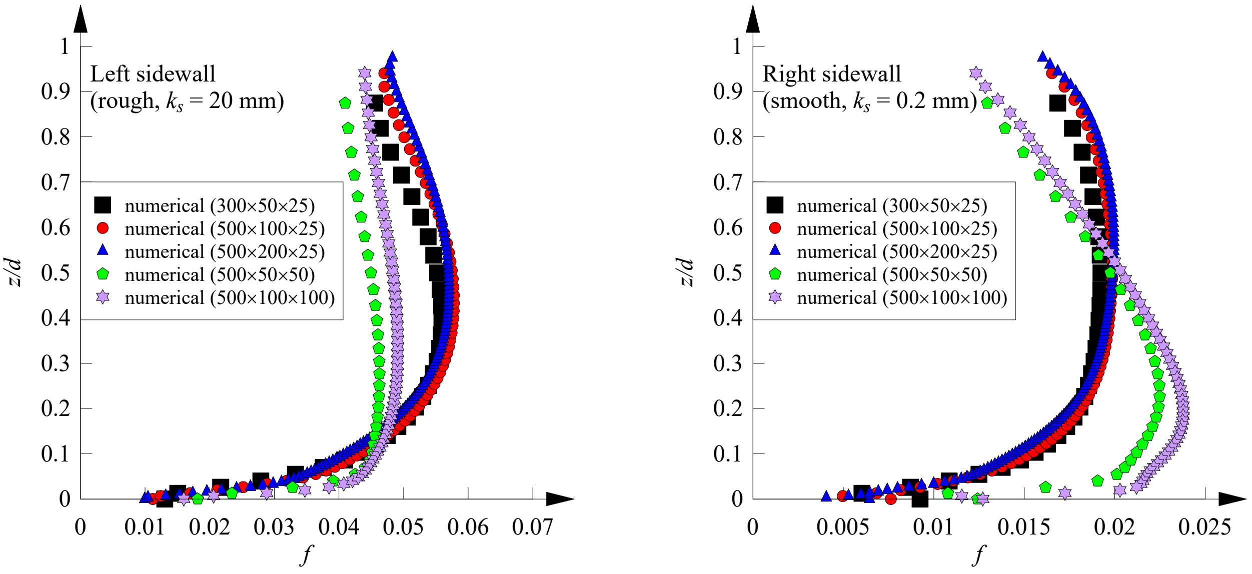

(d, Left) Friction factor distributions on left rough wall at outlet (x = 8 m)

(e, Right) Friction factor distributions on right smooth wall at outlet (x = 8 m)

Figure 4.2 – Mesh sensitivity test results of primary flow quantities in a culvert barrel channel with rough bed and rough left sidewall.

4.3 RESULTS

The rough left sidewall and bed produce an asymmetry in boundary shear stresses, which results in skewed longitudinal velocity contours, as shown in Figure 4.3 where the longitudinal *U*-velocity contours are computed at three cross-sections, for which measurements were performed by Wang et al. (2016a). The asymmetry in longitudinal velocities develops within the initial stage of boundary layer growth, resulting in noticeably lower velocities close to the rough (left) sidewall (y = 0.5 m, Fig. 4.3). At the downstream end of the test section (x = 8 m), the flow becomes fully developed as reported by Wang et al. (2016a). Approximately 40% of the flow area is rendered below U/U_{mean} = 1, comparable to the observation of Wang et al. (2016a).

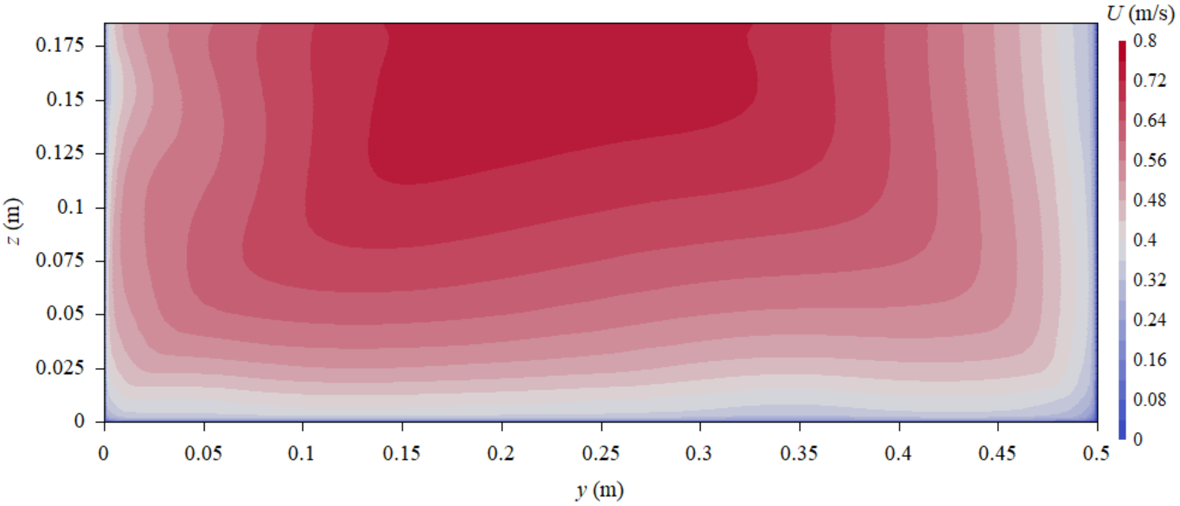

(a) x = 2 m

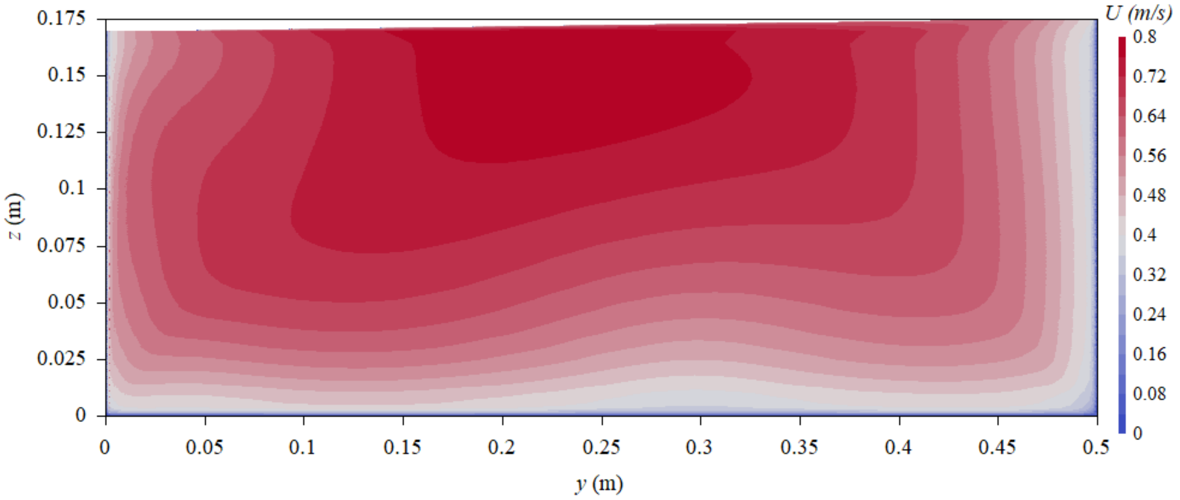

(b) x = 8 m

Figure 4.3 – Contour plots of longitudinal velocity component *U* at selected cross-sections in a culvert barrel channel with rough bed and rough left sidewall.

Figure 4.4 presents the lateral distributions of maximum longitudinal velocity U_{max} and its elevation z_{Umax} at several transverse locations y at the outlet (x = 8 m). The U_{max}, z and y data are respectively normalised by the cross-sectional average velocity U_{mean}, the water depth d and the channel width W. The results (Figure 4.4a) indicate that the low velocity zones next to the boundaries result in a velocity increase in the central part of the channel. These peak velocities occur at much lower elevations next to the boundaries than on the channel centre because of secondary flow motion. The data of Wang et al. (2016a) displayed similar trends, except that they showed larger U_{max} data occurring at lower elevation z_{Umax} in the central part of the channel. The difference is likely due to differences between the computed secondary circulations and those existing in the physical model. For 3D channels, both Xie (1998) and Wang et al. (2016a) commented on the locations of z_{Umax} and suggested a coincidence between these locations and those of minimum $u'(z_{u'max})$ away from the sidewall. Figure 4.4b shows that this is only seen for a small region towards the left sidewall (i.e. y/W = 0.8 – 0.9). The existence of local minima in u' is a consequence of complex secondary circulations beneath the free surface and highlights the complicated processes occurring therein.

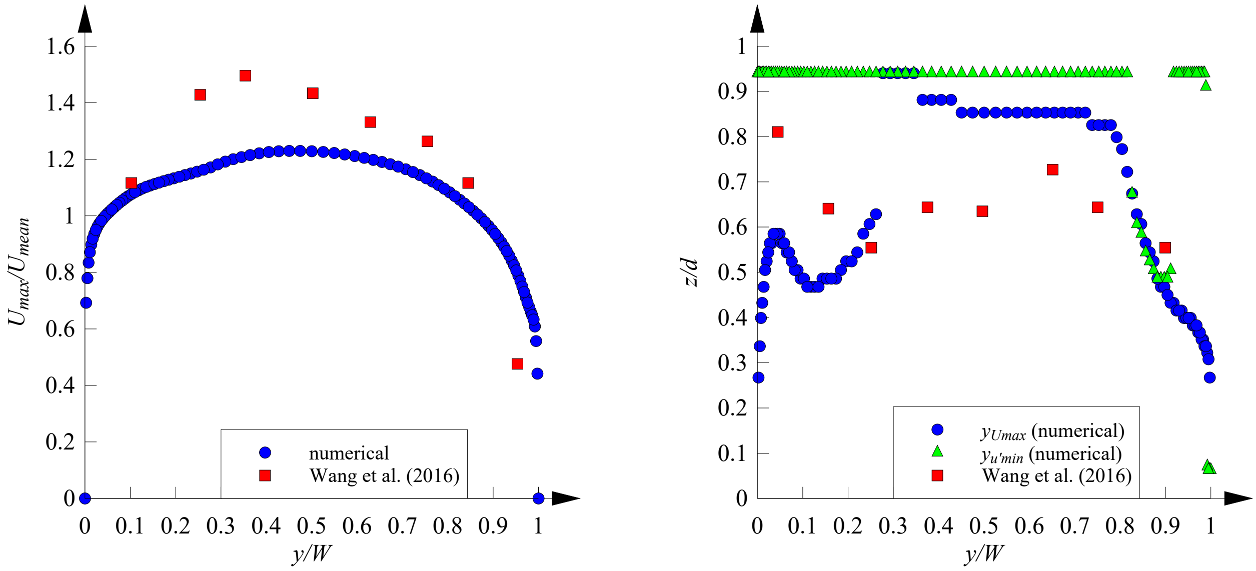

(a) Transverse distribution of U_{max} (b) Transverse distribution of z_{Umax}

Figure 4.4 – Transverse distributions of magnitudes and locations of maximum longitudinal velocity component $U_{\max}$ at x = 8 m

The lateral perturbation induced by the channel corners and boundary roughness leads to the formation of secondary currents (Nezu and Rodi, 1985; Nezu and Nakagawa, 1993). These are evident from the dips in velocity contours, seen in Figure 4.3, which become more pronounced as the flow develops downstream. Wang et al. (2016a) observed these velocity dips and attempted at visualising the secondary flow patterns by dye injection. They reported both bottom and free-surface recirculation cells next to the rough sidewall, at the corner between the rough bed and sidewall, near the channel bed, and underneath the free-surface on the left side. The computed secondary flow vectors at $x = 2$, 5 and 8 m are presented in Figure 4.5, where the recirculation cell centres are highlighted by red arrows. Figure 4.5 presents vector descriptions of the secondary current motions in the y-z plane ([4]). The numerical results suggest five recirculation cells as the flow evolves from upstream to downstream. In particular, the recirculation zones next to the left rough sidewall and the small vortex at the corner between the right smooth wall and the bed are successfully reproduced in the CFD modelling. An additional recirculation zone is observed on the bottom left corner with its centre at $y/W \approx 0.9$ and $z/d \approx 0.05$, which mirrors the rough sidewall recirculation about an imaginary line highlighted in yellow in Figure 4.5. This division introduces a soft boundary that limits the spread of corner-induced secondary cells due to difference between frictions on the bed and on the sidewall. Several researchers proposed a characteristic value $z/y \approx 0.8$ (Tracy, 1965; Yang et al., 2012), whereas the present data yields z/y between 1.0 and 1.3. The difference might be attributed to the different rates of growth of the boundary layers originating from the left and right sidewalls. Finally, some significant recirculation is observed next to the right smooth wall ($y = 0$), which was not visualised by Wang et al. (2016a). It might have been possible that the large stress imbalance between the right smooth wall and the rough bed led to strong velocity gradients causing the dye to be dispersed too quickly.

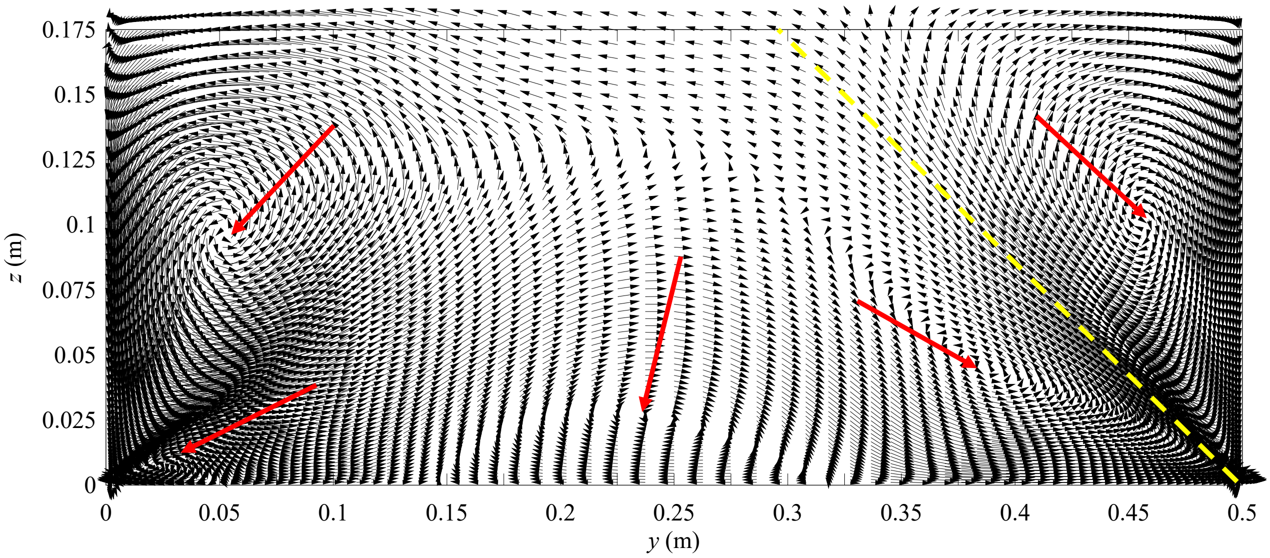

(a) $x = 2$ m

---

[4] That is, the (V, W) velocity vector.

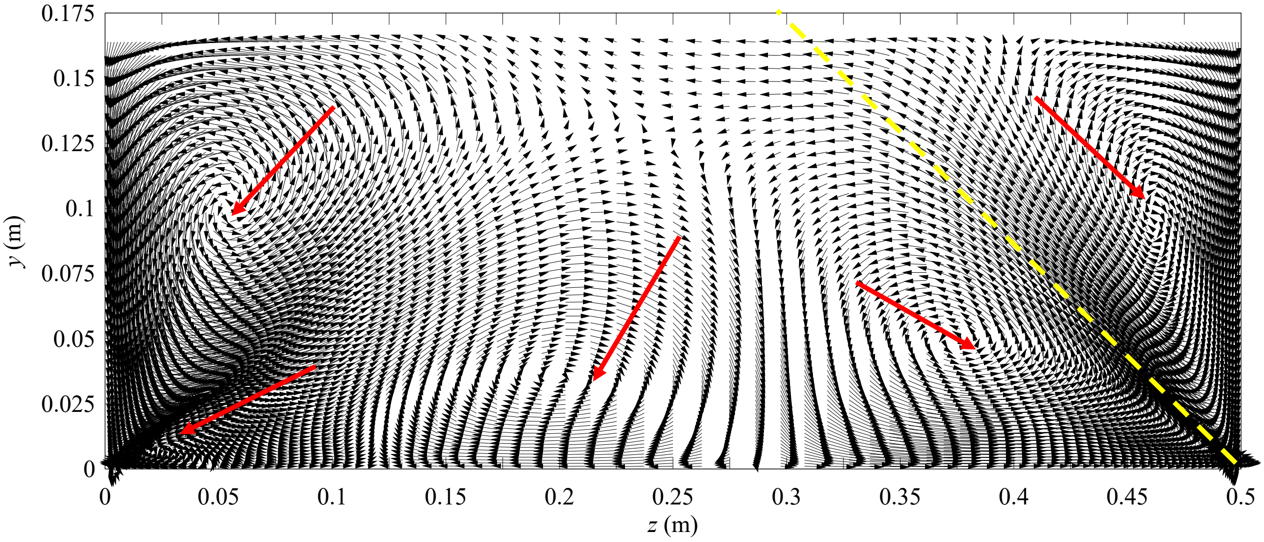

(b) $x = 8$ m

Figure 4.5– Vector description of secondary flow (V, W) patterns in in a culvert barrel channel with rough bed and rough left sidewall at selected cross-sections.

Figure 4.6 presents the contour plot of dimensionless secondary current strength, defined as $(V^2+W^2)^{0.5}/U$, where V is the time-averaged transverse velocity component and W is the time-averaged transverse velocity component. The results indicate strong wall-tangent motions of the order of 10% of the main flow next to the right smooth wall (Fig. 4.6). Further, significant secondary motions of dimensionless strength about 5% are observed next to the boundaries and along the soft boundaries that divide pairs of corner-induced eddies. The asymmetrical boundary roughness configuration tends to produce secondary patterns in specific regions which substantially exceed typical values (i.e. 1 – 2%) reported for open channel flows (Liggett, 1994).

The relationship between turbulent shear stress and the production of secondary flow may be demonstrated by simplifying and integrating the x-momentum equation along the bed, which yields (Yang et al., 2012):

$$UV - \nu \frac{\partial U}{\partial t} + \left\langle u'v' \right\rangle \approx 0$$

For a turbulent flow, the secondary flow (spanwise) velocity V is inversely proportional to the longitudinal velocity U and does balance the Reynolds stress $-\left\langle u'v' \right\rangle$, which originates from the spanwise velocity gradient $\partial U/\partial y$. Figure 4.7 presents the lateral distribution of $-\left\langle u'v' \right\rangle$ along the rough bed at the outlet (x = 8 m). Three regions of large $-\left\langle u'v' \right\rangle$ are identified, which respectively correspond to the three bottom vortices illustrated in Figure 4.6. The directions of the secondary currents directly correspond to the signs of $-\left\langle u'v' \right\rangle$. The zero-crossings in Figure 4.7 coincide with the locations where the wall-tangent motions diminish. The results corroborate with the analysis of Yang et al. (2012) and suggest that both the bed and the sidewall boundaries play a role in producing the complicated secondary flow patterns observed in the present configuration.

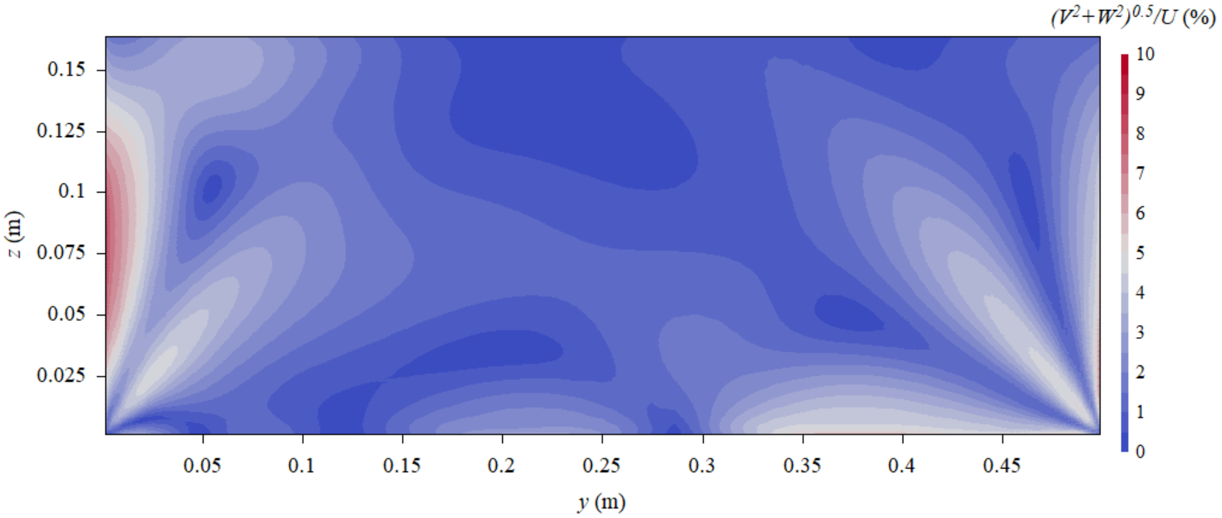

Figure 4.6 – Secondary flow strength $(V^2+W^2)^{0.5}/U$ at outlet (x = 8 m) of culvert barrel channel with rough bed and rough left sidewall

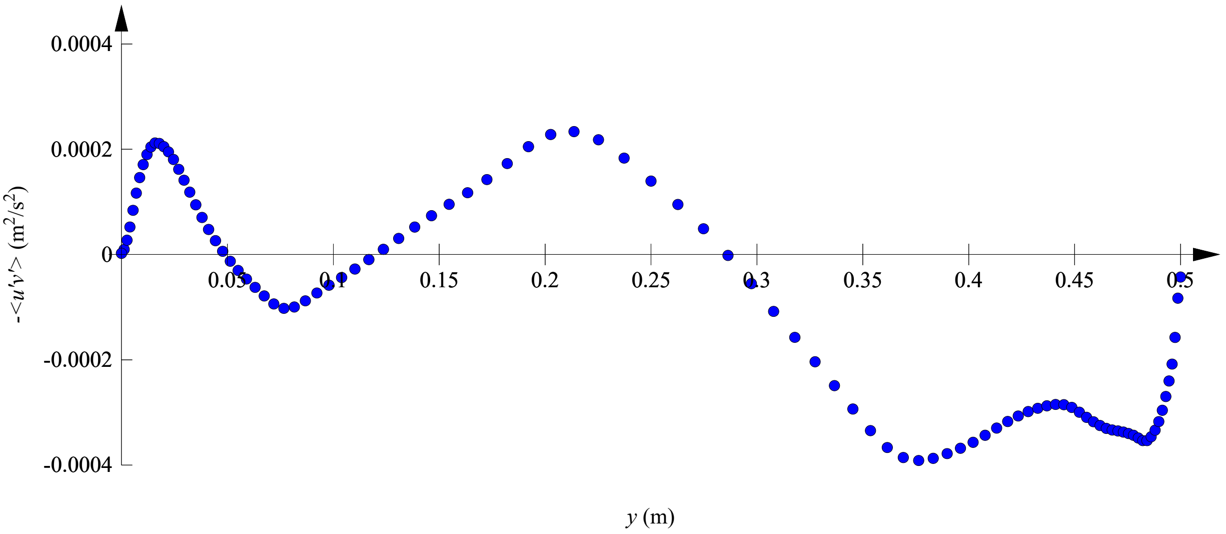

Figure 4.7 – Distribution of turbulent Reynolds shear stress $-\langle u'v' \rangle$ on the bottom at outlet (x = 8 m) of culvert barrel channel with rough bed and rough left sidewall.

Turbulence intensity contours are presented in Figure 4.8, where the turbulence intensity is defined as $Tu = u_{rms}/U$, where u_{rms} is the root-mean-square (rms) of the longitudinal velocity component. The data are shown at three longitudinal locations, corresponding to those measured by Wang et al. (2016a). The results indicate strong turbulent fluctuations next to the rough bed and rough sidewall, with *Tu* values up to 0.5 next to the rough boundaries. The turbulence intensity next to the right smooth wall remains constant at approximately 15%, except in the corner region. In the fully developed region (i.e. $x = 8$ m), *Tu* is dominantly above 10% in most parts of the channel.

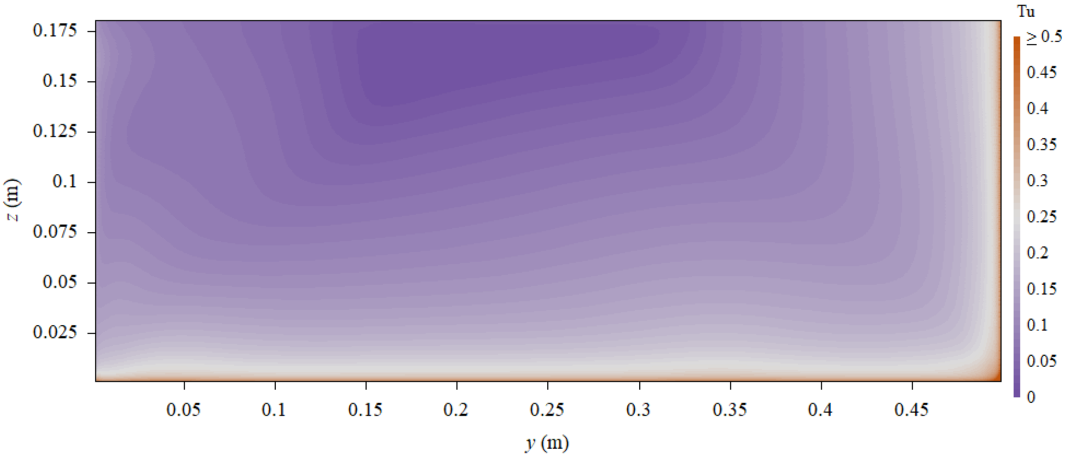

(a) $x = 2$ m

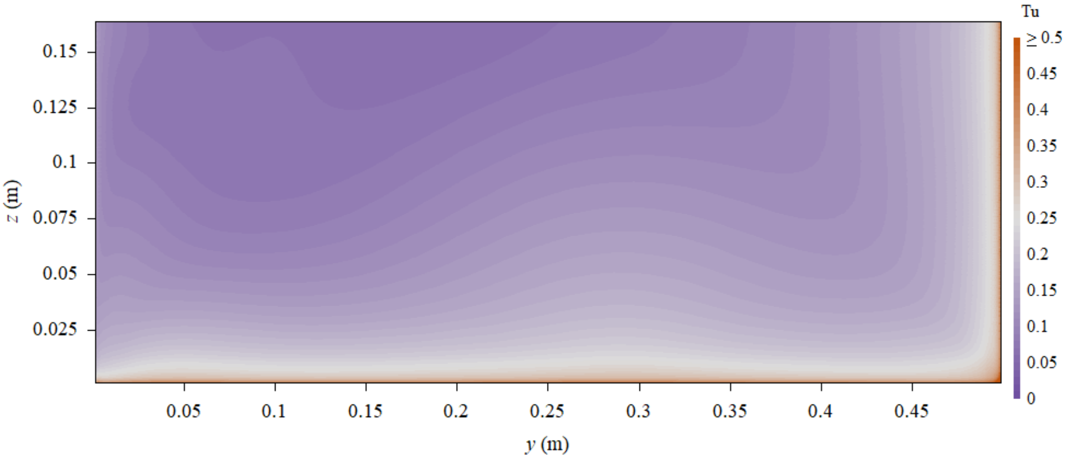

(b) $x = 8$ m

Figure 4.8 – Turbulence intensity contours at selected cross-sections in a culvert barrel channel with rough bed and rough left sidewall.

The turbulence intensity contours display dips similar to the longitudinal velocity contour plots. The similarity may be linked to a combination of secondary flow patterns and turbulence anisotropy. Figure 4.9 presents contours of ratios of pairs of turbulent velocity components at the downstream end of the test section ($x = 8$ m). The anisotropy ratio w_{rms} / u_{rms} is maintained at approximately 0.5 near the channel bed and increases towards the free surface, almost reaching unity at the interface between the free surface and the sidewalls, where v_{rms} is the root mean square of the spanwise velocity component. Such large w_{rms} / u_{rms} values are linked to upward motions induced by the sidewall secondary circulations, shown in Figure 4.5. Similarly, the ratio v_{rms} / u_{rms} is close to unity next to the channel bed due to the bottom vortex pair, seen in Figure 4.5, and decreases to approximately 0.5 along the sidewalls towards the free surface. Next to the boundaries, the wall-normal velocity fluctuations are significantly damped as seen in the contours of the ratio w_{rms} / v_{rms} in Figure 4.9c. Nezu (1977, 2005) proposed universal functions of *u'*, *v'* and *w'* based on self-similarity and a simplified *k*-*ε* model, which yields:

$$\frac{v_{rms}}{u_{rms}} = 0.71$$

$$\frac{w_{rms}}{u_{rms}} = 0.55$$

$$\frac{v_{rms}}{w_{rms}} = 1.3$$

A review of Figure 4.9 shows that Nezu's values are only representative of a small region in the core of the flow. Significant turbulence anisotropy exists next to the boundaries and the free surface, leading to complicated secondary flow patterns.

4.4 SUMMARY

3D CFD models were used to study the flow in a box culvert with rough bed and rough left sidewall. The RSM and VOF models were employed to achieve turbulence closure and free surface tracking. The results demonstrated the ability of CFD models to provide a high-fidelity database, useful for understanding the mechanisms responsible for improving fish passage in an asymmetrically roughened channel.

The effects of grid mesh on the primary flow quantities were examined between five different configurations – with a more than 10-fold increase in cell count from 375,000 to 5,000,000 (Table 4.2). The comparison suggested that the free surface profiles were non-sensitive to the grid and exhibited mesh independence even for the coarsest mesh. The velocity profiles agreed within 5 – 10 % between the configurations and appeared more sensitive to the aspect ratio than the cell count. The largest discrepancies were observed in the friction factors, despite all cases generating qualitatively similar results. The disagreement between the two finest meshes was between 5 – 10 %. As a further increase in cell count was infeasible, the margin of error for the finest mesh was deemed acceptable with small mesh effects on the results being acknowledged.

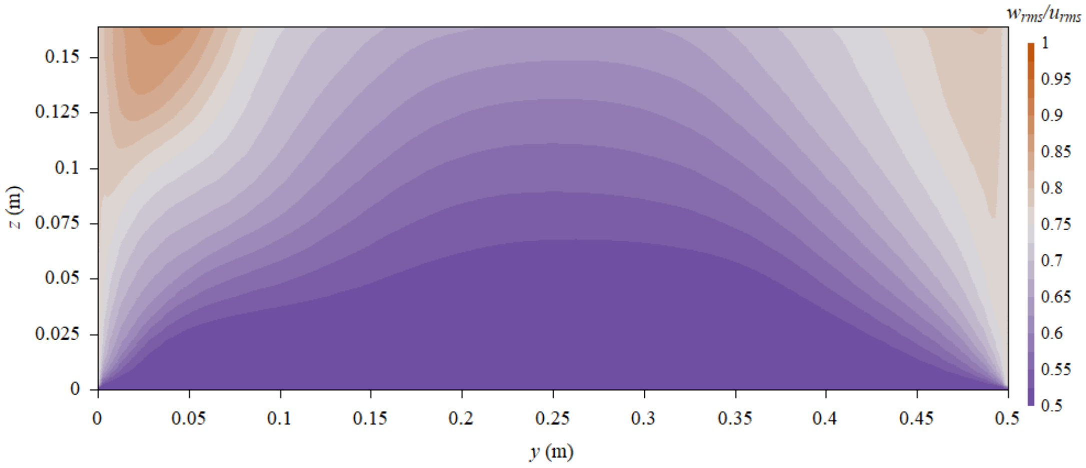

(a) Contours of w_{rms} / u_{rms}

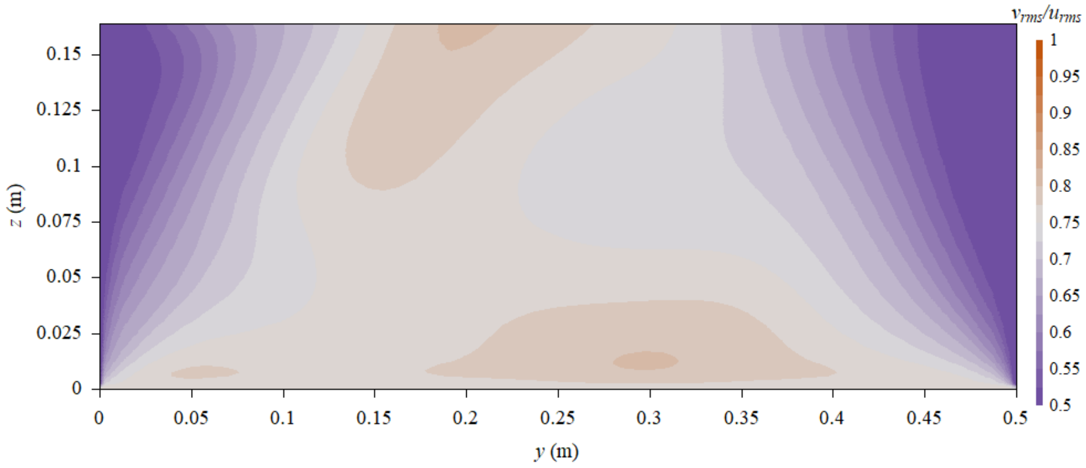

(b) Contours of v_{rms} / u_{rms}

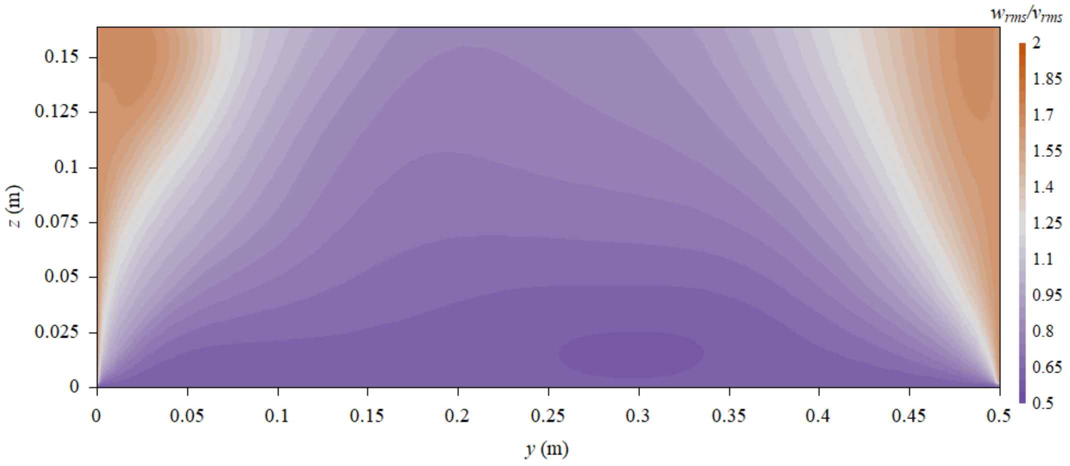

(c) Contours of w_{rms} / v_{rms}

Figure 4.9 – Turbulence anisotropy at outlet (x = 8 m) of culvert barrel channel with rough bed and rough left sidewall.

Comparisons between numerical and experimental data sets showed a good agreement in terms of free surface profiles for all configurations. Significant discrepancies were found in the velocity profiles which appeared to be linked to some inappropriate modelling of the surface roughness. This highlighted the limitation of the numerical model, but should not prevent the results from being interpreted in a more qualitative manner.

A review of numerical results highlighted complicated secondary flow patterns that were qualitatively consistent with the physical observations of Wang et al. (2016a). These secondary motions were responsible for multiple dips in the velocity contours and were substantially stronger than those in typical open channel flows, reaching up to 5-10% of the main flow next to the boundaries. A further analysis revealed a relationship between secondary motions and the distribution of wall-tangent Reynolds stress, which indicated that both bed and sidewall boundaries play a role in producing the desired flow patterns for fish passage.

In summary, the present numerical results provided valuable information on the evolution of flow patterns and secondary current generation mechanisms despite that mesh influence could have accounted for up to 10% of the velocity and boundary friction profiles. The experience underlined challenges to match experimental and numerical datasets in presence of complex surface geometries. Nevertheless, the numerical model was sufficient at providing supportive information which assists with the interpretation and diagnosis of lab data. Whilst itself insufficient, the complementary nature of numerical and physical models may allow a 'hybrid approach' to be formed which helps facilitate understandings and guide improvements of future designs.

5. BOX CULVERT WITH SMALL TRIANGULAR BAFFLES

5.1 PROBLEM SETUP

LES simulations were performed for a horizontal rectangular channel equipped with small triangular baffles in the bottom left corner. Four scenarios were tested for different combinations of flow rates and baffle heights. The flow conditions pertaining to the individual cases are summarised in Table 5.1, where Q is the volumetric flow rate, h_b is the side length of the isosceles triangular baffle, and L_b is the streamwise interval between two adjacent baffles. The full numerical results are reported in Appendix B. For Scenarios SC1 to SC3, Cabonce et al. (2017) performed detailed experiments in a 12 m long physical channel illustrated in Figure 5.1. Their results are used to validate the respective numerical models. Scenario SC4 was derived from SC3 by adding a 13 mm hole through the centroid of the baffle, to ventilate the recirculation zone (Cabonce et al., 2018). The provision of ventilation was introduced as a means to alleviate the disorienting effect of large negative velocities on small fish navigating the obstacle.

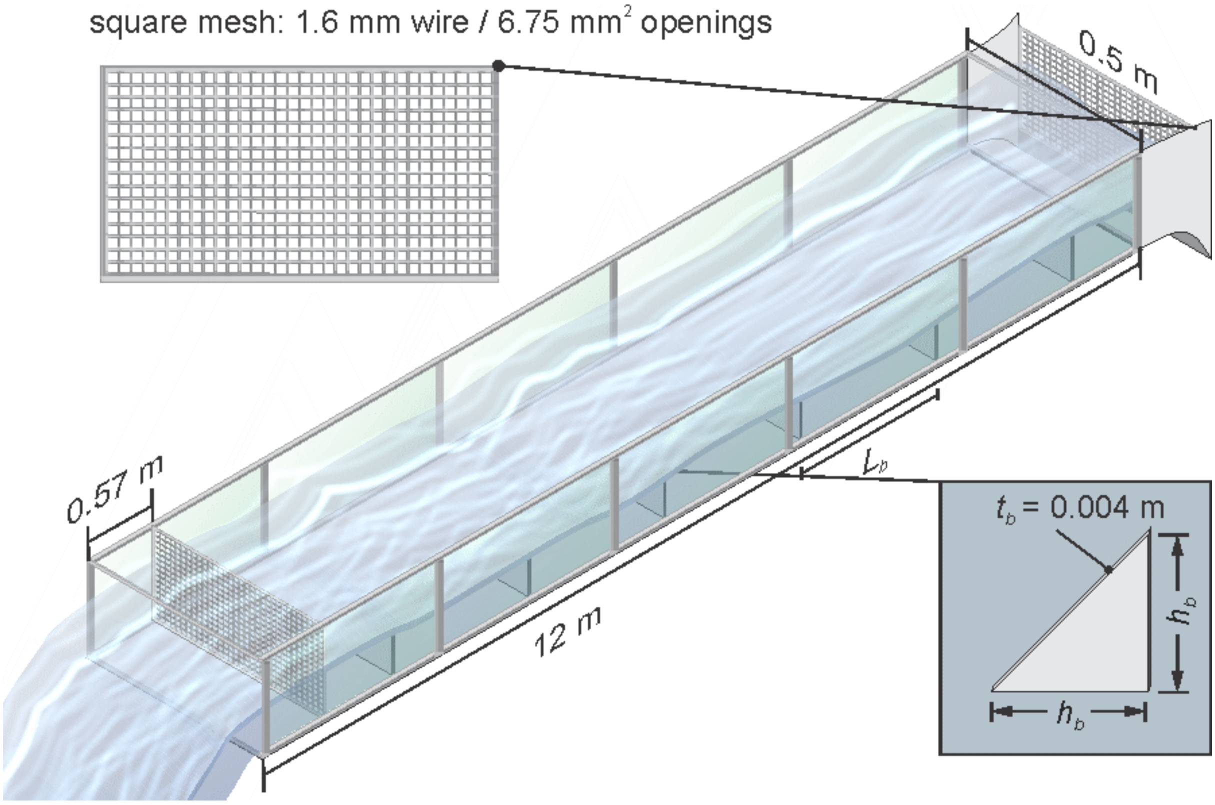

Figure 5.1 – Definition sketch of 12 m long channel equipped with small triangular corner baffles used by Cabonce et al. (2017) – Note the upstream and downstream mesh screens.

Table 5.1 – Summary of flow conditions for investigated scenarios

Scenario	Q (l/s)	h_b (m)	L_b (m)	d (m)	Remark
SC1	26.1	0.067	0.67	0.100	-
SC2	55.6	0.067	0.67	0.165	-
SC3	55.6	0.133	0.67	0.173	-
SC4	55.6	0.133	0.67	0.173	with 13 mm hole[*1]

Note: *1 – the hole on each baffle is centered at 40 mm from its edges

A mass flow rate is imposed on the periodic boundaries in accordance with the water flow rate through domain. At each time step, the mass flow is maintained by the correct pressure gradient which Fluent solves by iteration. Gravity is disabled and as such only the static pressure term was modelled (initially set to the gauge pressure). The simulations were performed on a custom-built Dell Precision T5810 workstation configured with an Intel® Xeon® E5-1680 v4 CPU and 128 GB RAM. The time discretisation was bounded second order implicit. The pressure-velocity coupling was solved using the SIMPLE solver. The spatial discretisation of the momentum equations is handled by a modified central differencing scheme based on the normalised variable diagram (NVD) approach (Leonard, 1991) to achieve second-order accuracy. This is a composite scheme that consists of a pure central differencing, a blend of the central differencing and the second-order upwind scheme, and the first-order upwind scheme (ANSYS). The hybrid formulation retains the low numerical diffusion and reduces the instability due to central differencing, and falls back onto the first-order scheme if unbounded solutions are produced.

Cuboid domains with a footprint of 0.67 m × 0.5 m were selected for the simulations. The vertical extent of each domain was determined from the free surface data of Cabonce et al. (2017). They observed experimentally that the free surface remained largely flat between two successive baffles in the fully developed region, albeit a localised dip immediately downstream of each baffle noticeable only for a large relative baffle h_b/d, where d is water depth. Since effects due to free surface perturbations were expected to be small, representing a flat free surface by a symmetry condition permitted a substantial increase in computational speed with minimum impact on reproduction of the bulk flow features. The longitudinal extent of the domain (0.67 m) was set to equal one baffle spacing (L_b), and preliminary simulations found that the fully developed flow field was very close to periodic (Appendix A). Figure 5.2 illustrates the final computation domain as well as the boundary conditions applied. A single isosceles triangular baffle was placed midway between the periodic inlet and its shadow outlet. The side and bottom walls as well as the baffle surfaces were set up as no-slip walls. The symmetry condition on the top face imposes a zero normal gradient for all fluid variables.

Each numerical domain was discretised into an unstructured hexahedral mesh. The resulting mesh configurations are summarised in Table 5.2. The resolution requirements of WMLES were used as a guide to specify the element sizes on the bounding edges non-contacting with the baffle, with the domain height assumed as δ. The sides of the baffle are discretised into 2 – 3 mm segments, and no constraint was specified for the contacting edge with the baffle. Herein relatively coarse meshes were selected with the goal to keep the computation time manageable ([5]) while preserving the most relevant flow features. The inability to specify the first layer of wall cells in the proximity of $y^+ = 1$ would result in under-characterisation of the boundary layers originating from the no-slip walls. The discrepancy was deemed to be acceptable as the separation created by each baffle was expected to have a dominating effect on the flow redistribution.

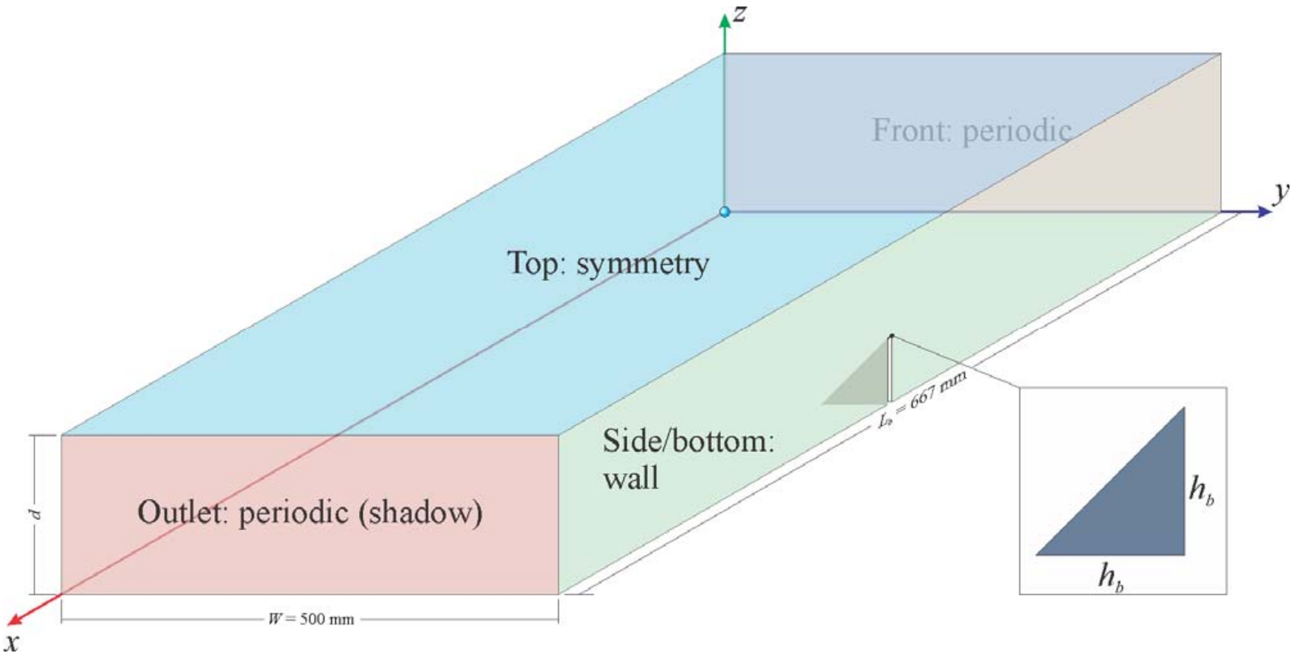

Figure 5.2 – Definition sketch of computational domain.

---

[5] The computational time was influenced by a number of factors. The reduction in domain length, from 12 m down to 0.6 m, allowed computational resources to be allocated more efficiently (e.g. increase the cell count around feature of interest).

Table 5.2 – Summary of mesh configurations used for the sensitivity tests

Scenario	No. Cells	Min. Cell Vol. (mm^3)	Max. Cell Vol. (mm^3)	Max. Aspect Ratio
SC1	549,917	5.82×10^{-2}	3.83×10^{2}	66
SC2	277,509	1.66×10^{-1}	1.06×10^{3}	33
SC3	567,517	4.81×10^{-2}	4.78×10^{2}	112
SC4	704,826	5.68×10^{-2}	3.85×10^{2}	21

5.2 VALIDATION AND RESULTS

5.2.1 Presentation

Each simulation started with an initial assumption of uniform velocity field and iterated until the correct pressure gradient was achieved such that the mass flow rate was consistent with that specified. After the settlement of the initial numerical instability, the solution was run for approximately 10 s before time-averaged statistics were sampled for a further 10 s at an interval of 0.001 s. For each time step, the solution was deemed to have converged once the normalised residuals for continuity and momentum equations decreased below 10^{-3}. It is expected that the numerical behaviour becomes reasonably stationary after several flow resident times (~ 1 s).

The numerical results for Scenarios SC1 to SC3 are validated in the following subsections against the detailed experimental measurements performed by Cabonce et al. (2017). The full results are reported in Appendix B. Note that the comparability between numerical and experimental results may be limited by the relatively short sampling window of 10 s chosen to keep computational time manageable ([6]).

5.2.2 Scenario 1 (SC1)

The numerical investigation of Scenario 1 (SC1) entails the examination of the hydrodynamic effects of regularly-spaced medium-size triangular baffles (h_b = 0.067 m, h_b/L_b = 0.1), in presence of a relatively small discharge (Q = 26.1 l/s), resulting in a moderate submergence (h_b/d = 0.67). Figure 5.3 presents the streamwise velocity (U) contours at several distances downstream of the baffle. The results correspond to the locations where physical measurements in the fully developed region were conducted by Cabonce et al. (2017). In Figure 5.3, $(x - x_b)$ is the downstream distance from the baffle and L_b is the spacing between two baffles (L_b = 0.67 m). The velocity contours are visually comparable to those reported by Cabonce et al. (2017), showing a slow-flowing region induced by the corner baffle and a fast-flowing zone on the opposite side of the channel, next to the

---

[6] For comparison, the physical data were sampled for 90 s at each sampling location.

smooth sidewall. Negative velocities are observed in the immediate wake of the baffle, and extend to approximately $(x\text{-}x_b)/L_b = 0.3$ (not shown) – consistent with the observations of Cabonce et al. (2017). The velocity contours next to the smooth wall appear to overestimate the local velocities, compared to the experimental data, largely due to the under-specification of the mesh resolution near the sidewall. The numerical model also did not account for the transverse pressure gradient due to free-surface inlination towards the smooth wall observed in the experimental data, which might have some effect on the flow redistribution across the channel. Some kinks are observable locally in the contours which could be an artifact owing to the relatively short sampling duration.

Typical velocity profiles at various transverse locations are compared with experimental data in Figure 5.4. The data indicate large flow disturbance induced by the baffle for $y > 0.335$ m, and some flow concentration about $y \approx 0.165$ m. The quantitative agreement is less satisfactory, with the numerical model showing a systematic overestimation than the experimental data. Since the mass flow rate was fixed for the numerical model, this likely implies a slightly over-reported flow rate by the experimental study. The agreement between physical and numerical data is generally better at the centre of the channel (i.e. $0.25 < y < 0.42$ m), than next to the sidewall boundaries. The disparity was also exacerbated by measurement difficulties in the vicinity of the baffle, linked to geometric confinement, negative velocities and strong streamline curvature, in addition to the challenge of maintaining an adequate near-wall mesh resolution. The intrusive presence of the Prandtl-Pitot tube may also disturb the experimental flow, noticeably when inserted into the corner behind baffle. Generally, the difference between data was not satisfactory, albeit expected.

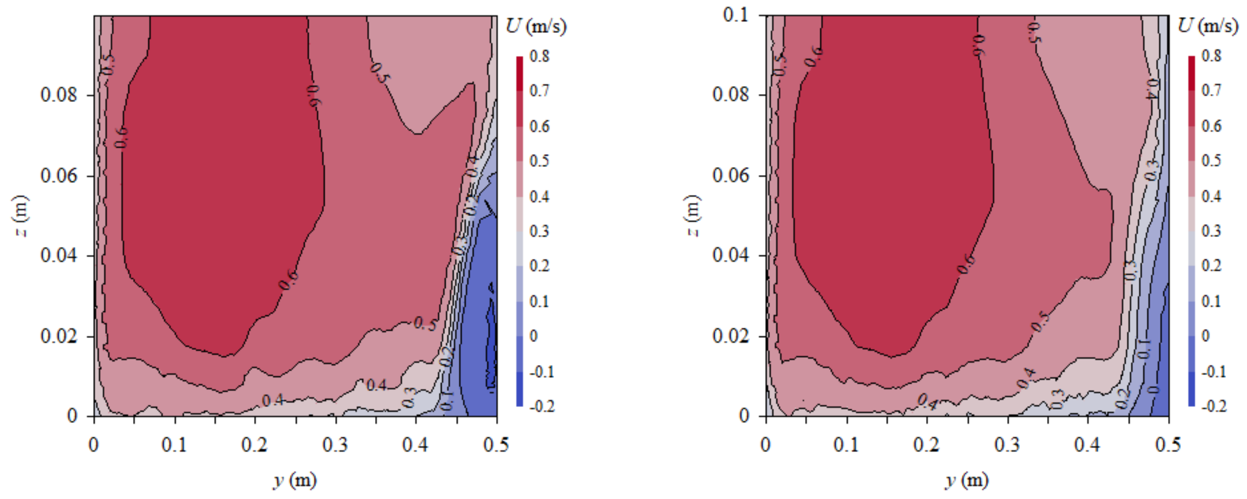

(a) $(x\text{-}x_b)/L_b = 0.05$

(b) $(x\text{-}x_b)/L_b = 0.235$

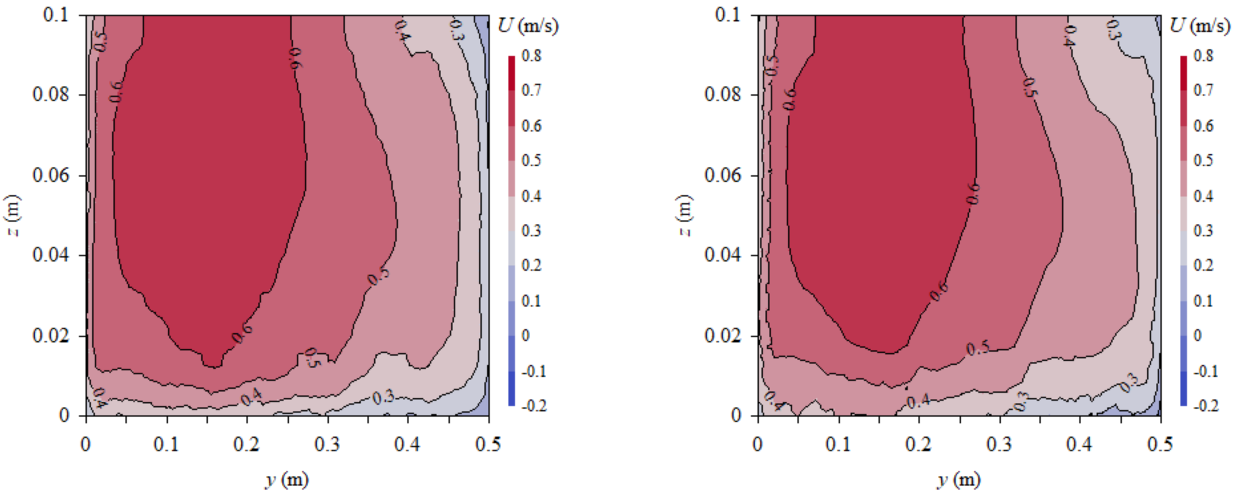

(c) $(x\text{-}x_b)/L_b = 0.5$ (d) $(x\text{-}x_b)/L_b = 0.765$

Figure 5.3 – Velocity contours behind baffle – Flow conditions: Q = 26.1 l/s, h_b = 0.067 m, L_b = 0.67 m, d = 0.1 m.

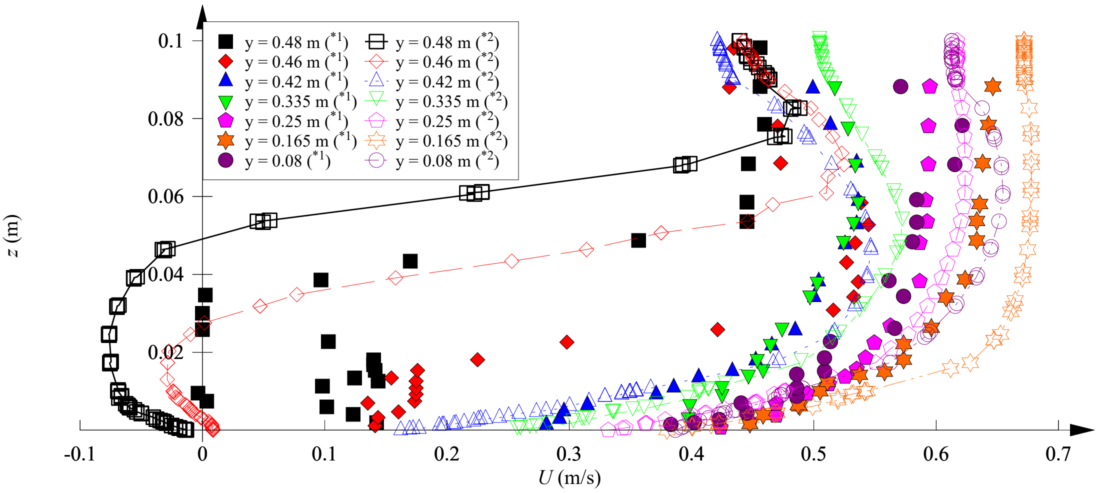

(a) $(x\text{-}x_b)/L_b = 0.05$

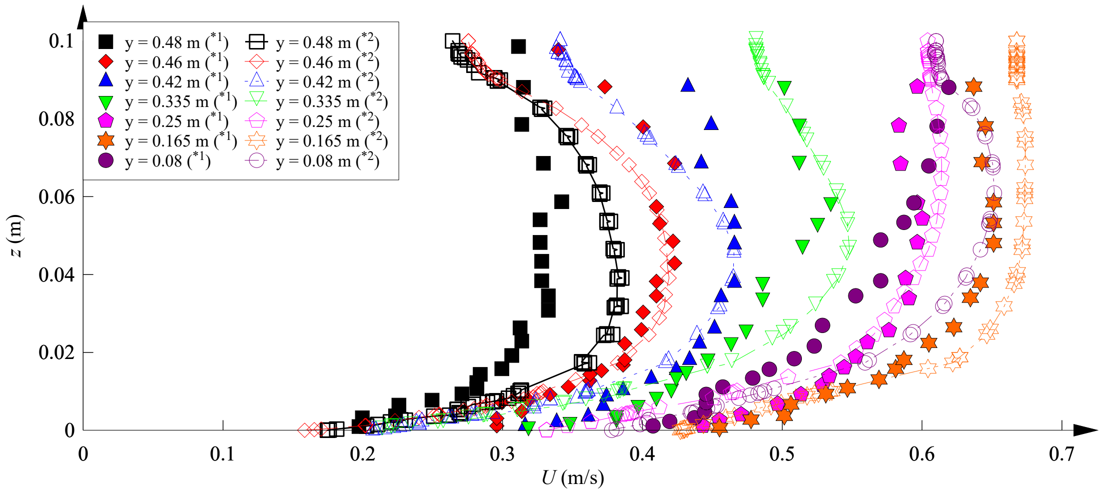

(b) $(x\text{-}x_b)/L_b = 0.765$

Figure 5.4 – Velocity profiles at different transverse locations across channel in a culvert barrel channel equipped with small triangular corner baffles – Flow conditions: $Q = 26.1$ l/s, $h_b = 0.067$ m, $L_b = 0.67$ m, $d = 0.1$ m – Notes: *1 – Experimental data by Cabonce et al. (2017); *2 – Large Eddy Simulation (present study).

The combination of aforementioned experimental and numerical constraints makes achieving satisfactory agreement in terms of the local velocity profiles a significant challenge, although it is still of much benefit for the numerical model to remain capable of reproducing local characteristic properties, in absence of a more comprehensive agreement. Figure 5.5 presents typical comparisons of transverse distributions of maximum streamwise velocity per vertical profile (U_{max}) between numerical and experimental data. Overall a good agreement is achieved regardless of the streamwise location relative to the baffle. A further inspection reveals a slight overestimation of U_{max} by the numerical model, more noticeable towards the smooth wall, which results from the limited mesh resolution. The discrepancy remains below 10% and the results demonstrate that the general flow redistribution is adequately reproduced. The results show that velocity maxima occur below the free surface, as a consequence of strong secondary circulations that span the full width of the channel. The flow is most concentrated in the range of $0.5 < y/d < 0.8$, though the limited amount of experimental data prevents more meaningful comparisons. Typical distributions of the vertical elevations of velocity maxima data (numerical and experimental) are shown in Figure 5.6.

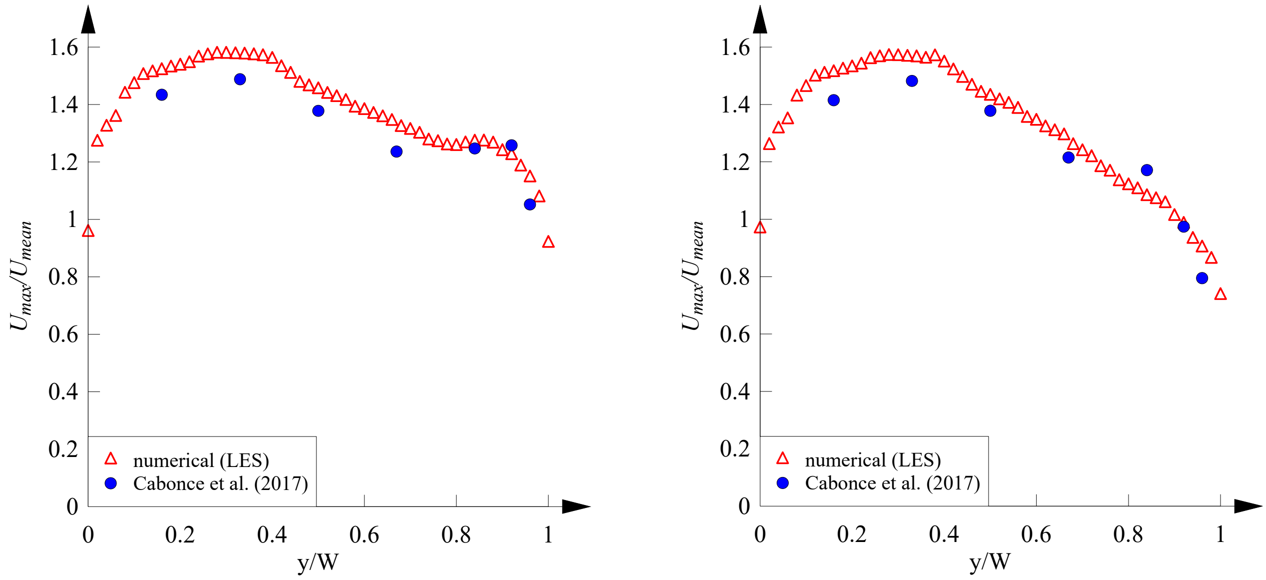

(a) $(x\text{-}x_b)/L_b = 0.05$

(b) $(x\text{-}x_b)/L_b = 0.235$

Figure 5.5 – Transverse distributions of streamwise velocity maxima – Flow conditions: Q = 26.1 l/s, h_b = 0.067 m, L_b = 0.67 m, d = 0.1 m.

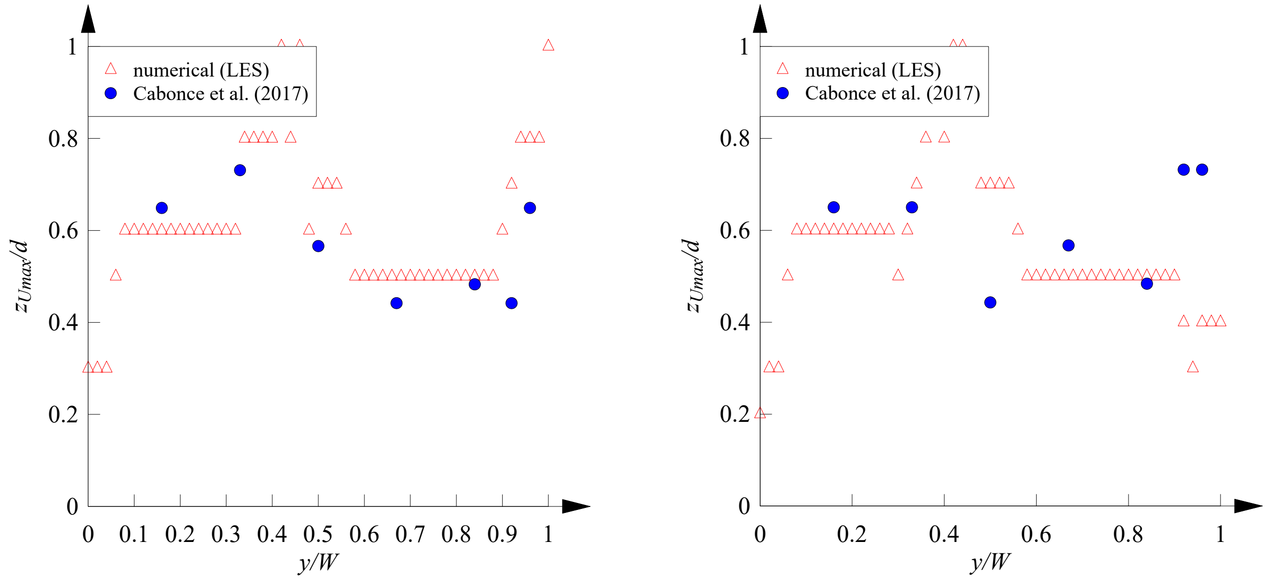

(a) $(x\text{-}x_b)/L_b = 0.05$

(b) $(x\text{-}x_b)/L_b = 0.765$

Figure 5.6 – Transverse distributions of elevations of streamwise velocity maxima – Flow conditions: Q = 26.1 l/s, h_b = 0.067 m, L_b = 0.67 m, d = 0.1 m.

5.2.3 Scenario 2 (SC2)

Scenario SC2 investigates the blockage effects of regularly-spaced medium-size baffles (h_b = 0.067 m, h_b/L_b = 0.1) subject to a moderately high discharge (Q = 56.6 l/s). The relative size of the blockage is substantially reduced, compared to Scenario SC1 (h_b/d = 0.4). Figure 5.7 presents the streamwise velocity (U) contours at various distances downstream of the baffle, corresponding to those reported for the fully developed region by Cabonce et al. (2017). The velocity contours compare closely to those in Cabonce et al. (2017), except next to the smooth wall where the numerical boundary layer appears underdeveloped. Remarkably, the numerical model correctly predicts the velocity dips about $y/W = 0.3$, which is linked to large secondary flow cells occupying both halves of the channel cross-section. Both physical and numerical data highlight a recirculation zone, in the wake of the baffle, that extends up to approximately $(x - x_b)/h_b = 3$. The numerical model yields notably smaller negative velocities (up to -0.2 m/s) than the experimental data (up to -0.8 m/s), which could be susceptible to strong streamline curvatures, which pose a significant measurement challenge. The area of velocity concentration on the smooth side of the channel appears to decay faster for the experimental data than for the numerical data, which could be on account of the under-modelled skin friction. In general, the numerical model is able to reproduce the flow patterns satisfactorily despite a relatively coarse mesh.

Figure 5.8 shows a typical comparison of vertical profiles of longitudinal velocity at various transverse locations between numerical and experimental results. The comparison shows basically that the baffle impact is most noticeable on the velocity profiles immediately adjacent to the left (baffled) wall (y = 0.46 and 0.48 m). The numerical model overestimates the velocity by up to 20% on the smooth half the channel, which could be linked to the mesh resolution. Overall, the numerical model reproduces the experimental data qualitatively, although achieving quantitative agreement locally still appears to be a significant challenge. Figure 5.9 presents typical comparisons of transverse distributions of streamwise velocity maxima between the numerical and experimental results. The agreement is very good for all locations downstream of the baffle. The numerical model yields slightly larger results than the experimental data, which might be in consequence of the limited mesh resolution. In general, the results demonstrate the model capability to satisfactorily reproduce the flow redistribution. The corresponding distributions of the elevations of the longitudinal velocity maxima for both numerical and experimental results are illustrated in Figure 5.10. Both datasets indicate that velocity maxima frequently occur below the free surface, with substantial variations across the channel. A direct comparison cannot be made as the large scatter implies significant uncertainties in both data.

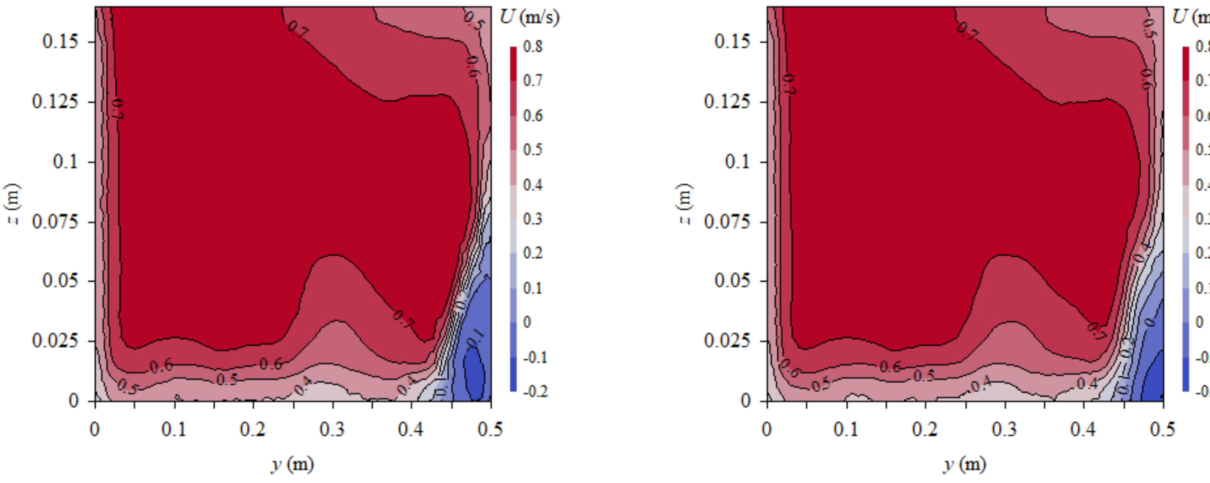

(a) $(x\text{-}x_b)/L_b = 0.05$ (b) $(x\text{-}x_b)/L_b = 0.235$

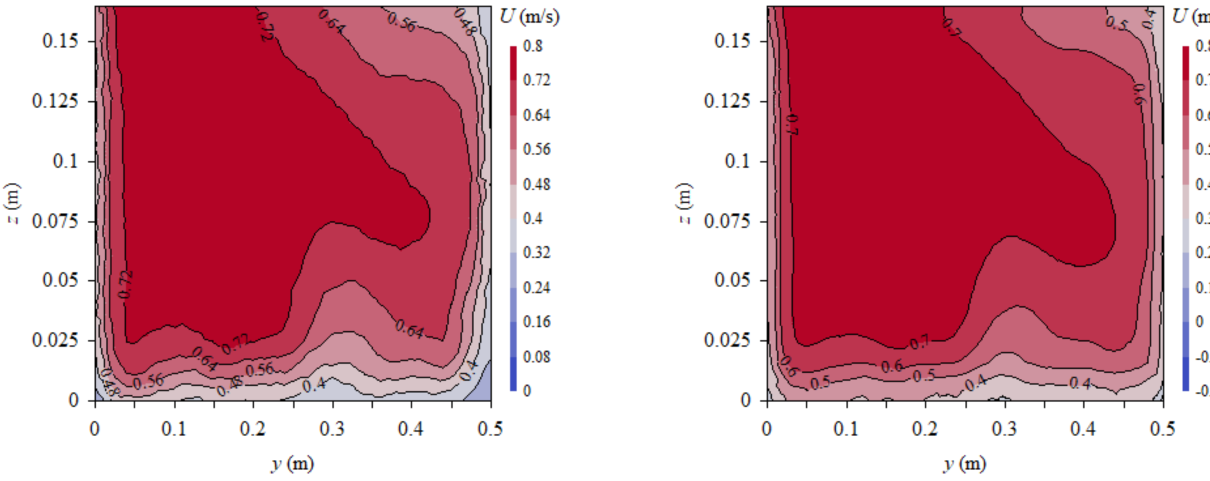

(c) $(x\text{-}x_b)/L_b = 0.5$ (d) $(x\text{-}x_b)/L_b = 0.765$

Figure 5.7 – Velocity contours behind baffle – Flow conditions: Q = 55.6 l/s, h_b = 0.067 m, L_b = 0.67 m, d = 0.165 m.

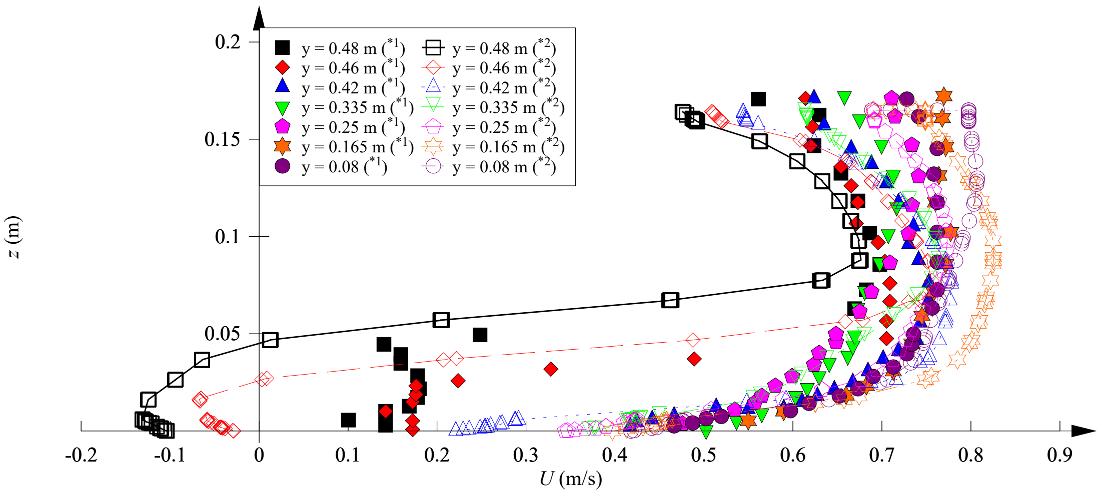

(a) $(x\text{-}x_b)/L_b = 0.05$

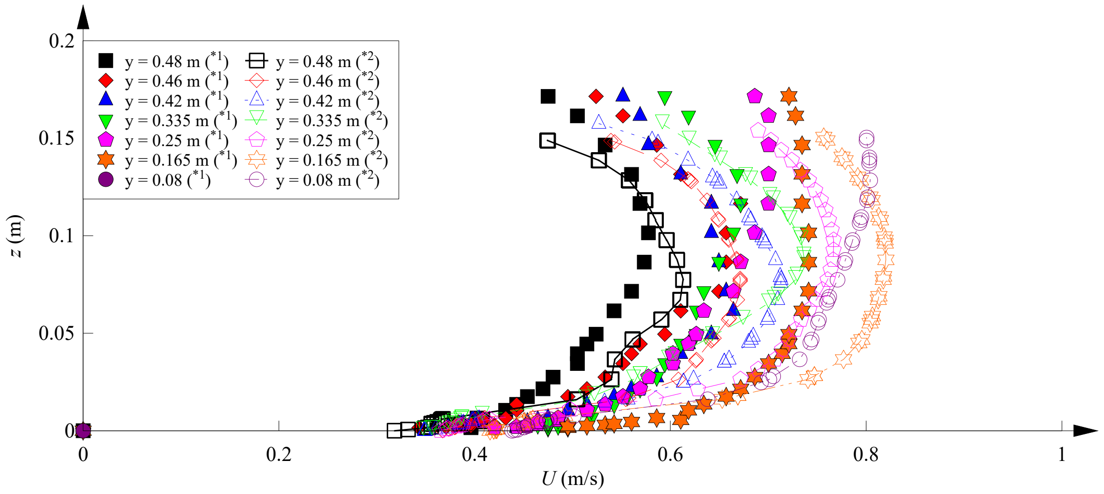

(b) $(x-x_b)/L_b = 0.765$

Figure 5.8 – Velocity profiles at different transverse locations across channel equipped with small triangular corner baffles – Flow conditions: Q = 55.6 l/s, h_b = 0.067 m, L_b = 0.67 m, d = 0.165 m – Notes: *1 – Experimental data by Cabonce et al. (2017); *2 – Large Eddy Simulation (present study).

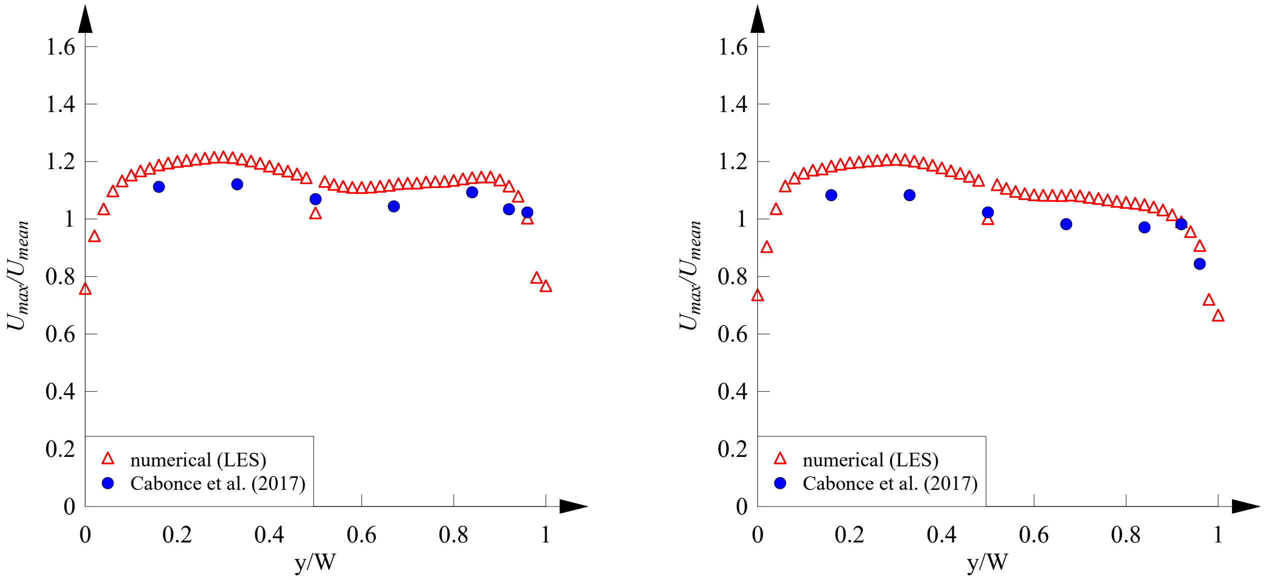

(a) $(x-x_b)/L_b = 0.05$

(b) $(x-x_b)/L_b = 0.765$

Figure 5.9 – Transverse distributions of streamwise velocity maxima – Flow conditions: Q = 55.6 l/s, h_b = 0.067 m, L_b = 0.67 m, d = 0.165 m.

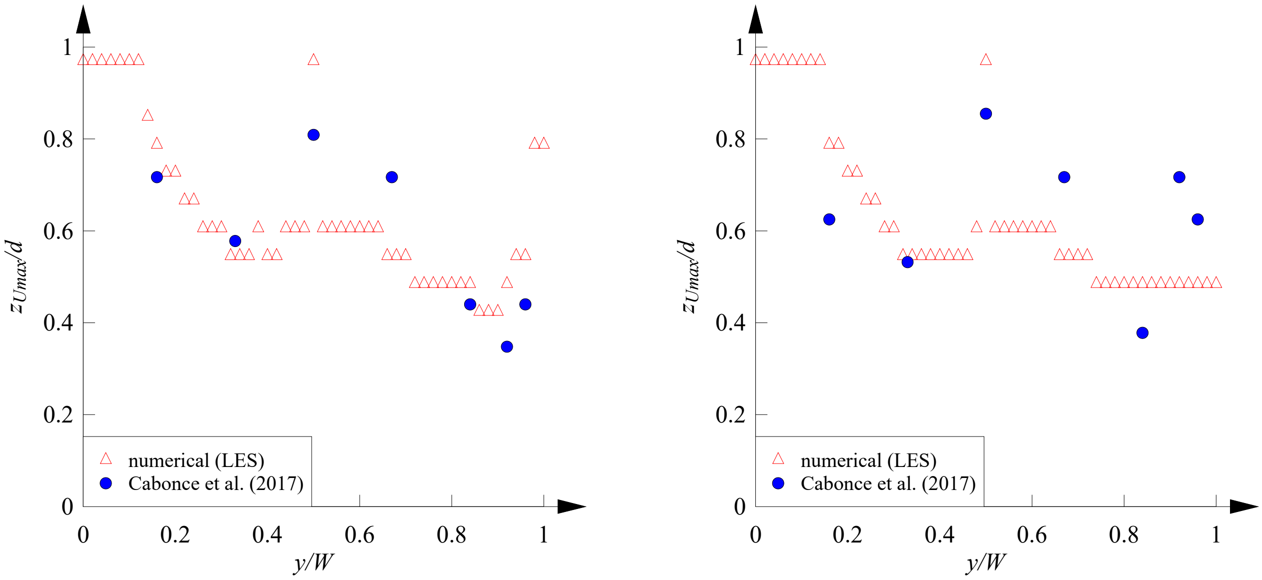

(a) $(x\text{-}x_b)/L_b = 0.05$ (b) $(x\text{-}x_b)/L_b = 0.765$

Figure 5.10 – Transverse distributions of elevations of streamwise velocity maxima – Flow conditions: $Q = 55.6$ l/s, $h_b = 0.067$ m, $L_b = 0.67$ m, $d = 0.165$ m.

5.2.4 Scenario 3 (SC3)

Scenario SC3 extends Scenario SC2 by enlarging the baffles to twice of their original size (h_b = 0.133 m), thus achieving a significant reduction in the relative spacing between baffles (h_b/L_b = 0.2). The close proximity between adjacent baffles promotes their interactions, and their compounding effects might result in a more complex flow field. Figure 5.11 presents the streamwise velocity (U) contours at several locations downstream of the baffle. The results are comparable to those in Cabonce et al. (2017). The underdevelopment of the boundary layer next to the smooth wall is noticeable, as in both Scenarios SC1 and SC2 because of insufficient mesh resolution. Both physical and numerical results show a recirculation zone generated by the baffle blockage, with negative velocities up to -0.3 m/s and -1 m/s for the numerical and experimental data respectively. The negative velocity zone is approximately equal in size with the baffle, and decays rapidly with increasing distance downstream. The physically-measured negative velocities appear very large (i.e. exceeding the bulk velocity), possibly because of measurement challenges using a Prandtl-Pitot tube. Both numerical and physical results identify the bulk of the flow occurring within $y < 0.35$ m, as well as a large dip in the velocity contours between $0.1 < y < 0.3$ m caused by the baffle influence. The numerical model appears to overestimate the velocities further downstream of the baffle, i.e. $(x\text{-}x_b)/L_b > 0.5$, which could be linked to the relatively coarse mesh. Occasionally, the computed velocity contours exhibit some local undulations, which might vanish with a longer sampling duration. Overall, the numerical model appears to be sufficiently detailed for establishing the major flow features, despite with a relatively coarse mesh.

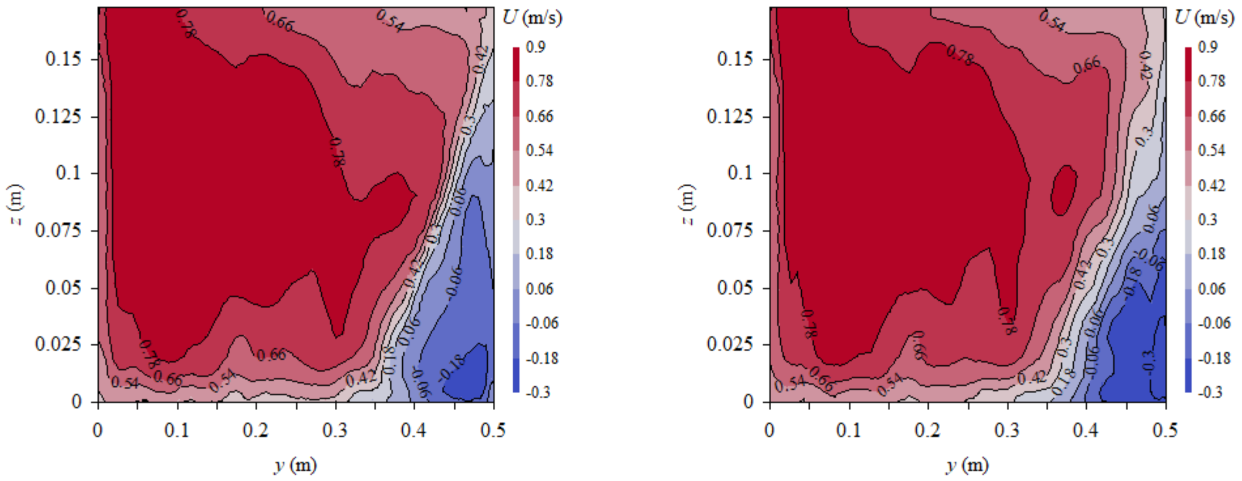

(a) $(x\text{-}x_b)/L_b = 0.05$ (b) $(x\text{-}x_b)/L_b = 0.235$

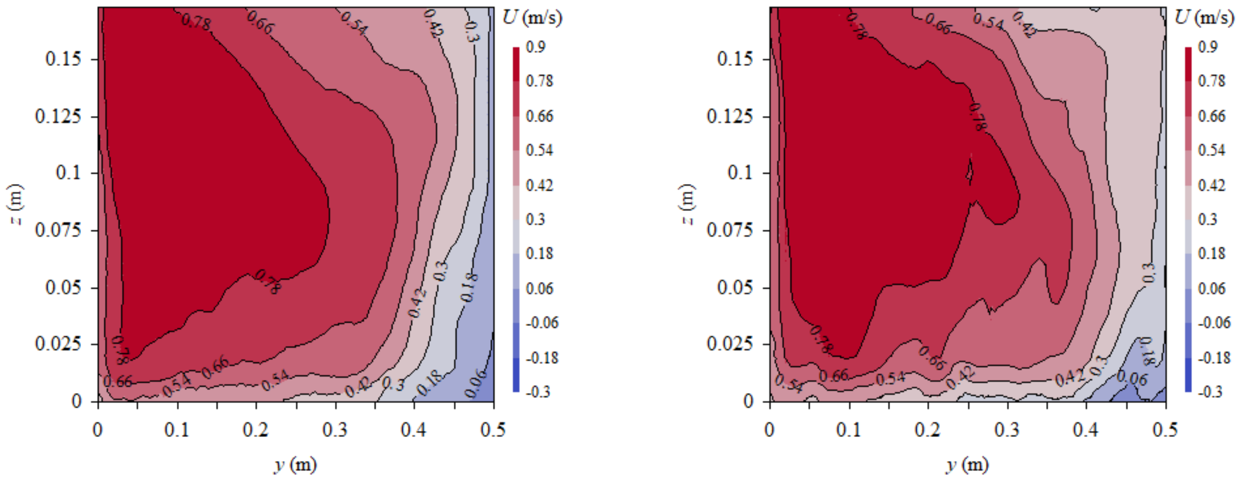

(c) $(x\text{-}x_b)/L_b = 0.5$ (d) $(x\text{-}x_b)/L_b = 0.765$

Figure 5.11 – Velocity contours behind baffle – Flow conditions: $Q = 55.6$ l/s, $h_b = 0.133$ m, $L_b = 0.67$ m, $d = 0.165$ m

Figure 5.12 shows some comparison in terms of velocity profiles at various transverse locations between numerical and experimental results. The ful results are presented in Appendix B. Close to the baffle, i.e. $(x\text{-}x_b)/L_b = 0.05$, experimental and numerical results generally agree within 10 % everywhere, except in the recirculation region, which might be some metrology issue. The difference increases with increasing distance downstream of the baffle up to $(x\text{-}x_b)/L_b = 0.765$, with the numerical model typically producing larger velocities near the smooth wall and smaller velocities next to the left (baffled) wall. The observation might be linked to some inadequately resolution of the boundary layers originating from smooth walls. Overall, the quantitative agreement between velocity profiles appear to be improved compared to Scenario SC1, although still less than satisfactory.

Figure 5.13 compares typical transverse distributions of streamwise velocity maxima between numerical and experimental results. A basic agreement is observed at all locations downstream of the baffle. The numerical results exhibit some local oscillations, which are expected to be dampened by increasing the sampling duration. Both physical and numerical data are consistent, showing a flow slowdown below the bulk velocity for $y/W > 0.8$, which is of substantially larger extent than in Scenarios SC1 and SC2. Overall, the numerical model satisfactorily replicates the major flow features reflecting the selected size and spacing of the baffles. The corresponding distributions of the elevations of the velocity maxima for both numerical and experimental results are illustrated in Figure 5.14. All the data show a clear trend where the maximum velocity is found closer to the free surface near the walls than in the middle of the channel. The agreement between data is satisfactory and noticeably improved compared to Scenarios SC1 and SC2 despite the similar mesh adopted. The observation suggests that the validation might be more dependant on the flow conditions than on the mesh.

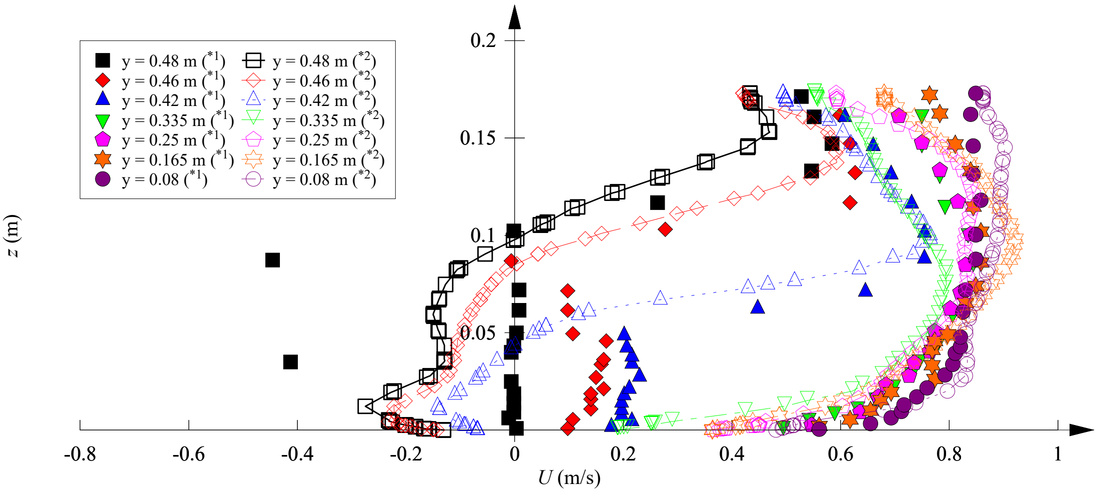

(a) $(x-x_b)/L_b = 0.05$

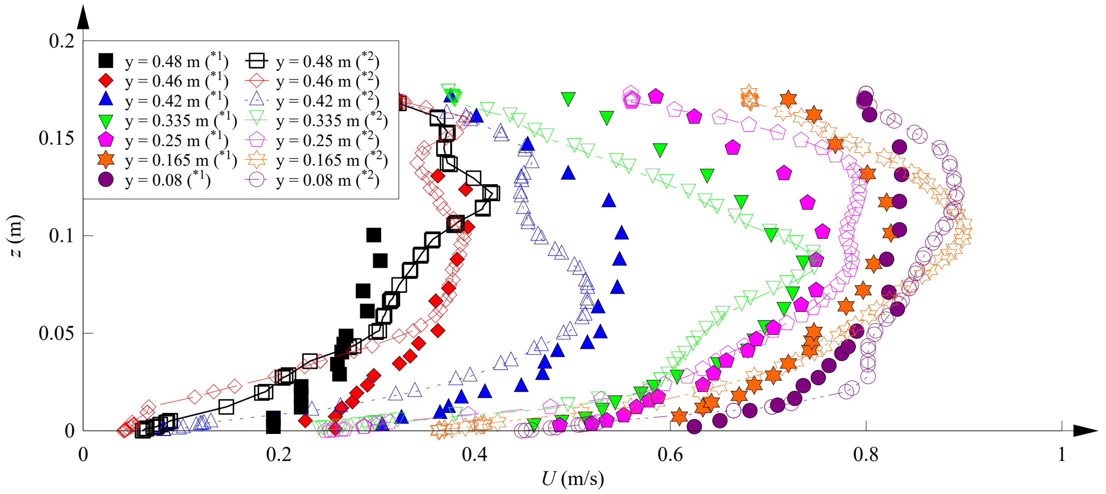

(b) $(x-x_b)/L_b = 0.765$

Figure 5.12 – Velocity profiles at different transverse locations across channel equipped with small triangular corner baffles – Flow conditions: $Q = 55.6$ l/s, $h_b = 0.133$ m, $L_b = 0.67$ m, $d = 0.173$ m – Notes: *1 – Experimental data by Cabonce et al. (2017); *2 – Large Eddy Simulation (present study).

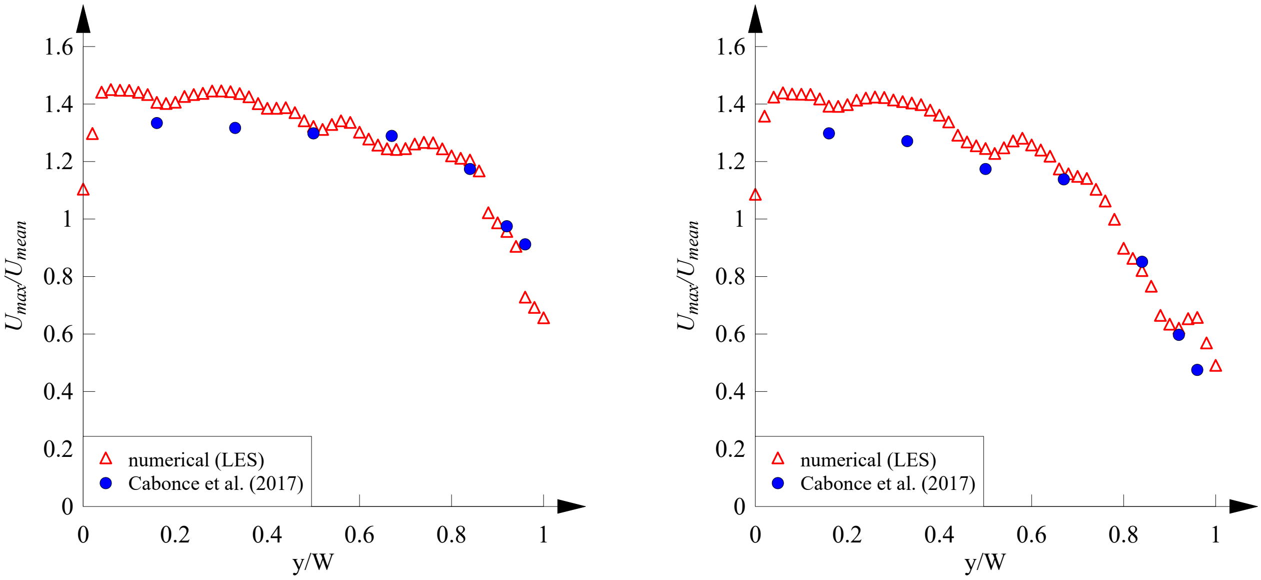

(a) $(x-x_b)/L_b = 0.05$

(b) $(x-x_b)/L_b = 0.765$

Figure 5.13 – Transverse distributions of streamwise velocity maxima – Flow conditions: $Q = 55.6$ l/s, $h_b = 0.133$ m, $L_b = 0.67$ m, $d = 0.173$ m.

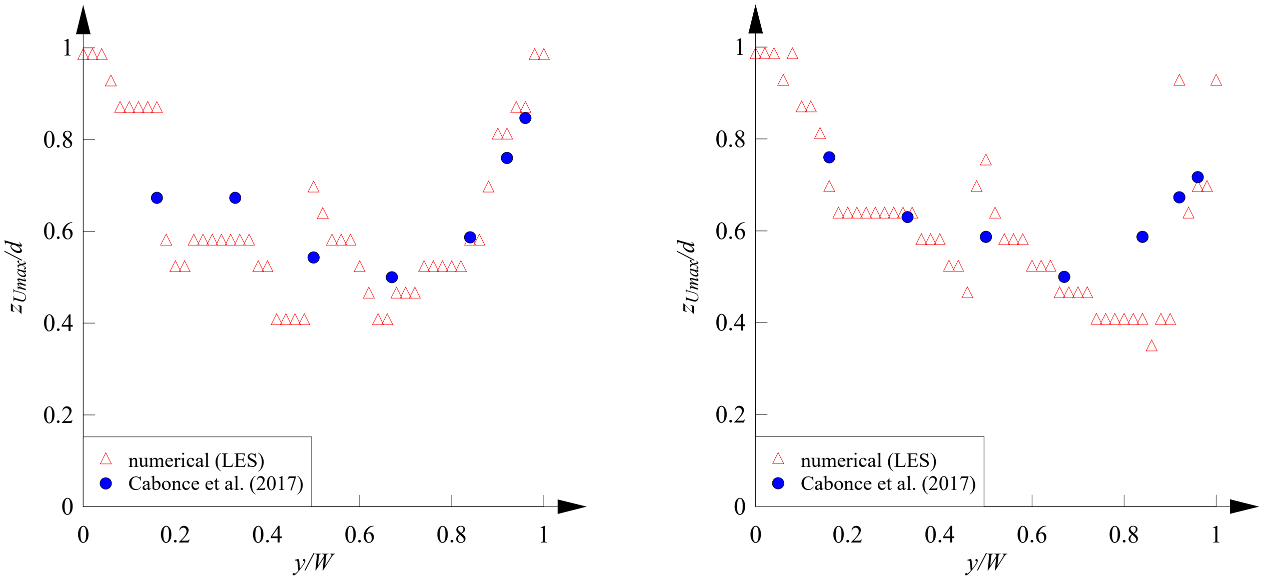

(a) $(x\text{-}x_b)/L_b = 0.05$ (b) $(x\text{-}x_b)/L_b = 0.765$

Figure 5.14 – Transverse distributions of elevations of streamwise velocity maxima – Flow conditions: $Q = 55.6$ l/s, $h_b = 0.133$ m, $L_b = 0.67$ m, $d = 0.173$ m.

5.3 APPLICATION

5.3.1 Presentation

The above validations (Section 5.2) suggest that the numerical models can replicate qualitatively the major flow features, even with a relatively coarse mesh. Yet, achieving quantitative agreement everywhere remains a significant challenge. Overall the numerical models are deemed useful for assessing changes in the bulk flow features when geometric changes are introduced. Herein the model used for Scenario SC3 is modified to assess the hydrodynamic effects of a 13 mm ventilation hole, located at 40 mm from the baffle edges as illustrated in Figure 5.15. The numerical model was run for 10 s prior to time statistics being sampled for a further 10 s at an interval of 0.001 s. The basic findings are reported in the following subsections and compared to the physical observations of Cabonce et al. (2018). The full numerical results are reported in Appendix B.

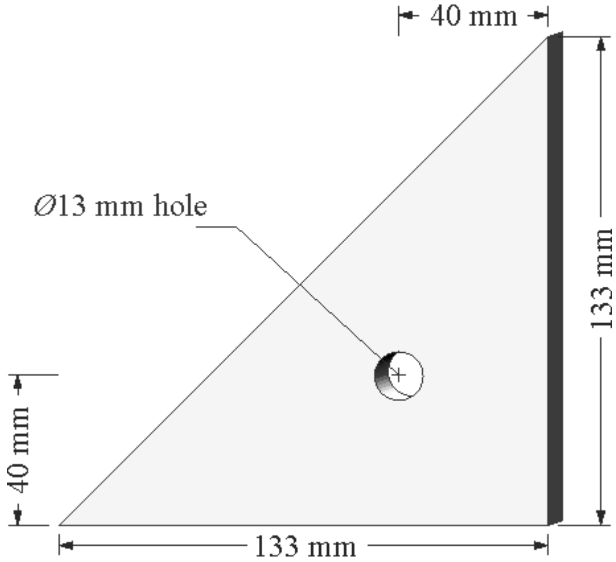

Figure 5.15 – Specification of baffle with hole.

5.3.2 Numerical results

The immediate effects of the ventilated corner baffle (Figure 5.15) are observed in Figure 5.16, presenting the streamwise velocity contours on *xz*-planes next to the left baffled wall ($(W-y)/W = 0.01$) and through the hole centre ($(W-y)/W = 0.08$). The velocities are exactly zero on the upstream face of the baffle, preceded by a small recirculation region due to upstream flow stagnation. A much stronger recirculation zone exists in the immediate wake of baffle with a streamwise extent of approximately three times the baffle size – consistent with the observations for Scenarios SC1 to SC3. The centre of the downstream recirculation zone is located at approximately $(x\text{-}x_b)/h_b = 1$, where negative velocities up to -0.4 to -0.5 m/s are identified. A concentration of high velocities up to 0.5 m/s is observed immediately downstream and above the baffle, which is due to flow detachment from the baffle edge. At the transverse position of the hole, the upstream recirculation zone diminishes drastically in size and occupies only a small portion upstream of the baffle toe. The downstream wake is of a similar extent to that adjacent to the wall, centred at approximately $(x\text{-}x_b)/h_b = 1$ with negative velocities up to -0.3 m/s. A fast jet of velocities reaching 0.7 m/s develops immediately downstream of the hole and quickly dissipates into the surrounding recirculatory motion, while drawing also some fluid from above. The persisting recirculation motions indicate strong streamline curvature, which could imply a non-hydrostatic pressure gradient. Figure 5.17 shows the contours of streamwise velocity fluctuations u_{rms} for the same locations as in Figure 5.16. The strongest velocity fluctuations are found near the jet exiting the hole attributed to the large velocity differentials with the surrounding fluid. Significant fluctuations up to 0.2 m/s are also identified in the upstream stagnation zone and for a substantial region downstream of the baffle from channel mid-height up to the free surface, which may have some contributions from the flow unsteadiness. Overall, the present observations suggest that a single hole provides insufficient ventilation behind the baffle; while the jet due to its presence increases the surrounding turbulence although to a rather limited extent.

The presence of the baffle divides the channel into a fast-flowing region and a slow recirculation region on each side. At the first downstream location ($(x\text{-}x_b)/L_b = 0.05$), the negative velocity zone is identified to be similar in size and shape compared to Scenario SC3.Figure 5.18 illustrates typical contours of streamwise velocity and velocity fluctuations immediately downstream of the baffle. The projection of high velocities due to the hole results in slightly more pronounced velocity dips towards the corner of the baffle, although the effect is restricted to a very small region. The velocity concentration on the opposite side of the channel is close in both shape and magnitude to Scenario SC3, suggesting that the ventilation provided by the hole is insufficient to penetrate the bulk flow. The recirculation zone occupies gradually smaller sizes with increasing distance downstream of the baffle, and a global positive flow is restored approximately for $(x\text{-}x_b)/L_b > 0.5$. From the re-attachment point, the initial flow concentration becomes reduced in size, and the boundary layer originating from the baffled wall appears much more developed compared to those next to the bottom and smooth wall, possibly because of the insufficient near wall mesh resolution ([7]). In general, the velocity contours at all locations behind baffle largely resemble those for the same configuration without the ventilation hole, suggesting that a larger opening may be warranted for introducing meaningful modifications to the recirculation flow field behind the baffle.

In general, much larger velocity fluctuations are identified on the baffled side of the channel than on the smooth side. The baffle edge and the ventilation hole induce regions with the strongest fluctuations, up to 0.2 m/s, immediately downstream of the baffle, similar in magnitude to those next to the left baffled sidewall (Figure 5.17). The sizes of turbulent cores evolve significantly with increasing distance downstream of the baffle, while large velocity fluctuations of approximately 0.1 m/s persist throughout. In contrast, the smooth half of the channel cross-section appears to experience much less turbulent fluctuations with magnitudes of at least an order less. Overall, whilst difficult to ascertain the individual contribution of the hole to any turbulence modification behind the baffle, it appears limited in extent as the flow dynamics remain dominated by the flow separation initiated by the baffle edge.

---

[7] as observed in Scenario SC3.

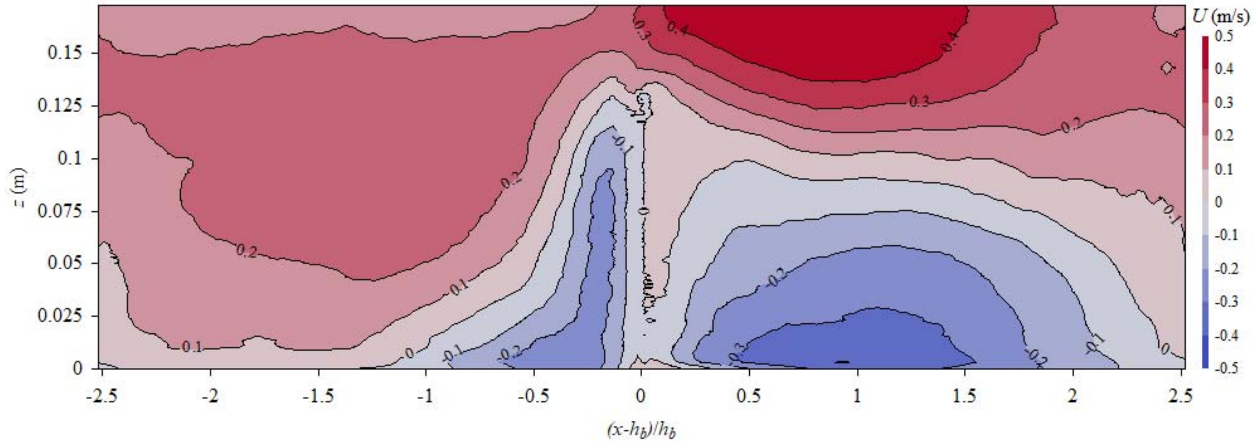

(a) $(W-y)/W = 0.01$ (wall)

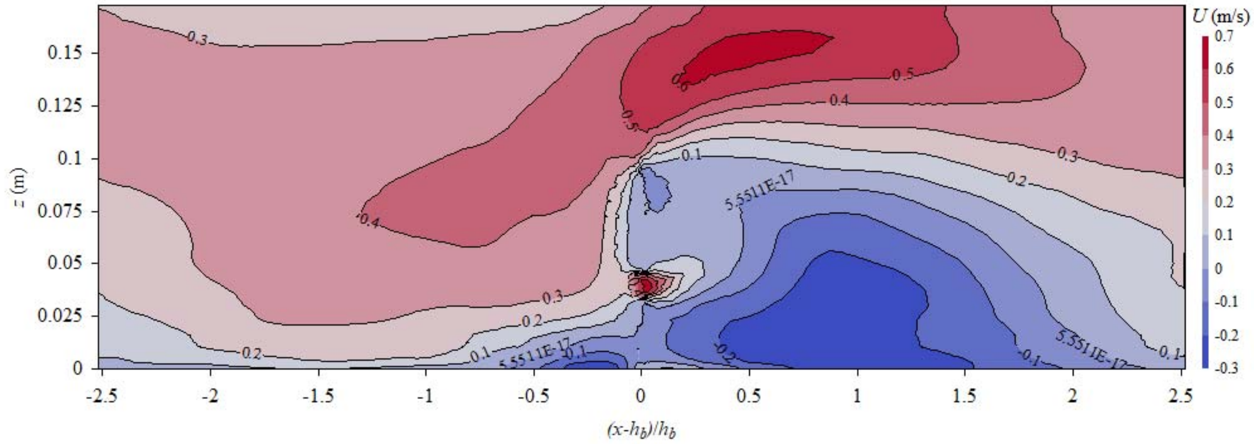

(b) $(W-y)/W = 0.08$ (hole)

Figure 5.16 – Longitudinal velocity contours at various distances from the baffled wall – Flow conditions: $Q = 55.6$ l/s, $h_b = 0.133$ m, $L_b = 0.67$ m, $d = 0.173$ m, ∅ = 13 mm hole.

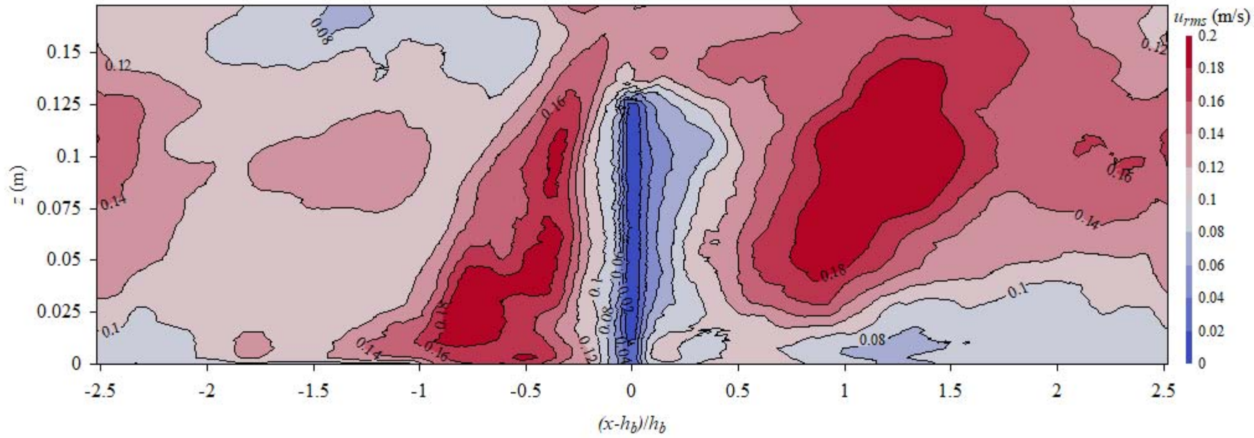

(a) $(W-y)/W = 0.01$ (wall)

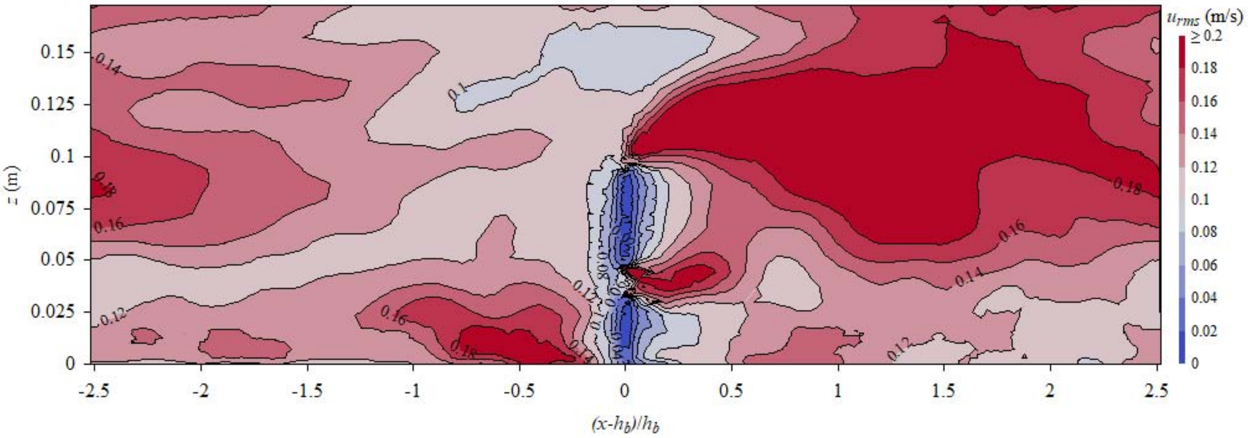

(b) $(W-y)/W = 0.08$ (wall)

Figure 5.17 – Contours of streamwise velocity fluctuations at various distances from the baffled wall – Flow conditions: $Q = 55.6$ l/s, $h_b = 0.133$ m, $L_b = 0.67$ m, $d = 0.173$ m, ∅ = 13 mm hole.

The velocity contour data (Fig. 5.18a and App. B) imply strong secondary motions within the channel. Herein the maximum streamwise velocity within a vertical profile and its corresponding elevation are found to be a function of the transverse position y/W for a given cross-section. The transverse distributions of maximum streamwise velocities and their corresponding locations at different locations downstream of the baffle are presented in Figure 5.19. The baffle is seen to have induced a strong flow deceleration on the baffled side of the channel for approximately $y > 0.7$, and a corresponding flow concentration on the opposite side. The maximum velocity peaks at $U_{max}/U_{mean} = 1.4$ near the smooth wall, and decreases steadily to about $y/W = 0.7 – 0.8$. For $y/W >$ 0.7 – 0.8, the maximum velocity decreases rapidly towards the wall because of interactions with the wake behind baffle. The ratio U_{max}/U_{mean} gradually decreases as the initial accelerating fluid past the baffle slows down with increasing downstream distance. Figure 5.19 reveals that the flow concentration around baffle edge is indeed the cause of the maximum velocities in that region. For the central portion of the channel ($0.2 < y/W < 0.7$), the maximum velocities occur near the channel mid-height rather than the free surface due to secondary currents. The present observations are qualitative and quantitatively similar to the numerical and experimental results for Scenario SC3, with no obvious effects due to the ventilation hole.

For completeness, the transverse distributions of maximum streamwise velocity fluctuations $u_{rms,max}$ and their corresponding elevations show maximum turbulent fluctuations above 10% of U_{mean} everywhere within the channel, which increases steadily towards $y/W = 1$. The baffle induces a significant spike in $u_{rms,max}/U_{mean}$ for $y/W < 0.6$, peaking at $u_{rms,max}/U_{mean} \approx 0.4$ at $y/W = 0.8$ and $(x-x_b)/L_b = 0.05$. The increase in turbulence levels reduces gradually with increasing distance downstream of the baffle, and becomes unnoticeable at $(x-x_b)/L_b = 0.765$. Further the maximum velocity fluctuations occur next to the wall for the most part of the channel, and occasionally near the free surface. For y > 0.6 and $(x\text{-}x_b)/L_b \leq 0.5$, the locations of maximum $u_{rms,max}/U_{mean}$ coincide with the baffle edge, where no effects due to the hole is ascertained.

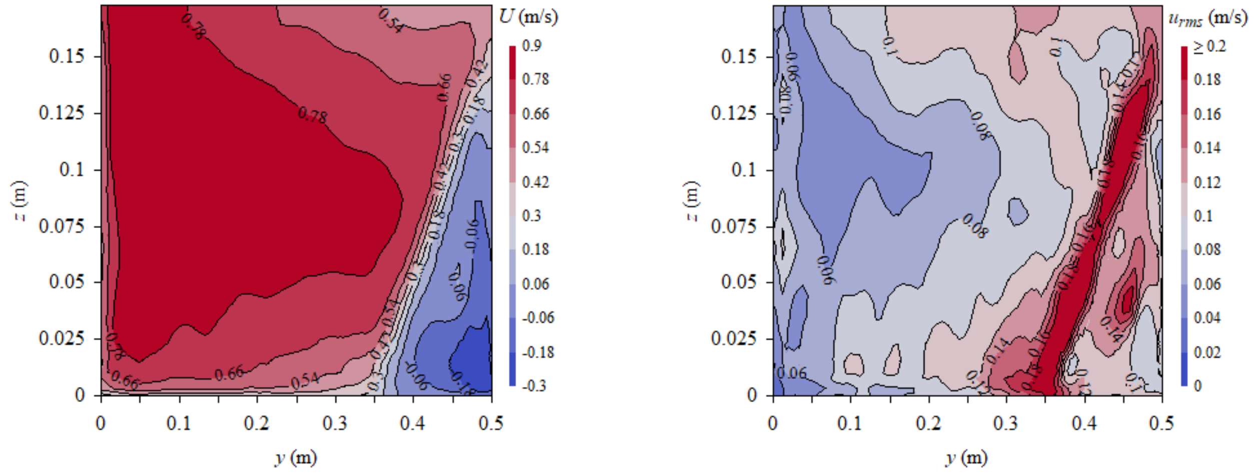

(a) Streamwise velocity (b) Streamwise velocity fluctuations

Figure 5.18 – Contours of time-averaged longitudinal velocity and velocity fluctuations immediately behind ventilated baffle – Flow conditions: Q = 55.6 l/s, h_b = 0.133 m, L_b = 0.67 m, d = 0.173 m, ∅ = 13 mm hole, $(x\text{-}x_b)/L_b = 0.05$.

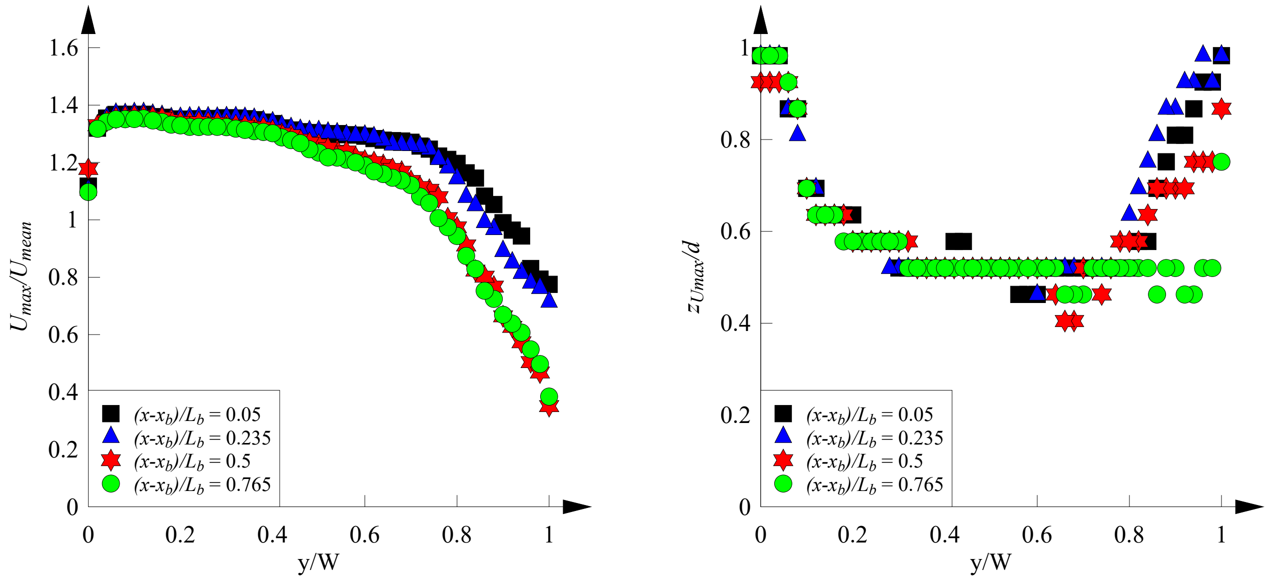

(a) Distributions of U_{max} (b) Distributions of z_{Umax}

Figure 5.19 – Transverse distributions of maximum streamwise velocities U_{max} and corresponding locations z_{Umax} – Flow conditions: Q = 55.6 l/s, h_b = 0.133 m, L_b = 0.67 m, d = 0.173 m, ∅ = 13 mm hole.

5.4 SUMMARY

Three-dimensional large eddy simulations were performed with a commercial package for several box culvert configurations equipped with small triangular corner baffle system. The initial design was proposed by Chanson and Uys (2016) with the intention to instigate slow velocity zones to facilitate upstream passage of fish with small body mass. Their performances in terms of fish passage and endurance were subsequently evaluated in a near-prototype scale facility by Cabonce et al. (2017,2018). The present study has succeeded in determining a feasible numerical configuration that achieves an acceptable balance between accuracy and efficiency, to gain further understanding of the hydrodynamic modifications introduced by the baffle system.

Validation tests were undertaken in terms of key flow parameters for three scenarios involving different combinations of discharge, baffle size and spacing. Comparisons with experimental data established the capacity of the numerical models to satisfactorily replicate the major flow features associated with the baffle albeit a relatively coarse mesh used. It was also recognised that achieving acceptable quantitative agreement everywhere in terms of the velocity profiles could be more challenging than previously perceived. Differences are often noted next the bed and behind the baffle, i.e. zones of interest in terms of fish passage. The implications are discussed in terms of low-velocity zones (LVZs) in section 6 (Fig. 6.1). Of the observed discrepancies, some were attributable to limitations of the measurement technique, including susceptibility to streamline curvatures and geometric confinement. In general, the present models were deemed fit for purpose to assess qualitatively the flow redistributions arising from installation of the baffle system.

Furthermore, one of the validated models was modified to assess the hydrodynamic effects of a circular opening of 1/10th the baffle size through its centroid. The hole was believed to reduce the severity of negative circulation behind the baffle by providing ventilation to the area, which reduces the chance of fish becoming disoriented while navigating the baffle (Cabonce et al., 2018). The results revealed a high-velocity jet exiting the hole, which quickly vanished into the surrounding fluid and caused an increase in local turbulence levels. The bulk of the recirculation zone remained largely unaffected, in comparison to the original model without hole. The observations warranted larger openings to provide adequate cavity ventilation for improved fish navigability.

In summary, the present work highlighted the relevance of numerical models for understanding open channel flows involving complex geometries. The present configuration established a means to achieve a substantial reduction in computational effort by modelling the free surface as a plane of symmetry and replacing the domain inlet and outlet with periodic boundaries. The configuration is applicable to fully developed culvert flows with flow patterns that are expected to be streamwise-periodic. A further improvement in efficiency was achieved by adopting a relatively coarse mesh together with a WMLES model since the flow redistributions were primarily governed by flow separation from the baffle edge. It is worth noting that the technique may not be very useful in situations where the free surface dynamics is of prime importance or the free surface elevation is not known beforehand. With the complexity of flow description and computational resource constraint combined, it is proposed that similar numerical models be applied as an assistive rather than predictive measure for optimising the design of derivatives of the present baffle system.

6. DISCUSSION

Research showed that low velocity zones (LVZs) are favoured swimming zones for fish (Lupandin, 2005; Cotel et al., 2006). In particular, small-bodied fish ([8]) prefer to swim next to the sidewall and in the channel corner during upstream passage (Wang et al., 2016b; Cabonce et al., 2017), basically to minimise their rate of works and energy expenditure (Wang and Chanson, 2018). Whilst fish swimming behaviours are relatively easy to observe, a good hydrodynamic assessment of LVZs generally requires complete characterisations of the cross-sections of interest, involving careful and extensive data acquisition under carefully-controlled flow conditions in laboratory. Properly validated numerical models may conveniently convey such information at an unparalleled level of details, compared to more traditional methods. This section aims to provide a comprehensive characterisation of the low velocity zones associated, for less-than-design flow conditions, with each roughness configuration, using the numerical models described in the previous chapters. More details are presented in Appendix C.

The quantitative extents of low velocity regions are calculated and the results are compared with detailed laboratory data in Figure 6.1. Figure 6.1 compares the extent of low velocity zones (LVZs) generated by culvert barrels with smooth walls, with rough bed and rough left sidewall, with small corner baffles and with ventilated baffles. Only flow regions with $U/U_{mean} < 1$ are considered. In Figure 6.1, the vertical axis represents the fraction of flow cross-sectional area associated with U/U_{mean} less than the characteristic value of the horizontal axis. Whilst all roughness configurations experience at least 30% of the flow area with $U/U_{mean} < 1$, their abilities to provide regions with lower longitudinal velocities, i.e. $U/U_{mean} < 0.75$ and $U/U_{mean} < 0.5$, vary drastically. The roughened channel exhibits a clear advantage over the smooth flume for $0.5 < U/U_{mean} < 0.85$ (Fig. 6.1a). The trend implies a more gradual transition between high and low velocity zones in the channel with a rough bed and rough left sidewall, which may be easier for the fish to adjust. Figure 6.1b shows low velocity zones associated with medium-size baffles ($h_b = 0.067$ m, $L_b = 0.67$ m). The data show streamwise variations induced by the flow separation at each baffle. The flow is most disturbed at the first cross-sections behind the baffle, i.e. $(x-x_b)/L_b = 0.05$ and 0.235, producing approximately 30%, 15% and 5% of flow areas with $U/U_{mean} < 1$, $U/U_{mean} < 0.75$ and $U/U_{mean} < 0.5$, respectively. The flow expansion during $0.5 < (x-x_b)/L_b < 0.765$ has seen a substantial decrease in the flow area for $U/U_{mean} < 0.5$ and a corresponding increase for $U/U_{mean} > 0.5$. This change might be detrimental to weak swimmers, as the negotiable region decreases in size even though the total area classified as

---

[8] The characteristic endurance speed of small-bodied Australian native fish specie is typically less than 0.6 m/s (Hurst et al., 2007; Rodgers et al., 2014).

low velocity (i.e. $U/U_{mean} < 1$) increases. The noticeable streamwise variations could also imply non-contiguous regions which may be non-traversable by certain fish species.

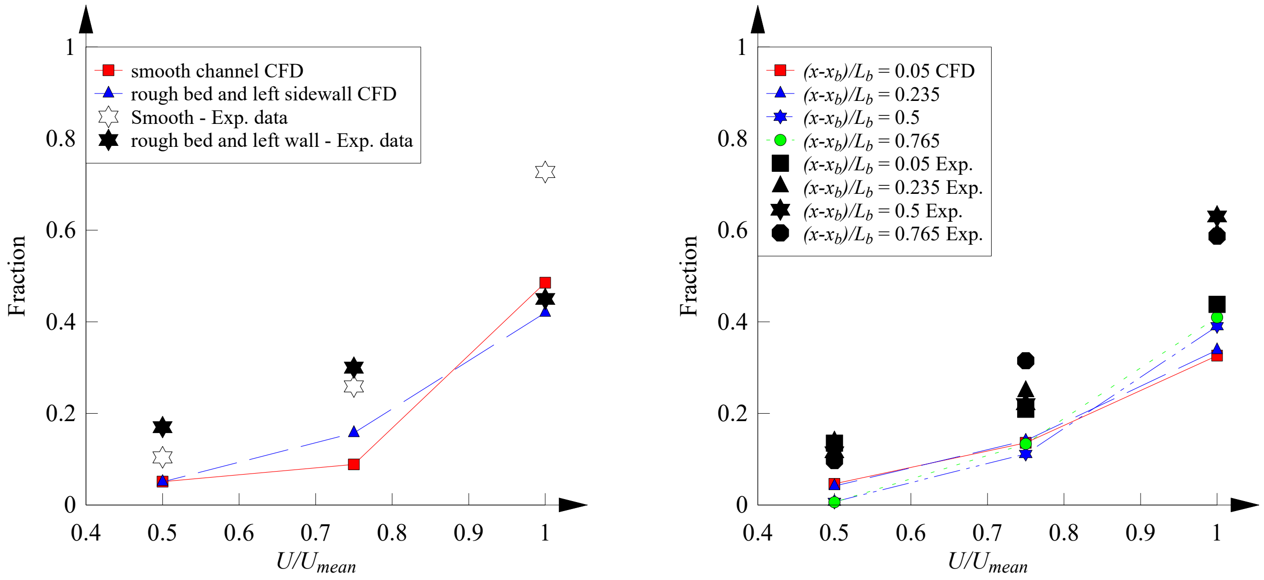

(a) Smooth and rough channel (no baffle) (b) $h_b = 0.067$ m, $L_b = 0.67$ m

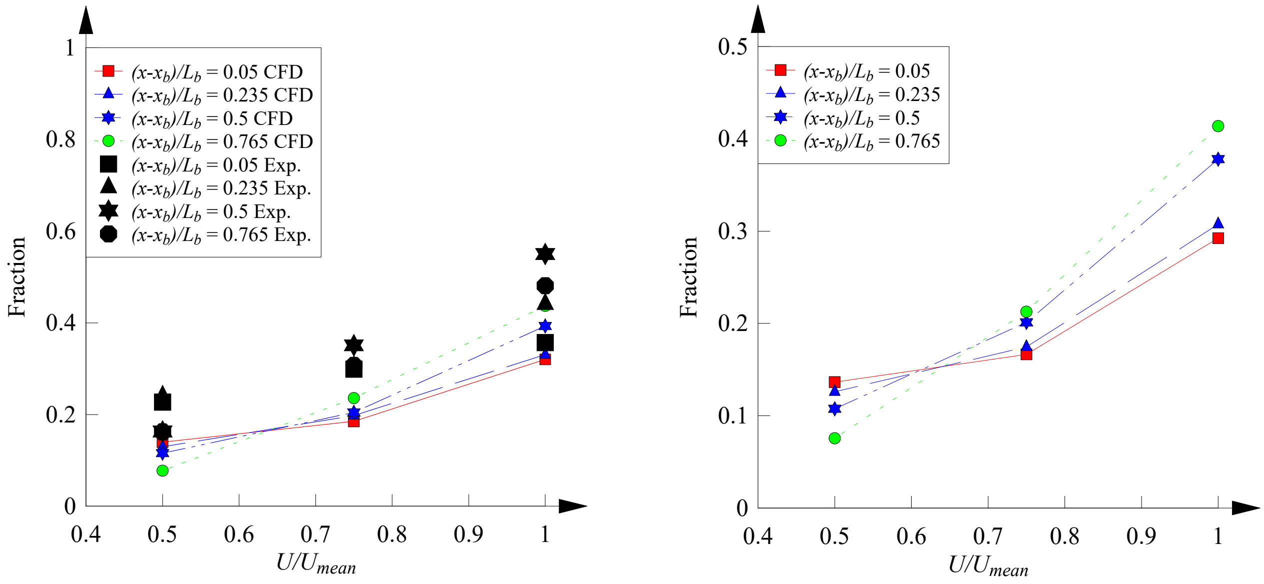

(c) $h_b = 0.133$ m, $L_b = 0.67$ m (d) $h_b = 0.133$ m, $L_b = 0.67$ m, $\varnothing = 13$ mm hole

Figure 6.1 – Fractions of low velocity regions produced by different barrel configurations – Flow conditions: $Q = 55.6$ l/s – Comparison with experimental data (black symbols) (Wang et al., 2016a; Cabonce et al., 2017).

Figure 6.1c illustrates the amount of velocity reduction due to large baffles ($h_b = 0.133$ m, $L_b = 0.67$ m). The different configuration results in a 50% decrease in the relative spacing L_b/h_b, compared to Figure 6.1b, and could limit the extent of streamwise variations, as previously discussed. The results confirm some improvement at all cross-sections downstream of the baffle. For $(x\text{-}x_b)/L_b <$

0.235, the configuration renders approximately 15%, 20% and 30% of flow area below 50%, 75% and 100% of the bulk velocity U_{mean}, respectively. As the flow expands for $(x\text{-}x_b)/L_b > 0.5$, a gradual decrease is observed for the slowest flowing areas with $U/U_{mean} < 0.5$, corresponding to an increase in area for $U/U_{mean} > 0.5$. It is worth noting that about 10% of the flow area remains below $0.5U_{mean}$ at the most remote location downstream of the baffle ($(x\text{-}x_b)/L_b = 0.765$), which significantly surpasses all other configurations. The result benefits from both an increase in relative size h_b/d and a decrease in relative spacing of the baffles. Figure 6.1d illustrates the effects of the same baffles ventilated with a 13 mm hole, showing no distinct advantage over the standard configuration.

A comparison between CFD and experimental data was systematically conducted, in terms of the percentage of flow cross-section area where the time-averaged longitudinal velocity U was less than U_{mean}, $0.75U_{mean}$ and $0.5U_{mean}$ ([9]). Graphical results are presented in Figures 6.1a to 6.1c. Overall the normalised coefficient of correlation between physical and numerical results was 0.675 with a standard error of 0.145. A good agreement was achieved with the smooth barrel and asymmetrical rough channel configurations, with a coefficient of correlation of 0.942 and standard error of 0.072, between experimental and CFD data.

Fish navigability also depends on the connectivity between the LVZ areas, in addition to the total relative size of low velocity zones (LVZs). Namely, a long, contiguous stretch of low velocity zone which meets certain velocity criteria is naturally more traversable than multiple, separate patches of LVZs. A single, large slow region is more suitable than multiple slow areas of smaller sizes. Consequently, one may aim to improve cross-sectional asymmetry, while minimising streamwise variations, to favour the development of a large contiguous stretch of traversable area, instead of smaller, discontinuous slow regions on either side of the channel. Figure 6.2 presents three-dimensional visualisations of low velocity zones ($U < 0.5U_{mean}$) for several boundary configurations. More results are presented in Appendix C.

In the smooth barrel, two equal-sized small LVZs occupy the sides and bottom of the channel, as expected from symmetry (Fig. 6.2a). The only traversable regions in this case are the bottom corners of the channel. Passage is impossible for species which require $U < 0.5U_{mean}$ as the compliant regions lie extremely close to the physical boundaries of the barrel. The channel with one rough sidewall and rough bed improves the passage ability significantly for $U < U_{mean}$, by inducing a large slow region on the roughened side of the channel. In addition to the corner circulations, an additional low velocity zone is identified above the channel bed at approximately $y/W = 0.2$ where

---

[9] A tabular comparison between CFD and experimental data is presented in Appendix C, in terms of the percentage of flow cross-section area where the time-averaged longitudinal velocity U was less than U_{mean}, $0.75U_{mean}$ and $0.5U_{mean}$ (Table C.1).

two large secondary flow cells meet. The observation suggests that such mechanisms may be utilised to create additional regions of slow flow. For the slowest flow areas with $U < 0.5U_{mean}$, the roughness asymmetry improves navigability slightly by favouring the rough side of the channel.

The small corner baffle can be effective at producing a slow-velocity region immediately behind the triangular baffle (Fig. 6.2c to 6.2e), although small baffles in high flows show a lack of streamwise connectivity in terms of low velocity zones (Fig. 6-2d). Though the baffle provides a seemingly obvious option for fish passage, caution must be taken where the strong recirculation may disorient the fish before they are able to adjust (Cabonce et al., 2017). The disorientating effect in the immediate wake of the baffle remains a major limitation, which may be reduced by providing ventilation to the recirculation region. An implementation of a single 13 mm circular opening through the centroid of the baffle reduced the recirculation strength, with successful improvement in upstream fish passage (Cabonce et al., 2018). However the present CFD study suggested that a more effective baffle ventilation strategy would be relevant.

In summary, the present investigation demonstrated the effects of various roughness configurations on the generation of LVZs. Both asymmetric roughness and small corner baffles are conducive to fish passage in distinguishing ways. Transverse asymmetry and streamwise uniformity are identified as desirable geometric traits which benefit the generation of large, contiguous traversable zones (Fig. 6.2). Corners, confluence of secondary flow cells and direct obstructions are highlighted as factors which help generate additional slow areas. The present observations may serve as guidelines for future optimisations of the geometric design of channels for improved fish passage.

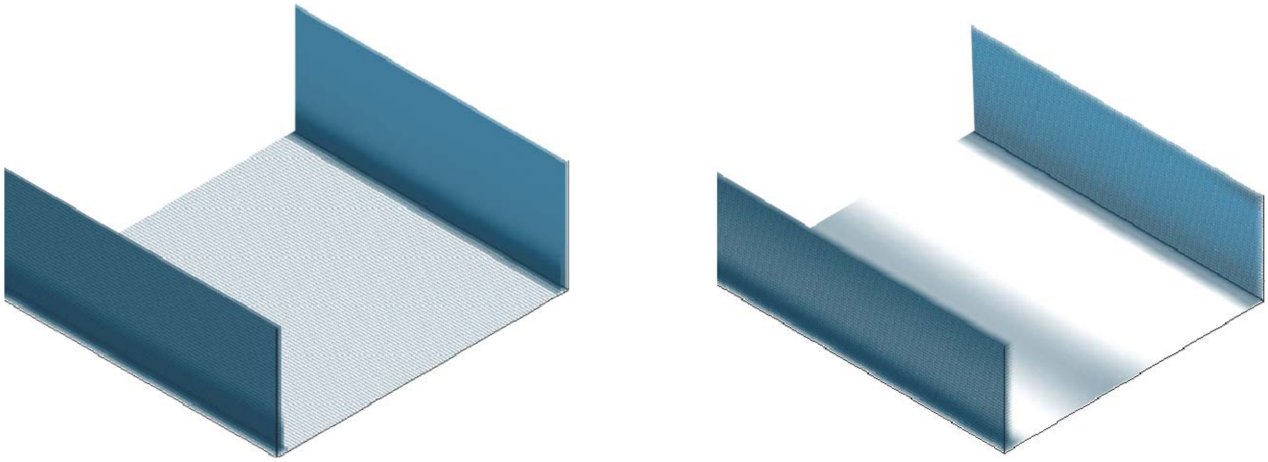

(a, Left) Smooth barrel channel

(b, Right) Rough bed and rough sidewall channel

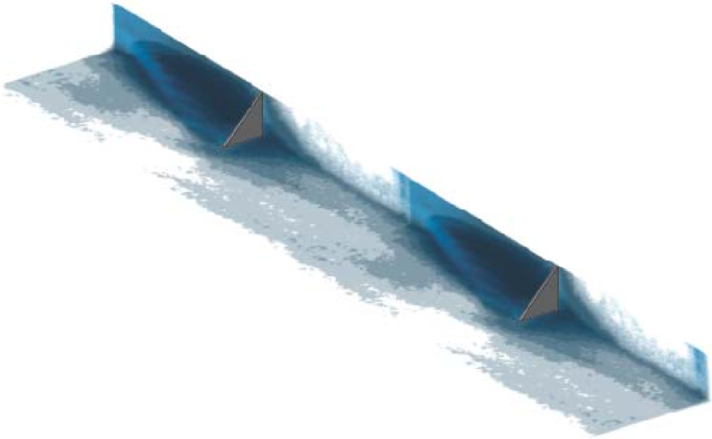

(c) Barrel channel with triangular baffle configuration: $Q = 0.0261$ m^3/s, $h_b = 0.067$ m, $L_b = 0.67$ m

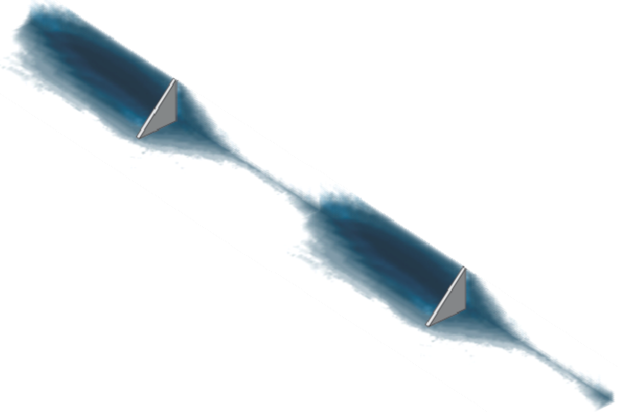

(d) Barrel channel with triangular baffle configuration: $Q = 0.0556$ m^3/s, $h_b = 0.067$ m, $L_b = 0.67$ m

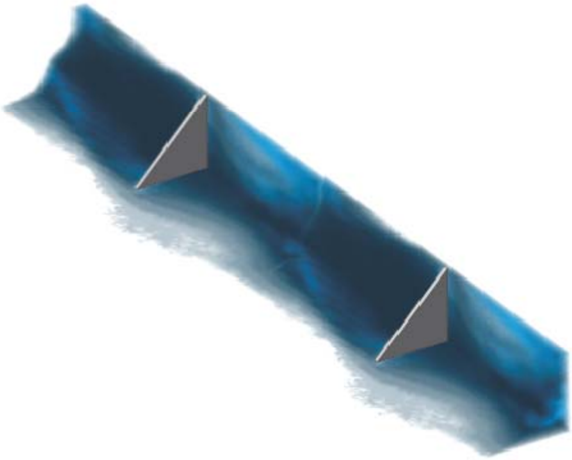

(e) Barrel channel with triangular baffle configuration: $Q = 0.0556$ m^3/s, $h_b = 0.133$ m, $L_b = 0.67$ m

Figure 6.2 - Three-dimensional flow visualisations of low-velocity zones ($U < 0.5U_{\text{mean}}$) in box culvert channels: CFD modelling results - Flow direction is from bottom right to top left, passage ability increases with darker colour shades.

7. CONCLUSION

Numerical 3D CFD investigations were undertaken to study the hydrodynamics of box culverts, with different types of boundary roughness configurations, for hydrodynamic conditions corresponding to less-than-design flows. The effects of smooth walls, rough bed and sidewall, and small triangular baffles were examined. The results offered insights onto how such boundary configurations may affect upstream fish passage and fostered the development of new apertures.

The numerical results were benchmarked against existing detailed physical datasets. A number of similarities and differences were noticed. Amongst the primary flow quantities, the free surface profile was the least sensitive to grid settings, with good agreement between numerical and experimental datasets. The streamwise velocity profile was well validated for the simple smooth barrel, while moderate to large differences were found in all other boundary configurations. The mesh-dependence of the streamwise velocity was evident for the asymmetrically roughened barrel, with up to 10% of uncertainties, in the final results. Present experience suggests that additional calibration might be warranted if the wall roughness entails a complex geometry which might degrade numerical predictions made by standard wall models. Whilst the validation outcomes pointed out to significant challenges in matching numerical and experimental data at levels of details beyond the most basic, the numerical modelling was successful at emulating the major flow features associated with bulk flow motion. The distributions of characteristic velocities and their locations characterising cross-sectional flow redistributions were well replicated, hinting the best use of the present models as a complementary tool to the physical experimental counterparts. Present numerical databases must be considered as a limited aid for dissecting experimental observations and devising future options.

With the associated limitations in mind, several recommendations may be proposed:

1. The standard k-ε model, when used in conjunction with the VOF model, adequately replicates the free surface and velocity profiles in a smooth culvert barrel;
2. More elaborate turbulence models such as RSM are required when secondary flow patterns are of importance;
3. LES simulations with relatively coarse grids without full wall resolution may be used to establish main flow features, when flow redistribution is governed by singular obstacles;
4. Periodic boundary conditions may be used to speed up substantially computations for fully developed flows;
5. Substituting the free surface with a symmetrical boundary further improves computation speed with minimum impact onto the result.

It is acknowledged that the numerical modelling was developed based upon validation data sets limited to small to moderate flow conditions, with unit discharges within 0.05 $m^2/s < q < 0.11\ m^2/s$. Detailed physical data sets for larger flow conditions would bring benefits to the research.

All in all, the present study highlighted the usefulness and limitations of different CFD numerical models and provided useful insights into the application to fish-friendly box culvert design. Importantly, a comprehensive verification and validation of the CFD modelling models is most critical. This step requires a complete and detailed physical data set, to compare systematically physical and numerical quantities of interest and to ensure that the basic flow physics is correctly reproduced in the CFD numerical model, as recommended by the American Institute of Aeronautics and Astronautics (Rizzi and Vos, 1998; Roache, 1998a). Further it is essential to have the high-quality physical data as references when validating numerical models, because "*validation [...] should be approached with great respect for the subtlety of nature*" (Roache, 1998b). In other words, the absence of basic "*experimental data means no validation*" (Roache, 2009; Chanson and Lubin, 2010).

Herein the CFD models were able to uncover distinct mechanisms responsible for generating low velocity zones (LVZs) by each type of roughness; these include channel corners, confluence between secondary flow cells and wakes. Further visualisation of the results helped to establish optimum size and spacing, as the most desirable traits for improving fish navigability. The findings underscore size and contiguity of LVZs as the most desirable traits for upstream fish passage, particularly for weak swimmers. The observations demonstrate the potential of future use of CFD numerical methods alongside physical studies for optimisation of box culvert barrel designs suitable for upstream fish passage.

8. ACKNOWLEDGEMENTS

The authors thank Dr Ludovic Cassan (IMFT, University of Toulouse) and Dr Nazanin Khezri (GHD, Brisbane) for their reviews of the report and most valuable comments. They acknowledge helpful discussions with Dr Hang Wang (The University of Queensland). The financial support of Australian Research Council (Grant LP140100225) is acknowledged.

APPENDIX A. PRELIMINARY INVESTIGATIONS

A.1 PRESENTATION

Prior to the present work, a preliminary investigation was performed to test the feasibility of LES applied to the full 12 m long channel. The flow conditions corresponded to Scenario SC1 detailed in Section 5.2. The computational domain was represented by a cuboid measuring 12 × 0.15 × 0.5 m (length × height × width), and a row of isosceles triangular baffles were inserted into the bottom left corner of the channel as shown in Figure 0.1 (not to scale). Compared to a typical wall-bounded open channel flow, the baffles create separation zones for which additional meshing requirements are essential. Ideally, a pure hexahedral mesh is desirable so as to minimise the potential numerical diffusion due to the presence of a free-surface. However, this might be difficult due to the rapid changes in geometry surrounding the corner baffles. As ANSYS Meshing experienced difficulties maintaining a structured hexahedral mesh around the baffles, the final mesh consisted of two adjoining blocks of tetrahedral and hexahedral elements sharing the same nodes on their interface. The meshing procedure produced a relatively fine tetrahedral mesh around the baffles and a uniform but coarser hexahedral grid in the adjacent block, with a total cell count of 622,111. Note that the mesh did not satisfy the resolution requirements of WMLES S-Omega and hence was only used for preliminary purposes.

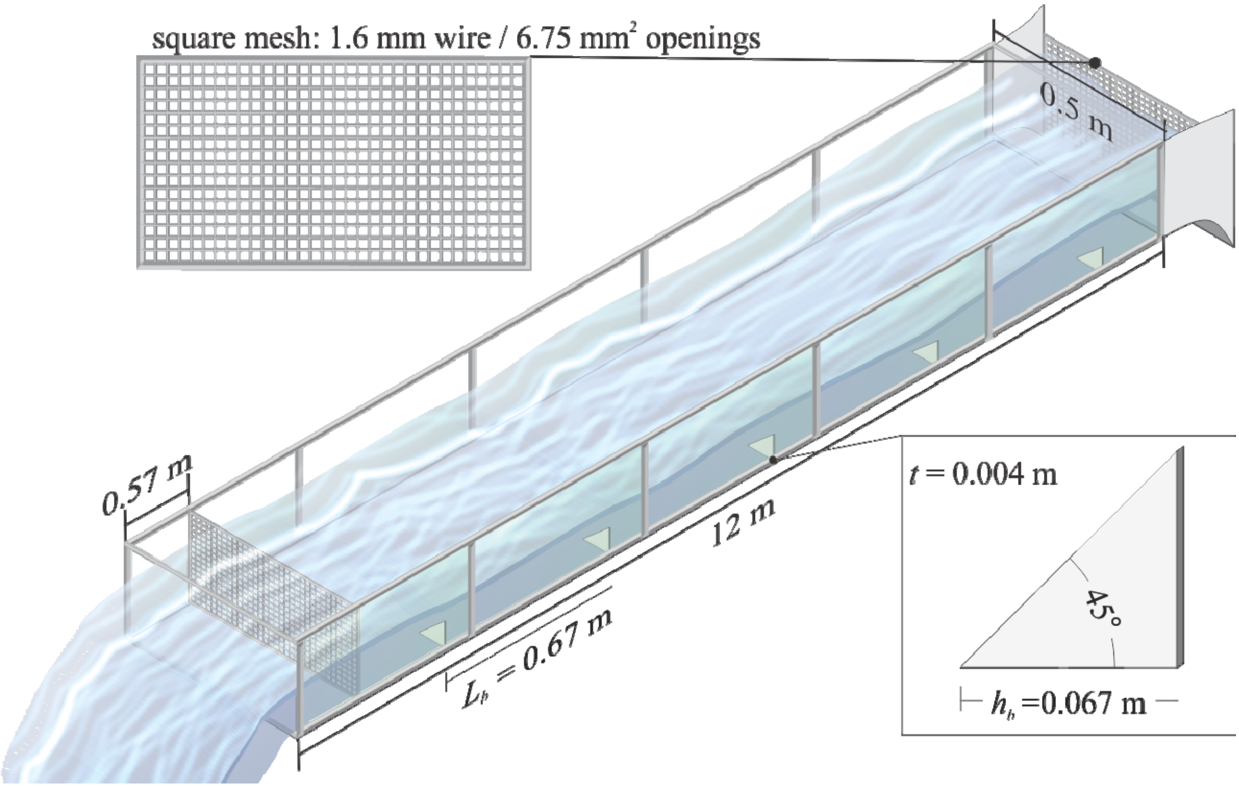

Figure 0.1 – Long channel setup for preliminary study.

A.2 FREE SURFACE TRACKING

The free-surface flow problem consists of a flowing secondary phase (i.e. water) with a primary phase (i.e. air) above it. The two fluids are immiscible and the interfacial length is significantly greater than the computational grid size. The Volume of Fluid (VOF) method originally described by Hirt and Nichols (1981) was adopted in light of these considerations.

The FLUENT implementation of VOF adopts a one-fluid model by solving the governing continuity and momentum equations for the mixture, which results in a velocity field shared by both phases. The mixture density, viscosity, and velocity are calculated as sums of the component phases weighted by their respective volume fractions (α_q), the local values of which are also used to assign the appropriate fluid properties to each control volume in the domain. An interface exists for $0 < \alpha_q < 1$, which is tracked by solving the volume fraction equation corresponding to one or more secondary phases:

$$\frac{\partial\left(\alpha_q \rho_q\right)}{\partial t} + \nabla \cdot \left(\alpha_q \rho_q \vec{u}\right) = S_q + \sum_{p=1}^{n} \dot{m}_{pq}$$

where ρ_q is the density of phase q, $\vec{u}$ is the mixture velocity, S_q is a source term, and $\dot{m}_{pq}$ is the mass flux from phase p to q. The interface shape is assumed to be piecewise linear and can be modelled by computing a set of surface normals $\vec{n}_i = \nabla \alpha_{pi}$ such that the volume fraction of phase q in each cell i bounded by the interface is α_{qi}.

A.3 NUMERICAL RESULTS

The triangular baffles lining the left sidewall create a simulation challenge as the rapid geometry variations at the baffle edges induce flow separation and transient behaviours. True stationary behaviours are difficult to achieve due to the close interactions between adjacent baffles. Herein the simulation was run for approximately two flow resident times (approximately 50 s) prior to data sampling to reduce the effects of flow instationarity. The data presented in the following paragraphs were sampled over 22 s, equalling to approximately one flow resident time.

The simulated time-averaged free-surface profiles at different transverse locations are presented in Figure 0.2. The physical data acquired by Cabonce et al. (2017) are provided for comparison (y = 0.25 m). The comparison reveals a systematic overestimation by the numerical model of the order of 10%, which could be due to the low vertical grid resolution (Δ_z = 0.01 m). Both models predict a decrease in free-surface elevation along the channel, resembling an H2 backwater profile (Chow, 1959). A small increase in water level is however observed in the experimental data which was likely caused by the upstream disturbance associated with the presence of the downstream screen. The numerical results show increasing levels of free-surface undulations towards the left sidewall (y

= 0.5 m), in phase with the baffles. Cabonce et al. (2017) also observed localised dips and rises in water level in response to the baffle arrangement, though this is not evident in their data possibly due to measurement difficulties.

Figure 0.3 illustrates the near-wall velocity and pressure fields between two successive baffles. The *x*-coordinates are centred at the first baffle location (x_b = 8.12 m) and both the *x*- and *z*-axes are normalised by the baffle height (h_b = 0.067 m). The data reveal a stagnation zone and a recirculation zone respectively upstream and downstream of each baffle, resulting in deviations from a hydrostatic pressure distribution. Visual inspections indicate that the recirculation zone behind each baffle has a length of approximately $3h_b$, consistent with the observations of Cabonce et al. (2017). A concentration of large velocities is identifiable directly above and behind each baffle, caused by vortex shedding from the baffle edge. The similarity of velocity and pressure contours between two successive baffles ($(x\text{-}x_b)/h_b$ = 0 and 10) suggest that the presence of the upstream baffle does not substantially alter the flow field around the downstream baffle.

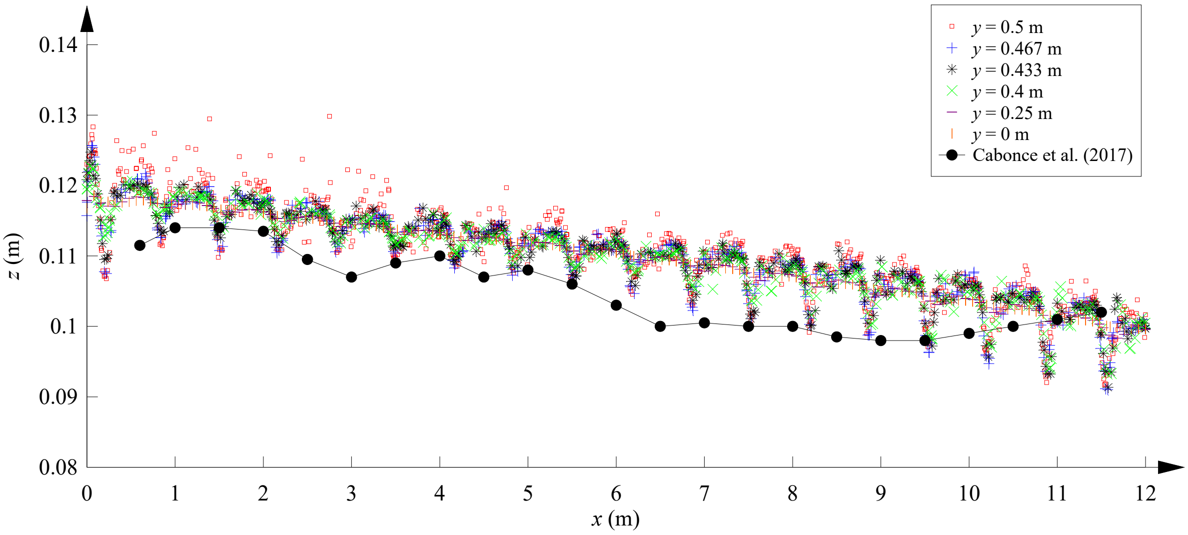

Figure 0.2 – Simulated free-surface profiles at different transverse locations – comparison with Cabonce et al. (2017) (y = 0.25 m).

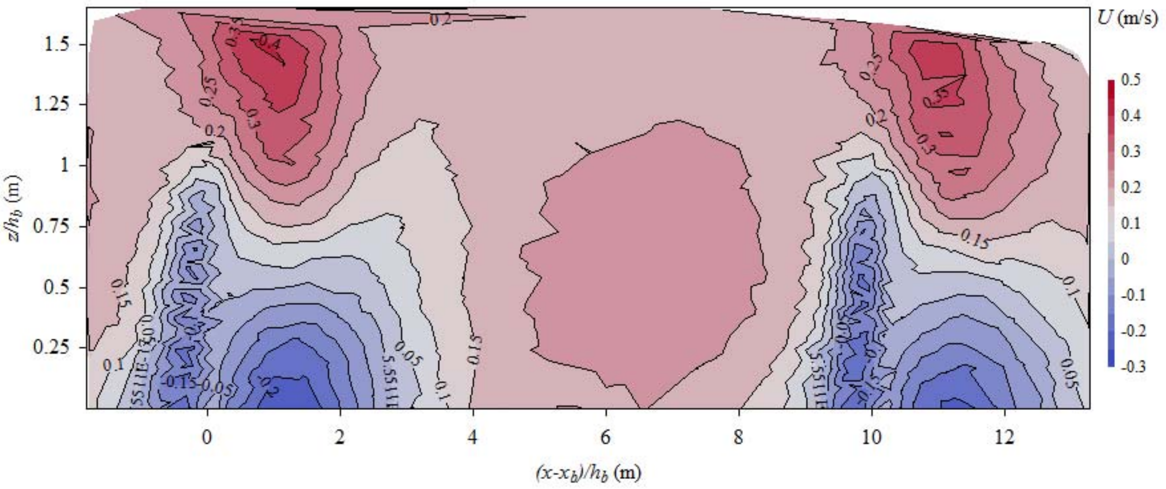

(A) Velocity contours

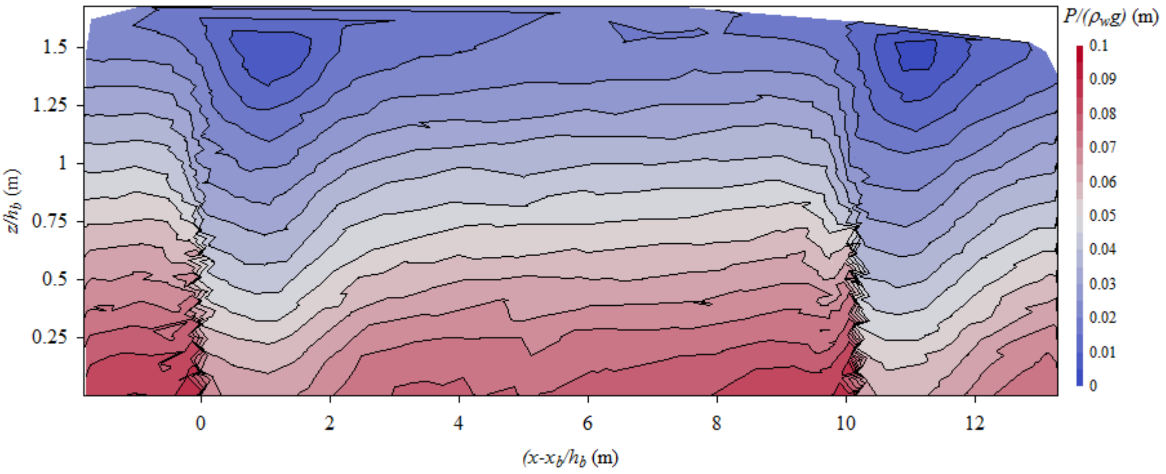

(B) Pressure contours

Figure 0.3 – Near-wall velocity and pressure contours (x_b = 8.12 m, y = 0.499 m).

Typical vertical distributions of time-averaged streamwise velocity U and fluctuations u_{rms} behind a baffle (x_b = 8.12 m) are presented in Figure 0.4. The flow appears fully developed and the velocity profiles display large variations across the channel width due to the baffle influence, which quickly attenuates away from the baffle. A large zone of flow reversal is evident near wall (y/W = 0.96), extending up to approximately 40% of the flow depth with peak negative velocities in excess of -0.1 m/s. The reduction in velocity behind the baffle results in noticeably greater velocities towards the smooth side of the channel. The velocity fluctuations are strongest next to the wall (y/W = 0.96), which remain significant throughout the water depth with a peak at approximately the baffle height. The magnitude of the velocity fluctuations quickly reduces away from the baffle, by up to an order of magnitude (~0.01 m/s) reaching the smooth sidewall. The results are in response of some complex flow patterns generated by the baffles that create a significant degree of asymmetry in the flow field. This is more evident in Figure 0.5, which illustrates time-averaged streamwise velocity contours at several longitudinal locations behind a baffle (x_b = 8.12 m). Some jaggedness may be seen at the interface between the tetrahedral and hexahedral meshes (x = 0.35 m) due to interpolation errors. The data reveal a significant reduction in mean velocity behind the baffle, and a corresponding flow concentration towards the smooth side of the channel. Negative velocities due to flow reversal are still observable at $(x-x_b)/h_b = 2.4$, but completely disappear by $(x-x_b)/h_b = 5.0$. The velocity contours display significant dips in the central part of the channel, which were not reflected in the experimental data of Cabonce et al. (2017). It remains unclear whether this reflects true physical behaviour or has been a result of modelling limitations (e.g. meshing).

Cabonce et al. (2017) alluded to secondary motions and transverse momentum exchange as being responsible for the dips in the streamwise velocity contours. The baffles are largely liable for the generation of these secondary circulations, which are illustrated in Figure 0.6. The data indicate the presences of very complex secondary flow structures that evolve as the flow propagates between the baffles, which have noticeable effects on the redistribution of momentum between slow and fast flowing regions (Hinze, 1967; Schlichting, 1979; Montes, 1998). Figure 0.7 shows the distributions of the cross-sectional maximum velocity U_{max}/U_{mean} and their corresponding locations as functions of the transverse distance from the smooth wall ($y/W = 0$). The data suggest that the presence of baffles results in a flow concentration in the central part of the channel, producing maximum velocities significantly greater than the bulk velocity spanning most of the channel width ($U_{max}/U_{mean} \approx 1.5$ for $0.2 < y/W < 0.8$). The ratio U_{max}/U_{mean} exhibits sharp decreases next to the walls ($y/W = 0$ and 0.5), with an accelerated rate of decay towards the baffled side of the channel ($y/W = 0.5$). Whilst the results appear qualitatively consistent with the data of Cabonce et al. (2017), the numerical results significantly overestimate U_{max}/U_{mean} for $0.5 < y/W < 0.9$ which might be due to the relatively coarse mesh resolution adopted for the preliminary simulation. A review of the data indicate that U_{max} occurs slightly below the surface, typically between $z/d = 0.7$ and 0.9. These values are close to the smooth chute observations by Cabonce et al. (2017) but exceed their baffle results by a considerable margin. The discrepancy between numerical and experimental data highlights some limitations in the present study.

The effect of a baffle on the distribution of wall shear stress in the surrounding region is illustrated in Figure 0.8. Large concentrations of wall stress are observable immediately above and beside the baffle caused by flow contraction. The flow reversal also appears to be responsible for a zone of relatively large wall stress a short distance behind the baffle. The range of wall stress magnitudes appears to be consistent with measurements by Cabonce et al. (2017), performed with a Prandtl-Pitot tube. Their results however did not reveal the stress concentrations due to flow contraction, possibly due to the instrument not performing well in regions characterised by large streamline curvature or transient behaviours (e.g. around and behind a baffle).

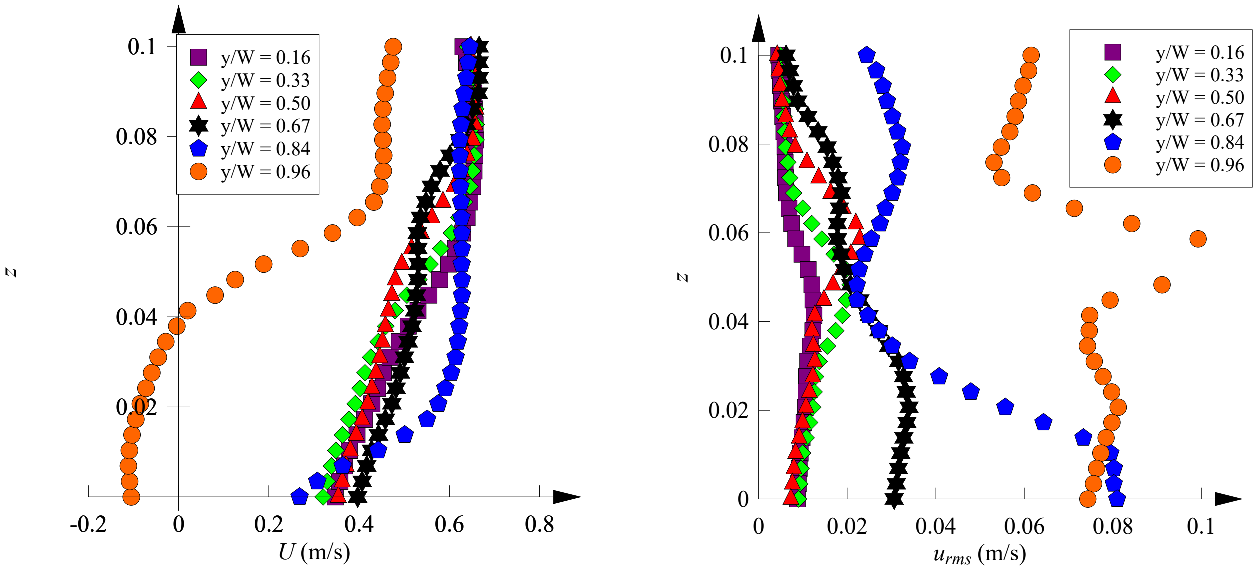

Figure 0.4 – Vertical distributions of mean and RMS velocity distributions behind a baffle (x_b = 8.12 m).

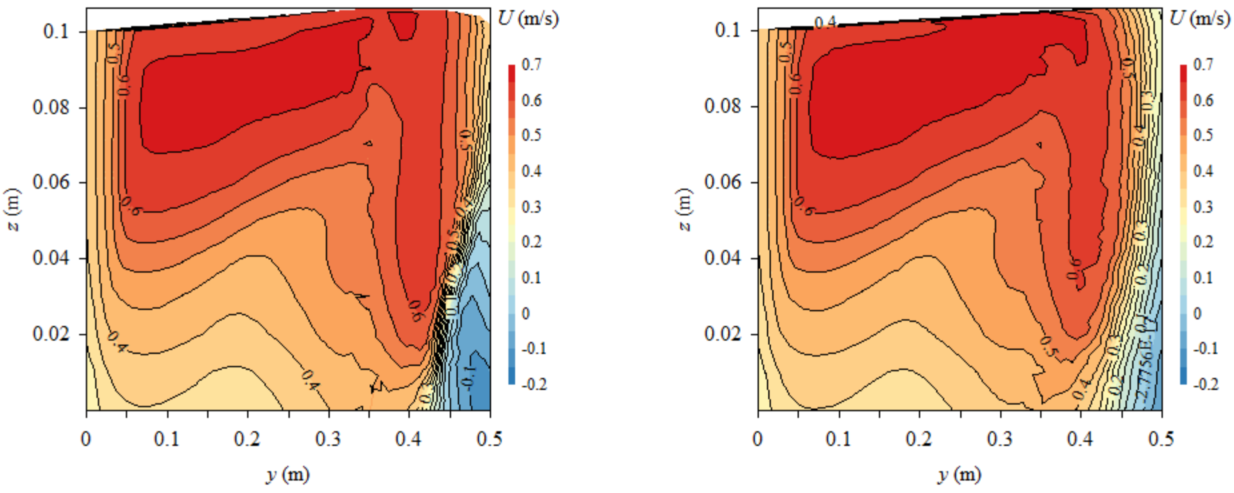

(A) $(x\text{-}x_b)/h_b = 0.5$

(B) $(x\text{-}x_b)/h_b = 2.4$

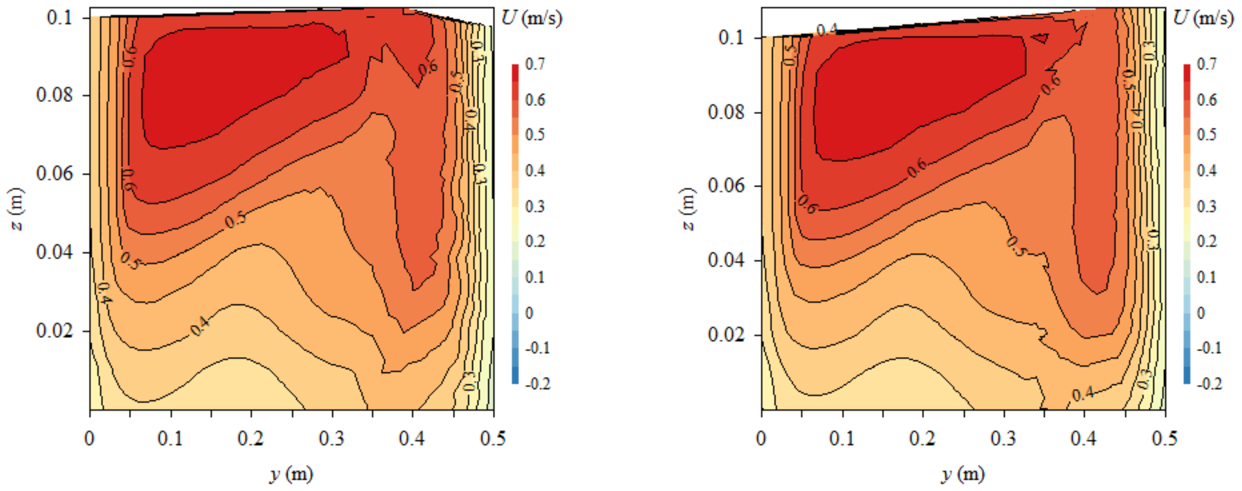

(C) $(x-x_b)/h_b = 5.0$

(D) $(x-x_b)/h_b = 7.6$

Figure 0.5 – Velocity contours behind a baffle (x_b = 8.12 m).

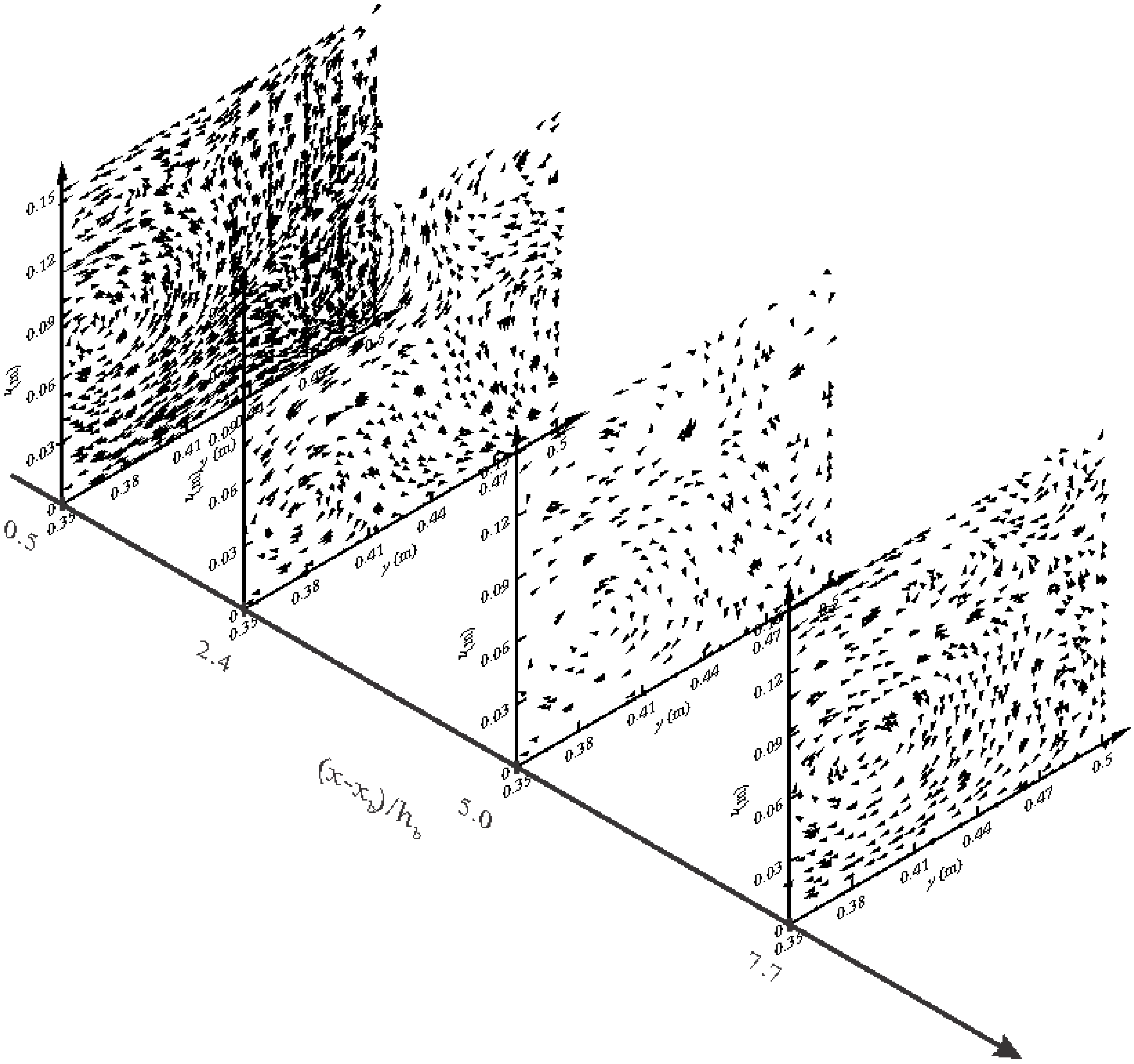

Figure 0.6 – Secondary flow patterns behind a baffle (x_b = 8.12 m).

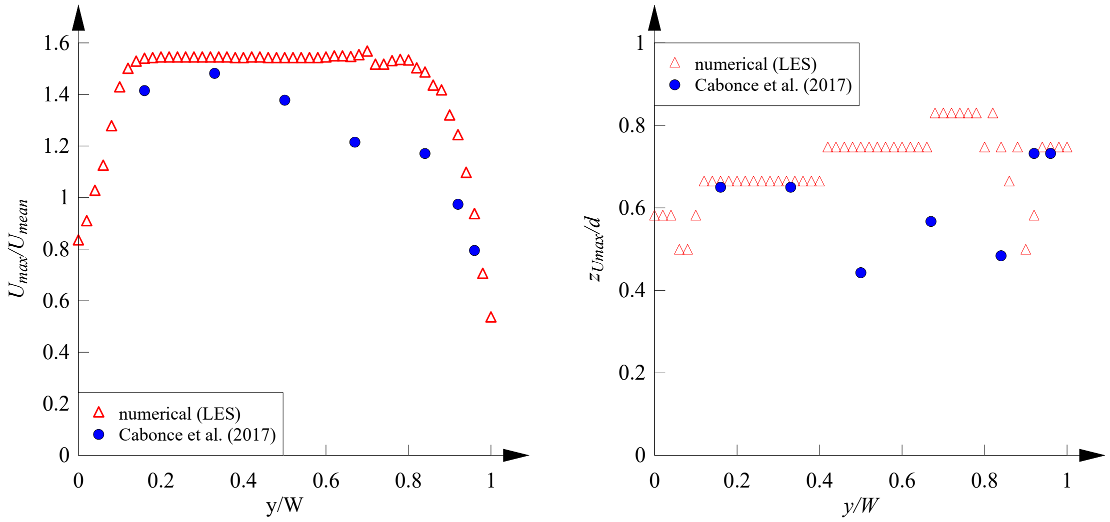

(C) $(x - x_b)/h_b = 2.4$, U_{max}/U_{mean}

(D) $(x - x_b)/h_b = 2.4$ m, z_{Umax}/d

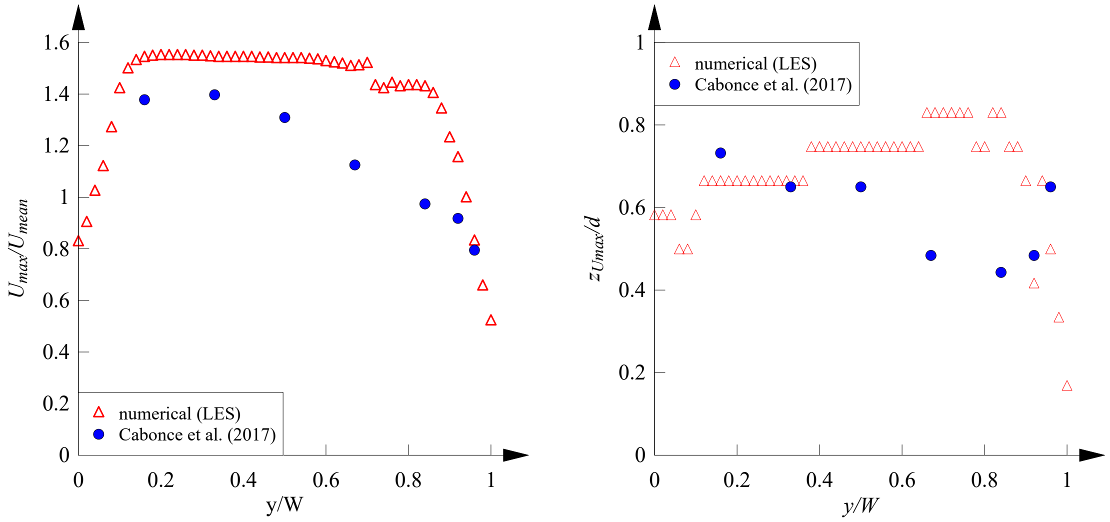

(E) $(x - x_b)/h_b = 5.0$, U_{max}/U_{mean}

(F) $(x - x_b)/h_b = 5.0$, z_{Umax}/d

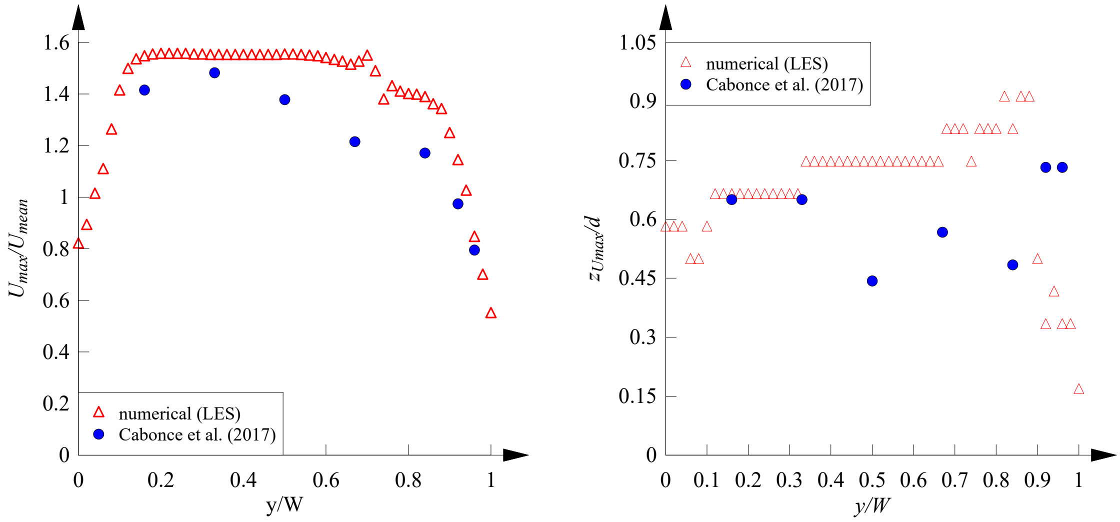

(G) $(x - x_b)/h_b = 7.6$, U_{max}/U_{mean}

(H) $(x - x_b)/h_b = 7.6$, z_{Umax}/d

Figure 0.7 – Distributions of maximum cross-sectional velocities and corresponding locations – $x_b = 8.12$ m, $h_b = 0.067$ m.

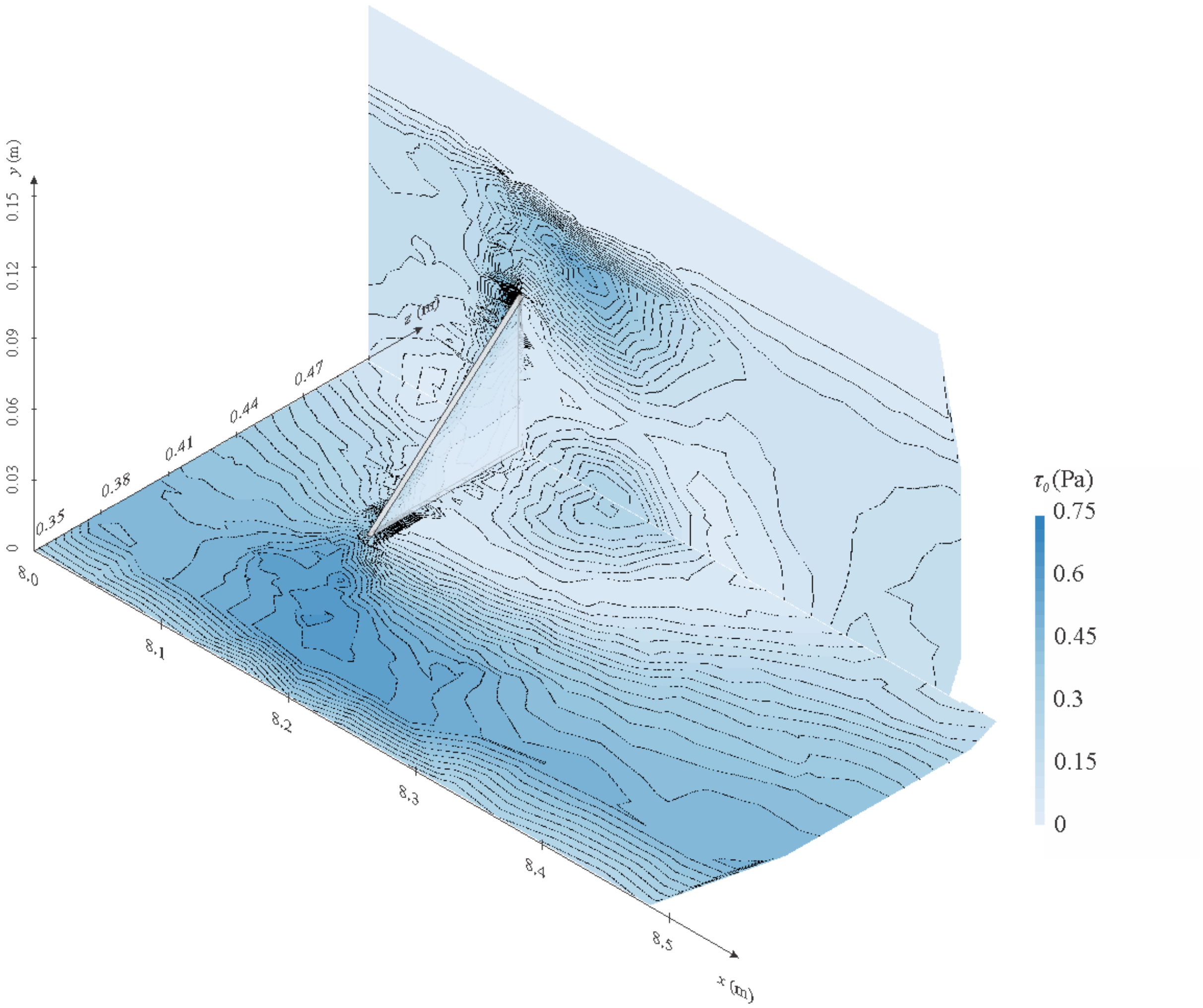

Figure 0.8 – Wall shear stress contours around a baffle (x_b = 8.12 m).

Discussion: low-velocity zones (LVZs)

In a baffled barrel, the rapid changes in wall geometry induce significant secondary flow motions which are responsible for intense momentum redistributions within the cross-section. The resulting flow field consists of various zones characterised by higher or lower velocities than the bulk velocity U_{mean}. Table 0.1 and Figure 0.9 summarise present observations of velocity reduction at several streamwise locations behind a baffle (x_b = 8.12 m). Such locations are believed to be conducive to fish passage as reported by Lupandin (2005) and Cotel et al. (2006). The data suggest that the baffles were capable of rendering approximately 40% of the entire flow area under the bulk velocity U_{mean}, which should create favourable swimming conditions for small-bodied fish species. Similarly, a moderate reduction in velocity was registered over approximately 20% of the flow area, with velocities below $0.75U_{mean}$. Great velocity reductions below $0.5U_{mean}$ were recorded for approximately 20% of the flow area immediately behind the baffle, which decreased to below 5% beyond midway between two successive baffles. It appears that the zones with the least and most significant velocity reductions (i.e. $U < U_{mean}$ and $U < 0.5U_{mean}$) respectively increased and decreased in size with increasing distance downstream of the leading baffle, while the flow area where $U < 0.75U_{mean}$ remained approximately constant in size. The present data are compared with those reported by Cabonce et al. (2017) and the agreement is reasonable. A scrutiny of Figure shows that the numerical model tends to over-predict and under-predict the sizes of the flow regions where $U < U_{mean}$ and $U < 0.5U_{mean}$ respectively with increasing distance downstream of the baffle. Importantly, both the experimental and numerical results highlight a considerable increase in the sizes of extremely-low velocity areas relative to a smooth chute (i.e. 5-10% of flow area with $U < 0.5U_{mean}$) but did not show substantial performance increase above a chute with a rough bottom and a rough sidewall (i.e. 17% of flow area with $U < 0.5U_{mean}$).

Table 0.1 – Observations of low velocity regions behind a baffle

$(x\text{-}x_b)/h_b$	U_{max} (m/s)	*Numerical**1 *(% area with U > than)*			*Experimental**2 *(% area with U > than)*		
		U_{mean}	$0.75U_{mean}$	$0.5U_{mean}$	U_{mean}	$0.75\ U_{mean}$	$0.5\ U_{mean}$
0.5	0.67	37.5	24.1	19.5	39.6	17.3	14.9
2.4	0.67	42.6	20.8	10.4	30.5	20.6	14.3
5.0	0.67	48.7	17.5	3.1	43.7	18.3	12.1
7.6	0.67	46.7	19.8	4.9	30.7	19.3	10.3

Notes: *1 – $x_b = 8.12$ m, $h_b = 0.67$ m;
*2 – Experimental results of Cabonce et al. (2017).

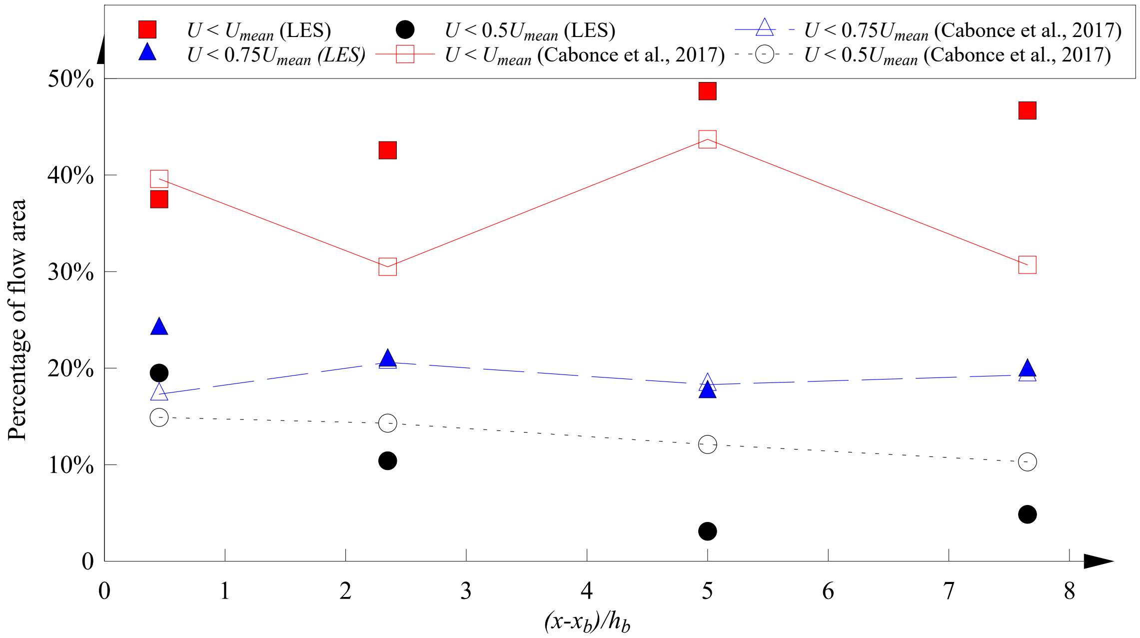

Figure 0.9 – Observations of low velocity zones downstream of a baffle ($x_b = 8.12$ m).

APPENDIX B. BOX CULVERT WITH SMALL TRIANGULAR BAFFLES: NUMERICAL RESULTS

B.1 PROBLEM SETUP

LES simulations were performed for a horizontal rectangular channel equipped with small triangular baffles in the bottom left corner. The boundary and flow conditions are summarised in Table B.1, where Q is the volumetric flow rate, h_b is the side length of the isosceles triangular baffle, and L_b is the streamwise interval between two adjacent baffles. Scenarios SC1 to SC3, Cabonce et al. (2017) performed detailed experiments in a 12 m long physical channel. Their results are used to validate the respective numerical models. Scenario SC4 was derived from SC3 by adding a 13 mm hole through the centroid of the baffle, to ventilate the recirculation zone (Cabonce et al., 2018).

Table B.2 – Summary of flow conditions and mesh configurations for investigated scenarios

Scenario	Q (l/s)	h_b (m)	L_b (m)	d (m)	Remark	No. Cells	Min. Cell Vol. (mm^3)	Max. Cell Vol. (mm^3)	Max. Aspect Ratio
SC1	26.1	0.067	0.67	0.100	-	549,917	5.82×10^{-2}	3.83×10^{2}	66
SC2	55.6	0.067	0.67	0.165	-	277,509	1.66×10^{-1}	1.06×10^{3}	33
SC3	55.6	0.133	0.67	0.173	-	567,517	4.81×10^{-2}	4.78×10^{2}	112
SC4	55.6	0.133	0.67	0.173	with 13 mm hole*1	704,826	5.68×10^{-2}	3.85×10^{2}	21

Note: *1 – the hole on each baffle is centered at 40 mm from its edges

The simulations were performed on a custom-built Dell Precision T5810 workstation configured with an Intel® Xeon® E5-1680 v4 CPU and 128 GB RAM. The time discretisation was bounded second order implicit. The pressure-velocity coupling was solved using the SIMPLE solver. The spatial discretisation of the momentum equations is handled by a modified central differencing scheme based on the normalised variable diagram (NVD) approach (Leonard, 1991) to achieve second-order accuracy. This is a composite scheme that consists of a pure central differencing, a blend of the central differencing and the second-order upwind scheme, and the first-order upwind scheme (ANSYS). The hybrid formulation retains the low numerical diffusion and reduces the instability due to central differencing, and falls back onto the first-order scheme if unbounded solutions are produced.

Cuboid domains with a footprint of 0.67 m × 0.5 m were selected for the simulations. The vertical extent of each domain was determined from the free surface data of Cabonce et al. (2017). They observed experimentally that the free surface remained largely flat between two successive baffles in the fully developed region, albeit a localised dip immediately downstream of each baffle noticeable only for a large relative baffle h_b/d, where d is water depth. Since effects due to free surface perturbations were expected to be small, representing a flat free surface by a symmetry condition permitted a substantial increase in computational speed with minimum impact on reproduction of the bulk flow features. The longitudinal extent of the domain (0.67 m) was set to equal one baffle spacing (L_b), and preliminary simulations found that the fully developed flow field was very close to periodic (Appendix A). A single isosceles triangular baffle was placed midway between the periodic inlet and its shadow outlet. The side and bottom walls as well as the baffle surfaces were set up as no-slip walls. The symmetry condition on the top face imposes a zero normal gradient for all fluid variables.

Each numerical domain was discretised into an unstructured hexahedral mesh. The resulting mesh configurations are summarised in Table B.1. The resolution requirements of WMLES were used as a guide to specify the element sizes on the bounding edges non-contacting with the baffle, with the domain height assumed as δ. The sides of the baffle are discretised into 2 – 3 mm segments, and no constraint was specified for the contacting edge with the baffle. Herein relatively coarse meshes were selected with the goal to keep the computation time manageable while preserving the most relevant flow features. The inability to specify the first layer of wall cells in the proximity of $y^+ = 1$ would result in under-characterisation of the boundary layers originating from the no-slip walls. The discrepancy was deemed to be acceptable as the separation created by each baffle was expected to have a dominating effect on the flow redistribution.

Each numerical simulation started with an initial assumption of uniform velocity field and iterated until the correct pressure gradient was achieved such that the mass flow rate was consistent with that specified. After the settlement of the initial numerical instability, the solution was run for approximately 10 s before time-averaged statistics were sampled for a further 10 s at an interval of 0.001 s. For each time step, the solution was deemed to have converged once the normalised residuals for continuity and momentum equations decreased below 10^{-3}. It is expected that the numerical behaviour becomes reasonably stationary after several flow resident times (~ 1 s). Note that the comparability between numerical and experimental results may be limited by the relatively short sampling window of 10 s chosen to keep computational time manageable. For comparison, the physical data were sampled for 90 s at each sampling location.

B.2 RESULTS

B2.1 Scenario 1 (SC1)

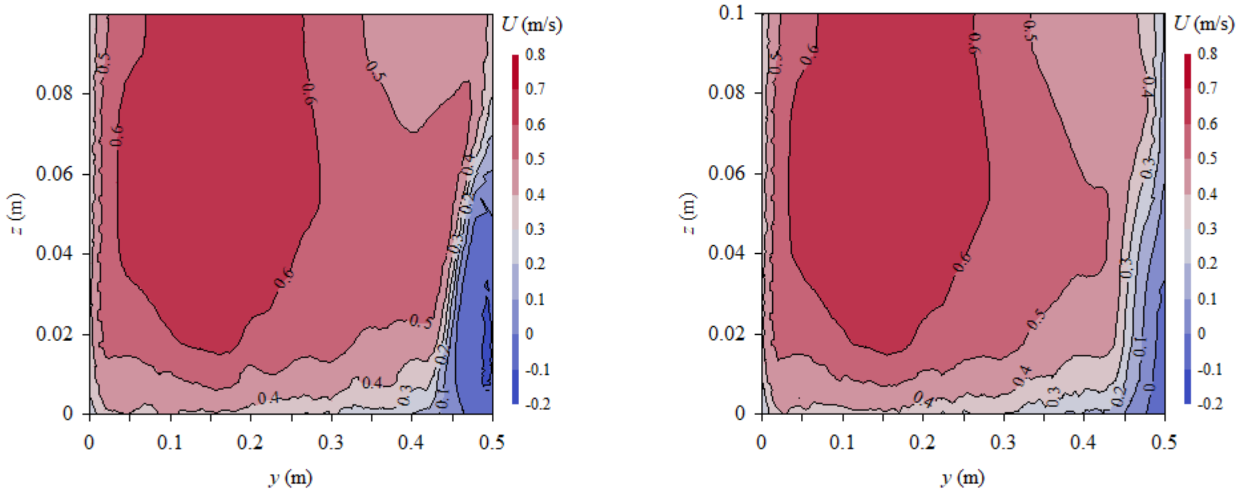

(a) $(x-x_b)/L_b = 0.05$ (b) $(x-x_b)/L_b = 0.235$

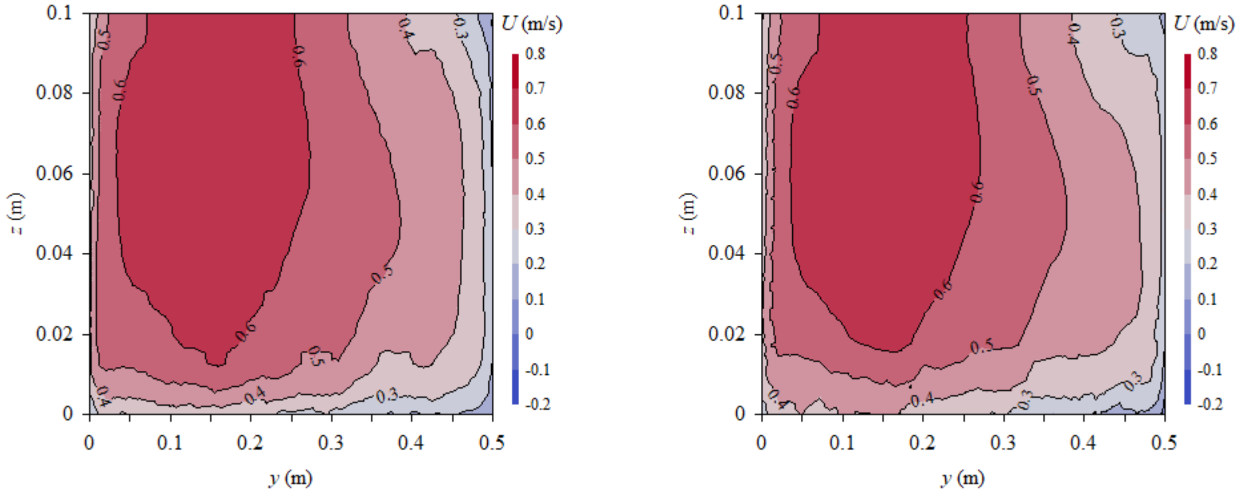

(c) $(x-x_b)/L_b = 0.5$ (d) $(x-x_b)/L_b = 0.765$

Figure B.1 – Velocity contours behind baffle – Flow conditions: Q = 26.1 l/s, h_b = 0.067 m, L_b = 0.67 m, d = 0.1 m.

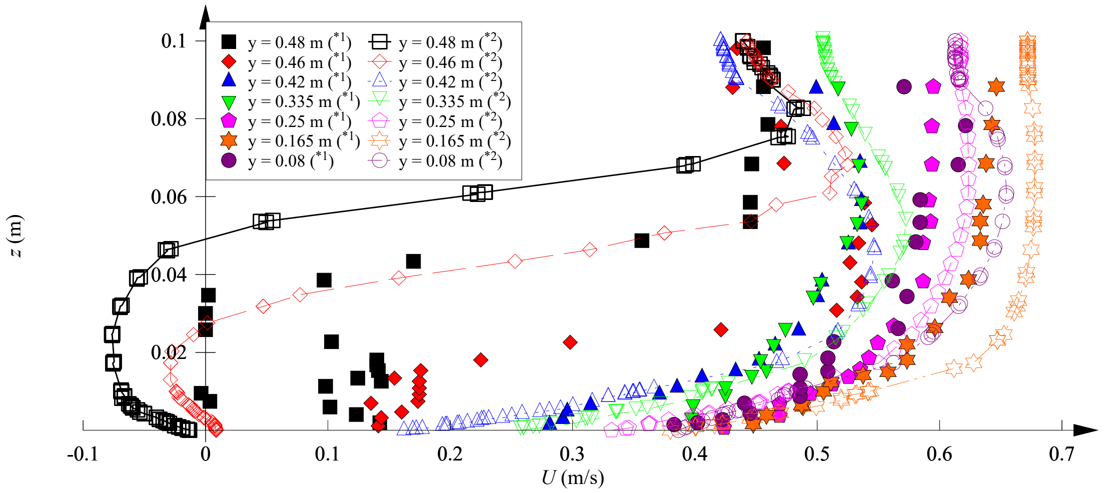

(a) $(x-x_b)/L_b = 0.05$

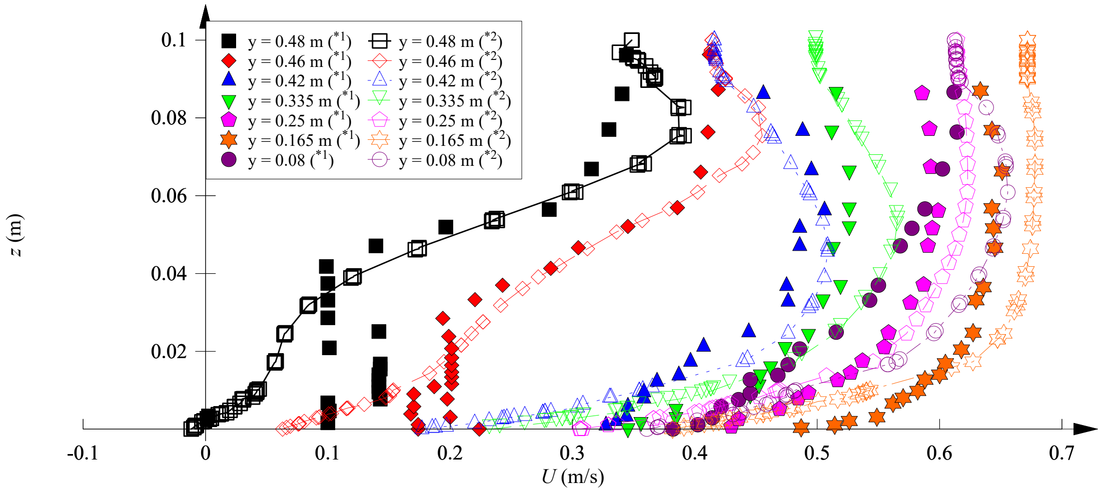

(b) $(x-x_b)/L_b = 0.235$

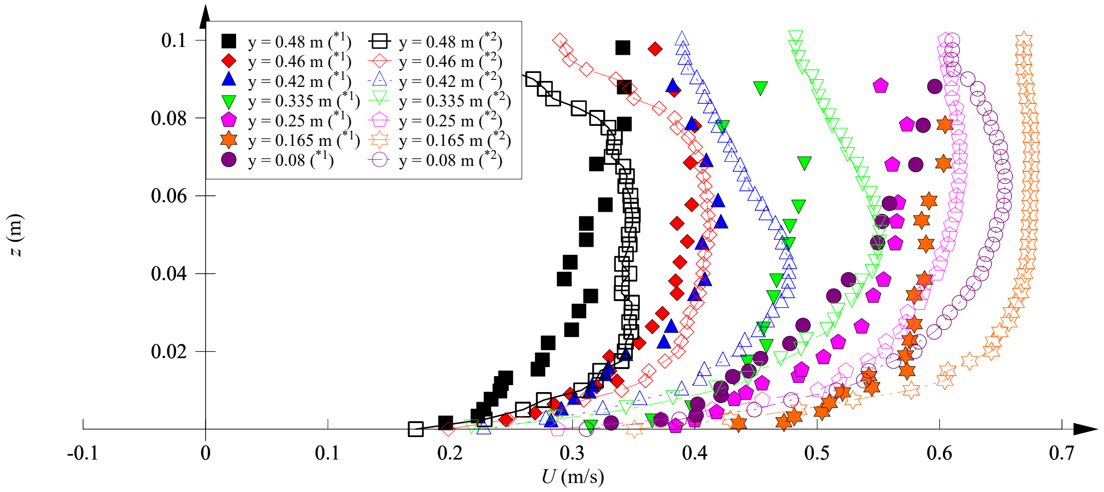

(c) $(x-x_b)/L_b = 0.5$

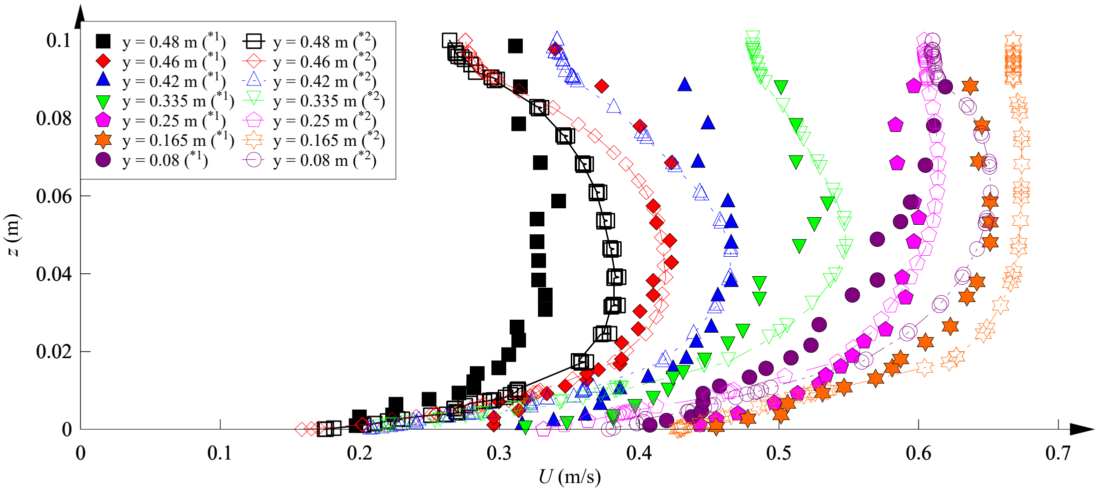

(d) $(x-x_b)/L_b = 0.765$

Figure B.2 – Velocity profiles at different transverse locations across channel in a culvert barrel channel equipped with small triangular corner baffles – Flow conditions: $Q = 26.1$ l/s, $h_b = 0.067$ m, $L_b = 0.67$ m, $d = 0.1$ m – Notes: *1 – Experimental data by Cabonce et al. (2017); *2 – Large Eddy Simulation (present study).

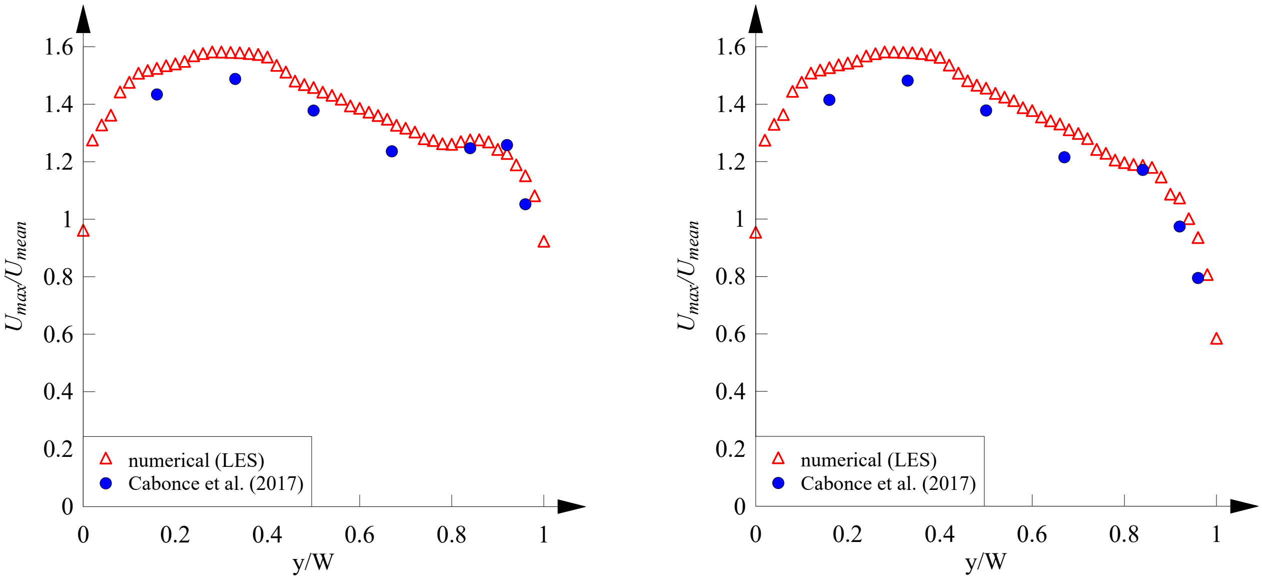

(a) $(x-x_b)/L_b = 0.05$

(b) $(x-x_b)/L_b = 0.235$

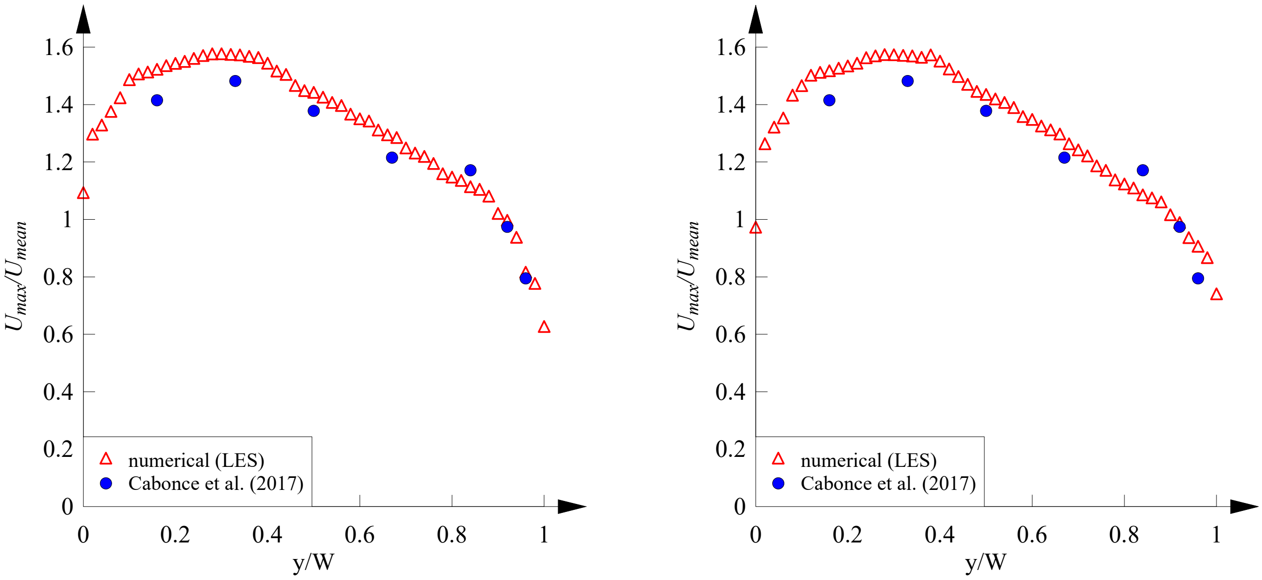

(c) $(x\text{-}x_b)/L_b = 0.5$

(d) $(x\text{-}x_b)/L_b = 0.235$

Figure B.3 – Transverse distributions of streamwise velocity maxima – Flow conditions: $Q = 26.1$ l/s, $h_b = 0.067$ m, $L_b = 0.67$ m, $d = 0.1$ m.

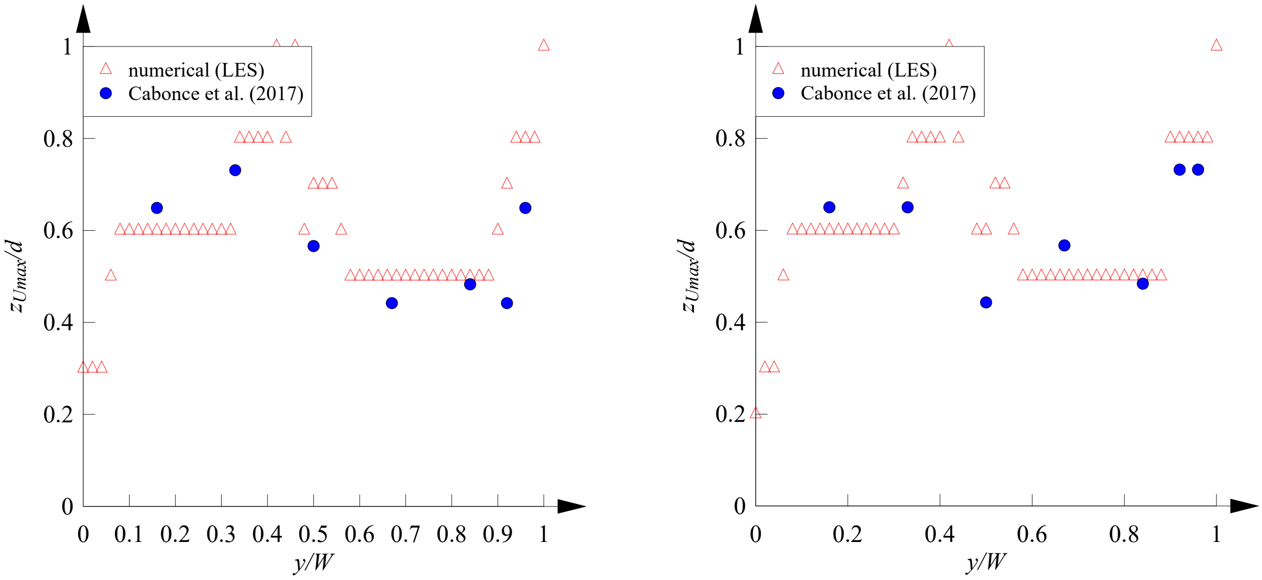

(a) $(x\text{-}x_b)/L_b = 0.05$

(b) $(x\text{-}x_b)/L_b = 0.235$

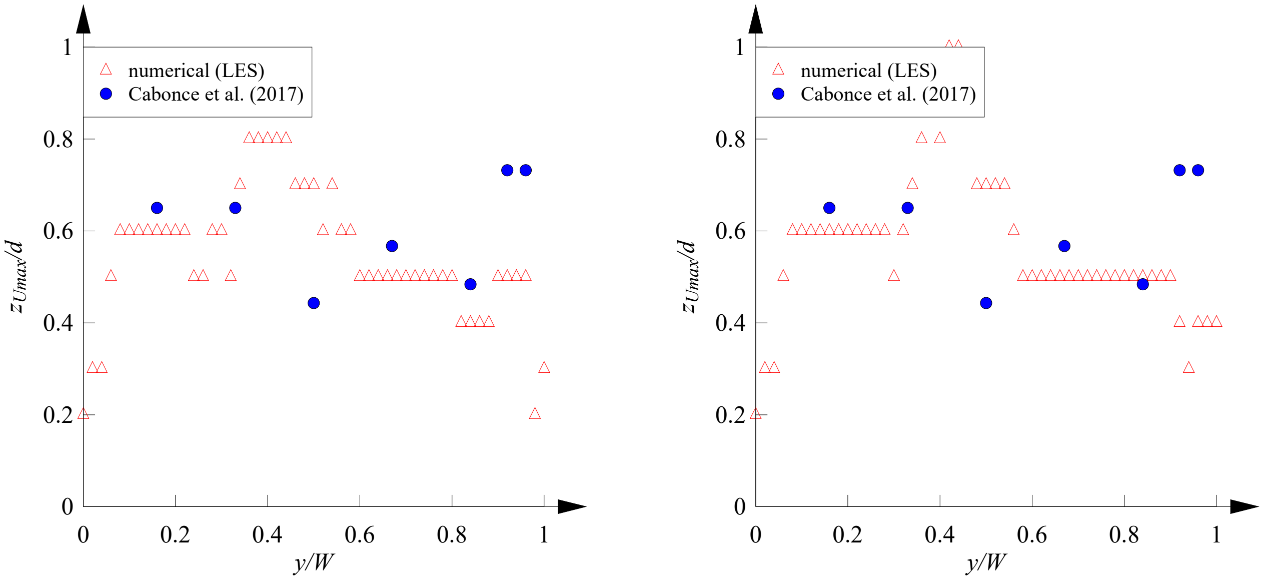

(c) $(x-x_b)/L_b = 0.5$ (d) $(x-x_b)/L_b = 0.765$

Figure B.4 – Transverse distributions of elevations of streamwise velocity maxima – Flow conditions: $Q = 26.1$ l/s, $h_b = 0.067$ m, $L_b = 0.67$ m, $d = 0.1$ m.

B.2.2 Scenario 2 (SC2)

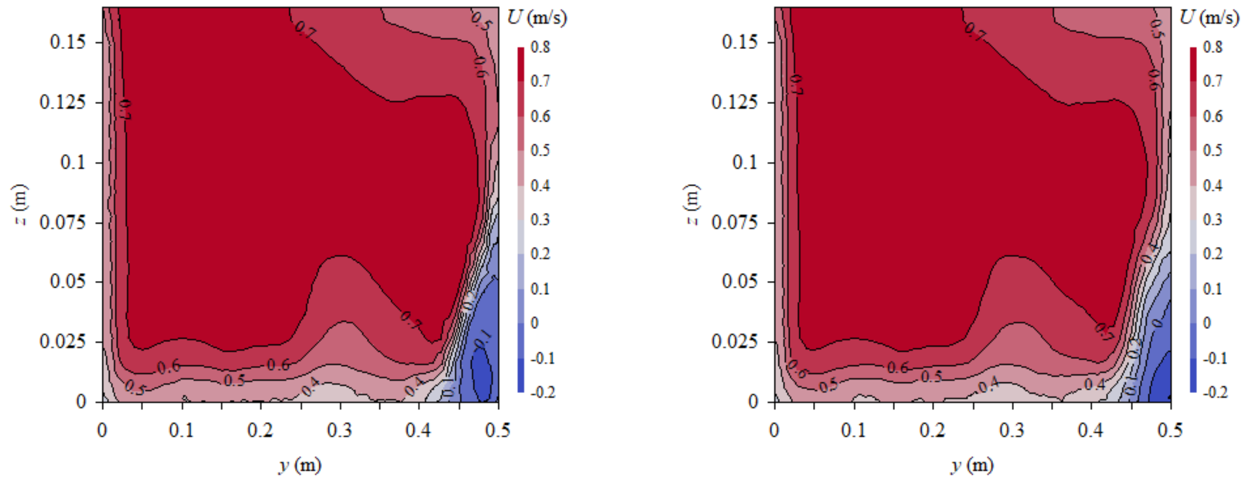

(a) $(x-x_b)/L_b = 0.05$ (b) $(x-x_b)/L_b = 0.235$

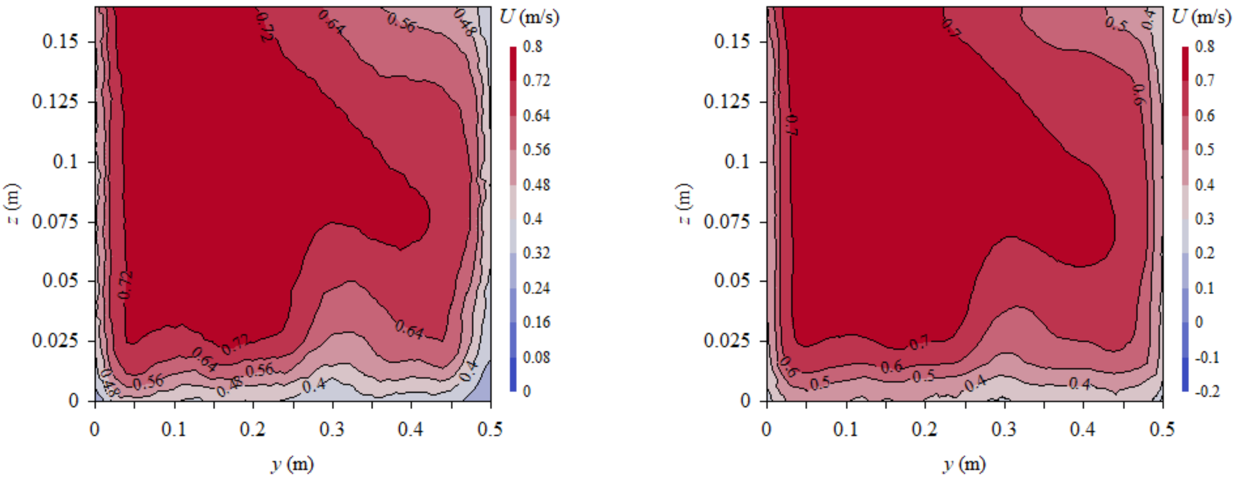

(c) $(x\text{-}x_b)/L_b = 0.5$ (d) $(x\text{-}x_b)/L_b = 0.765$

Figure B.5 – Velocity contours behind baffle – Flow conditions: Q = 55.6 l/s, h_b = 0.067 m, L_b = 0.67 m, d = 0.165 m.

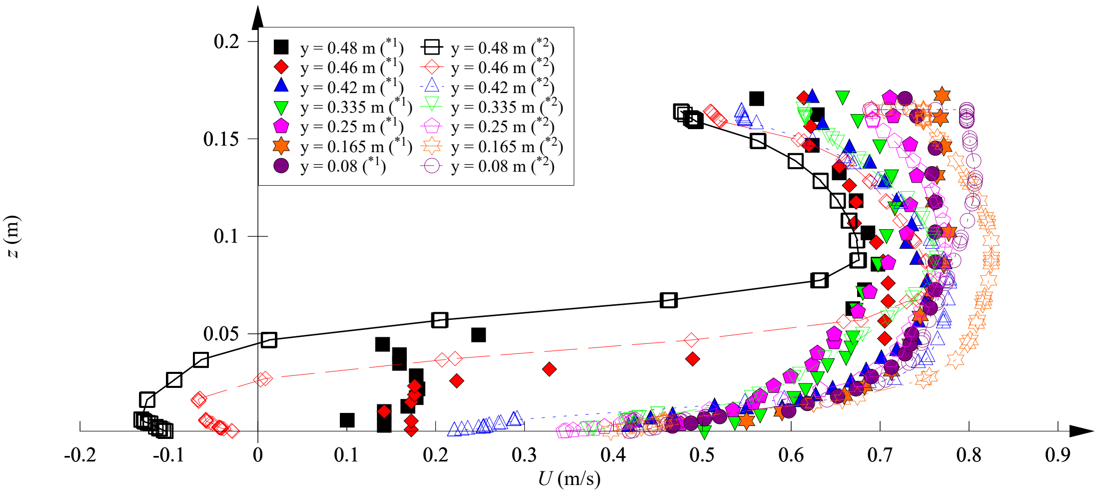

(a) $(x\text{-}x_b)/L_b = 0.05$

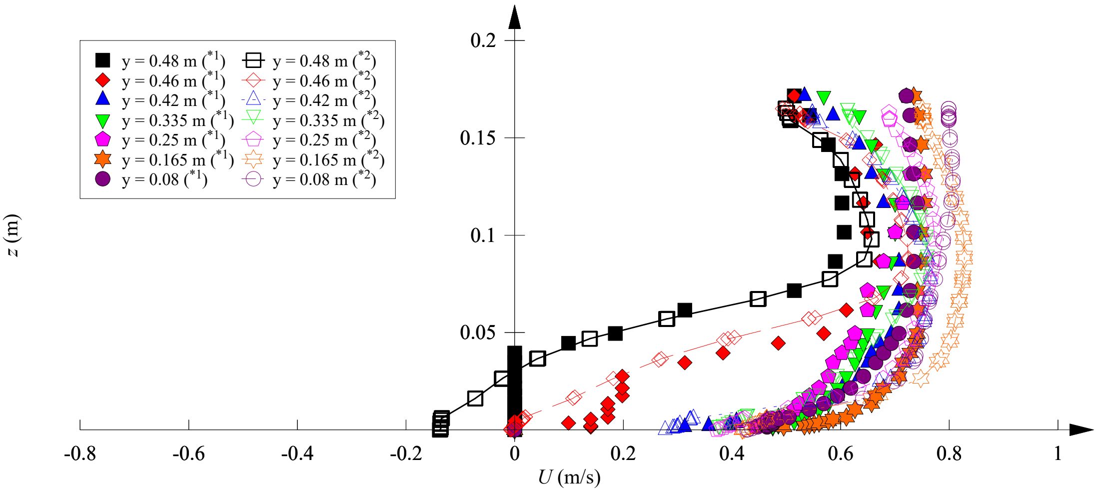

(b) $(x\text{-}x_b)/L_b = 0.235$

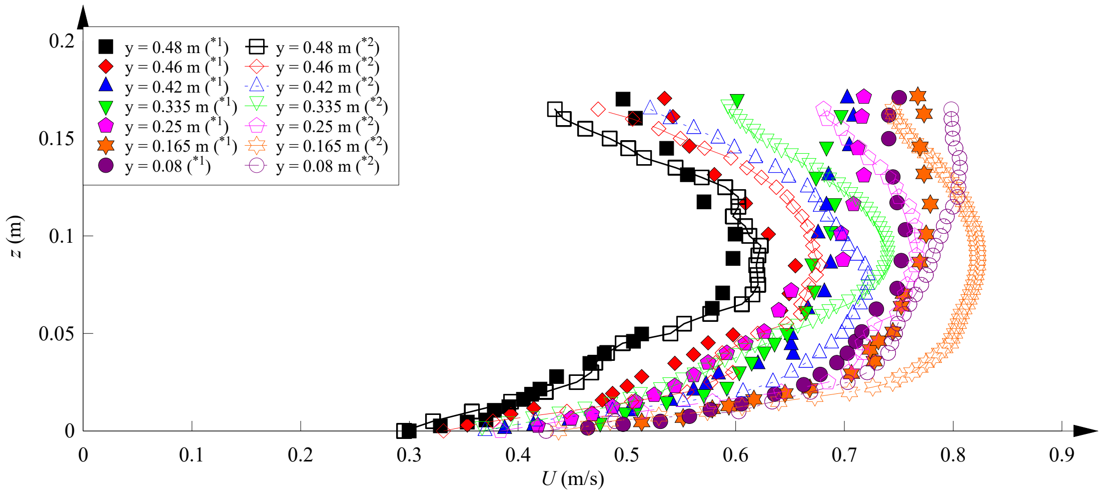

(c) $(x\text{-}x_b)/L_b = 0.5$

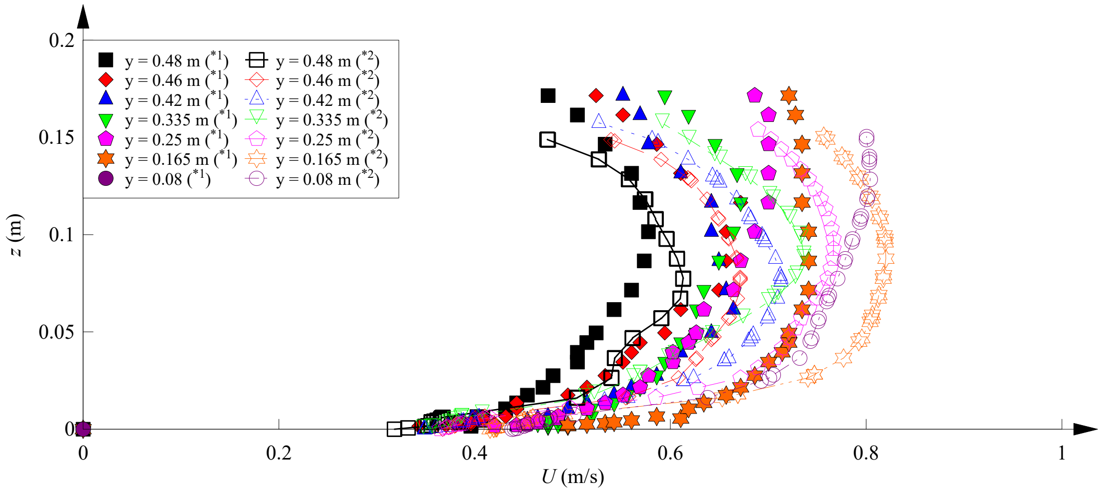

(d) $(x\text{-}x_b)/L_b = 0.765$

Figure B.6 – Velocity profiles at different transverse locations across channel equipped with small triangular corner baffles – Flow conditions: Q = 55.6 l/s, h_b = 0.067 m, L_b = 0.67 m, d = 0.165 m – Notes: *1 – Experimental data by Cabonce et al. (2017); *2 – Large Eddy Simulation (present study).

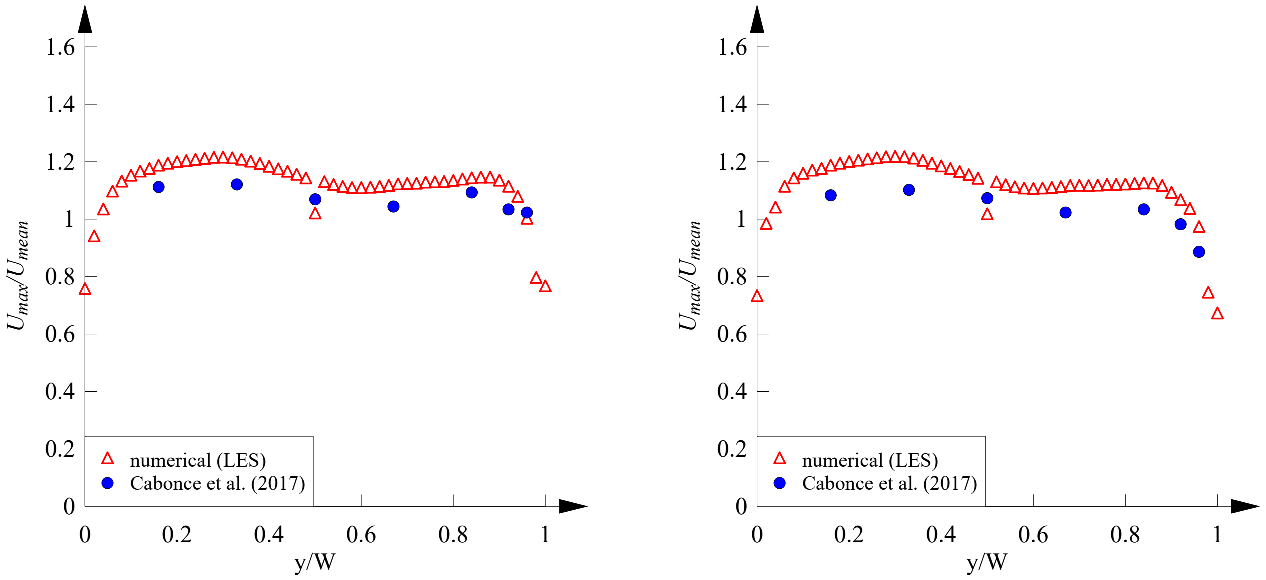

(a) $(x\text{-}x_b)/L_b = 0.05$ (b) $(x\text{-}x_b)/L_b = 0.235$

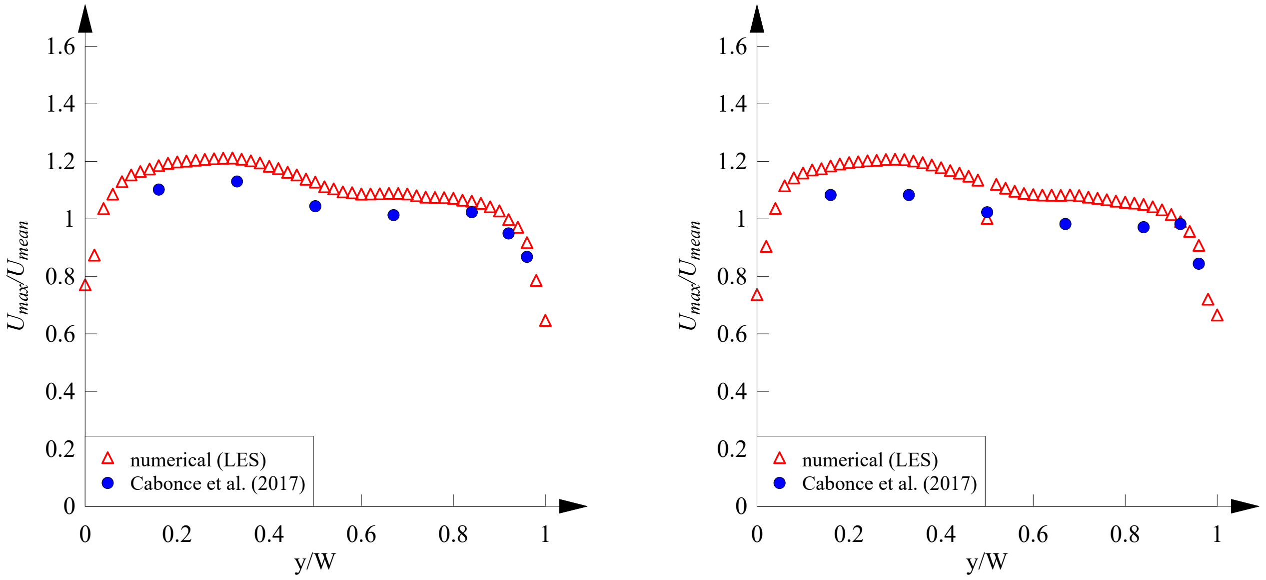

(c) $(x\text{-}x_b)/L_b = 0.5$ (d) $(x\text{-}x_b)/L_b = 0.765$

Figure B.7 – Transverse distributions of streamwise velocity maxima – Flow conditions: $Q = 55.6$ l/s, $h_b = 0.067$ m, $L_b = 0.67$ m, $d = 0.165$ m.

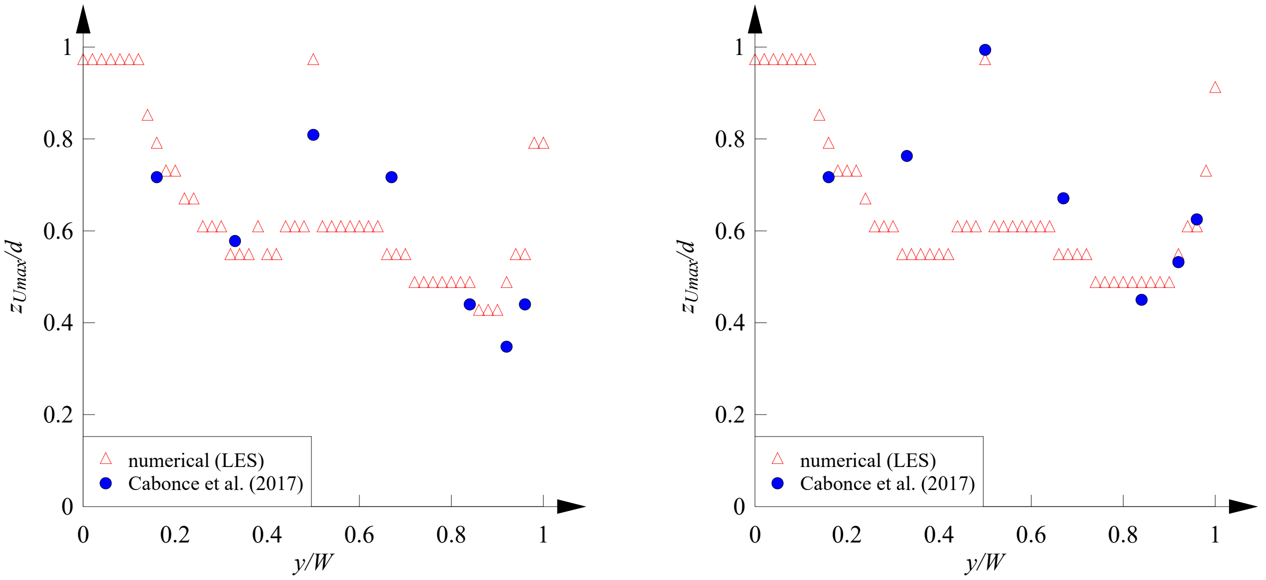

(a) $(x-x_b)/L_b = 0.05$ (b) $(x-x_b)/L_b = 0.235$

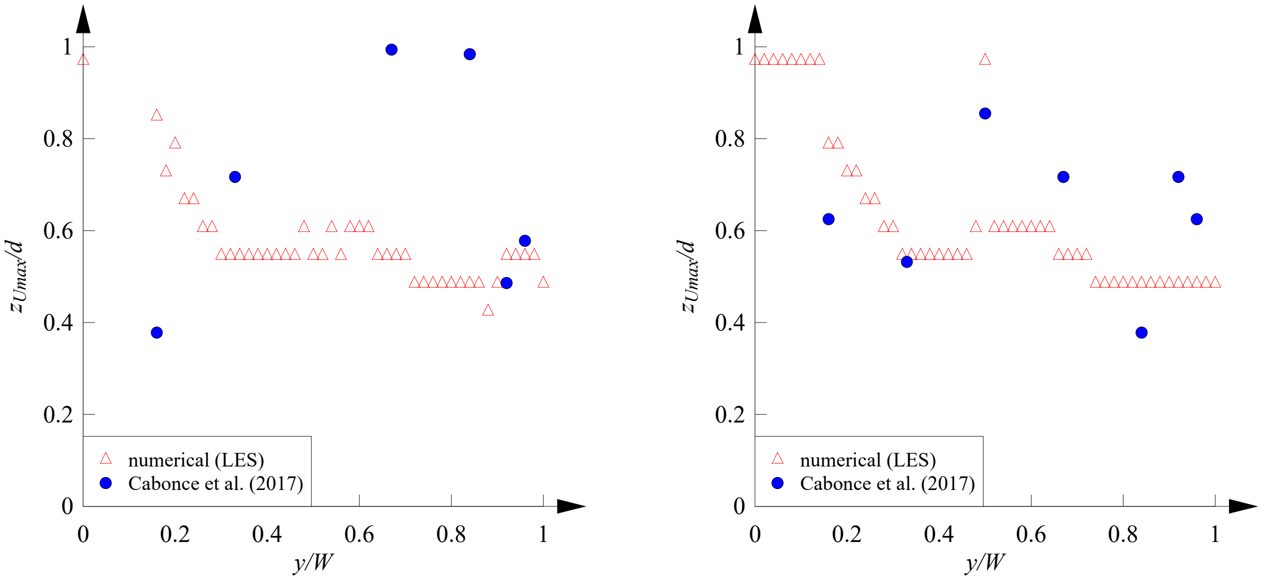

(c) $(x-x_b)/L_b = 0.5$ (d) $(x-x_b)/L_b = 0.765$

Figure B.8 – Transverse distributions of elevations of streamwise velocity maxima – Flow conditions: $Q = 55.6$ l/s, $h_b = 0.067$ m, $L_b = 0.67$ m, $d = 0.165$ m.

B.2.3 Scenario 3 (SC3)

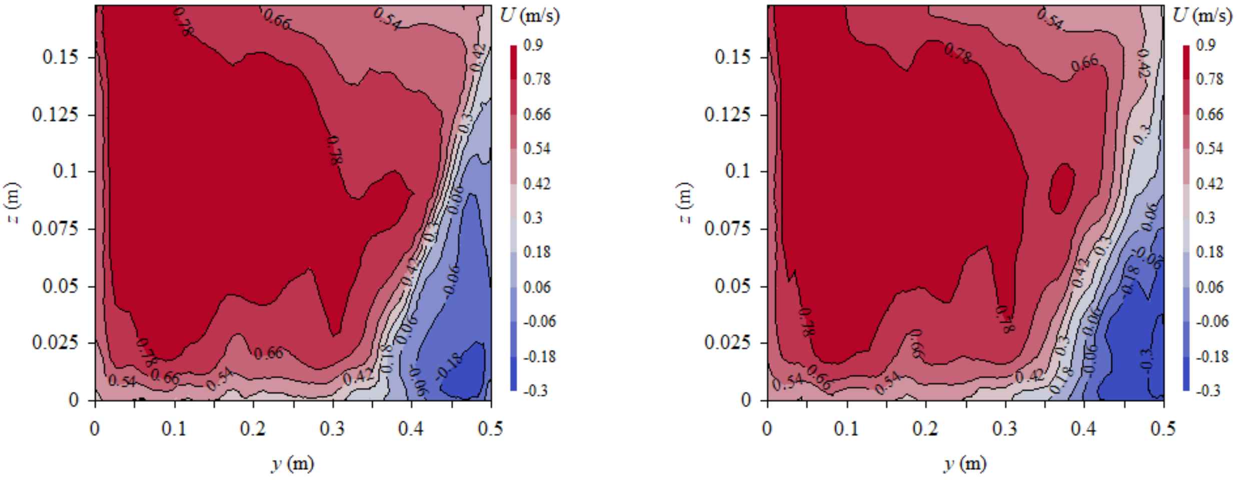

(a) $(x-x_b)/L_b = 0.05$ (b) $(x-x_b)/L_b = 0.235$

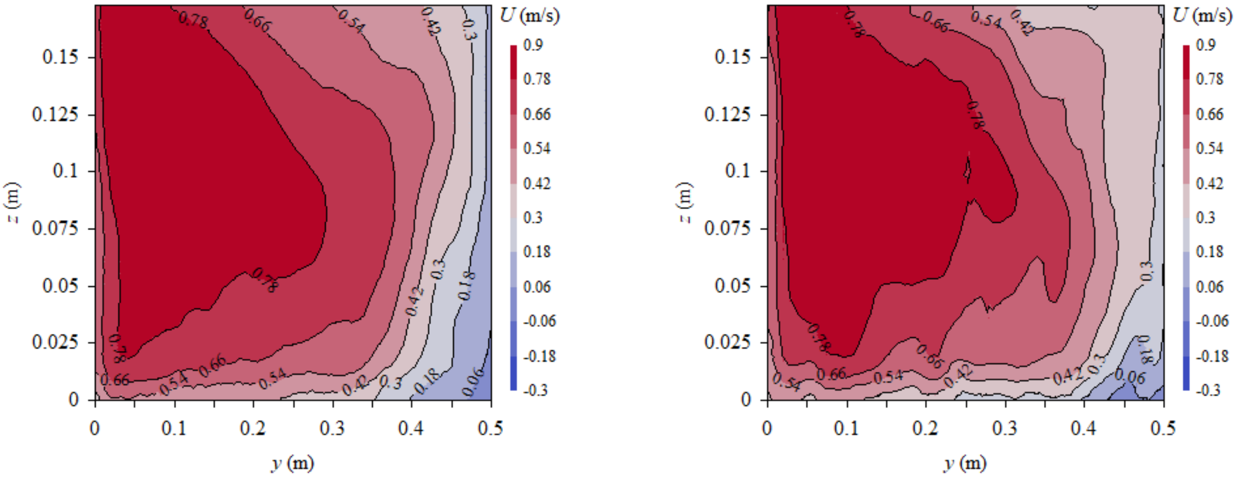

(c) $(x-x_b)/L_b = 0.5$ (d) $(x-x_b)/L_b = 0.765$

Figure B.9 – Velocity contours behind baffle – Flow conditions: Q = 55.6 l/s, h_b = 0.133 m, L_b = 0.67 m, d = 0.165 m

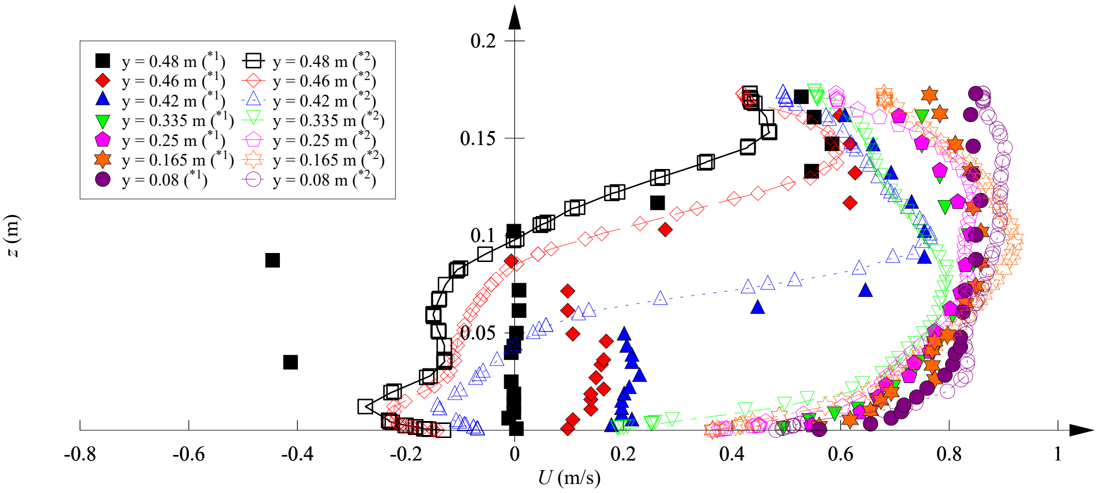

(a) $(x-x_b)/L_b = 0.05$

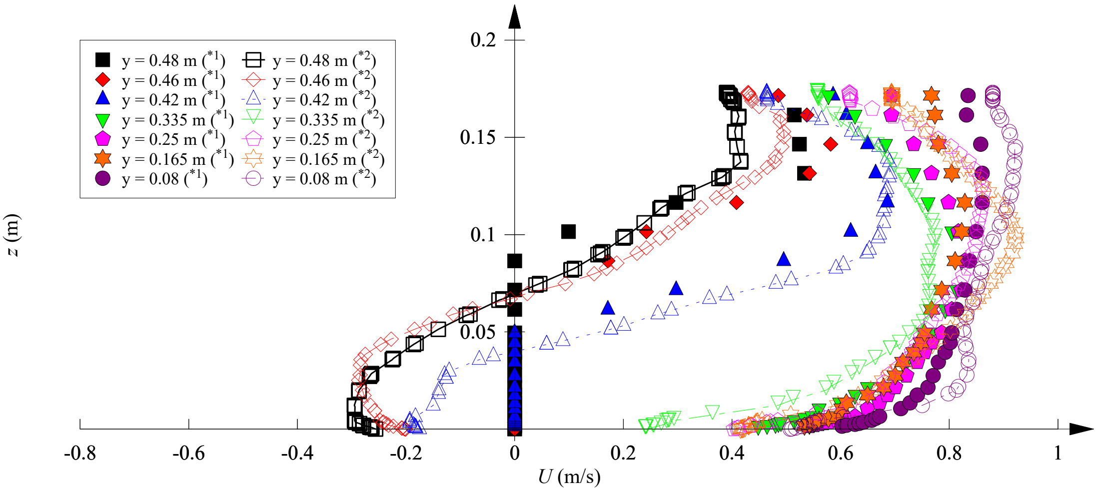

(b) $(x-x_b)/L_b = 0.235$

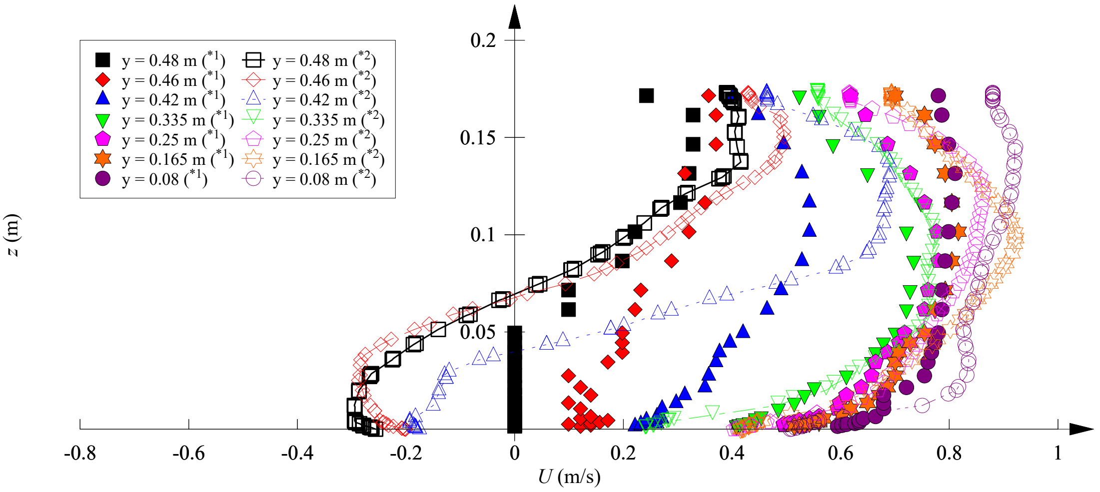

(c) $(x-x_b)/L_b = 0.5$

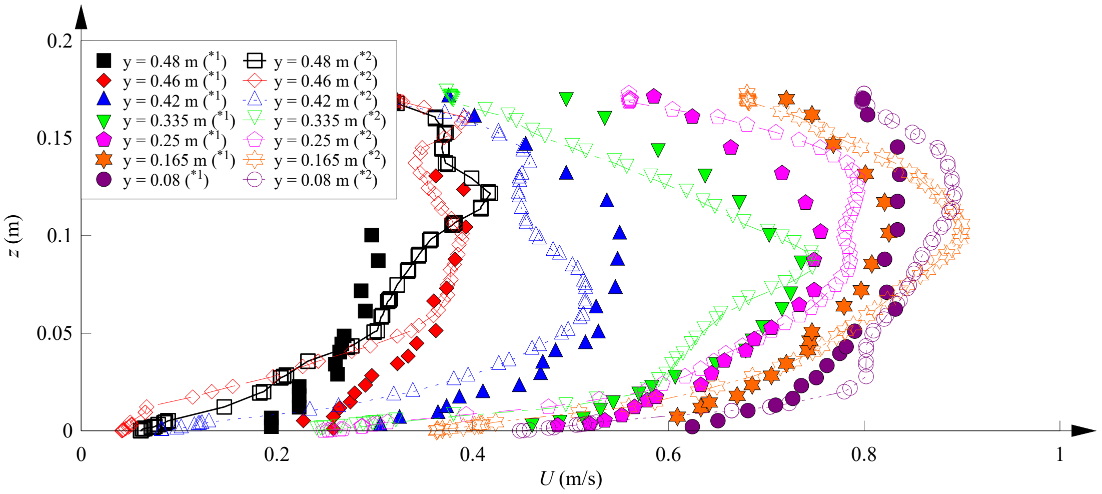

(d) $(x-x_b)/L_b = 0.765$

Figure B.10 – Velocity profiles at different transverse locations across channel equipped with small triangular corner baffles – Flow conditions: Q = 55.6 l/s, h_b = 0.133 m, L_b = 0.67 m, d = 0.173 m – Notes: *1 – Experimental data by Cabonce et al. (2017); *2 – Large Eddy Simulation (present study).

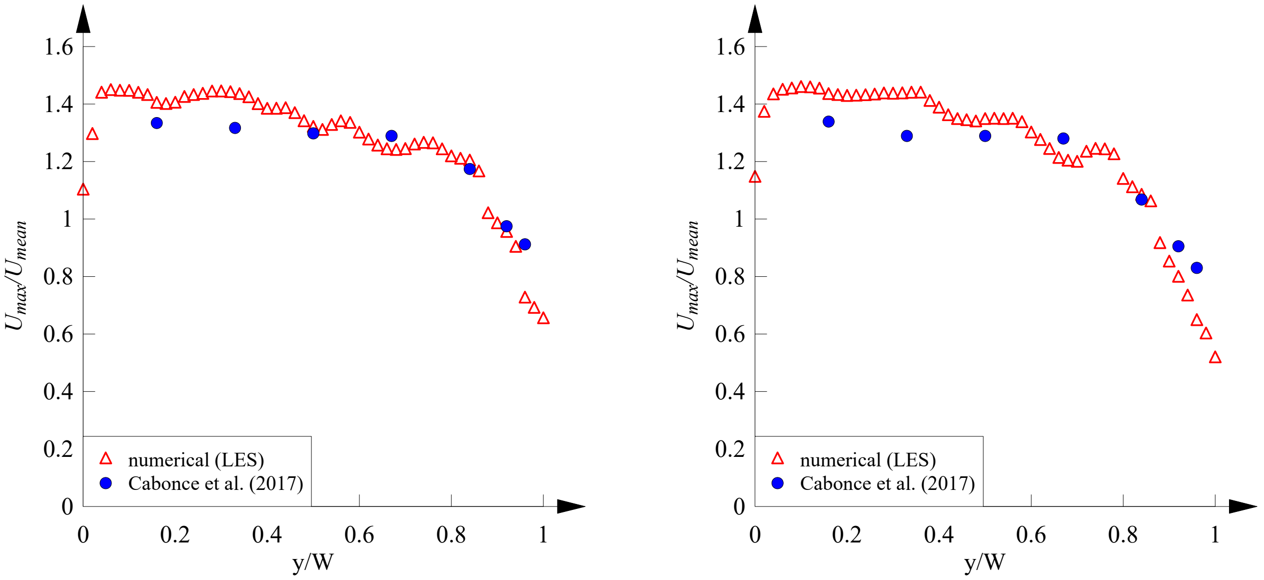

(a) $(x-x_b)/L_b = 0.05$

(b) $(x-x_b)/L_b = 0.235$

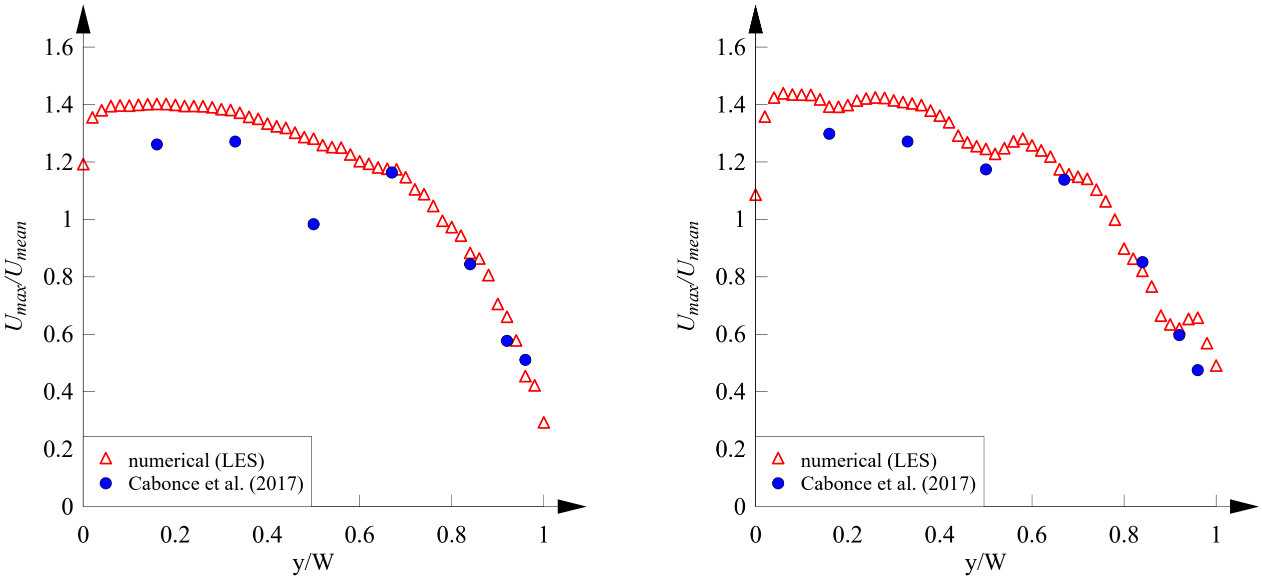

(c) $(x\text{-}x_b)/L_b = 0.5$ (d) $(x\text{-}x_b)/L_b = 0.765$

Figure B.11 – Transverse distributions of streamwise velocity maxima – Flow conditions: Q = 55.6 l/s, h_b = 0.133 m, L_b = 0.67 m, d = 0.173 m.

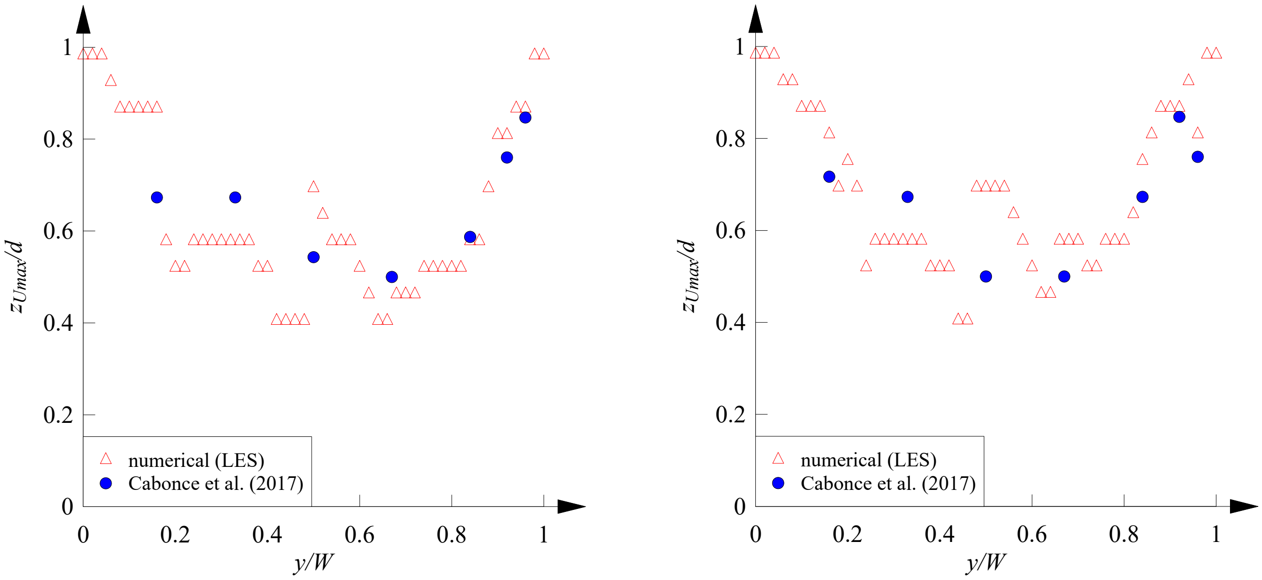

(a) $(x\text{-}x_b)/L_b = 0.05$ (b) $(x\text{-}x_b)/L_b = 0.235$

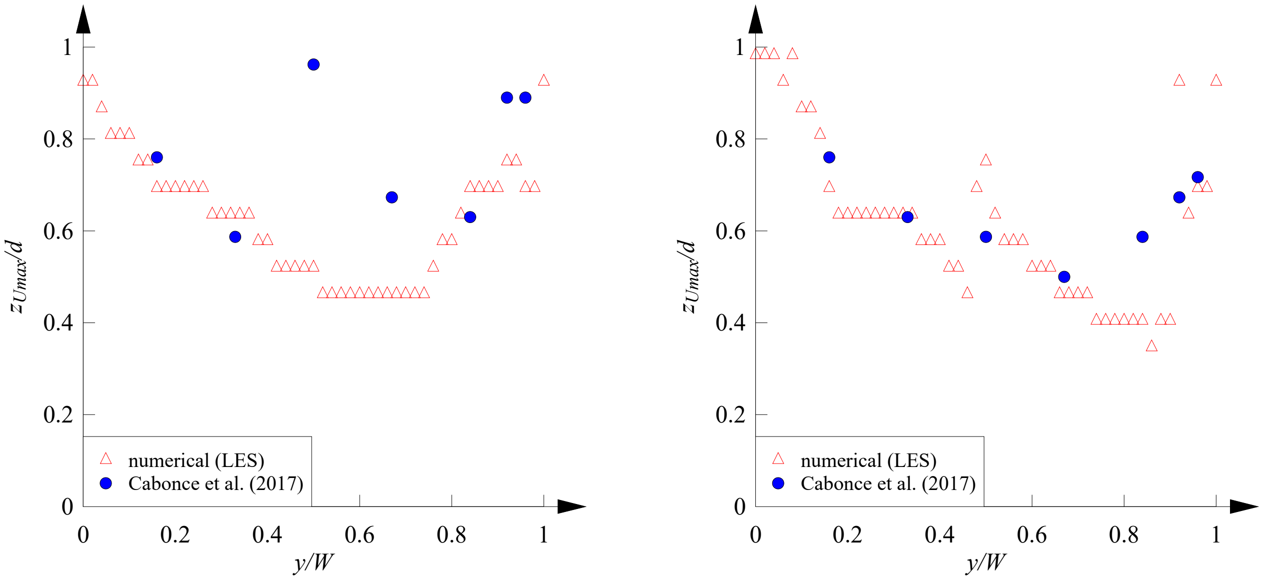

(c) $(x\text{-}x_b)/L_b = 0.5$ (d) $(x\text{-}x_b)/L_b = 0.765$

Figure B.12 – Transverse distributions of elevations of streamwise velocity maxima – Flow conditions: $Q = 55.6$ l/s, $h_b = 0.133$ m, $L_b = 0.67$ m, $d = 0.173$ m.

B.2.4 Scenario 4 (SC4)

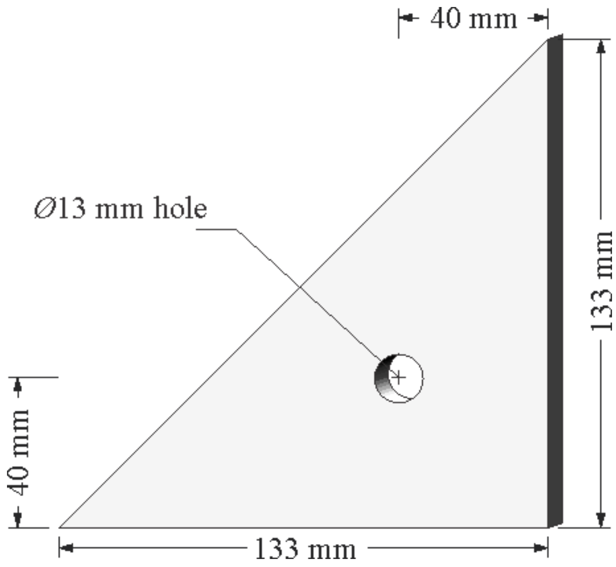

Figure B.13 – Specification of baffle with hole.

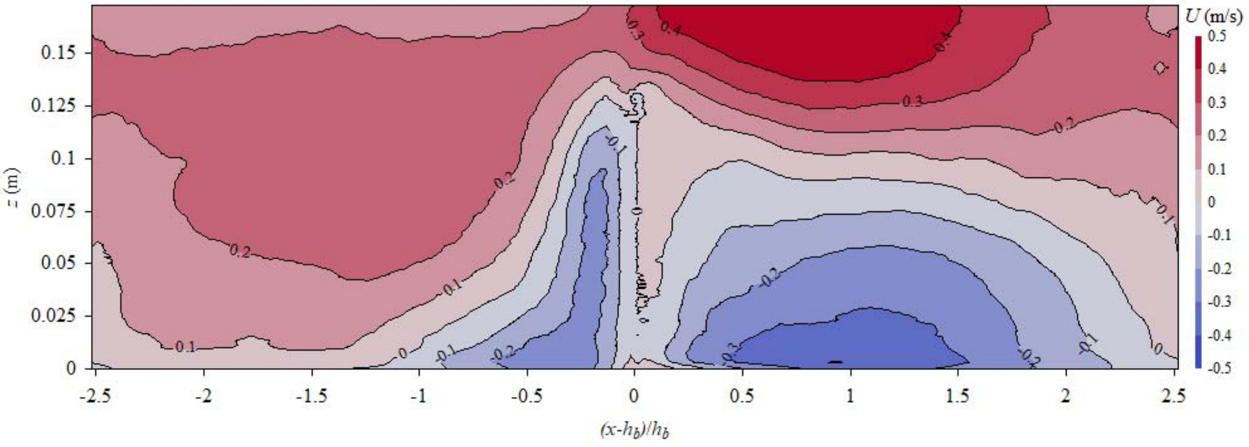

(a) $(W - y)/W = 0.01$ (wall)

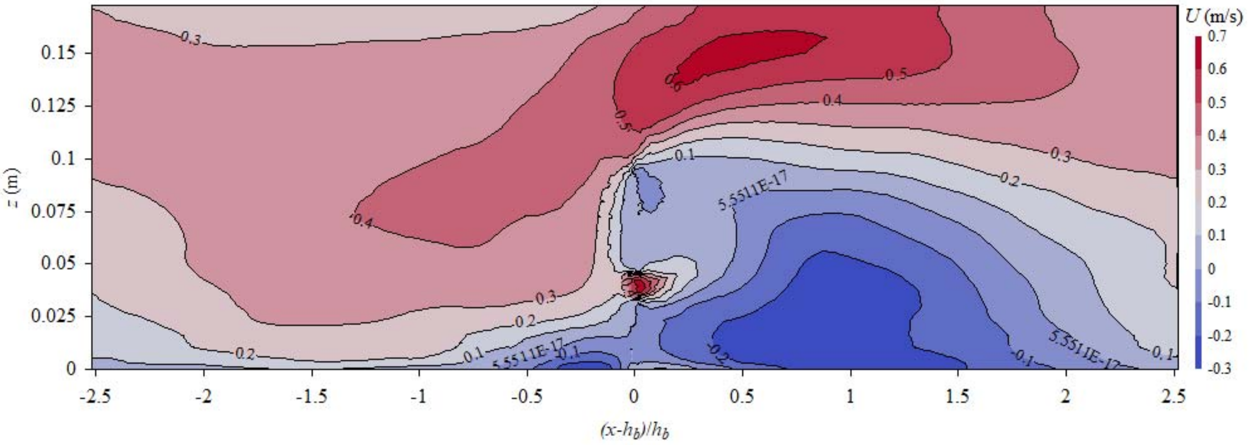

(b) $(W - y)/W = 0.08$ (hole)

Figure B.14 – Longitudinal velocity contours at various distances from the baffled wall – Flow conditions: $Q = 55.6$ l/s, $h_b = 0.133$ m, $L_b = 0.67$ m, $d = 0.173$ m, $\varnothing = 13$ mm hole.

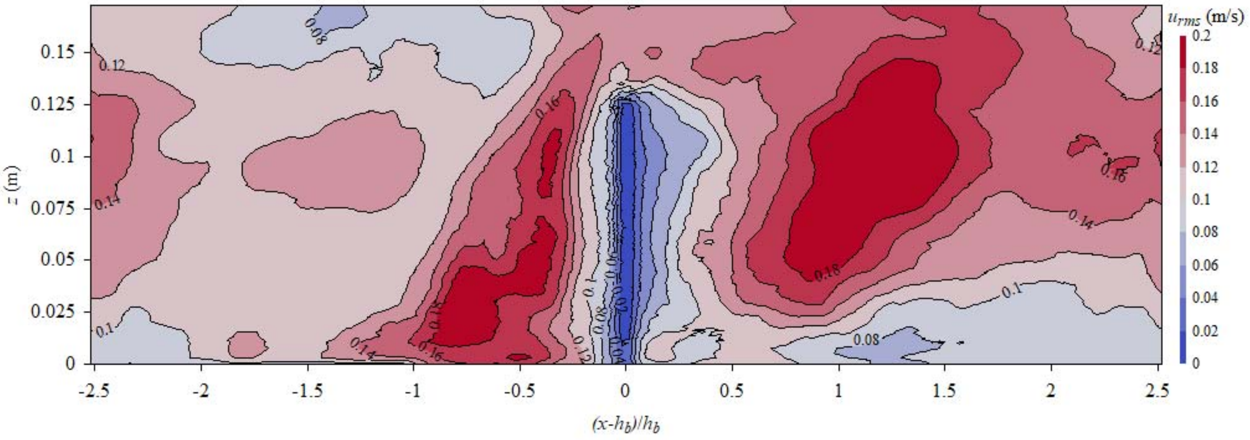

(a) $(W - y)/W = 0.01$ (wall)

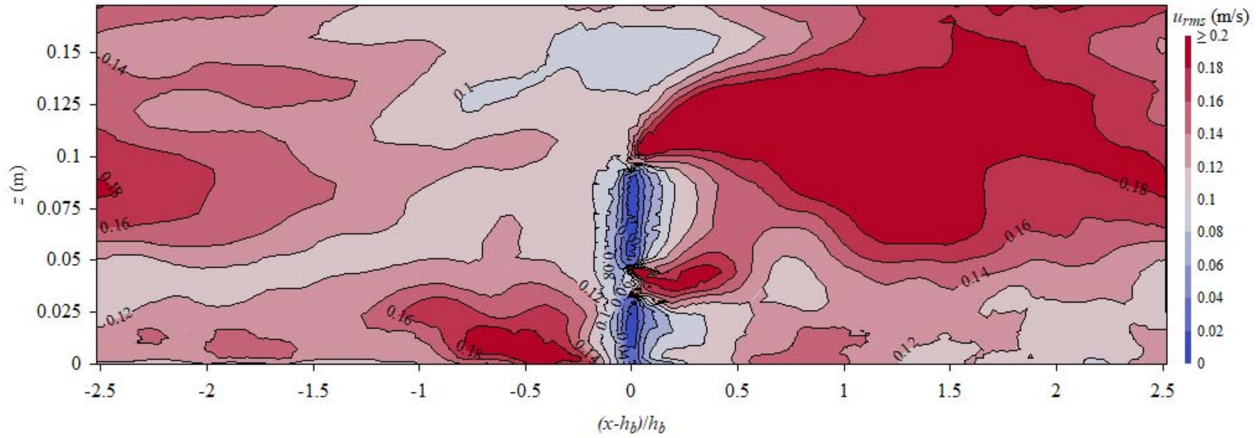

(b) $(W - y)/W = 0.08$ (wall)

Figure B.15 – Contours of streamwise velocity fluctuations at various distances from the baffled wall – Flow conditions: $Q = 55.6$ l/s, $h_b = 0.133$ m, $L_b = 0.67$ m, $d = 0.173$ m, $\varnothing = 13$ mm hole.

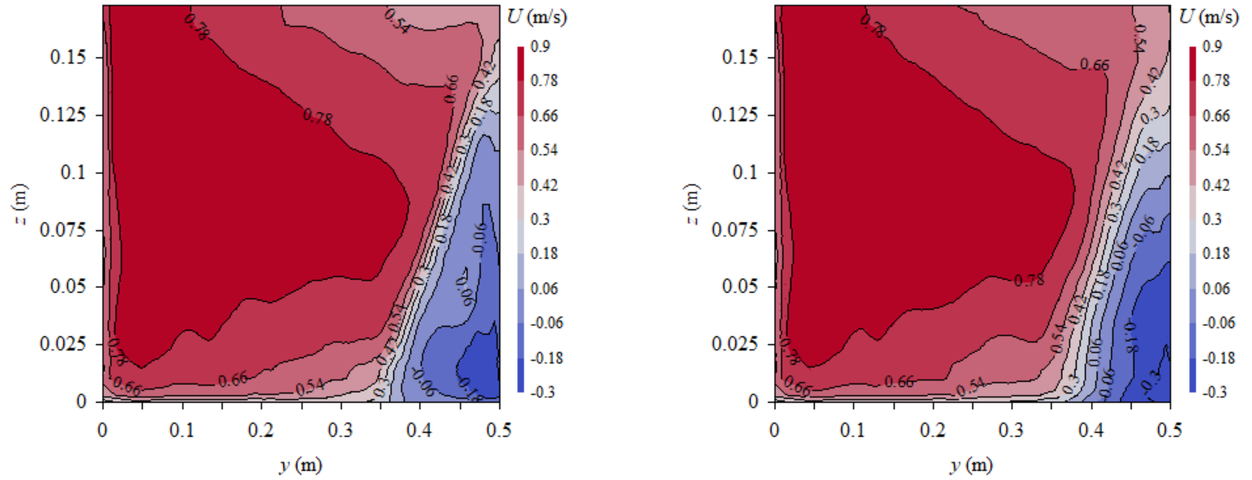

(a) $(x\text{-}x_b)/L_b = 0.05$

(b) $(x\text{-}x_b)/L_b = 0.235$

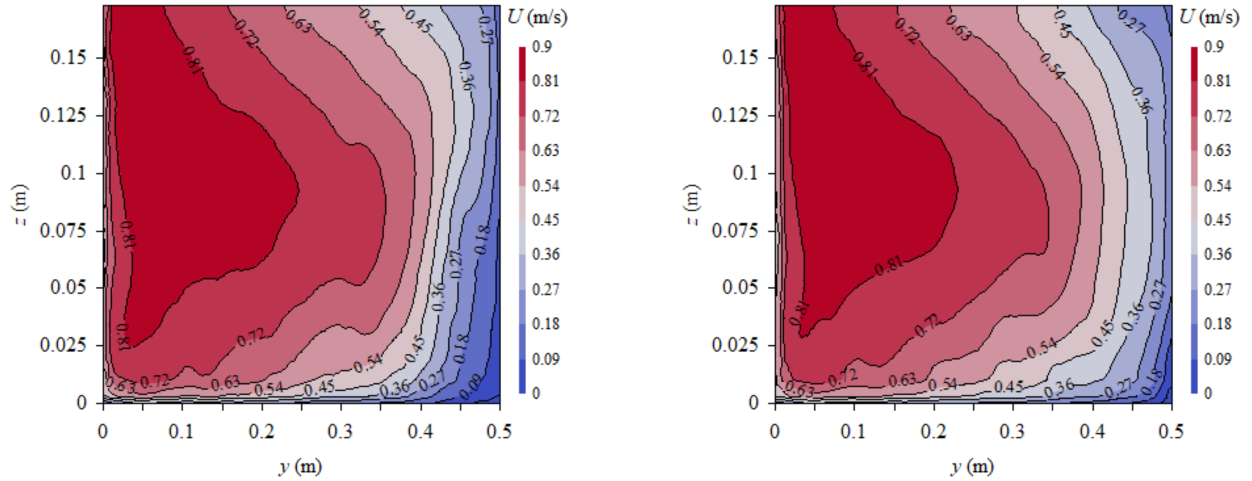

(c) $(x\text{-}x_b)/L_b = 0.5$

(d) $(x\text{-}x_b)/L_b = 0.765$

Figure B.16 – Velocity contours behind baffle – Flow conditions: $Q = 55.6$ l/s, $h_b = 0.133$ m, $L_b =$

0.67 m, $d = 0.173$ m, ∅ = 13 mm hole.

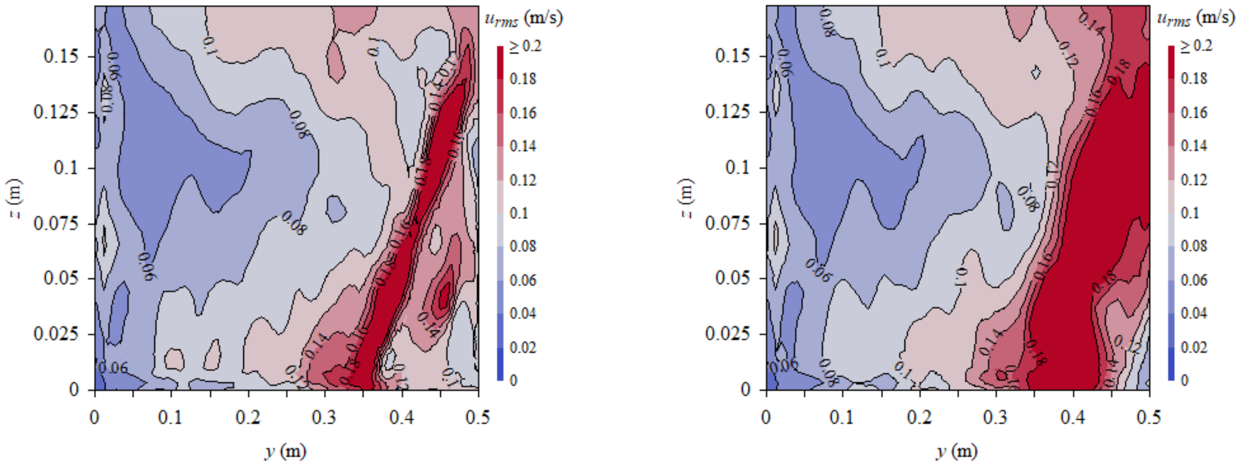

(a) $(x\text{-}x_b)/L_b = 0.05$ (b) $(x\text{-}x_b)/L_b = 0.235$

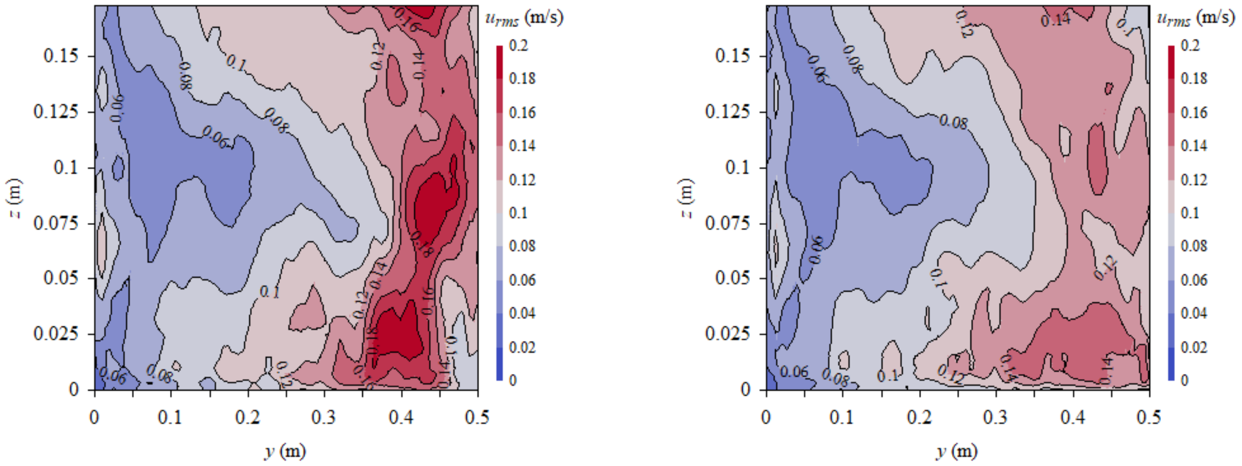

(c) $(x\text{-}x_b)/L_b = 0.5$ (d) $(x\text{-}x_b)/L_b = 0.765$

Figure B.17 – Velocity contours of streamwise velocity fluctuations behind baffle – Flow conditions: $Q = 55.6$ l/s, $h_b = 0.133$ m, $L_b = 0.67$ m, $d = 0.173$ m, ∅ = 13 mm hole.

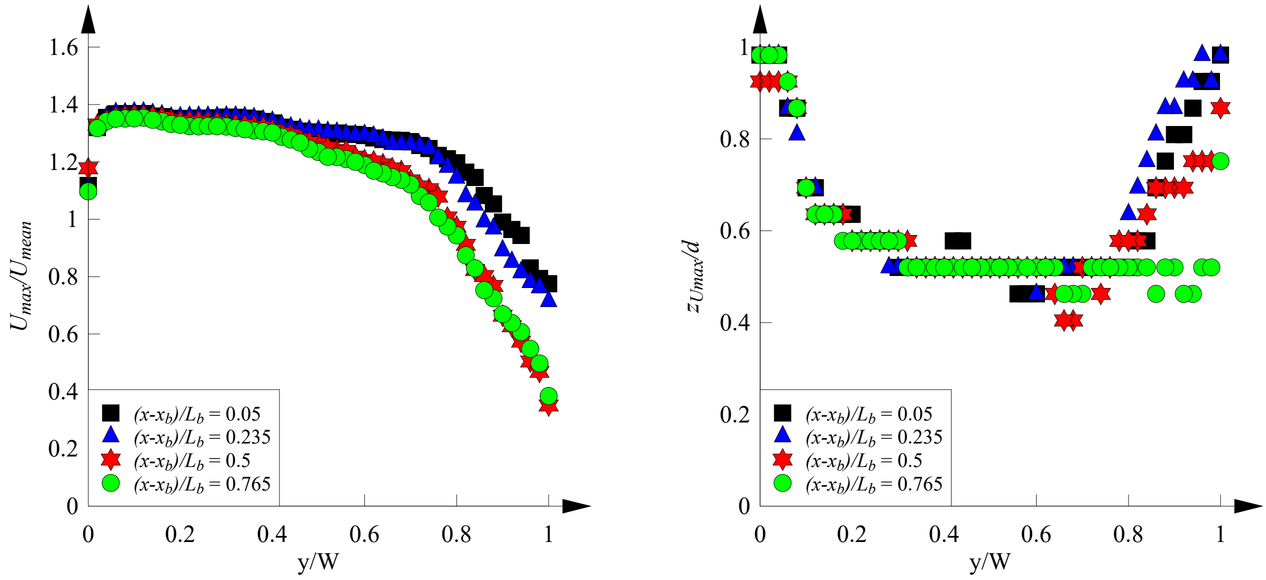

(a) Distributions of U_{max} (b) Distributions of z_{Umax}

Figure B.18 – Transverse distributions of maximum streamwise velocities U_{max} and corresponding locations z_{Umax} – Flow conditions: $Q = 55.6$ l/s, $h_b = 0.133$ m, $L_b = 0.67$ m, $d = 0.173$ m, ∅ = 13 mm hole.

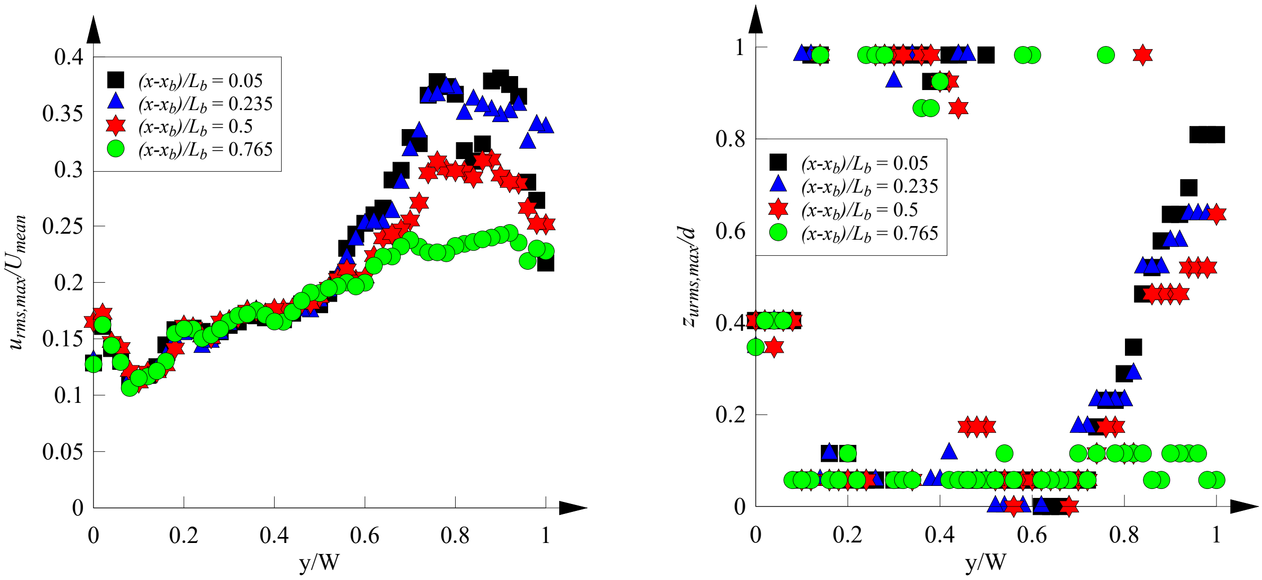

(a) Distributions of $u_{rms,max}$ (b) Distributions of $z_{urms,max}$

Figure B.19 – Transverse distributions of maximum streamwise velocity fluctuations $u_{rms,max}$ and corresponding locations $z_{urms,max}$ – Flow conditions: $Q = 55.6$ l/s, $h_b = 0.133$ m, $L_b = 0.67$ m, $d = 0.173$ m, ∅ = 13 mm hole.

APPENDIX C. ON LOW VELOCITY ZONES PRODUCED BY DIFFERENT CULVERT CONFIGURATION SYSTEMS

C.1 PRESENTATION

Research showed that low velocity zones (LVZs) are favoured swimming zones for fish (Lupandin, 2005; Cotel, 2006), and small-bodied fish like to keep next to the wall and in the flume corner while swimming (Wang et al., 2016b; Cabonce et al., 2017; Wang and Chanson, 2017). Whilst fish swimming behaviours are relatively easy to observe, a good assessment of low velocity zones generally requires complete characterisations of the cross-sections of interest involving careful and extensive data acquisition under carefully-controlled flow conditions in laboratory. On the other hand, properly validated numerical models conveniently convey such information at an unparalleled level of detail compared to traditional methods. This appendix aims to provide a comprehensive characterisation of the low velocity zones associated with each roughness configuration using the numerical models described in the previous chapters.

Table C.1 compares the low velocity regions' relative area for culvert barrels with smooth walls, with rough bed and rough left sidewall, with small corner baffles and with ventilated baffles. The CFD results are compared to experimental observations, presenting the cross-sectional average velocity U_{mean}, the cross-sectional maximum water velocity $(U_{max})_M$, as well as the percentage of flow cross-section area where the time-averaged longitudinal velocity U was less than U_{mean}, $0.75U_{mean}$ and $0.5U_{mean}$ (Table C.1, last three columns). In the smooth boundary channel, both physical and numerical results indicate that 5-10% of the flow area experience time-averaged velocities less than $0.5U_{mean}$. This relative surface area is considerably higher in both rough channel and triangular baffle channel, with about 5-25% of the flow area experiencing $U < 0.5U_{mean}$, depending upon the configuration.

Beyond the total size of low velocity zones (LVZs), it is reasonable to infer that fish navigability also depends on the connectivity between LVZs. Namely, a long, contiguous stretch of low velocity zone which meets certain velocity criteria is naturally more traversable than multiple, separate patches of low-velocity. A single, large slow region is more suitable than multiple slow areas of smaller sizes. Consequently, one may wish to improve cross-sectional asymmetry while minimising streamwise variations to favour the development of a large contiguous stretch of traversable area instead of smaller, equal-sized slow regions on both sides of the channel.

Figures C.1 to C.5 illustrate how the nature of the low velocity zones depends on the roughness type. Areas meeting and failing the specified velocity criteria are highlighted in black and grey, respectively. In the smooth barrel (Fig. C.1), two equal-sized small LVZs occupy the sides and bottom of the channel, as expected from symmetry. The only traversable regions in this case are the bottom corners of the channel. Passage is impossible for species which require $U < 0.5U_{mean}$ as the compliant regions lie extremely close to the physical boundaries of the barrel.

Figure C.2 shows that the channel with one rough sidewall and rough bed improves the passage ability significantly for $U < U_{mean}$, by inducing a large slow region on the roughened side of the channel. In addition to the corner circulations, an additional low velocity zone is identified above the channel bed at approximately $y = 0.2$ where two large secondary flow cells meet. The observation suggests that such mechanisms may be utilised to create additional regions of slow flow. For the slowest flow areas with $U < 0.5U_{mean}$, the roughness asymmetry improves navigability slightly by favouring the rough side of the channel.

A review of Figure C.3 indicates that even the smallest corner baffle can be effective at producing a slow-velocity region immediately behind the obstruction. Though the baffle provides a seemingly obvious option for fish passage, caution must be taken where the strong recirculation may disorient the fish before they are able to adjust (Cabonce et al., 2017, 2018). More, the disadvantage of a singular obstacle becomes noticeable further downstream. For $(x - x_b)/L_b = 0.765$, the low velocity regions appear significantly altered from those upstream. The availability for $U < 0.5U_{mean}$ is nearly depleted, which attributes to the inability of the channel configuration to maintain contiguous slow regions for certain criteria.

Figure C.4 shows that the caveats of the previous system may be avoided by upsizing the corner baffle. The equivalent reduction in relative spacing limits the streamwise flow variation by increasing the mutual sheltering between adjacent elements, whereas the increase in relative submergence immediately results in a larger slow area. For a criterion $U < 0.5U_{mean}$, the baffled corner remains traversable for the full distance between adjacent baffles. The disorientating effect in the immediate wake of the baffle remains the principal limitation of this configuration, which may be reduced by providing ventilation to the recirculation region. An implementation of this strategy with a single 13 mm circular opening through the centroid of the baffle is shown in Figure C.5. The results are largely similar to those of Figure C.4, suggesting that a more effective ventilation strategy would be relevant.

Table C.1 - Comparison between CFD and experimental observations of cross-sectional maximum velocities and percentage of wetted cross-section with time-averaged velocity range in the fully-developed flow region of a box culvert channel (x ~ 8 m)

Ref.	S_o	W (m)	Q (m^3/s)	h_b (m)	L_b (m)	d (m)	U_{mean} (m/s)	X	$(U_{max})_M$ (m/s)	% flow area with $U <$ U_{mean}	% flow area with $U <$ $0.75U_{mean}$	% flow area with $U <$ $0.5U_{mean}$
Present study												
Smooth			0.0556	N/A	N/A	0.192	0.686	N/A	0.641	48.5%	8.9%	5.1%
Rough bed and sidewall	0	0.5	0.0556	N/A	N/A	0.1743	0.638	N/A	0.855	42.0%	15.7%	5.0%
Baffles	0	0.5	0.0261	0.067	0.67	0.1	0.606	0.05	0.679	66.8%	20.6%	7.6%
								0.235	0.679	67.3%	25.2%	7.9%
								0.5	0.677	68.6%	28.4%	5.1%
								0.765	0.676	69.1%	31.3%	4.5%
			0.0556	0.067	0.67	0.165	0.674	0.05	0.828	32.6%	13.6%	4.6%
								0.235	0.829	33.8%	14.1%	4.1%
								0.5	0.824	39.0%	11.2%	0.7%
								0.765	0.822	41.0%	13.3%	0.6%
			0.0556	0.133	0.67	0.173	0.643	0.05	0.929	32.0%	18.5%	14.0%
								0.235	0.935	33.1%	19.8%	12.9%
								0.5	0.898	39.3%	20.5%	11.6%
								0.765	0.921	43.7%	23.6%	7.7%
Baffles with hole	0	0.5	0.0556	0.133	0.67	0.173	0.643	0.05	0.880	29.2%	16.6%	13.6%
								0.235	0.882	30.8%	17.5%	12.6%
								0.5	0.876	37.8%	20.1%	10.8%
								0.765	0.870	41.4%	21.3%	7.6%
Wang et al. (2016a)												
Rough bed and sidewall	0	0.4785	0.0261	N/A	N/A	0.129	0.423	N/A	0.755	45%	30%	17%
			0.0556	N/A	N/A	0.1743	0.667	N/A	0.957			
Cabonce et al. (2017)												
Smooth	0	0.5	0.0261	N/A	N/A	0.096	0.544	N/A	0.569	70.8%	36.4%	5.3%
			0.0556	N/A	N/A	0.162	0.686	N/A	0.714	72.7%	25.9%	10.4%
Baffles	0	0.5	0.0261	0.067	0.67	0.121	0.431	0.048	0.642	39.6%	17.3%	14.9%
								0.235	0.640	30.5%	20.6%	14.3%
								0.500	0.602	43.7%	18.3%	12.1%
								0.765	0.649	30.7%	19.3%	10.3%
			0.0556	0.067	0.67	0.1625	0.684	0.048	0.767	43.8%	20.9%	13.5%
								0.235	0.754	59.1%	24.8%	13.8%
								0.500	0.774	63.0%	22.0%	11.5%
								0.765	0.741	58.7%	31.5%	9.7%
			0.0556	0.133	0.67	0.173	0.643	0.048	0.858	51.9%	26.3%	17.5%
								0.235	0.861	38.8%	22.5%	16.6%
								0.500	0.817	67.9%	31.5%	26.1%
								0.765	0.835	54.2%	28.9%	14.4%
			0.0261	0.133	1.33	0.1035	0.504	0.048	0.786	35.7%	29.9%	22.7%
								0.235	0.774	44.1%	30.5%	24.0%
								0.500	0.741	55.0%	35.1%	16.3%
								0.765	0.744	48.1%	30.7%	16.2%

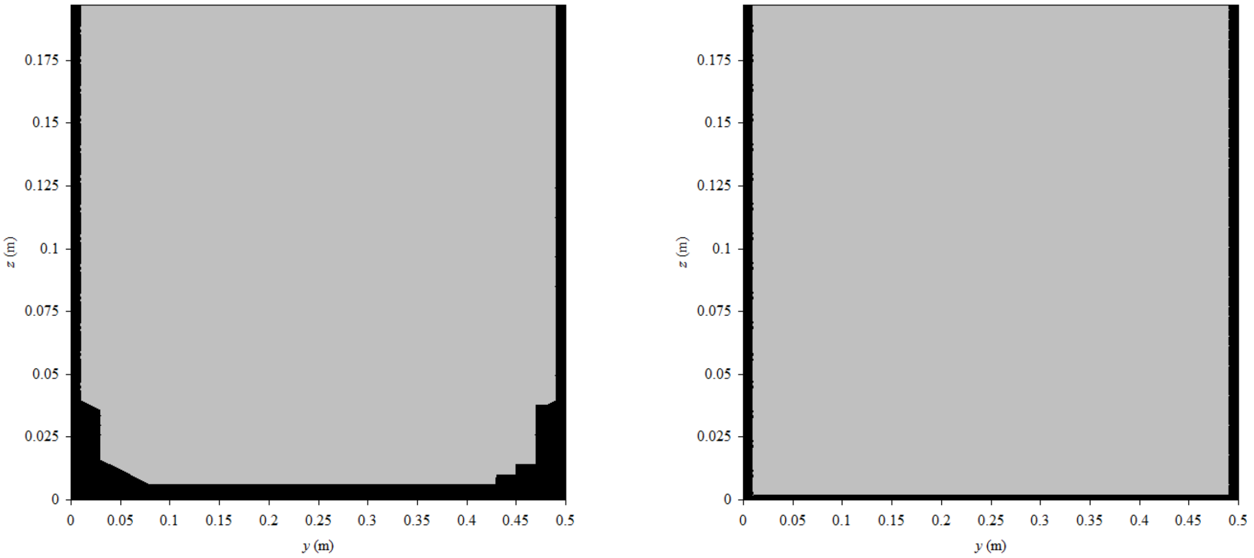

(a) $U/U_{mean} < 0.75$ (b) $U/U_{mean} < 0.5$

Figure C.1 – Low velocity regions in smooth barrel (no baffle)– Flow conditions: Q = 55.6 l/s, k_s = 0.2 mm.

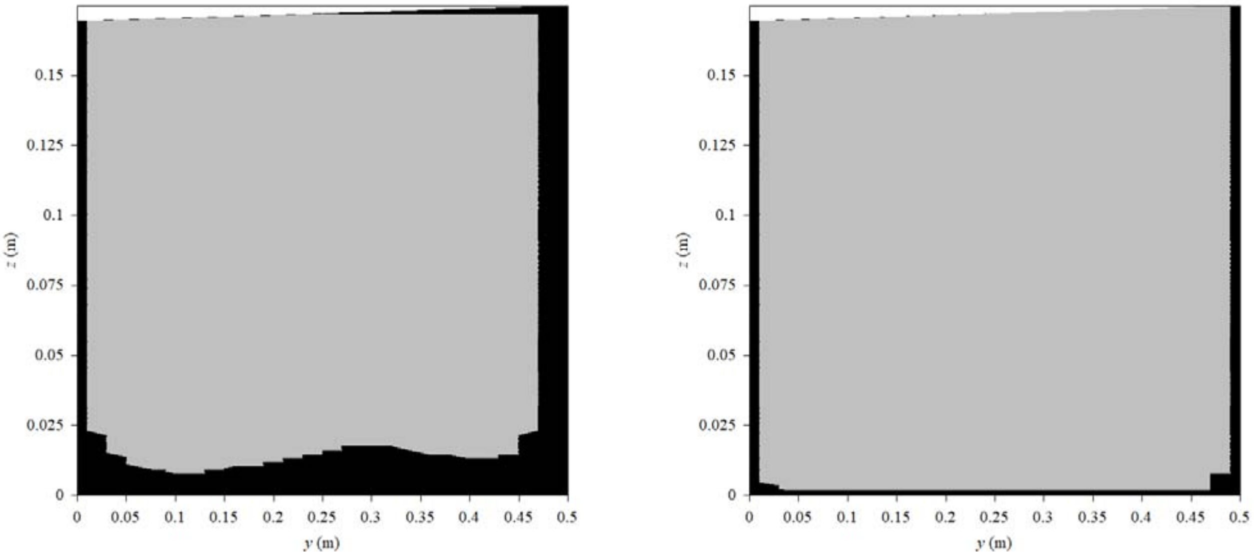

(a) $U/U_{mean} < 0.75$ (b) $U/U_{mean} < 0.5$

Figure C.2 – Low velocity regions in barrel with rough bed and rough left sidewall – Flow conditions: Q = 55.6 l/s, k_s = 0.2 mm (smooth), k_s = 20 mm (rough).

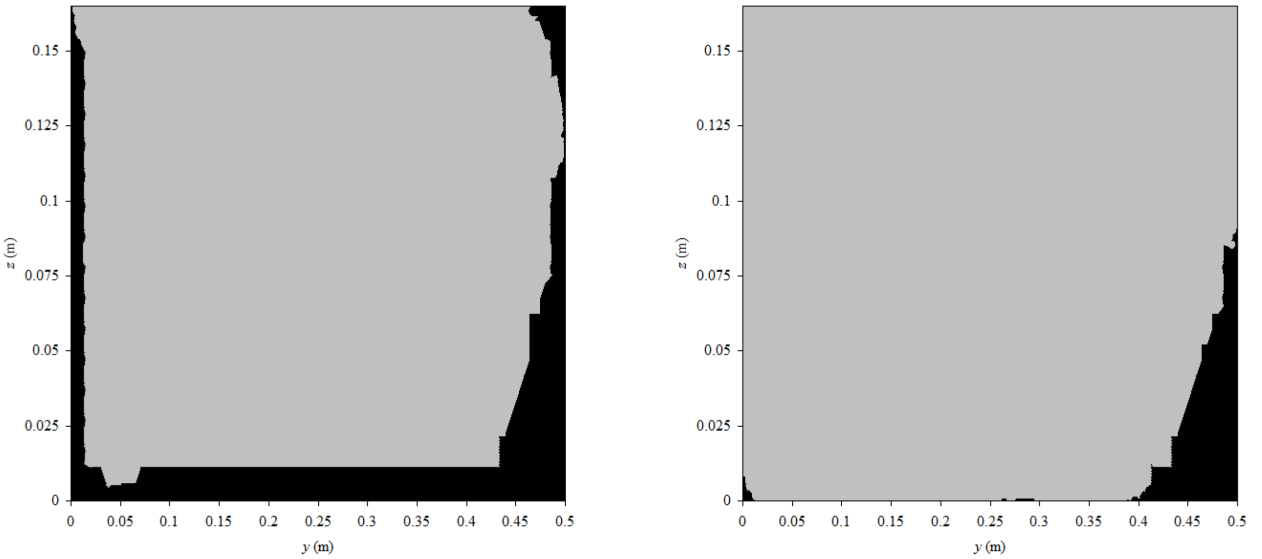

(a) $U/U_{mean} < 0.75$, $(x - x_b)/L_b = 0.05$ (b) $U/U_{mean} < 0.5$, $(x - x_b)/L_b = 0.05$

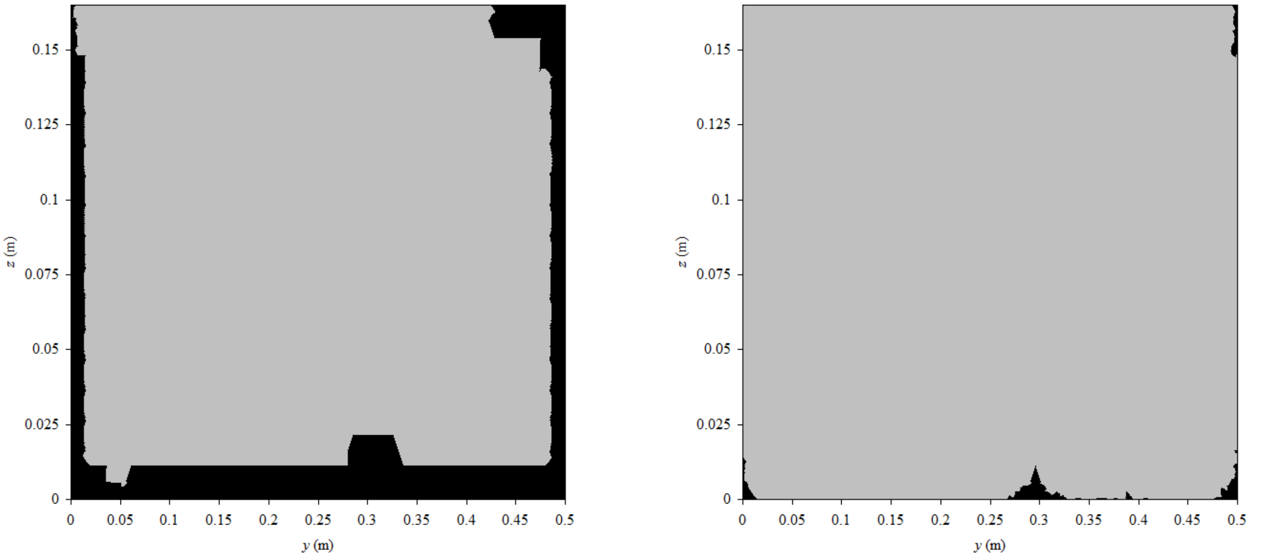

(c) $U/U_{mean} < 0.75$, $(x - x_b)/L_b = 0.765$ (d) $U/U_{mean} < 0.5$, $(x - x_b)/L_b = 0.765$

Figure C.3 – Low velocity regions in barrel with triangular baffles – Flow conditions: $Q = 55.6$ l/s, $h_b = 0.067$ m, $L_b = 0.67$ m.

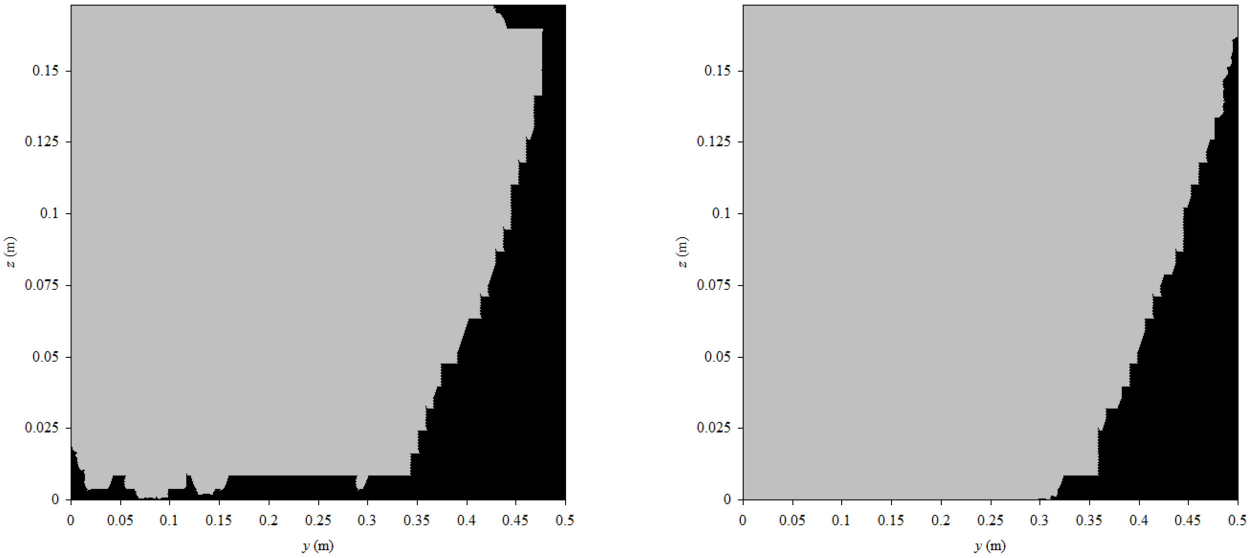

(a) $U/U_{mean} < 0.75$, $(x - x_b)/L_b = 0.05$ (b) $U/U_{mean} < 0.5$, $(x - x_b)/L_b = 0.05$

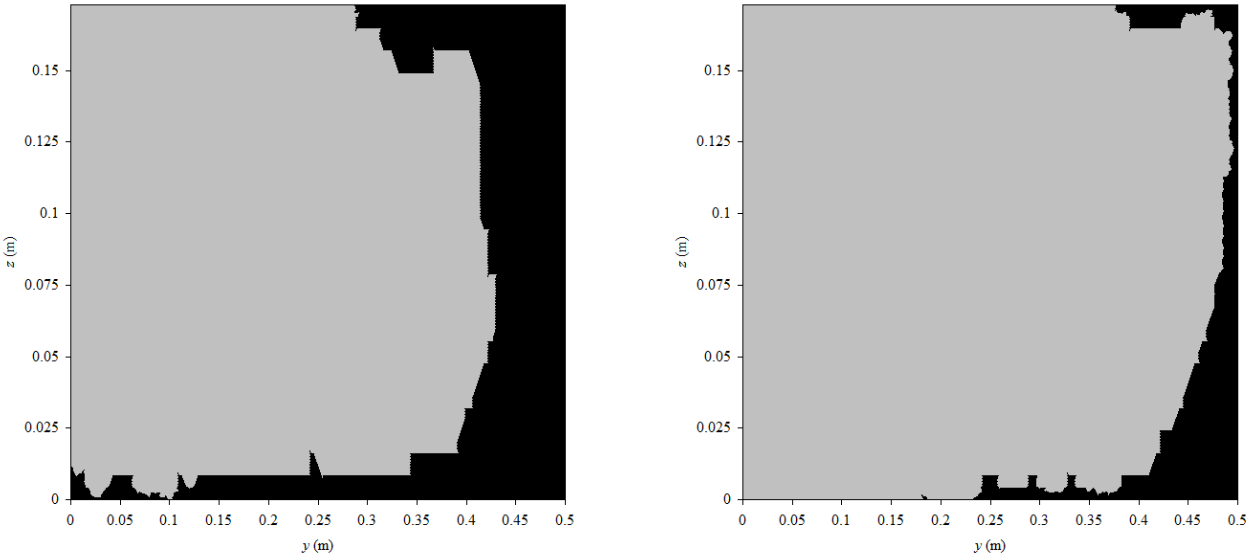

(c) $U/U_{mean} < 0.75$, $(x - x_b)/L_b = 0.765$ (d) $U/U_{mean} < 0.5$, $(x - x_b)/L_b = 0.765$

Figure C.4 – Low velocity regions in barrel with triangular baffles – Flow conditions: $Q = 55.6$ l/s, $h_b = 0.133$ m, $L_b = 0.67$ m.

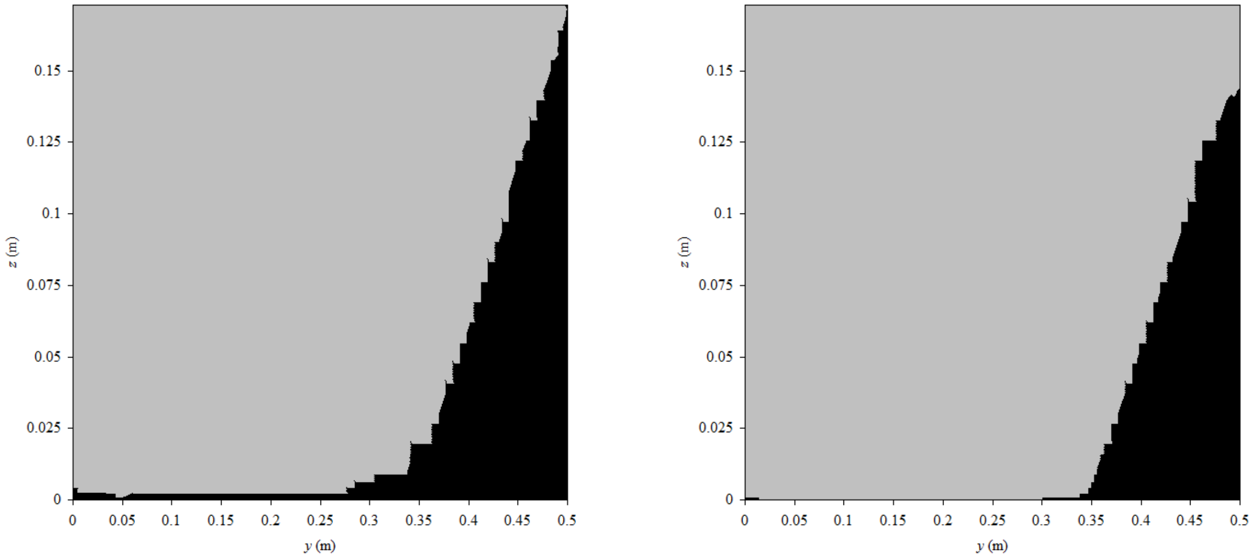

(a) $U/U_{mean} < 0.75$, $(x - x_b)/L_b = 0.05$ (b) $U/U_{mean} < 0.5$, $(x - x_b)/L_b = 0.05$

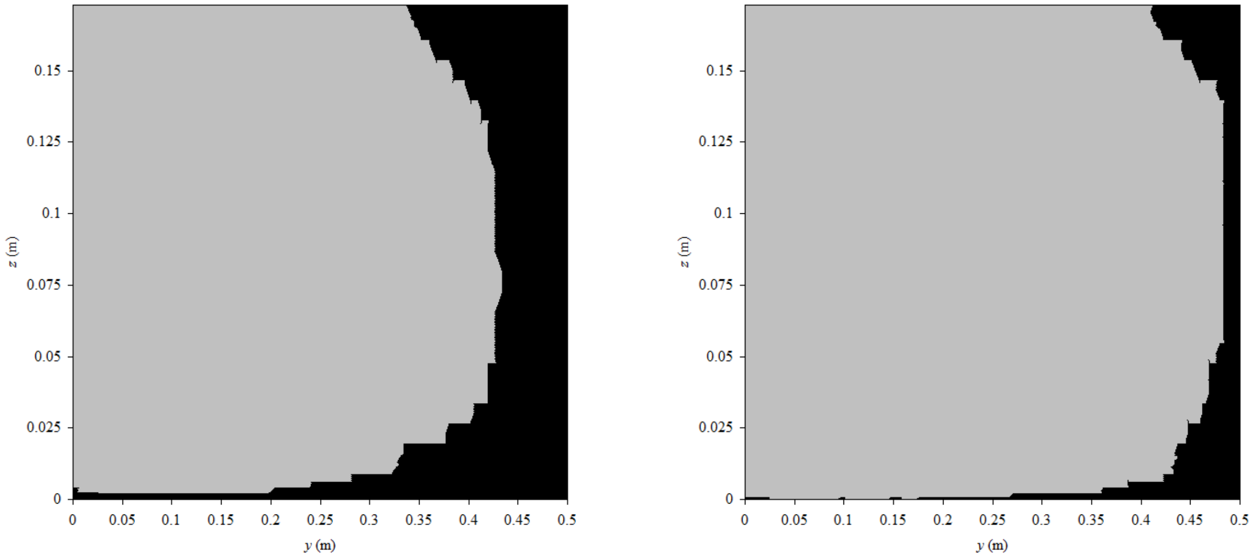

(c) $U/U_{mean} < 0.75$, $(x - x_b)/L_b = 0.765$ (d) $U/U_{mean} < 0.5$, $(x - x_b)/L_b = 0.765$

Figure C.5 – Low velocity regions in barrel with triangular baffles – Flow conditions: $Q = 55.6$ l/s, $h_b = 0.133$ m, $L_b = 0.67$ m, $\varnothing = 13$ mm hole.

C.2 DISCUSSION

The present investigation demonstrated the effects of various roughness configurations on the generation of LVZs. Both asymmetrical boundary roughness and small corner baffles are conducive to fish passage in distinguishing ways. Asymmetry and streamwise uniformity are identified as desirable geometric traits which benefit the generation of large, contiguous traversable zones (Fig. C.6). Figure C.6 presents three-dimensional zone plots of low-velocity zones (LVZs) for several boundary configurations. Corners, confluence of secondary flow cells and direct obstructions are highlighted as factors which help generate additional slow areas. The present observations may serve as guidelines for future optimisations of the geometric design of channels for improved fish passage.

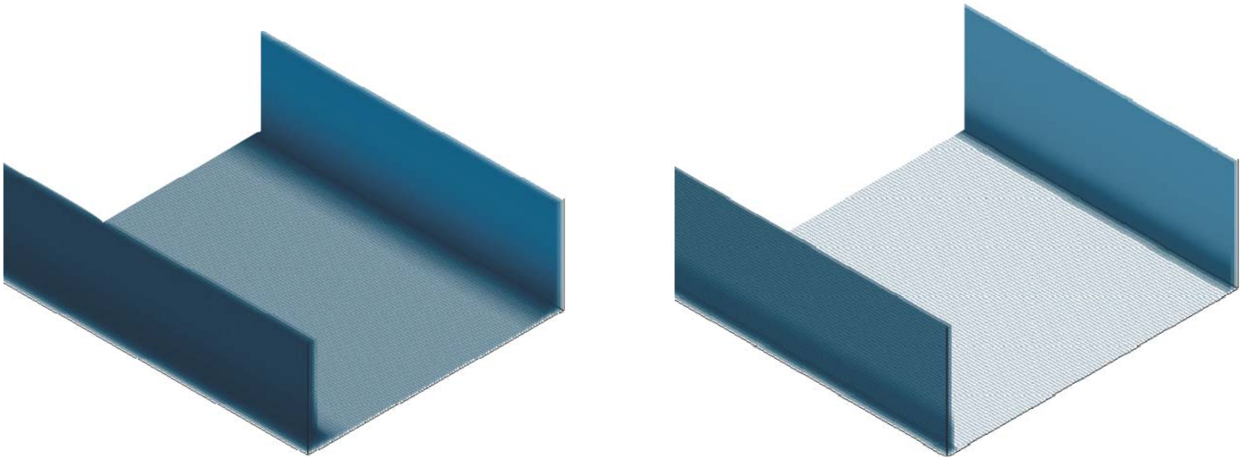

(a1) $U < 0.75U_{\text{mean}}$ (a2) $U < 0.5U_{\text{mean}}$

(a) Smooth barrel channel

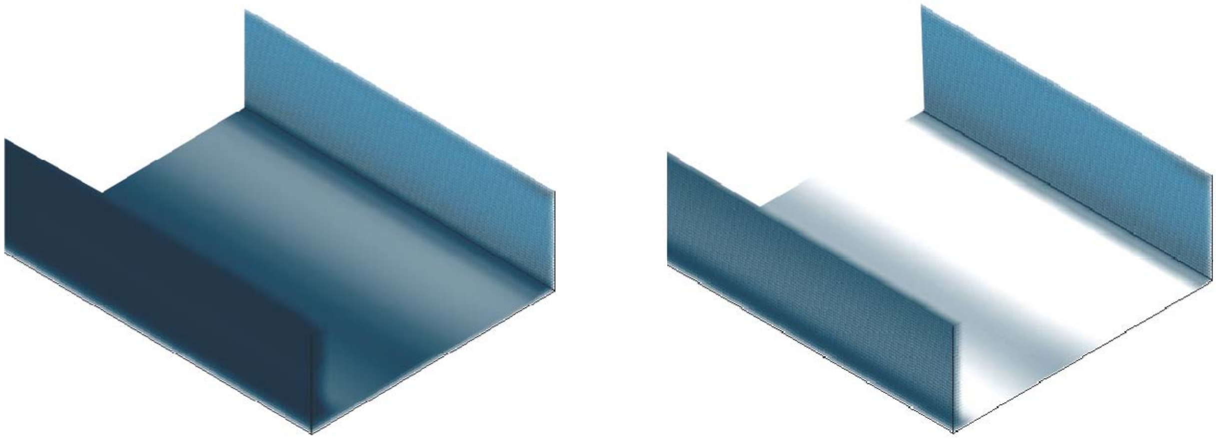

(b1) $U < 0.75U_{\text{mean}}$ (b2) $U < 0.5U_{\text{mean}}$

(b) Rough bed and rough sidewall channel

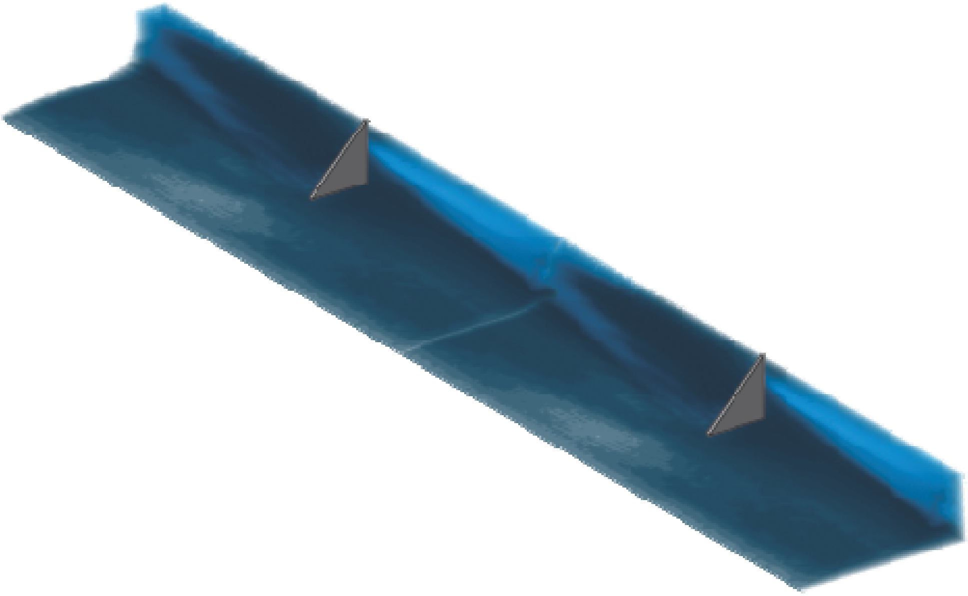

(c1) $U < 0.75U_{mean} - Q = 0.0261$ m^3/s, $h_b = 0.067$ m, $L_b = 0.67$ m

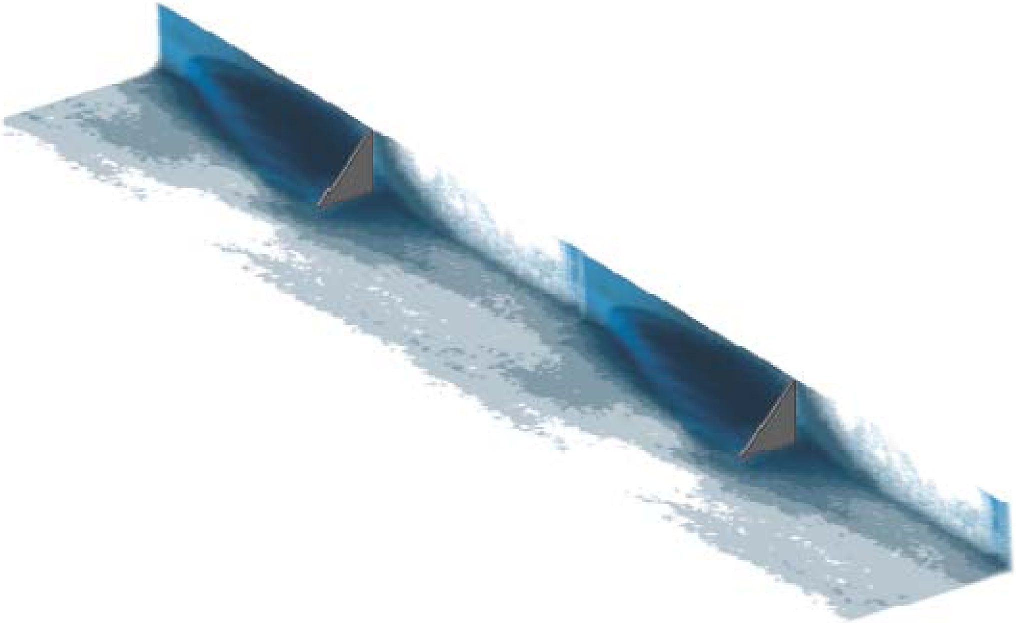

(c2) $U < 0.5U_{mean} - Q = 0.0261$ m^3/s, $h_b = 0.067$ m, $L_b = 0.67$ m

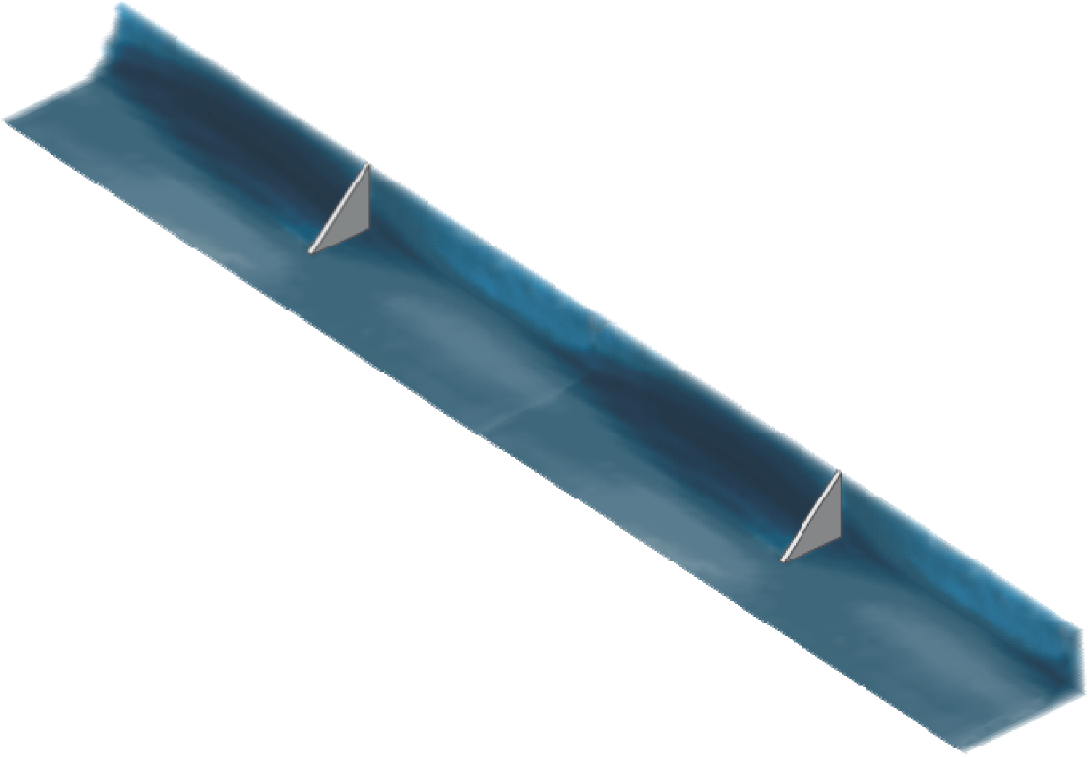

(c3) $U < 0.75U_{mean}$ – $Q = 0.0556$ m^3/s, $h_b = 0.067$ m, $L_b = 0.67$ m

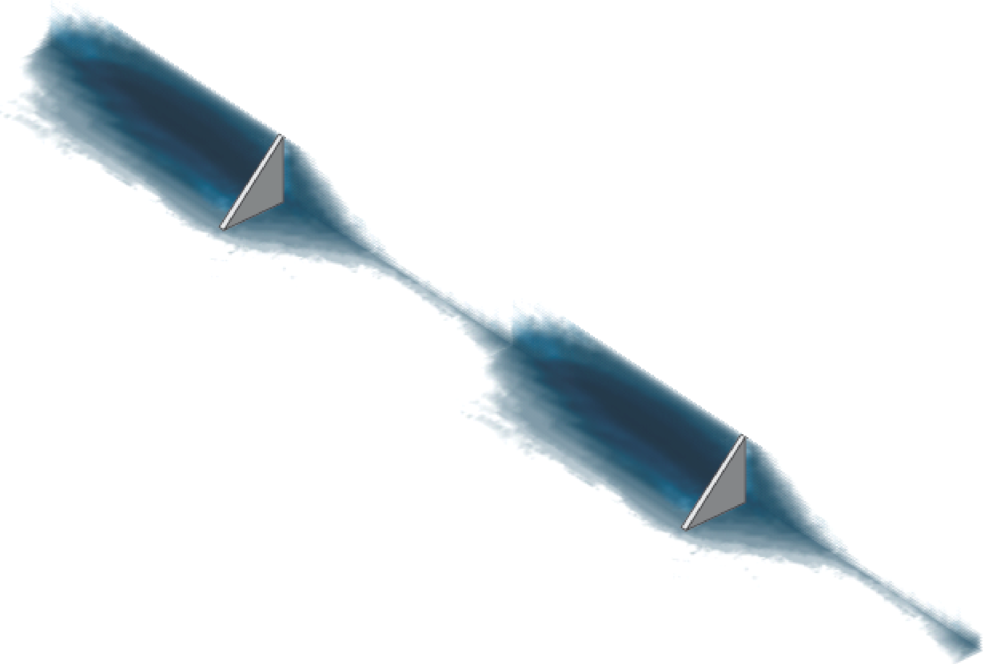

(c4) $U < 0.5U_{mean}$ – $Q = 0.0556$ m^3/s, $h_b = 0.067$ m, $L_b = 0.67$ m

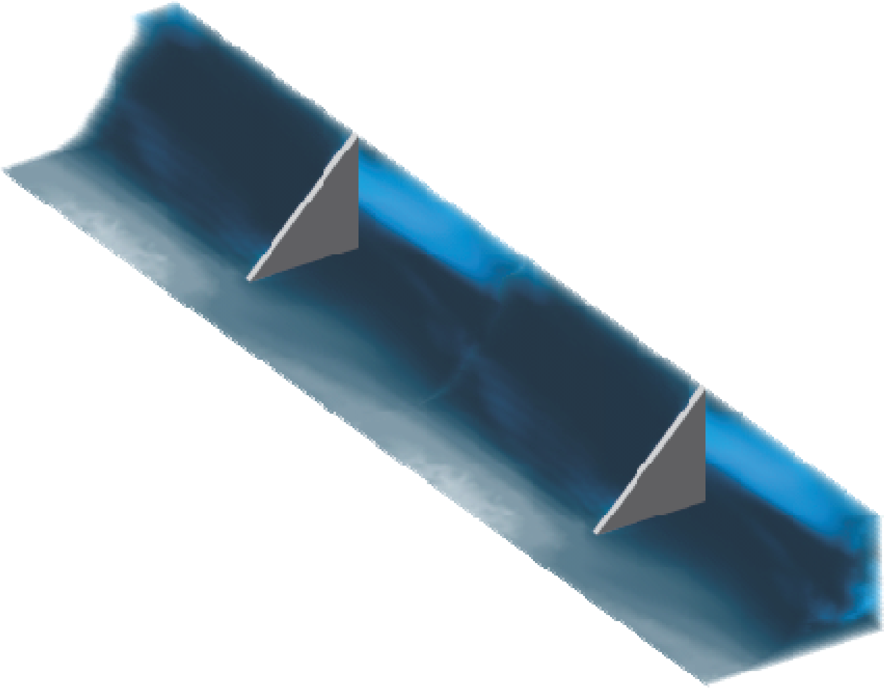

(c5) $U < 0.75U_{mean} - Q = 0.0556$ m^3/s, $h_b = 0.133$ m, $L_b = 0.67$ m

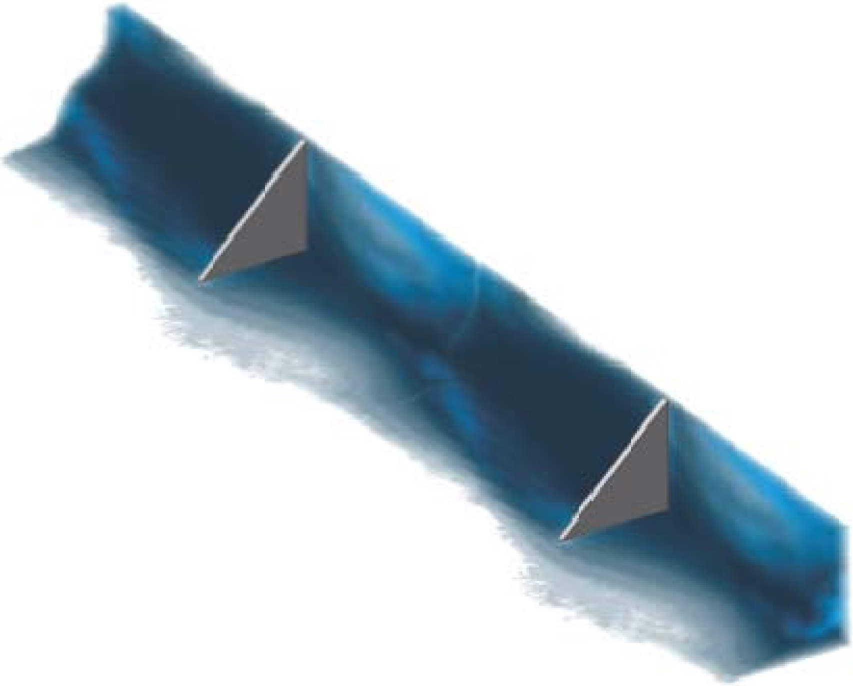

(c6) $U < 0.5U_{mean} - Q = 0.0556$ m^3/s, $h_b = 0.133$ m, $L_b = 0.67$ m

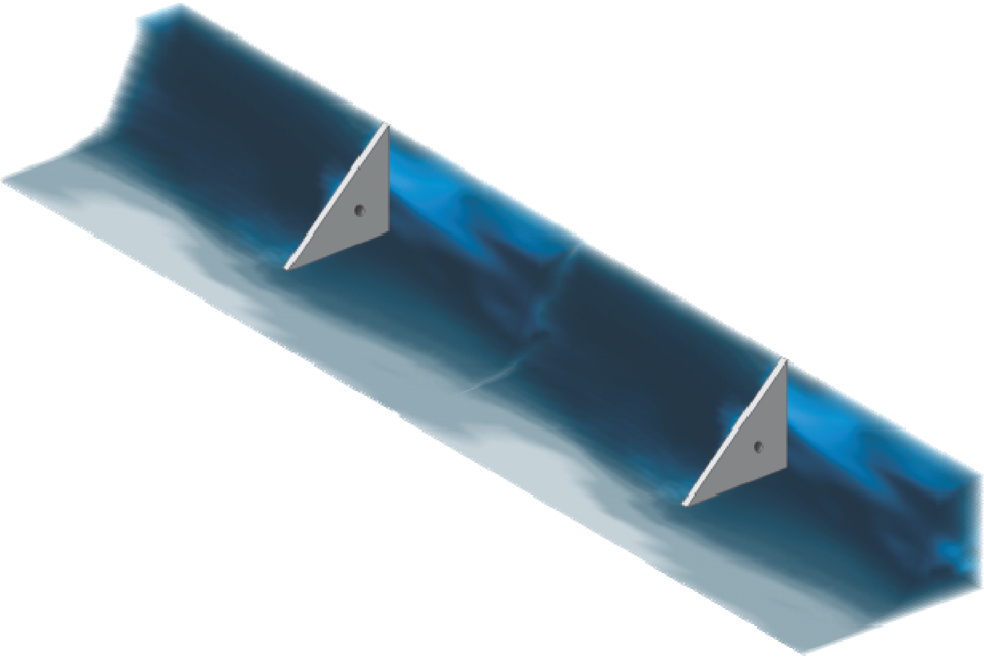

(c7) $U < 0.75U_{mean} - Q = 0.0556$ m^3/s, $h_b = 0.133$ m, $L_b = 0.67$ m, Ø 13 mm hole

(c8) $U < 0.5U_{mean} - Q = 0.0556$ m^3/s, $h_b = 0.133$ m, $L_b = 0.67$ m, Ø 13 mm hole

(c) Culvert barrel channel with triangular baffle configurations

Figure C.6 - Three-dimensional flow visualisation of low-velocity zones (LVZs) in box culvert channels: CFD modelling results - Flow direction is from bottom right to top left, passage ability increases with darker colour shades.

REFERENCES

ANSYS® Academic Research, Release 18.0, Help System, *ANSYS FLUENT User's Guide*, ANSYS, Inc.

Apelt, C.J., and Xie, Q. (2011). "Measurements of the Turbulent Velocity Field in a Non-Uniform Open Channel." Proc. 34th IAHR World Congress, Brisbane, Australia, 26 June-1 July, Engineers Australia Publication, Eric Valentine, Colin Apelt, James Ball, Hubert Chanson, Ron Cox, Rob Ettema, George Kuczera, Martin Lambert, Bruce Melville and Jane Sargison Editors, pp. 3338-3345 (ISBN 978-0-85825-868-6).

Baki, A.B., Zhu, D.Z., and Rajaratnam, N. (2014). "Mean flow characteristics in a rockramp-type fish pass." *Journal of Hydraulic Engineering*, ASCE, Vol. 140, No. 2, pp. 156-168.

Behlke, C.E., Kane, D.L., McLeen, R.F., and Travis, M.T. (1991). "Fundamentals of culvert design for passage of weak-swimming fish." *Report FHW A-AK-RD-90-10*, Department of Transportation and Public Facilities, State of Alaska, Fairbanks, USA, 178 pages.

Bresse, J.A. (1860). "Cours de Mécanique Appliquée Professé à l'Ecole des Ponts et Chaussées." ('Course in Applied Mechanics lectured at the Pont-et-Chaussées Engineering School.') *Mallet-Bachelier*, Paris, France (in French).

Cabonce, J., Fernando, R., Wang, H., and Chanson, H. (2017). "Using triangular baffles to facilitate upstream fish passage in box culverts: physical modelling." *Report 107/17*, School of Civil Engineering, The University of Queensland, Australia, 132 pages.

Cabonce, J., Wang, H., and Chanson, H. (2018). "Smart Baffles to Assist Upstream Culvert Passage of Small-Bodied Fish." *Proceedings of 7th IAHR International Symposium on Hydraulic Structures ISHS 2018*, Aachen, Germany, 15-18 May 2018, 11 pages.

Cassan, L., Tien, T.D., Courret, D., Laurens, P., and Dartus, D. (2014). "Hydraulic resistance of emergent macroroughness at large Froude numbers: design of nature-like fishpasses." *Journal of Hydraulic Engineering*, ASCE, Vol. 140, Paper 04014043, 9 pages.

Chanson, H. (2000). "Introducing originality and innovation in engineering teaching: the hydraulic design of culverts." *European Journal of Engineering Education*, Vol. 25, No. 4, pp. 377-391 (DOI: 10.1080/03043790050200421).

Chanson, H. (2004). "The hydraulics of open channel flow: an introduction." *Butterworth-Heinemann,* 2nd edition, Oxford, UK, 630 pages.

Chanson, H. (2009). "Applied Hydrodynamics: An Introduction to Ideal and Real Fluid Flows." *CRC Press*, Taylor & Francis Group, Leiden, The Netherlands, 478 pages (ISBN: 978-0-415-49271-3)

Chanson, H. (2014). "Applied Hydrodynamics: An Introduction." *CRC Press*, Taylor and Francis Group, Leiden, The Netherlands, 448 pages & 21 video movies (ISBN 978-1-138-00093-3).

Chanson, H., and Lubin, P. (2010). "Discussion of Verification and Validation of a Computational Fluid Dynamics (CFD) Model for Air Entrainment at Spillway Aerators." *Canadian Journal of Civil Engineering*, Vol. 37, No. 1, pp. 135-138 (DOI: 10.1139/L09-133)

Chanson, H., and Uys, W. (2016)."Baffle designs to facilitate fish passage in box culverts: a preliminary study." *Proceedings of 6th IAHR International Symposium on Hydraulic Structures*, Hydraulic Structures and Water System Management, B. Crookston and B. Tullis Editors, 27-30 June, Portland OR, USA, pp. 295-304 (DOI: 10.15142/T300628160828).

Chou, P. Y. (1945). "On velocity correlations and the solutions of the equations of turbulent fluctuation." *Quarterly of Applied Mathematics*, Vol. 3, No. 1, pp. 38-54.

Chow, V.T. (1959). "Open channel hydraulics." *McGraw-Hill*, New York, USA.

Cotel, A.J., Webb, P.W., and Trittico, H. (2006). "Do brown trout choose locations with reduced turbulence?" *Transactions of the American Fisheries Society*, Vol. 135, pp. 610-619.

Daly, B.J., and Harlow, F.H. (1970). "Transport equations in turbulence." *Physics of Fluids*, Vol. 13, pp. 2634-2649.

David, L., Calluaud, D., Pineau, G., and Texier, A. (2012). "Fishway hydrodynamics and global approaches for insuring the upstream migration around dams." *Proc. 4th IAHR International Symposium on Hydraulic Structures*, APRH - Associação Portuguesa dos Recursos Hídricos (Portuguese Water Resources Association), J. Matos, S. Pagliara and I. Meireles Eds., 9-11 February 2012, Porto, Portugal, Paper 4, 15 pages (CD-ROM).

Duguay, J., and Lacey, R.W.J. (2014). "Effect of fish baffles on the hydraulic roughness of slip-lined culverts." *Journal of Hydraulic Engineering*, ASCE, Vol. 141, No. 1, Paper 04014065, 10 pages (DOI: 10.1061/(ASCE)HY.1943-7900.0000942).

Fairfull, S., and Witheridge, G. (2003). "Why do fish need to cross the road? Fish passage requirements for waterway crossings." *NSW Fisheries*, Cronulla NSW, Australia, 14 pages.

Feurich, R., Boubee, J., and Olsen, N.R.B. (2012). "Improvement of fish passage in culverts using CFD." *Ecological Engineering*, Vol. 47, pp. 1-8.

Fu, S., Launder, B.E., and Leshziner M.A. (1987). "Modelling strongly swirling recirculating jet flow with Reynolds-stress transport closures." *Proc. 6th Symposium on Turbulent Shear Flows*, Toulouse, France.

Gibson, M.M., and Launder, B.E. (1978). "Ground effects on pressure fluctuations in the atmospheric boundary layer." *Journal of Fluid Mechanics*, Vol. 86, pp. 491-511.

Heaslip, B.M. (2015). "Substrate roughening improves swimming performance of two small bodied riverine fish species: implications for culvert design." *Honours Thesis*, School of Biological Sciences, The University of Queensland, Brisbane, Australia, 32 pages.

Hinze, J.O. (1959). "Turbulence." *McGraw-Hill Publ.*, 1st Edition, New York, USA.

Hinze, J.O. (1967). "Secondary Currents in Wall Turbulence." *Physics of Fluids*, Supplement, pp. 122-125.

Hirt, C., and Nichols, B. (1981). "Volume of Fluid (VOF) method for the dynamics of free boundaries." *Journal of Computational Physics*, Vol. 39, No. 1, pp. 201-225.

Hotchkiss, R. (2002). "Turbulence investigation and reproduction for assisting downstream migrating juvenile salmonids, Part I." *BPA Report DOE/BP-00004633-I*, Bonneville Power Administration, Portland, Oregon, 138 pages.

Hunt, M., Clark, S., and Tkach, R. (2012). "Velocity distributions near the inlet of corrugated steep pipe culverts." *Canadian Journal of Civil Engineering*, Vol. 39, pp. 1243-1251.

Hurst, T.P., Kay, B.H., Ryan, P.A., and Brown, M.D. (2007). "Sublethal Effects of Mosquito Larvicides on Swimming Performance of Larvivorous Fish *Melanotaenia duboulayi* (Atheriniformes: Melanotaeniidae)." *Ecotoxicology*, Vol. 100, No. 1, pp. 61-65.

Johnson, M.F., and Rice, S.P. (2014). "Animal perception in gravel-bed rivers: scales of sensing and environmental controls on sensory information." *Canadian Journal of Fisheries and Aquatic Sciences*, Vol. 71, pp. 945-057.

Lacey, R.W.J., and Rennie, C.D. (2012). "Laboratory investigation of turbulent flow structure around a bed-mounted cube at multiple flow stages." *Journal of Hydraulic Engineering*, ASCE, Vol. 138, No. 1, pp. 71-84.

Larinier, M. (2002). "Fish passage through culverts, rock weirs and estuarine obstructions." *Bulletin Français de Pêche et Pisciculture*, Vol. 364, No. 18, pp. 119-134.

Launder, B.E. (1989). "Second-moment closure and its use in modelling turbulent industrial flows." *International Journal for Numerical Methods in Fluids*, Vol. 9, pp. 963-985.

Launder, B.E., and Spalding, D.B. (1972). "Lectures in mathematical models of turbulence." Academic Press, London, England.

Launder, B.E., and Spalding, D.B. (1974). "The numerical computation of turbulent flows." *Computer Methods in Applied Mechanics and Engineering*, Vol. 3, pp. 269-289.

Leonard, A. (1974). "Energy cascade in large eddy simulation of turbulent fluid flows" *Advances in Geophysics*, Vol. 18A, pp. 561-583.

Leonard, B.P. (1991). "The ULTIMATE conservative difference scheme applied to unsteady one-dimensional advection." *Computer Methods in Applied Mechanics and Engineering*, Vol. 88, pp. 17-74.

Lien, F. S., and Leschziner, M.A. (1994). "Assessment of turbulent transport models including non-linear RNG eddy-viscosity formulation and second-moment closure." *Computers and Fluids*, Vol. 23, No. 8, pp. 983-1004.

Liggett, J.A. (1994). "Fluid mechanics." McGraw-Hill, New York, USA.

Lupandin, A.I. (2005). "Effect of flow turbulence on swimming speed of fish." *Biology Bulletin*, Vol. 32, No. 5, pp. 461-466.

Montes, J.S. (1998). "Hydraulics of open channel flow." *ASCE Press*, New-York, USA, 697 pages.

Nezu, I. (1977). "Turbulent structures in open-channel flows." *Ph.D. Thesis*, Kyoto University., Japan.

Nezu, I. (1985). "Experimental study on secondary currents in open-channel flow." *In 21st Congress of IAHR*, Melbourne, Australia, Vol. 2, pp. 114-119.

Nezu, I. (2005). "Open-channel flow turbulence and its research prospect in the 21st century." *Journal of Hydraulic Engineering*, Vol. 131, No. 4, pp. 229-246.

Nezu, I., and Rodi, W. (1986). "Open-Channel Flow Measurements with a Laser Doppler Anemometer." *Journal of Hydraulic Engineering*, ASCE, Vol. 112, No. 5, pp. 335-355.

Nezu, I., Nakagawa, H., and Jirka, G. H. (1994). "Turbulence in open-channel flows." *Journal of Hydraulic Engineering*, Vol. 120, No. 10, pp. 1235-1237.

Nikora, V., Aberle, J., Biggs, B., Jowett, I., and Sykes, J. (2003). "Effects of fish size, time-to-fatigue and turbulence on swimming performance: a case study of Galaxias maculatus." *Journal of Fish Biology*, Vol. 63, pp. 1365-1382.

Olsen, A. and Tullis, B. (2013). "Laboratory study of fish passage and discharge capacity in slip-lined, baffled culverts." *Journal of Hydraulic Engineering*, ASCE, Vol. 139, No. 4, pp. 424–432.

Papanicolaou, A.N. and Talebbeydokhti, N. (2002). Discussion of "Turbulent open-channel flow in circular corrugated culverts." *Journal of Hydraulic Engineering*, Vol. 128, No. 5, pp. 424-432.

Patankar, S.V., and Spalding, D.B. (1972). "A calculation procedure for heat, mass and momentum transfer in three-dimensional parabolic flows." *International Journal of Heat and Mass Transfer*, Vol. 15, No. 10, pp. 1787-1806.

Pavlov, D.S., Lupandin, I.A., and Skorobogatov, M.A. (2000). "The effects of flow turbulence on the behaviour and distribution of fish." *Journal of Ichthyol*, Vol. 40, pp. S232-S261.

Pope, S.B. (2000). "Turbulent Flows." *Cambridge University Press*, 771 pages.

Rizzi, A., and Vos, J. (1998). "Toward Establishing Credibility in Computational Fluid Dynamics Simulations." *AIAA Journal*, Vol. 36, No. 5, pp. 668-675.

Roache, R.L. (1998a). "Verification of Codes and Calculations." *AIAA Journal*, Vol. 36, No. 5, pp. 696-702.

Roache, R.L. (1998b). "Verification and Validation in Computational Science and Engineering." *Hermosa Publishers*, Albuquerque NM, USA, 446 pages.

Roache, R.L. (1998). "Verification of Codes and Calculations." *AIAA Journal*, Vol. 36, No. 5, pp. 696-702.

Roache, P.J. (2009). "Perspective: Validation - What does it mean?" *Journal of Fluids Engineering*, ASME, Vol. 131, March, Paper 034503, 4 pages.

Rodgers, E.M., Cramp, R.L., Gordos, M., Weier, A., Fairfull, S., Riches, M., and Franklin, C.E. (2014). "Facilitating upstream passage of small-bodied fishes: linking the thermal dependence of swimming ability to culvert design." *Marine and Freshwater Research*, Vol. 65, pp. 710-719 (DOI: 10.1071/MF13170).

Rodi, W., Constantinescu, G., and Stoesser, T. (2013). "Large-Eddy Simulation in Hydraulics," *IAHR Monograph*, CRC Press, Taylor & Francis Group, Leiden, The Netherlands, 252 pages.

Rotta, J. C. (1951). "Statistische theorie nichthomogener turbulenz." *Zeitschrift für physic*, Vol. 129, No. 6, pp. 547-572 (in German).

Pope, S.B., (2000). "Turbulent flows." *Cambridge University Press.*

Schlichting, H. (1979). "Boundary layer theory." *McGraw-Hill*, New York, USA, 7th edition.

Shur, M.L., Spalart, P. R., Strelets, M. K., and Travin, A. K. (2008). "A hybrid RANS-LES approach with delayed-DES and wall-modelled LES capabilities". *International Journal of Heat and Fluid Flow*, Vol. 29, No. 6, pp. 1638-1649.

Tarrade, L., Manceau, R., Texier, A., David, L., and Larinier, M. (2005). "Etude numérique des écoulements hydrodynamiques turbulents dans une passe à poisons." *Proc. 17ème Congrès Français de Mécanique*, Troyes, France (in French).

Tracy, H. J. (1965). "Turbulent flow in a three-dimensional channel." *Journal of Hydraulic Engineering*, Vol. 91, No. 6, pp. 9–35.

Xie, Q. (1998). "Turbulent flows in non-uniform open channels: experimental measurements and numerical modelling." *Ph.D. Thesis*, Dept. of Civil Eng., University Of Queensland, Australia, 339 pages.

Wang, R.W., David, L., and Larinier, M. (2010). "Contribution of experimental fluid mechanics to the design of vertical slot fish passes." *Knowledge and Management of Aquatic Ecosystems,* Vol. 396, No. 2, 21 pages.

Wang, H., Beckingham, L.K., Johnson, C.Z., Kiri, U.R., and Chanson, H. (2016a). "Interactions between large boundary roughness and high inflow turbulence in open channel: a physical study into turbulence properties to enhance upstream fish migration." *Hydraulic Model Report No. CH103/16*, School of Civil Engineering, The University of Queensland, Brisbane, Australia, 74 pages (ISBN 978-1-74272-156-9).

Wang, H., Chanson, H., Kern, P., and Franklin, C. (2016b). "Culvert hydrodynamics to enhance upstream fish passage: fish response to turbulence." *Proceedings of 20th Australasian Fluid Mechanics Conference*, Perth WA, Australia, 5-8 December, Paper 682, 4 pages.

Wang, H., and Chanson, H. (2017). "Baffle Systems to Facilitate Upstream Fish Passage in Standard Box Culverts: How About Fish-Turbulence Interplay?" *Proceedings of 37th IAHR World Congress*, IAHR & USAINS Holding Sdn. Bhd. Publ., Editors Aminuddin Ab. Ghani, Ngai Weng Chan, Junaidah Ariffin, Ahmad Khairi Abd Wahab, Sobri Harun, Amir Hashim Mohamad Kassim and Othman Karim, Kuala Lumpur, Malaysia, 13-18 August, Vol. 3, Theme 3.1, pp. 2586-2595

Wang, H., and Chanson, H. (2018). "On Upstream Fish Passage in Standard Box Culverts: Interactions between Fish and Turbulence." *Journal of Ecohydraulics*, IAHR (DOI: 10.1080/24705357.2018.1440183) (ISSN 2470-5357 [Print] 2470-5365 [Online]). (In Print).

Yang, S. Q., Tan, S. K., and Wang, X. K. (2012). "Mechanism of secondary currents in open channel flows." *Journal of Geophysical Research: Earth Surface*, Vol. 117, No. F4 (DOI: 10.1029/2012JF002510).

Bibliography

Bradshaw, P. (1971). "An Introduction to Turbulence and its Measurement." *Pergamon Press*, Oxford, UK, The Commonwealth and International Library of Science and technology Engineering and Liberal Studies, Thermodynamics and Fluid Mechanics Division, 218 pages.

Bradshaw, P. (1976). "Turbulence." *Springer-Verlag*, Topics in Applied Physics, Vol. 12, Berlin, Germany, 335 pages.

Bradshaw, P., and Gregory, N. (1961). "The Determination of Local Turbulent Skin Friction from Observations in the Viscous Sub-Layer." *Aeronautical Research Council Technical Report No. 3202*, Ministry of Aviation, UK, 19 pages.

Bradshaw, P., Cebeci, T., and Whitelaw, J.H. (1981). "Engineering Calculation Methods for Turbulent Flow." *Academic Press*, London, UK, 331 pages.

Cabonce, J., Fernando, R., Wang, H., and Chanson, H. (2017). "Culvert Baffles to Facilitate Upstream Fish Passage." *Proceedings of 13th Hydraulics in Water Engineering Conference HIWE2017*, Engineers Australia, Sydney, 13-16 November, 9 pages (ISBN 978-1-925627-03-9).

Biswas, R., Strawn, R.C. (1998). "Tetrahedral and hexahedral mesh adaptation for CFD problems." *Elsevier Applied Numerical Math*, Vol. 26, No. 1, pp. 135-151.

Hirsch, C. (2007). "Numerical computation of internal and external flows: the fundamentals of Computational Fluid Dynamics." *Butterworth-Heinemann*, 2nd edition, 680 pages.

Nezu, I., and Rodi, W. (1985). "Experimental Study on Secondary Currents in Open Channel Flow." *Proceedings 21st IAHR Biennial Congress*, Melbourne, Australia, pp. 114-119.

Nezu. I., Tominaga, A., and Nakagawa, H. (1993). "Field Measurements of Secondary Currents in Straight Rivers." *Journal of Hydraulic Engineering*, ASCE, Vol. 119, No. 5, pp. 598-614 (DOI: 10.1061/(ASCE)0733-9429(1993)119:5(598)).

Rodi, W. (2017). "Turbulence Modeling and Simulation in Hydraulics: A Historical Review." *Journal of Hydraulic Engineering*, ASCE, Vol. 143, No. 5, Paper 03117001, 20 pages (DOI: 10.1061/(ASCE)HY.1943-7900.0001288).

Tennekes, H., and Lumley, J.L. (1972). "A First Course in Turbulence." *MIT Press*, Cambridge MA, USA, 300 pages.

Wang, H., and Chanson, H. (2017). "How a better understanding of Fish-Hydrodynamics Interactions might enhance upstream fish passage in culverts." *Research Report No. CE162*, School of Civil Engineering, The University of Queensland, Brisbane, Australia, 43 pages (ISBN 978-1-74272-192-7).

Wang, H., and Chanson, H. (2018). "Modelling Upstream Fish Passage in Standard Box Culverts: Interplay between Turbulence, Fish Kinematics, and Energetics." *River Research and Applications*, Vol. 34, No. 3, pp.244-252 (DOI: 10.1002/rra.3245) (ISSN 1535-1467).

Wang, H., Uys, W., and Chanson, H. (2018). "Alternative Mitigation Measures for Fish Passage in Standard Box Culverts: Physical Modelling." *Journal of Hydro-environment Research*, IAHR, Vol. xx (DOI: 10.1016/j.jher.2017.03.001) (ISSN 1570-6443). (In Print)

Internet bibliography

Upstream fish passage in box culverts: how do fish and turbulence interplay?	{http://staff.civil.uq.edu.au/h.chanson/fish_culvert.html}

YouTube video movie

Fish-friendly waterways and culverts - Integration of hydrodynamics and fish turbulence interplay & interaction	{https://youtu.be/GGWTWDOmoSQ}

Open Access Repositories

OAIster	{http://www.oclc.org/en/oaister.html}
UQeSpace	{http://espace.library.uq.edu.au/}

Bibliographic reference of the Report CH111/18

The Hydraulic Model research report series CH is a refereed publication published by the School of Civil Engineering at the University of Queensland, Brisbane, Australia.

The bibliographic reference of the present report is:

ZHANG, G., and CHANSON, H. (2018). "Numerical Investigations of Box Culvert Hydrodynamics with Smooth, Unequally Roughened and Baffled Barrels to Enhance Upstream Fish Passage." *Hydraulic Model Report No. CH111/18*, School of Civil Engineering, The University of Queensland, Brisbane, Australia, 129 pages (ISBN 978-1-74272-197-2).

HYDRAULIC MODEL RESEARCH REPORT CH

The Hydraulic Model Report CH series is published by the School of Civil Engineering at the University of Queensland. Orders of any reprint(s) of the Hydraulic Model Reports should be addressed to the School Secretary.

School Secretary, School of Civil Engineering, The University of Queensland
Brisbane 4072, Australia - Tel.: (61 7) 3365 3619 - Fax: (61 7) 3365 4599
Url: http://http://www.civil.uq.edu.au// Email: enquiries@civil.uq.edu.au

Report CH	**Unit price**	Quantity	**Total price**
ZHANG, G., and CHANSON, H. (2018). "Numerical Investigations of Box Culvert Hydrodynamics with Smooth, Unequally Roughened and Baffled Barrels to Enhance Upstream Fish Passage." *Hydraulic Model Report No. CH111/18*, School of Civil Engineering, The University of Queensland, Brisbane, Australia, 129 pages (ISBN 978-1-74272-197-2).	AUD$60.00		
KIRI, U., LENG, X., and CHANSON, H. (2018). "Positive Surge Propagation in a Non-Rectangular Asymmetrical Channel." *Hydraulic Model Report No. CH110/18*, School of Civil Engineering, The University of Queensland, Brisbane, Australia (ISBN 978-1-74272-196-5).	AUD$60.00		
LENG, X., and CHANSON, H. (2018). "Two-phase Flow Characteristics of a Breaking Tidal Bore Roller: Microscopic Properties." *Hydraulic Model Report No. CH110/18*, School of Civil Engineering, The University of Queensland, Brisbane, Australia pages (ISBN 978-1-74272-195-8).	AUD$60.00		
REUNGOAT, D., LENG, X., and CHANSON, H. (2017). "Suspended Sediment Processes in the Garonne River Tidal Bore: Arcins Channel on 14-15 November 2016." *Hydraulic Model Report No. CH108/17*, School of Civil Engineering, The University of Queensland, Brisbane, Australia, 166 pages (ISBN 978-1-74272-187-3).	AUD$60.00		
CABONCE, J., FERNANDO, R., WANG, H., and CHANSON, H. (2017). "Using Triangular Baffles to Facilitate Upstream Fish Passage in Box Culverts: Physical Modelling." *Hydraulic Model Report No. CH107/17*, School of Civil Engineering, The University of Queensland, Brisbane, Australia, 130 pages (ISBN 978-1-74272-186-6).	AUD$60.00		
LENG, X., and CHANSON, H. (2018). "Simultaneous Velocity Profiling in Unsteady Turbulent Flows Using an Array of Two Vectrino Profilers." *Hydraulic Model Report No. CH106/17*, School of Civil Engineering, The University of Queensland, Brisbane, Australia, 118 pages (ISBN 978-1-74272-183-5).	AUD$60.00		
ZHANG, G., CHANSON, H. (2017). "Application of Local Optical Flow Methods to High-Velocity Air-Water Flows: Validation and Application to Skimming Flows on Stepped Chutes." *Hydraulic Model Report No. CH105/17*, School of Civil Engineering, The University of Queensland, Brisbane, Australia, 59 pages (ISBN 978-1-74272-182-8).	AUD$60.00		
BERTOLA, N.J., WANG, H., and CHANSON, H. (2017). "Air Bubble Entrainment at Vertical Plunging Jets: a Large-Scale Experimental Study." *Hydraulic Model Report No. CH104/17*, School of Civil Engineering, The University of Queensland, Brisbane, Australia, 256 pages (ISBN 978-1-74272-181-1).	AUD$60.00		

WANG, H., BECKINGHAM, L.K., JOHNSON, C.Z., KIRI, U.R., and CHANSON, H. (2016). "Interactions between Large Boundary Roughness and High Inflow Turbulence in Open channel: a Physical Study into Turbulence Properties to Enhance Upstream Fish Migration." Hydraulic Model Report No. CH103/16, School of Civil Engineering, The University of Queensland, Brisbane, Australia, 74 pages (ISBN 978-1-74272-156-9).	AUD$60.00		
REUNGOAT, D., LENG, X., and CHANSON, H. (2016). "Hydrodynamic and Sedimentary Processes of Tidal Bores: Arcins Channel, Garonne River in August-September-October 2015." *Hydraulic Model Report No. CH102/16*, School of Civil Engineering, The University of Queensland, Brisbane, Australia, 270 pages (ISBN 978-1-74272-155-2).	AUD$60.00		
LENG, X., and CHANSON, H. (2016). "Unsteady Turbulent Velocity Profiling in Open Channel Flows and Tidal Bores using a Vectrino Profiler." *Hydraulic Model Report No. CH101/15*, School of Civil Engineering, The University of Queensland, Brisbane, Australia, 118 pages (ISBN 978-1-74272-145-3).	AUD$60.00		
WANG, H., and CHANSON, H. (2016). "Velocity Field in Hydraulic Jumps at Large Reynolds Numbers: Development of an Array of Two Dual-Tip Phase-detection Probes." *Hydraulic Model Report No. CH100/15*, School of Civil Engineering, The University of Queensland, Brisbane, Australia, 77 pages (ISBN 978 1 74272 143 9).	AUD$60.00		
SUARA. K., BROWN, R., and CHANSON, H. (2015). "Turbulence and Mixing in the Environment: Multi-Device Study in a Sub-tropical Estuary." *Hydraulic Model Report No. CH99/15*, School of Civil Engineering, The University of Queensland, Brisbane, Australia, 167 pages (ISBN 978 1 74272 138 5).	AUD$60.00		
LENG, X., and CHANSON, H. (2015). "Unsteady Turbulence during the Upstream Propagation of Undular and Breaking Tidal Bores: an Experimental Investigation." *Hydraulic Model Report No. CH98/15*, School of Civil Engineering, The University of Queensland, Brisbane, Australia, 235 pages & 4 video movies (ISBN 978 1 74272 135 4).	AUD$60.00		
ZHANG, G., and CHANSON, H. (2015). "Hydraulics of the Developing Flow Region of Stepped Cascades: an Experimental Investigation." *Hydraulic Model Report No. CH97/15*, School of Civil Engineering, The University of Queensland, Brisbane, Australia, 76 pages (ISBN 978 1 74272 134 7).	AUD$60.00		
LENG, X., and CHANSON, H. (2014). "Turbulent Advances of Breaking Bores: Experimental Observations." *Hydraulic Model Report No. CH96/14*, School of Civil Engineering, The University of Queensland, Brisbane, Australia, 40 pages (ISBN 978 1 74272 130 9).	AUD$40.00		
WANG, H, MURZYN, F., and D., CHANSON, H. (2014). "Pressure, Turbulence and Two-Phase Flow Measurements in Hydraulic Jumps." Hydraulic Model Report No. CH95/14, School of Civil Engineering, The University of Queensland, Brisbane, Australia, 154 pages (ISBN 9781742720616978174272 1064).	AUD$60.00		
REUNGOAT, D., CHANSON, H., and KEEVIL, C. (2014). "Turbulence, Sedimentary Processes and Tidal Bore Collision in the Arcins Channel, Garonne River (October 2013)." *Hydraulic Model Report No. CH94/14* School of Civil Engineering, The University of Queensland, Brisbane, Australia, 145 pages (ISBN 9781742721033).	AUD$60.00		
LENG, X., and CHANSON, H. (2014). "Propagation of Negative Surges in Rivers and Estuaries: Unsteady Turbulent Mixing including the Effects of Bed Roughness." *Hydraulic Model Report No. CH93/13*, School of Civil Engineering, The University of Queensland, Brisbane, Australia, 108 pages (ISBN 9781742720944).	AUD$60.00		

WUTHRICH, D., and CHANSON, H. (2014). "Aeration and Energy Dissipation over Stepped Gabion Spillways: a Physical Study." *Hydraulic Model Report No. CH92/13*, School of Civil Engineering, The University of Queensland, Brisbane, Australia, 171 pages and 5 video movies (ISBN 9781742720944).	AUD$60.00		
WANG, H., and CHANSON, H. (2013). "Free-Surface Deformation and Two-Phase Flow Measurements in Hydraulic Jumps". *Hydraulic Model Report No. CH91/13*, School of Civil Engineering, The University of Queensland, Brisbane, Australia, 108 pages (ISBN 9781742720746).	AUD$60.00		
SIMON, B., and CHANSON, H. (2013). "Turbulence Measurements in Tidal Bore-like Positive Surges over a Rough Bed". *Hydraulic Model Report No. CH90/12*, School of Civil Engineering, The University of Queensland, Brisbane, Australia, 176 pages (ISBN 9781742720685).	AUD$60.00		
REUNGOAT, D., CHANSON, H., and CAPLAIN, B. (2012). "Field Measurements in the Tidal Bore of the Garonne River at Arcins (June 2012)." Hydraulic Model Report No. CH89/12, School of Civil Engineering, The University of Queensland, Brisbane, Australia, 121 pages (ISBN 9781742720616).	AUD$60.00		
CHANSON, H., and WANG, H. (2012). "Unsteady Discharge Calibration of a Large V-Notch Weir." *Hydraulic Model Report No. CH88/12*, School of Civil Engineering, The University of Queensland, Brisbane, Australia, 50 pages & 4 movies (ISBN 9781742720579).	AUD$60.00		
FELDER, S., FROMM, C., and CHANSON, H. (2012). "Air Entrainment and Energy Dissipation on a 8.9° Slope Stepped Spillway with Flat and Pooled Steps." *Hydraulic Model Report No. CH86/12*, School of Civil Engineering, The University of Queensland, Brisbane, Australia, 82 pages (ISBN 9781742720531).	AUD$60.00		
FELDER, S., and CHANSON, H. (2012). "Air-Water Flow Measurements in Instationary Free-Surface Flows: a Triple Decomposition Technique." *Hydraulic Model Report No. CH85/12*, School of Civil Engineering, The University of Queensland, Brisbane, Australia, 161 pages (ISBN 9781742720494).	AUD$60.00		
REICHSTETTER, M., and CHANSON, H. (2011). "Physical and Numerical Modelling of Negative Surges in Open Channels." *Hydraulic Model Report No. CH84/11*, School of Civil Engineering, The University of Queensland, Brisbane, Australia, 82 pages (ISBN 9781742720388).	AUD$60.00		
BROWN, R., CHANSON, H., McINTOSH, D., and MADHANI, J. (2011). "Turbulent Velocity and Suspended Sediment Concentration Measurements in an Urban Environment of the Brisbane River Flood Plain at Gardens Point on 12-13 January 2011." *Hydraulic Model Report No. CH83/11*, School of Civil Engineering, The University of Queensland, Brisbane, Australia, 120 pages (ISBN 9781742720272).	AUD$60.00		
CHANSON, H. "The 2010-2011 Floods in Queensland (Australia): Photographic Observations, Comments and Personal Experience." *Hydraulic Model Report No. CH82/11*, School of Civil Engineering, The University of Queensland, Brisbane, Australia, 127 pages (ISBN 9781742720234).	AUD$60.00		
MOUAZE, D., CHANSON, H., and SIMON, B. (2010). "Field Measurements in the Tidal Bore of the Sélune River in the Bay of Mont Saint Michel (September 2010)." *Hydraulic Model Report No. CH81/10*, School of Civil Engineering, The University of Queensland, Brisbane, Australia, 72 pages (ISBN 9781742720210).	AUD$60.00		
JANSSEN, R., and CHANSON, H. (2010). "Hydraulic Structures: Useful Water Harvesting Systems or Relics." *Proceedings of the Third International Junior Researcher and Engineer Workshop on Hydraulic Structures (IJREWHS'10)*, 2-3 May 2010, Edinburgh, Scotland, R. JANSSEN and H. CHANSON (Eds), Hydraulic Model Report CH80/10, School of Civil Engineering, The University of Queensland, Brisbane, Australia, 211 pages (ISBN 9781742720159).	AUD$60.00		

CHANSON, H., LUBIN, P., SIMON, B., and REUNGOAT, D. (2010). "Turbulence and Sediment Processes in the Tidal Bore of the Garonne River: First Observations." *Hydraulic Model Report No. CH79/10*, School of Civil Engineering, The University of Queensland, Brisbane, Australia, 97 pages (ISBN 9781742720104).	AUD$60.00		
CHACHEREAU, Y., and CHANSON, H., (2010). "Free-Surface Turbulent Fluctuations and Air-Water Flow Measurements in Hydraulics Jumps with Small Inflow Froude Numbers." *Hydraulic Model Report No. CH78/10*, School of Civil Engineering, The University of Queensland, Brisbane, Australia, 133 pages (ISBN 9781742720036).	AUD$60.00		
CHANSON, H., BROWN, R., and TREVETHAN, M. (2010). " Turbulence Measurements in a Small Subtropical Estuary under King Tide Conditions." *Hydraulic Model Report No. CH77/10*, School of Civil Engineering, The University of Queensland, Brisbane, Australia, 82 pages (ISBN 9781864999969).	AUD$60.00		
DOCHERTY, N.J., and CHANSON, H. (2010). "Characterisation of Unsteady Turbulence in Breaking Tidal Bores including the Effects of Bed Roughness." *Hydraulic Model Report No. CH76/10*, School of Civil Engineering, The University of Queensland, Brisbane, Australia, 112 pages (ISBN 9781864999884).	AUD$60.00		
CHANSON, H. (2009). "Advective Diffusion of Air Bubbles in Hydraulic Jumps with Large Froude Numbers: an Experimental Study." *Hydraulic Model Report No. CH75/09*, School of Civil Engineering, The University of Queensland, Brisbane, Australia, 89 pages & 3 videos (ISBN 9781864999730).	AUD$60.00		
CHANSON, H. (2009). "An Experimental Study of Tidal Bore Propagation: the Impact of Bridge Piers and Channel Constriction." *Hydraulic Model Report No. CH74/09*, School of Civil Engineering, The University of Queensland, Brisbane, Australia, 110 pages and 5 movies (ISBN 9781864999600).	AUD$60.00		
CHANSON, H. (2008). "Jean-Baptiste Charles Joseph BÉLANGER (1790-1874), the Backwater Equation and the Bélanger Equation." *Hydraulic Model Report No. CH69/08*, Div. of Civil Engineering, The University of Queensland, Brisbane, Australia, 40 pages (ISBN 9781864999211).	AUD$60.00		
GOURLAY, M.R., and HACKER, J. (2008). "Reef-Top Currents in Vicinity of Heron Island Boat Harbour, Great Barrier Reef, Australia: 2. Specific Influences of Tides Meteorological Events and Waves." *Hydraulic Model Report No. CH73/08*, Div. of Civil Engineering, The University of Queensland, Brisbane, Australia, 331 pages (ISBN 9781864999365).	AUD$60.00		
GOURLAY, M.R., and HACKER, J. (2008). "Reef Top Currents in Vicinity of Heron Island Boat Harbour Great Barrier Reef, Australia: 1. Overall influence of Tides, Winds, and Waves." *Hydraulic Model Report CH72/08*, Div. of Civil Engineering, The University of Queensland, Brisbane, Australia, 201 pages (ISBN 9781864999358).	AUD$60.00		
LARRARTE, F., and CHANSON, H. (2008). "Experiences and Challenges in Sewers: Measurements and Hydrodynamics." *Proceedings of the International Meeting on Measurements and Hydraulics of Sewers*, Summer School GEMCEA/LCPC, 19-21 Aug. 2008, Bouguenais, Hydraulic Model Report No. CH70/08, Div. of Civil Engineering, The University of Queensland, Brisbane, Australia (ISBN 9781864999280).	AUD$60.00		
CHANSON, H. (2008). "Photographic Observations of Tidal Bores (Mascarets) in France." *Hydraulic Model Report No. CH71/08*, Div. of Civil Engineering, The University of Queensland, Brisbane, Australia, 104 pages, 1 movie and 2 audio files (ISBN 9781864999303).	AUD$60.00		

CHANSON, H. (2008). "Turbulence in Positive Surges and Tidal Bores. Effects of Bed Roughness and Adverse Bed Slopes." *Hydraulic Model Report No. CH68/08*, Div. of Civil Engineering, The University of Queensland, Brisbane, Australia, 121 pages & 5 movie files (ISBN 9781864999198)	AUD$70.00		
FURUYAMA, S., and CHANSON, H. (2008). "A Numerical Study of Open Channel Flow Hydrodynamics and Turbulence of the Tidal Bore and Dam-Break Flows." *Report No. CH66/08*, Div. of Civil Engineering, The University of Queensland, Brisbane, Australia, May, 88 pages (ISBN 9781864999068).	AUD$60.00		
GUARD, P., MACPHERSON, K., and MOHOUPT, J. (2008). "A Field Investigation into the Groundwater Dynamics of Raine Island." *Report No. CH67/08*, Div. of Civil Engineering, The University of Queensland, Brisbane, Australia, February, 21 pages (ISBN 9781864999075).	AUD$40.00		
FELDER, S., and CHANSON, H. (2008). "Turbulence and Turbulent Length and Time Scales in Skimming Flows on a Stepped Spillway. Dynamic Similarity, Physical Modelling and Scale Effects." *Report No. CH64/07*, Div. of Civil Engineering, The University of Queensland, Brisbane, Australia, March, 217 pages (ISBN 9781864998870).	AUD$60.00		
TREVETHAN, M., CHANSON, H., and BROWN, R.J. (2007). "Turbulence and Turbulent Flux Events in a Small Subtropical Estuary." Report No. CH65/07, Div. of Civil Engineering, The University of Queensland, Brisbane, Australia, November, 67 pages (ISBN 9781864998993)	AUD$60.00		
MURZYN, F., and CHANSON, H. (2007). "Free Surface, Bubbly flow and Turbulence Measurements in Hydraulic Jumps." *Report CH63/07*, Div. of Civil Engineering, The University of Queensland, Brisbane, Australia, August, 116 pages (ISBN 9781864998917).	AUD$60.00		
KUCUKALI, S., and CHANSON, H. (2007). "Turbulence in Hydraulic Jumps: Experimental Measurements." *Report No. CH62/07*, Div. of Civil Engineering, The University of Queensland, Brisbane, Australia, July, 96 pages (ISBN 9781864998825).	AUD$60.00		
CHANSON, H., TAKEUCHI, M, and TREVETHAN, M. (2006). "Using Turbidity and Acoustic Backscatter Intensity as Surrogate Measures of Suspended Sediment Concentration. Application to a Sub-Tropical Estuary (Eprapah Creek)." *Report No. CH60/06*, Div. of Civil Engineering, The University of Queensland, Brisbane, Australia, July, 142 pages (ISBN 1864998628).	AUD$60.00		
CAROSI, G., and CHANSON, H. (2006). "Air-Water Time and Length Scales in Skimming Flows on a Stepped Spillway. Application to the Spray Characterisation." *Report No. CH59/06*, Div. of Civil Engineering, The University of Queensland, Brisbane, Australia, July (ISBN 1864998601).	AUD$60.00		
TREVETHAN, M., CHANSON, H., and BROWN, R. (2006). "Two Series of Detailed Turbulence Measurements in a Small Sub-Tropical Estuarine System." *Report No. CH58/06*, Div. of Civil Engineering, The University of Queensland, Brisbane, Australia, Mar. (ISBN 1864998520).	AUD$60.00		
KOCH, C., and CHANSON, H. (2005). "An Experimental Study of Tidal Bores and Positive Surges: Hydrodynamics and Turbulence of the Bore Front." *Report No. CH56/05*, Dept. of Civil Engineering, The University of Queensland, Brisbane, Australia, July (ISBN 1864998245).	AUD$60.00		
CHANSON, H. (2005). "Applications of the Saint-Venant Equations and Method of Characteristics to the Dam Break Wave Problem." *Report No. CH55/05*, Dept. of Civil Engineering, The University of Queensland, Brisbane, Australia, May (ISBN 1864997966).	AUD$60.00		
CHANSON, H., COUSSOT, P., JARNY, S., and TOQUER, L. (2004). "A Study of Dam Break Wave of Thixotropic Fluid: Bentonite Surges down an Inclined plane." *Report No. CH54/04*, Dept. of Civil Engineering, The University of Queensland, Brisbane, Australia, June, 90 pages (ISBN 1864997710).	AUD$60.00		

CHANSON, H. (2003). "A Hydraulic, Environmental and Ecological Assessment of a Sub-tropical Stream in Eastern Australia: Eprapah Creek, Victoria Point QLD on 4 April 2003." *Report No. CH52/03*, Dept. of Civil Engineering, The University of Queensland, Brisbane, Australia, June, 189 pages (ISBN 1864997044).	AUD$90.00		
CHANSON, H. (2003). "Sudden Flood Release down a Stepped Cascade. Unsteady Air-Water Flow Measurements. Applications to Wave Run-up, Flash Flood and Dam Break Wave." *Report CH51/03*, Dept of Civil Eng., Univ. of Queensland, Brisbane, Australia, 142 pages (ISBN 1864996552).	AUD$60.00		
CHANSON, H,. (2002). "An Experimental Study of Roman Dropshaft Operation : Hydraulics, Two-Phase Flow, Acoustics." *Report CH50/02*, Dept of Civil Eng., Univ. of Queensland, Brisbane, Australia, 99 pages (ISBN 1864996544).	AUD$60.00		
CHANSON, H., and BRATTBERG, T. (1997). "Experimental Investigations of Air Bubble Entrainment in Developing Shear Layers." *Report CH48/97*, Dept. of Civil Engineering, University of Queensland, Australia, Oct., 309 pages (ISBN 0 86776 748 0).	AUD$90.00		
CHANSON, H. (1996). "Some Hydraulic Aspects during Overflow above Inflatable Flexible Membrane Dam." *Report CH47/96*, Dept. of Civil Engineering, University of Queensland, Australia, May, 60 pages (ISBN 0 86776 644 1).	AUD$60.00		
CHANSON, H. (1995). "Flow Characteristics of Undular Hydraulic Jumps. Comparison with Near-Critical Flows." *Report CH45/95*, Dept. of Civil Engineering, University of Queensland, Australia, June, 202 pages (ISBN 0 86776 612 3).	AUD$60.00		
CHANSON, H. (1995). "Air Bubble Entrainment in Free-surface Turbulent Flows. Experimental Investigations." *Report CH46/95*, Dept. of Civil Engineering, University of Queensland, Australia, June, 368 pages (ISBN 0 86776 611 5).	AUD$80.00		
CHANSON, H. (1994). "Hydraulic Design of Stepped Channels and Spillways." *Report CH43/94*, Dept. of Civil Engineering, University of Queensland, Australia, Feb., 169 pages (ISBN 0 86776 560 7).	AUD$60.00		
POSTAGE & HANDLING (per report)	AUD$10.00		
GRAND TOTAL			

OTHER HYDRAULIC RESEARCH REPORTS

Reports/Theses	**Unit price**	**Quantity**	**Total price**
ZHANG, G. (2017). "Free-Surface Aeration, Turbulence, and Energy Dissipation on Stepped Chutes with Triangular Steps, Chamfered Steps, and Partially Blocked Step Cavities." *Ph.D. thesis*, The University of Queensland, School of Civil Engineering, 361 pages (DOI: 10.14264/uql.2017.906).	AUD$100.00		
WANG, H. (2014). "Turbulence and Air Entrainment in Hydraulic Jumps." *Ph.D. thesis*, School of Civil Engineering, The University of Queensland, Brisbane, Australia, 341 pages & Digital appendices (DOI: 10.14264/uql.2014.542).	AUD$100.00		
SIMON, B. (2014). "Effects of Tidal Bores on Turbulent Mixing: a Numerical and Physical Study in Positive Surges." *Ph.D. thesis*, School of Civil Engineering, The University of Queensland, Brisbane, Australia, 259 pages & 7 movies (DOI: 10.14264/uql.2014.19).	AUD$100.00		

KHEZRI, N. (2014). "Modelling Turbulent Mixing and Sediment Process Beneath Tidal Bores: Physical and Numerical Investigations." *Ph.D. thesis*, School of Civil Engineering, The University of Queensland, Brisbane, Australia, 267 pages.	AUD$100.00		
FELDER, S. (2013). "Air-Water Flow Properties on Stepped Spillways for Embankment Dams: Aeration, Energy Dissipation and Turbulence on Uniform, Non-Uniform and Pooled Stepped Chutes." *Ph.D. thesis*, School of Civil Engineering, The University of Queensland, Brisbane, Australia.	AUD$100.00		
REICHSTETTER, M. (2011). "Hydraulic Modelling of Unsteady Open Channel Flow: Physical and Analytical Validation of Numerical Models of Positive and Negative Surges." *MPhil thesis*, School of Civil Engineering, The University of Queensland, Brisbane, Australia, 112 pages.	AUD$80.00		
TREVETHAN, M. (2008). "A Fundamental Study of Turbulence and Turbulent Mixing in a Small Subtropical Estuary." *Ph.D. thesis*, Div. of Civil Engineering, The University of Queensland, 342 pages.	AUD$100.00		
GONZALEZ, C.A. (2005). "An Experimental Study of Free-Surface Aeration on Embankment Stepped Chutes." *Ph.D. thesis*, Dept of Civil Engineering, The University of Queensland, Brisbane, Australia, 240 pages.	AUD$80.00		
TOOMBES, L. (2002). "Experimental Study of Air-Water Flow Properties on Low-Gradient Stepped Cascades." *Ph.D. thesis*, Dept of Civil Engineering, The University of Queensland, Brisbane, Australia.	AUD$100.00		
CHANSON, H. (1988). "A Study of Air Entrainment and Aeration Devices on a Spillway Model." *Ph.D. thesis*, University of Canterbury, New Zealand.	AUD$60.00		
POSTAGE & HANDLING (per report)	AUD$10.00		
GRAND TOTAL			

CIVIL ENGINEERING RESEARCH REPORT CE

The Civil Engineering Research Report CE series is published by the School of Civil Engineering at the University of Queensland. Orders of any of the Civil Engineering Research Report CE should be addressed to the School Secretary.

School Secretary, School of Civil Engineering, The University of Queensland
Brisbane 4072, Australia
Tel.: (61 7) 3365 3619 Fax: (61 7) 3365 4599
Url: http://http://www.civil.uq.edu.au// Email: enquiries@civil.uq.edu.au

Recent Research Report CE	**Unit price**	**Quantity**	**Total price**

WANG, H., and CHANSON, H. (2017). "How a better understanding of Fish-Hydrodynamics Interactions might enhance upstream fish passage in culverts." *Research Report No. CE162*, School of Civil Engineering, The University of Queensland, Brisbane, Australia, 43 pages (ISBN 978-1-74272-192-7).	AUD$15.00		
CALLAGHAN, D.P., NIELSEN, P., and CARTWRIGHT, N. (2006). "Data and Analysis Report: Manihiki and Rakahanga, Northern Cook Islands - For February and October/November 2004 Research Trips." *Research Report CE161*, Division of Civil Engineering, The University of Queensland (ISBN No. 1864998318).	AUD$10.00		
GONZALEZ, C.A., TAKAHASHI, M., and CHANSON, H. (2005). "Effects of Step Roughness in Skimming Flows: an Experimental Study." *Research Report No. CE160*, Dept. of Civil Engineering, The University of Queensland, Brisbane, Australia, July (ISBN 1864998105).	AUD$10.00		
CHANSON, H., and TOOMBES, L. (2001). "Experimental Investigations of Air Entrainment in Transition and Skimming Flows down a Stepped Chute. Application to Embankment Overflow Stepped Spillways." *Research Report No. CE158*, Dept. of Civil Engineering, The University of Queensland, Brisbane, Australia, July, 74 pages (ISBN 1 864995297).	AUD$10.00		
HANDLING (per order)	AUD$10.00		
GRAND TOTAL			

Note: Prices include postages and processing.

PAYMENT INFORMATION

1- VISA Card

Name on the card :	
Visa card number :	
Expiry date :	
Amount :	AUD$ ....

2- Cheque/remittance payable to: THE UNIVERSITY OF QUEENSLAND and crossed "Not Negotiable".

N.B. For overseas buyers, cheque payable in Australian Dollars drawn on an office in Australia of a bank operating in Australia, payable to: THE UNIVERSITY OF QUEENSLAND and crossed "Not Negotiable".

Orders of any Research Report should be addressed to the School Secretary.

School Secretary, School of Civil Engineering, The University of Queensland
Brisbane 4072, Australia - Tel.: (61 7) 3365 3619 - Fax: (61 7) 3365 4599
Url: http://http://www.civil.uq.edu.au// Email: enquiries@civil.uq.edu.au